The Pennsylvania State University

The Graduate School

ADVANCED GRID-STIFFENED COMPOSITE SHELLS FOR APPLICATIONS IN HEAVY-LIFT HELICOPTER ROTOR BLADE SPARS

A Doctoral Dissertation in

Aerospace Engineering

by

Sreenivas Narayanan Nampy

Submitted in Partial Fulfillment

of the Requirements

for the Degree of

Doctor of Philosophy

December 2012

The dissertation of Sreenivas Narayanan Nampy was reviewed and approved* by the following:

Edward C. Smith
Professor of Aerospace Engineering
Dissertation Advisor, Chair of Committee

Charles E. Bakis
Distinguished Professor of Engineering Science and Mechanics

Farhan S. Gandhi
Professor of Aerospace Engineering

Clifford J. Lissenden
Professor of Engineering Science and Mechanics

George A. Lesieutre
Professor and Head of Aerospace Engineering

*Signatures are on file in the Graduate School.

Abstract

Modern rotor blades are constructed using composite materials to exploit their superior structural performance compared to metals. Helicopter rotor blade spars are conventionally designed as monocoque structures. Blades of the proposed Heavy Lift Helicopter are envisioned to be as heavy as 800 lbs when designed using the monocoque spar design. A new and innovative design is proposed to replace the conventional spar designs with light weight grid-stiffened composite shell. Composite stiffened shells have been known to provide excellent strength to weight ratio and damage tolerance with an excellent potential to reduce weight. Conventional stringer–rib stiffened construction is not suitable for rotor blade spars since they are limited in generating high torsion stiffness that is required for aeroelastic stability of the rotor. As a result, off-axis (helical) stiffeners must be provided. This is a new design space where innovative modeling techniques are needed. The structural behavior of grid-stiffened structures under axial, bending, and torsion loads, typically experienced by rotor blades need to be accurately predicted. The overall objective of the present research is to develop and integrate the necessary design analysis tools to conduct a feasibility study in employing grid-stiffened shells for heavy-lift rotor blade spars.

Upon evaluating the limitations in state-of-the-art analytical models in predicting the axial, bending, and torsion stiffness coefficients of grid and grid-stiffened structures, a new analytical model was developed. The new analytical model based on the smeared stiffness approach was developed employing the stiffness matrices of the constituent members of the grid structure such as an arch, helical, or straight beam representing circumferential, helical, and longitudinal stiffeners. This analysis has the capability to model various stiffening configurations such as angle-grid, ortho-grid, and general-grid. Analyses were performed using an existing state-of-the-art and newly developed model to predict the torsion, bending, and axial stiffness of grid and grid-stiffened structures with various stiffening configurations. These predictions were compared to results generated using finite element analysis (FEA) to observe excellent correlation (within 6%) for a range of parameters for grid and grid-stiffened structures such as grid density, stiffener angle, and aspect ratio of the stiffener cross-section. Experimental results from cylindrical grid specimen testing were compared with analytical prediction using the new analysis. The new analysis predicted stiffness coefficients with nearly 7% error compared to FEA results. From the parametric studies conducted, it was observed that the previous state-of-the-art analysis on the other hand exhibited errors of the order of 39% for certain designs. Stability evaluations were also conducted by integrating the new analysis with established stability formulations. A design study was conducted to evaluate the potential weight savings of a simple grid-stiffened rotor blade spar structure compared to a baseline monocoque design. Various design constraints such as stiffness, strength, and stability were imposed. A manual search was conducted for design parameters such as stiffener density, stiffener angle, shell laminate, and stiffener aspect ratio that provide lightweight grid-stiffened designs compared to the baseline. It was found that a weight saving of 9.1% compared to the baseline is possible without violating any of the design constraints.

Table of Contents

List of Figures

List of Tables

List of Symbols

$()^g$	Denotes grid layer or grid
$()^{os}$, $()^{oe}$, $()^{oc}$	Orthogrid topology; simple, elastic, and clamped support
α_{sc}	Shear correction factor
β	Fiber orientation angle
$\boldsymbol{\Delta}_c$	Displacement vector in (r, ψ, z) coord. sys
$\boldsymbol{A}^g$	In-plane stiffness matrix of the grid layer
$\boldsymbol{F}_c$	Force vector in (r, ψ, z) coord. sys
$\boldsymbol{k}_{bc}$, $\boldsymbol{K}_{bc}$	Local and global stiffness matrices of a beam-column
$\boldsymbol{T}_s$	Transformation matrix for lamina strains
δ_x, δ_y, δ_ψ, δ_z	Beam end deflections
δ_x, δ_y, δ_z	Beam deflections in x, y, and z directions

ε_L^t, ε_L^c	Tensile and compressive strains of stiffeners in the fiber direction
ε_x, ε_y, ε_ψ	In-plane normal strains
γ_{xy}, $\gamma_{x\phi}$	Engineering shear strains
γ_{xz}, γ_{yz}, $\gamma_{\psi z}$	Transverse shear strains
κ_x, κ_y, κ_{xy}	Curvatures, twist
λ_{GS}, λ_M	Buckling loads of grid-stiffened, monocoque structures
ν_{12}	Poisson ratio
$\overline{\alpha}_y$, $\overline{\alpha}_z$	Non-dimensional shear correction parameters
$\overline{\lambda}$	Compr. buckling load ratio parameter
$\overline{d}_0$	Straight distance between longitudinal stiffeners
$\overline{EI}$	Bending stiffness ratio parameter
$\overline{f}$	Failure load ratio parameter
$\overline{GJ}$	Torsion stiffness ratio parameter
$\overline{W}$	Weight ratio parameter
ϕ_x, ϕ_y, ϕ_ψ, ϕ_z	Beam end rotations
ψ	Helix pitch angle, circumferential coordinate of the cylinder
σ_L^t, σ_L^c	Lamina tensile and compressive max. allowable stresses in fiber direction

σ_T^t, σ_T^c	Lamina tensile and compressive max. allowable stresses in transverse to fiber direction
θ	Stiffener orientation angle
ξ	Helix angle: angle between the helical beam and the cylinder base
ζ_1	Geometry parameter in Halpin-Tsai equation
${}_ca_{66}$	Shear compliance of cylindrical grid
B_t	A transformation matrix (t,n,b) to (r,ψ,z)
c, s	$\sin\theta$, $\cos\theta$
d_0, d_{90}, d_θ	Spacing between longitudinal, transverse, and angle stiffeners
D_o	Outer diameter of the cylinder
e_o	Node offset in stiffener overlap section
e_s	Grid layer offset from the reference surface of the grid-stiffened structure
E_{11}, E_{22}	Elastic modulus in 1, 2 direction
E_f, E_m	Elastic modulus of fiber, matrix
EA_b	Axial stiffness of the rotor blade
EI_b^f, EI_b^l	Flap, lag bending stiffness of the rotor blade
EI_t, EI_n, EI_b	Beam bending stiffness with respect to t, n, and b axes

EI_x, EI_y, EI_z — Beam bending stiffness with respect to x, y, and z axes

EI_x, EI_y, EI_z — Beam bending stiffness with respect to x, y, and z axes

EI_m — Bending stiffness of the baseline

F_x, F_y, F_z — Beam forces in x, y, and z directions

f_{gs}, f_m — Failure loads of grid-stiffened, monocoque structures

G_t — A transformation matrix (t, n, b) to (r, ψ, z)

G_{12}, G_{23} — Shear modulus in ply local coordinates

GA — shear stiffness of the beam

GJ_b — Torsion stiffness of the rotor blade

GJ_m — Torsion stiffness of the baseline

h_s, b_s — Height and width of the stiffener cross-section

K_{gs}, K_m — Stiffness of grid-stiffened, monocoque structures

l — General notation for beam length

l — General notation for beam length

L_0, L_{90}, L_θ — Length of the longitudinal, transverse, and angle stiffeners

L_a — Length of the unitcell in tube axial direction

l_x, l_y — Unit-cell dimensions

m_x, m_y, m_ψ, m_z	plate or shell loads per unit length
M_x, M_y, M_z	Beam moments in x, y, and z directions
n_x, n_y, n_ψ, n_z	plate or shell loads per unit length
P_a, F_a, T_a	Applied tip transverse, axial loads, torque on the specimens
R_i, R_o	Inner and outer radii of the shell
R_s	Radius of the grid-stiffened shell at shell mid-plane
t_m	Thickness of the monocoque shell
t_s, t_p	Shell and plate thickness
u, v, w	Longitudinal, transverse, and out-of-plane deflection of plate or shell
V_i	Input vector of design variables
W_m	Weight of monocoque shell
W_s	Weight of shell attached to the grid layer
w_{gE}, u_{gE}, ϕ_{gE}	Tip transverse bending, axial extension, twist of grid specimens
x, y, z	Longitudinal, transverse, and normal coordinates
${\tau_{LT}^{a}}^2$	Lamina allowable shear stress
N_{a1}, N_a	No. of angle stiffeners in one direction, both directions. $N_a = 2N_{a1}$

Acknowledgments

I'm greatly indebted to my parents, Mr. Narayanan and Mrs. Lalitha, my sister Sreelekshmi, Ammachu and in-laws for their unrelenting support, kindness, prayers, encouragement, and love through out. I'm just fortunate to be a part of this family. My dear wife, Sudha has always been with me thick and thin. Her love, patience, understanding, and critique has been a constant encouragement. I'm happy that I have you and I love you. Our sweet daughter, Diya makes us smile and I owe her a doll with long hair.

I take this opportunity to express my sincere respect to those teachers who have motivated me right from my childhood. You taught me to be ambitious. I always cherish the wisdom you have passed on to me.

Thank you Almighty for all the wonderful things.

I'm deeply obliged to Prof. Ed Smith for everything he has done for me. No words can describe the kindness and understanding he has shown to help me each and every time. He always guided me in the right direction, both in academics and research, including this arduous endeavor. His nurturing has helped me to become a better person. He gave me the courage to venture into the world of research and made me who I'm today.

I would like to express my sincere gratitude to Prof. Charles E. Bakis for all his support and constant encouragement. His technical insights have been essential for the completion of this work. He was always helpful and ready to share his knowledge.

A big thank you to both Prof. Gandhi and Prof. Lissenden for serving in my committee and providing their valuable time, feedback, and suggestions.

Dr. McLaughlin has been a pleasure to work with and learn from. He was always encouraging and taught me to look at the bright side. Thank you, Dr. Lesieutre for your help in getting this done.

Dr. Kevin Koudela of Applied Research Lab at Penn State University for his technical comments and insights during our regular meetings.

I'm grateful for all the help I have received from the Penn State Aerospace department staff.

How could I not thank those numerous Rotorcraft center friends and colleagues for the wonderful times I have had as a graduate student. A special thanks to Abraham Matthew for being so helpful over these years. Thank you, Mihir and Tensen for all the help you have provided in many different ways. They mean a lot to me.

Sujith Nair, Padma Kumar, Nitish Mathew: those great times we have had on and off campus are very precious which I cherish to this day. I learned and continue to learn a lot from you guys.

Thank you Vikas Argod and Abdul Aziz for helping me with high performance computing resources.

I really enjoyed being with Tom Gibson and Di-Anne Gibson. Those little things, those excursions, parties, and constant support, all made me feel at home.

I'm happy to have all those friends at home and abroad who have given me their moral support and help.

I'm thankful for the financial support provided by the Vertical Lift Research Center of Excellence (VLRCOE) of the Department of Aerospace Engineering at Penn State University. I would like to thank our sponsor, the U.S. Army for their financial support to conduct this research.

This research is partially funded by the U.S. Government under Agreement No. W911W6–06–2–0008. The U.S. Government is authorized to reproduce and distribute reprints notwithstanding any copyright notation thereon. The views and conclusions contained in this document are those of the authors and should not be interpreted as representing the official policies, either expressed or implied, of the U.S. Government.

Chapter 1

Introduction

1.1 Background and Motivation

Modern helicopter rotor blades are typically fabricated from composite materials due to their superior strength to weight ratio, fatigue tolerance, resistance to corrosion, and the ability to use automated fabrication techniques. The blade as a whole experiences operational loads due to aerodynamic pressure along with gravitational and inertial effects which originate from steady flight, maneuver, or gust conditions. Generally, these force resultants cause axial tension, bending, shear, and torsion loads in all parts of the blade along with local pressure loads imposed on the skin. In addition to these, environmental factors such as temperature, moisture, and skin erosion also affect the integrity of the structure. The blades are therefore designed to withstand critical combination of these loads while keeping the weight of the blade structure to a minimum.

The composition and construction of the blade structure are dictated by the mission requirements the aircraft must be designed to satisfy. The main rotor of the conventional helicopter is the sole source of propulsion and lifting surface of the aircraft, Hence the design of it is directly controlled by the empty weight, payload requirements, and the speed and range of the aircraft. Additionally, the blades have to be designed to withstand numerous threats ranging from low to high velocity impact to be certified for use in military aircraft. While the blades are not expected to retain their original structural integrity after an impact event, they must be designed to sustain a flight long enough to get the aircraft to safety.

1.1.1 Heavy-lift helicopter blades

Johnson et al. [1] conducted the rotor system investigations of three heavy-lift rotorcraft designs. The blades of these aircraft are envisioned to be much larger and heavier than the rotor blades currently in operation. The rotors may have a diameter in the range of 23–27.5 m (76–90 ft) with blades having chord dimensions in the range of 0.9–1.5 m (3–5 ft) at $3/4$ of the blade radius. The model of the Large Civil Tiltrotor (LCTR) aircraft is shown in Fig 1.1. Designing such large, wing-like, blades for minimized weight is a challenging task, especially when constraints such as strength and stiffness have to be met. The spar structures of composite rotor blades, are currently designed as monocoque D-spars with single or multi-cell cross-section configurations. Examples of typical cross-sections of certain blades are shown in Fig. 1.2.

Zhang and Smith [2] conducted an extensive laminate design study with stiffness and strength constraints using the conventional single cell D-spar designs for heavy-lift helicopter blades. They concluded that a single blade could weigh nearly 360 kg ($\approx$ 800 lb). The weight predictions for different blade designs are shown in Fig. 1.3. These heavy designs are mainly driven by the high torsion stiffness and strength requirements.

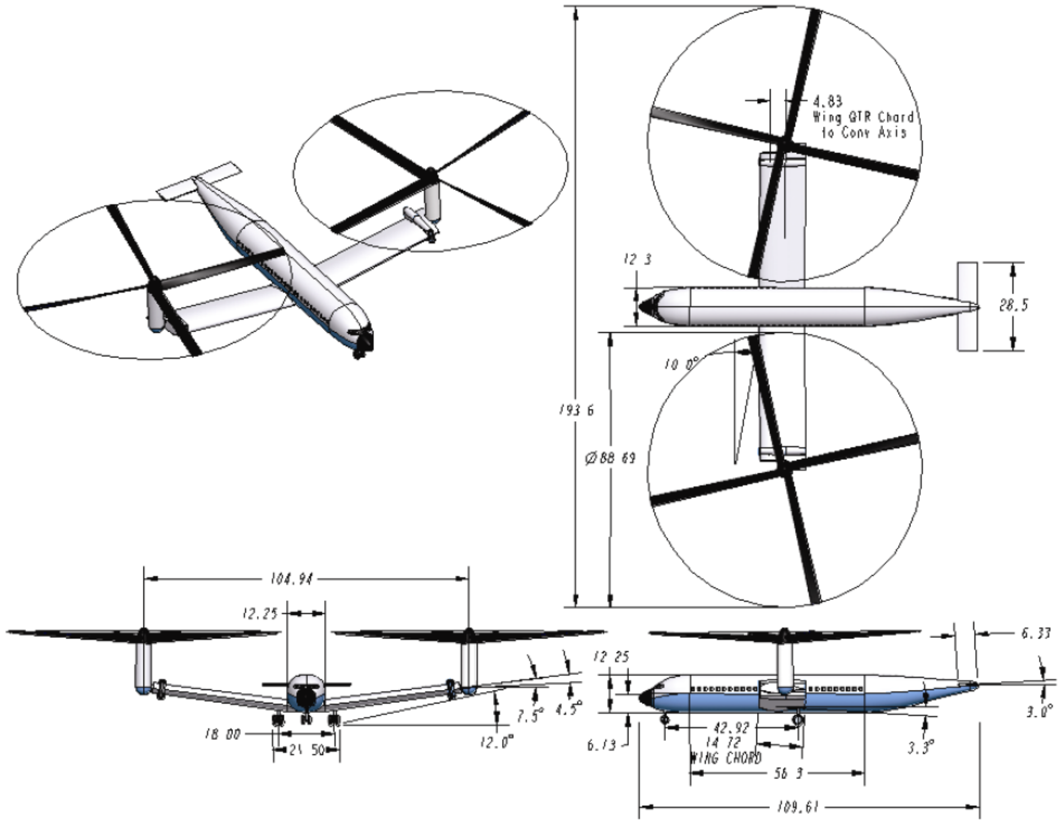

Figure 1.1. Large Civil Tiltrotor (LCTR) [1]. Number of blades per rotor- 4. Blade chord at 0.75*R*- 3.07 ft (0.94 m)

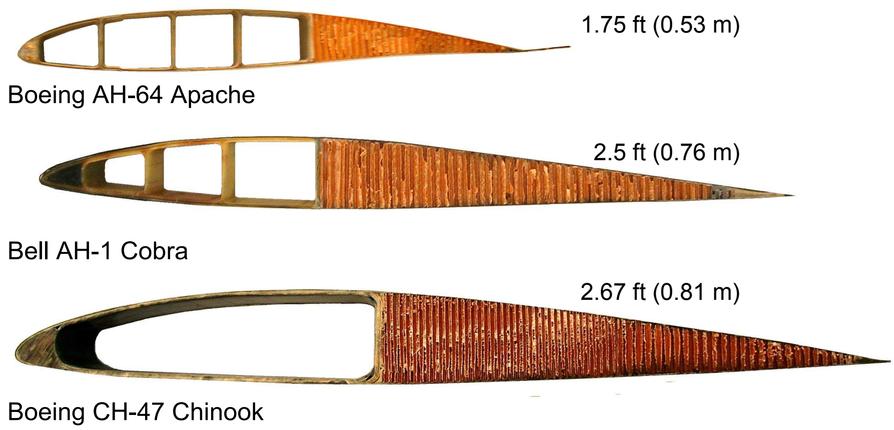

Figure 1.2. Rotor blade cross-sections showing different spars designs. Source: Lab display articles

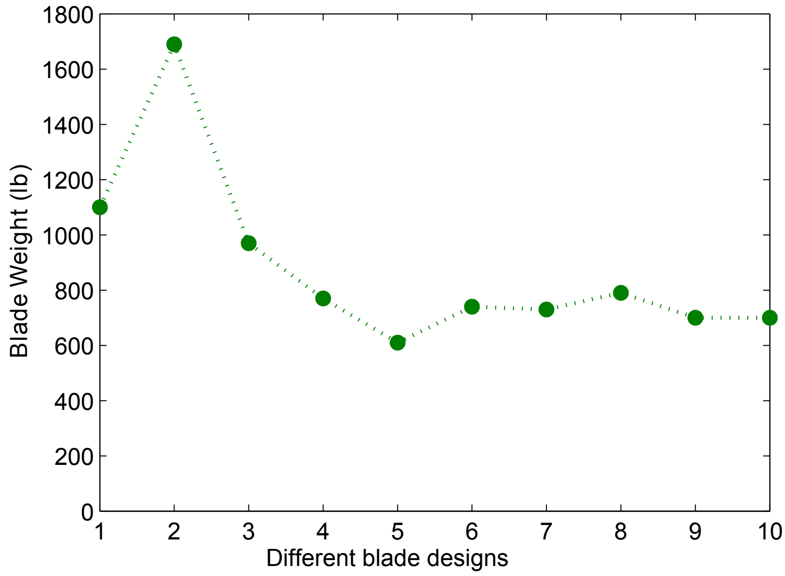

Figure 1.3. Heavy-lift blade weights of various designs from the monocoque laminate design study [2]

The D-spar being the primary load bearing component of the blade, sufficient number of 0° and 45° plies need to be added to the spar laminate to provide sufficient axial, bending, and torsion stiffness to maintain aeroelastic stability. The lamina strains must be limited to prevent material failure as well. As a consequence of the above design requirements, the spar laminates become thicker in the design process. Introducing design constraints such as fatigue strength, damage tolerance, sufficient residual strength after impact, environmental factors, etc., could further increase the blade weight.

The impacts of having such heavy and large rotor blades are multiple fold. The blades experience extremely high stresses along the length due to bending and twisting deformations under the aerodynamic loads. It could also lead to high control loads in the hub that could eventually be detrimental to the airframe and payload. Also, a weight reduction in rotor system is a gain in the payload carrying capacity. Therefore, it is desirable that the blade weight is reduced.

A design domain that has a large wing-like structures subject to helicopter rotor blade loads introduces new design challenges. The loading conditions and the in-flight responses of the rotor blades are significantly different from that of a fixed wing. In order to achieve the goal to obtain a lighter blade, new and innovative structural design concepts need to be introduced and the new design space has to be explored. The initial step in addressing these challenges is to explore how large lightweight structures are currently designed for aerospace applications.

1.1.2 Large lightweight structures

The aerospace industry employs several design methodologies to address various structural and operational requirements. Components such as airplane fuselages, launch vehicle shrouds, etc., are seldom constructed as monocoque structures. Instead, rib–stringer construction generally termed as *semi-monocoque* design is generally adopted. The reasons include, but are not limited to, reduced weight while providing high stiffness and strength, automated manufacturing process, ease of maintenance, increased damage tolerance, and so on. A semi-monocoque structure with ribs (transverse or circumferential) and stringers (longitudinal) oriented orthogonal to each other acting as the primary load bearing entity and a skin (shell or plate) attached to the rib–stringer grid structure by welds or fasteners [3] in the case of metallic structures. In the case of fiber reinforced polymer composites, the stiffeners and the skin are attached using fasteners, adhesives, or co-curing of these components.

In a semi-monocoque design, the primary function of the skin is to provide a smooth profile which can support the aerodynamic pressure loads. These loads are in turn transmitted to the ribs and stringers. This results in the skin resisting the shear loads while the axial and bending loads are reacted by the combined action of the stiffeners and the skin. In general, stiffened structures are characterized by a skin (plate or shell) with attached stiffeners oriented in one or more directions. The classical stiffening configuration is when the ribs and stringers are orthogonal and parallel to the structural axes. In the absence of the skin, the framework of stiffeners is termed grid structure. A grid structure could consist of stiffeners oriented in a 3D space forming truss-like patterns. The individual members can be straight or curved depending on the shape profile. In the context of the present research, the terminology is confined to those structures that have the stiffeners confined to a surface that is planar or cylindrical.

A famous example of a successful application of grid structures in a fuselage construction is the Vickers Wellington Bomber of the second world war. Figure 1.4 [4] shows the aircraft fuselage frame where the grid construction is clearly visible. The material used for geodesic construction was an aluminum alloy for lightweight designs. The grid structure was designed to act as a skeleton for the flexible skin that formed the aerodynamic surface. The purpose of such a construction was to increase the survivability against anti-aircraft projectiles with the notion that a skin-damaged aircraft would still be airworthy for a safe return. Also, the fuselage grid structure could still retain a sufficient degree of structural integrity after sustaining a localized damage due to the redundant loads paths provided by the stiffeners.

Almost all aircraft designs employ classical rib–stringer construction for fuselage and wing structures. The fuselage section of a passenger airliner is shown in Fig. 1.5 [5]. There are innumerable examples to demonstrate the robustness, cost, and weight savings of rib–stringer construction; from bridges to automobiles to spacecraft structures. In summary, semi-monocoque structures provide excellent strength to weight ratio while facilitating light-weight designs.

Figure 1.4. Grid fuselage of the Vickers Wellington bomber [4]

Figure 1.5. Airbus A380 aircraft fuselage showing rib–stringer construction [5]

1.1.3 Composite semi-monocoque structures

Composite materials are known for their superior performance in weight critical aerospace applications compared to similar metallic designs. The high strength and stiffness exhibited by composite plies in their fiber direction made them a promising candidate for grid designs. The integrally stiffened all-composite structures, generally referred to as advanced grid-stiffened (AGS) structures, were originally developed by McDonnel-Douglas Corporation in the early 1970s. In that period, McDonnell Douglas and NASA [6] identified the limitations of the conventional stiffening configuration, rib–stringer construction called ortho-grid, in resisting shear loads. Their research identified a unique configuration where the stiffeners form a network of equilateral triangles called *isogrid*. It was also recognized to be a good candidate for automated winding process. This was a giant leap in terms of weight savings from the conventional manufacturing methods where the individual components were connected together using fasteners. Also, the isogrid configuration was demonstrated to be superior to ortho-grid design in resisting in-plane loads without any weight or out-of-plane bending stiffness penalty.

Under the US Army's Advanced Composite Airframe Program (ACAP), Bell Helicopter Textron (along with Sikorsky) was awarded a contract to design and develop an all-composite helicopter. The main objective of the ACAP program was to reduce weight, cost and improve military helicopter characteristics by the application of advanced composite material construction. The company developed several airframe prototypes and completed their testing by the end of 1982 [7]. The Bell ACAP helicopter, D-292 is shown in Fig. 1.6. D-292's entire elongated pod-and-boom airframe is constructed of glass-reinforced plastic (GRP), graphite, and Kevlar. D-292's basic load-bearing structure is constructed primarily of graphite/epoxy. The flooring and most of the aircraft's exterior shell structure are made of a more ballistic-tolerant Kevlar/epoxy or glass/epoxy blend.

Figure 1.6. Bell ACAP D-292 experimental aircraft in flight (top). Vertical drop test of a D-292 airframe (bottom). The truss-like tailboom structure is also shown [8]

D-292 aircraft featured a weight reduction of 22% in the airframe structure, a 17% savings in cost, survivability in a vertical crash, and reduced radar signature. These comparisons were made with contemporary aircraft with conventional metal construction. The ACAP program proved successful in meeting its objectives to demonstrate the use of advanced composites in a fully militarized airframe [8]. The hexagonal semi-monocoque tailboom construction is particularly relevant to the present research since its structural configuration was adopted to reduce weight as well as to increase the damage tolerance while maintaining the stringent strength and stiffness requirements.

Remarkable advancements in composite manufacturing techniques during the last couple of decades makes it feasible to economically and efficiently fabricate grid-stiffened structures. Two notable examples are the Tooling Reinforced Integral Grid (TRIG) concept from Stanford University and the hybrid Tooling concept from the Air Force Research Laboratory [9]. The section of the conical AGS payload shroud fabricated using hybrid tooling is shown in Fig. 1.7. The AGS shroud weighed only 37 kg (82 lbs) whereas the existing aluminum shroud structure, that this design replaced, weighed 97 kg (212 lbs). In addition to a remarkable 60% reduction in weight, the AGS shroud program demonstrated 88% reduction in manufacturing time, a 300% strength increase, and an impressive 10 times stiffness increase over the existing aluminum designs. This AGS shroud was a part of the space vehicle that was launched in the February of 1997. This was also the first successful space flight of an AGS structure.

Figure 1.7. Conical grid-stiffened structure with off-axis (helical) stiffeners [9]

The fabrication of AGS structures using automated continuous wet filament winding and co-curing of the stiffeners and the skin, significantly reduced the cost of manufacturing [10, 11]. The automated filament winding of composite grid is shown in Fig. 1.8 [11]. AGS structures possess excellent resistance to damage propagation and delamination while exhibiting high strength to weight ratios [9, 11–13]. They are therefore used currently in rotorcraft and aircraft wing and fuselage components, rocket interstages, payload shrouds, etc. The energy absorption characteristics of grid-stiffened composite panels were studied using experimental evaluation and numerical simulations [14, 15]. It was demonstrated that they are superior to the conventional laminated shells.

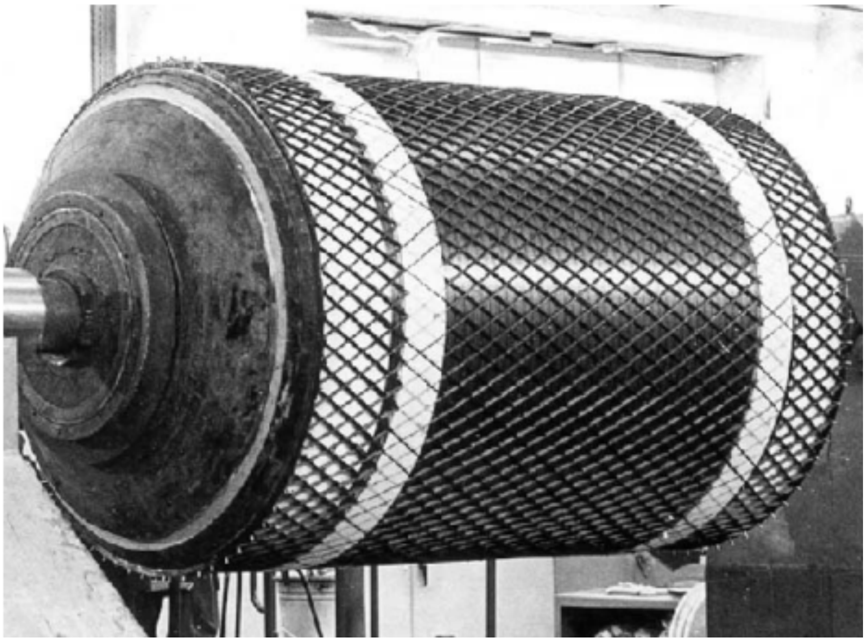

Figure 1.8. Automated filament winding of a grid structure with helical stiffeners [11]

Recent accomplishments in the large scale use of composite materials in airframe construction include aircraft such as the Boeing 787 and Airbus A380 commercial aircraft. The A380 program used glass reinforced aluminum (Glare) and carbon fiber reinforced plastic (CFRP) in the fuselage and wing sections. Altogether, composite materials accounted for nearly 16% by weight of the A380 airframe [16] saving about 15 tons over the weight of an equivalent all-metal structure (total empty aircraft weight is nearly 170 tons.)

The advantages composite grid-stiffened structures in terms of their high strength to weight ratio, damage tolerance, and the design opportunities arising from the arrangement of stiffeners in off-axis orientations were recognized and applied successfully by various aerospace programs as described. The advantages of grid-stiffened structures coupled with advanced grid fabrication techniques make them an excellent candidate for large lightweight aerospace applications. Considering the larger size and increased weight of the heavy-lift rotor blades compared to the conventional rotor blades in operation, the present study aims to evaluate the potential of employing grid-stiffened composite structures for heavy-lift rotor blade spars.

In the context of application of grid structures for rotor blade spars, a study conducted in the early 1970s by Lockheed-California and the US Army Air Mobility R&D Lab must be mentioned. This was a feasibility study on using composite grid designs (including off-axis stiffeners) for a helicopter main rotor blade spar [17, 18]. The purpose of this study was to investigate the survivability of the blade structure against 23 mm High Explosive Incendiary Tracer (HEI-T) projectiles. The grid spar specimen from that study is shown in Fig 1.9. The driving force behind this research was that the grid structures are crack-insensitive due to redundant load paths provided by the stiffeners despite localized damage. The fabrication was done by hand to generate grids with an elongated-oval cross-section as shown in Fig. 1.10. Apart from the conventional rib–stringer configuration, off-axis stiffeners were also used to enhance the torsional stiffness. The composite grid spar was provided with a nominal wrap of $[\pm 45]_s$ laminate. The whole blade structure had an additional $[\pm 45]_s$ wrap, which acted as the skin structure.

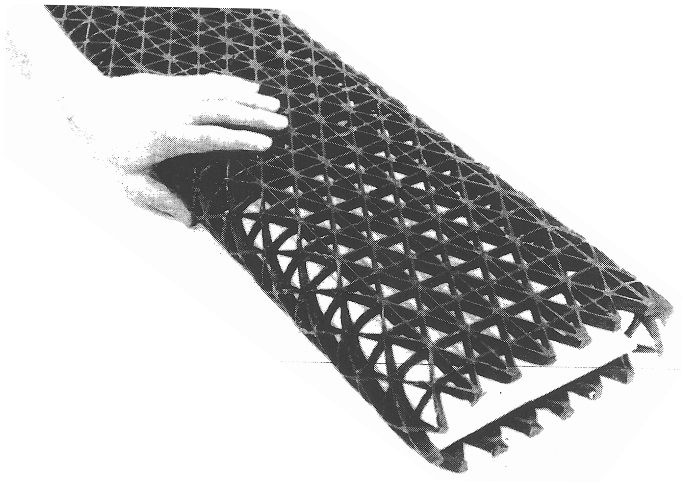

Figure 1.9. Lockheed grid spar made from Graphite/Epoxy material with longitudinal, transverse, and off-axis stiffeners [18]

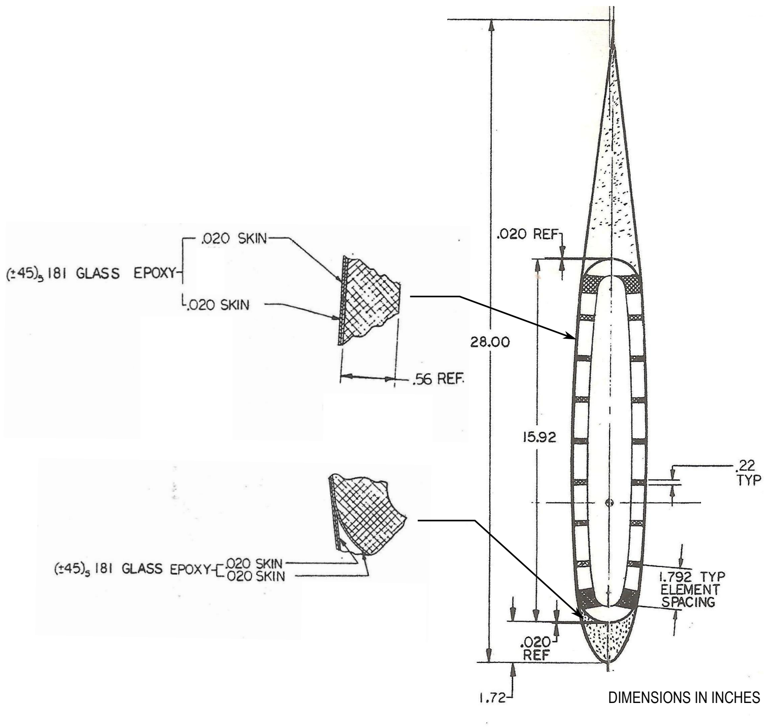

Figure 1.10. Lockheed geodesic blade section showing the geometry and composition of grid spar and skin wrap [18]

The hand-wound fabrication process had several limitations resulting in large discrepancies between analytical predictions and experimental results. The fatigue studies performed on the ballistic damaged grid specimen by applying cyclic loading, which was estimated to be equivalent to over 23 hours of flight time, demonstrated excellent damage tolerance characteristics. The study concluded that the grid spar is a promising concept to increase the survivability of the blades. The lack of efficient and robust grid fabrication methodology was cited as the key limiting factor in grid spar applications. Based on the literature review conducted, this [18] is the only study prior to the present research that investigated the application of composite grids in helicopter rotor blade spar design.

Apart from the strength requirements, the torsional and bending stiffness requirements are high for the helicopter rotor blades. Therefore, stiffening configurations other than the conventional ortho-grid (rib–stringer) must be considered. Various grid configurations [19] are illustrated in Fig. 1.11. Together, the ribs and stringers in an ortho-grid construction provide excellent resistance to bending, axial, and circumferential loads and are therefore utilized in compression and pressure loaded structures. Inclusion of oblique (angle or off-axis) stiffeners, which are oriented at an arbitrary angle with respect to the longitudinal axis, provide additional functionality in resisting in-plane shear, which is analogous to the off-axis plies in composite laminates. When a structure has only angle stiffeners, generally provided in symmetric $\pm\theta$ pairs with respect to the longitudinal axis, the configuration is termed *angle-grid*. A configuration with both ortho- and angle-grid, when appropriately arranged, results in a generalized configuration called *general-grid*. As shown in the figure, AL-grid and AT-grid are examples where the former has the no transverse stiffeners and the latter has no longitudinal stiffeners. The isogrid configuration is also illustrated. It should be noted that additional angle stiffener pairs can be added to the configuration such as, $\pm\theta_1$, $\pm\theta_2$, $\pm\theta_3$, ... $\pm\theta_n$. In the present study, the number of oblique stiffener pair is restricted to one symmetric pair.

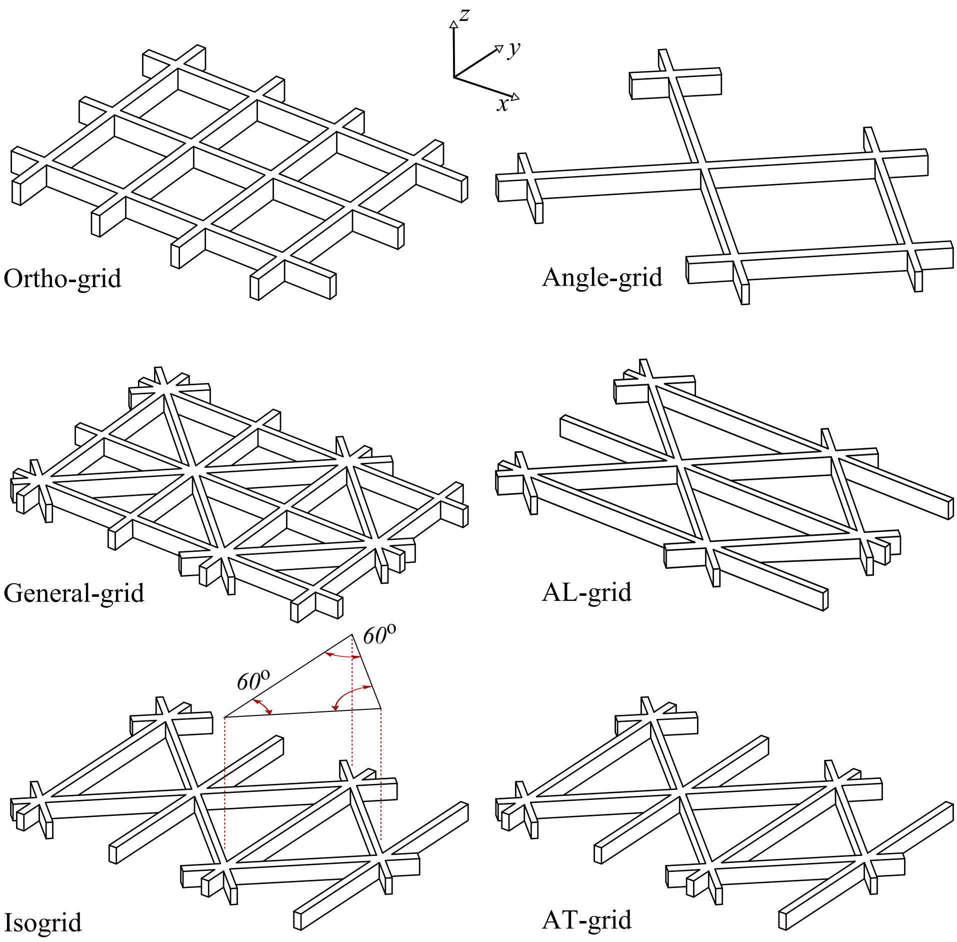

Figure 1.11. Different grid configurations [19]. *x* refers to the longitudinal direction

The grid-stiffened structures offer a greater degree of design flexibility compared to a conventional monocoque design. The ability to manipulate the design variables such as the geometry of the stiffener cross-section, stiffener orientation, stiffening configurations (topology), and choice of different material systems open up a large design space where a comprehensive optimization study can be performed when required.

1.2 Grid-stiffened heavy-lift helicopter blade spar

Considering the advantages of grid-stiffened structures, it is proposed to replace the conventional D-spar laminate with an AGS structure for the heavy-lift helicopter blade spar. A concept is illustrated in Fig. 1.12. The concept include an elliptical cross-sectioned spar in recognition of the fact that such a geometry would be conducive to automated fabrication and would also fit the cross-sectional shape of the blade. In the present investigation however, the spar geometry is idealized to a circular cross-section to simplify the analysis. The filler regions shown in the aft and fore sections of the spar are for demonstration purpose only since the design of these sections is out of the scope of the present investigation. Also, only the spar, which is a grid-stiffened structure, is considered in this study.

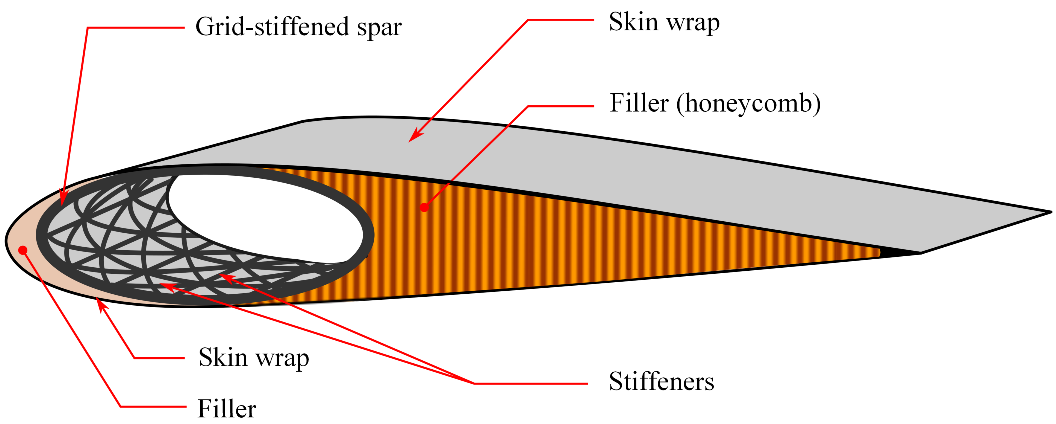

Figure 1.12. Heavy-lift helicopter rotor blade cross-section showing grid-stiffened spar concept. Present study idealizes the spar structure to a circular cylindrical cross-section

AGS structures are primarily used in applications where the geometry of the structure is large compared to the individual stiffeners . The design domain changes dramatically when the scope of its application is in the domain of a helicopter blade spar designs. The controlling loading cases are different, for example, compared to a space launch vehicle fairing or an aircraft fuselage. In addition, the structural integrity requirements such as stiffness, strength, and stability are different. As such, the applicability of the various analysis tools currently available are to be evaluated before they can be applied. This is particularly true in the case of computationally efficient analytical models.

1.3 State-of-the-art analysis tools

Several methods exist to analyze AGS structures. Those that are widely employed are based on (i) finite element formulations and (ii) equivalent (smeared) stiffness approach. The finite element models consist of commercially available codes or models with specially developed elements utilized to analyze stiffened structures. These tools are capable of modeling the exact geometry of the AGS structures. The Equivalent (smeared) Stiffness Models (ESM) on the other hand are approximate closed-form formulations, but rather simple and efficient for preliminary studies [19–21]. The principle behind ESM is that the grid layer (consists of stiffeners in one or more directions) is represented as an equivalent plate/shell continuum by smearing the stiffness characteristics of individual stiffeners, in any given direction, over their spacing. The key assumption to perform smearing of the stiffness components is that the stiffeners are 'closely' spaced. The accuracy and applicability of an ESM also depend on the assumptions involved in terms of various deflection modes of the stiffeners that are incorporated in the formulation [20].

A limitation of ESM is that it does not provide any physical insight into the failure mechanisms of grid-stiffened structures [12, 22, 23]. Predicting the strength of grid and grid-stiffened structures analytically is complicated by the fact that the structure has abrupt geometric and stiffness changes in its profile. As an example, the skin-stiffener bonding can fail when the stiffeners exhibit excessive deformation, such as in the case of buckling [24], which cannot be captured using traditional ESM. Most of the ESM are simplified to apply to certain specific cases. The models developed in [6, 13, 25] neglected the torsion of the ribs which can significantly influence the transverse bending behavior of planar grids [20].

There are other modeling tools such as the branched plate and shell approach [26, 27] that utilize finite element formulations and preserve the spatial discreteness of the stiffeners and the stiffener-skin interaction effects. Since these models are capable of representing the stiffeners and plate/shell of grid-stiffened structures discretely, they provide sufficiently accurate results with the proper selection of elements, meshing scheme, and solution strategies. The stiffeners are modeled using either beam, shell, or solid elements. The attached shell structure is modeled using shell or solid elements depending on the nature of the problem. It is required to have the element mesh match with the geometry of individual components of the grid-stiffened structure. As a consequence, a topology change would require a re-mesh or a complete regeneration of the geometry of certain parts or even the entire model. This could lead to longer development cycles and undesirable modeling complications. Also, these models could be prohibitively expensive in a design environment owing to a large number of iterations required and the need for high performance computing resources.

Analytical–numerical hybrid models also exist where both ESM and finite element models are coupled to analyze stiffened structures. Chen and Tsai [20] employed the ESM approach to calculate the effective properties of the laminate and input those parameters in a finite element model for a detailed structural analysis. On the contrary, tools such as HyperSizer® [28] accepts input from a simplified, coarse-meshed finite element results and interprets the loads or stresses to generate smeared models for rapid analysis. Although it is possible to predict the deflections, strains, and buckling loads of grid and grid-stiffened structures using numerical models with varying degrees of accuracy, computationally efficient and robust analytical models are desired for preliminary analysis and design.

There exists several tools that are designed specifically for the buckling analysis and sizing of stiffened structures. One of the notable ones is PANDA2, a code developed by Bushnell [29]. This code is designed to perform preliminary weight reduction optimization studies of stiffened panels. It employes a multitude of solution strategies such as exact closed-form models by means of finite strip method (FSM) [30] and discretized branched shell models to predict buckling and post-buckling characteristics. Another tool that is being used to analyze shell and stiffened shell structures is STAGS [31]. STAGS is a general purpose finite element implementation to perform nonlinear static and dynamic analysis of shell structures. Stiffened panels can also be analyzed for instabilities and strength, in both linear and nonlinear domains. An extensive review of various codes available for stiffened shells/panel instability and failure analyses is provided by Venkataraman [32].

Since the present study is in the realm of rotor blade spar analysis where the bending and torsion stiffness requirements are stringent, computationally efficient models that can predict the stiffness characteristics of closed cross-section cylindrical grid-stiffened structures with various stiffening configurations (topology) is required. ESM models were developed and extensively employed by many studies [12, 13, 19, 20, 22, 33] for the buckling analysis of stiffened panels and cylindrical (both closed and open section) shells under different loading conditions. They derived the equivalent stiffness coefficients of stiffened structures using force-displacement relations assuming that the unit cell is flat. This assumption simplified the solution greatly when the effects of curvature of the stiffeners are ignored. In fact, the simple ESM developed in the studies cited, predicted the stability characteristics of stiffened cylindrical shell with reasonable accuracy compared to finite element results or experiments. This is due to two reasons: (*i*) the diameters of the structures analyzed were large, (*ii*) buckling modes (both due to compression and torsion) are characterized primarily by the out-of-plane (radial direction) deformation of the stiffened shells due to axial and circumferential buckle wave interaction.

Block [34] developed stability equations using strain energy principle to predict the global buckling of ortho-grid stiffened cylinders. The effect of stiffener eccentricity was included in the derivation and the study concluded that ignoring eccentricity could lead to significant errors in stability predictions. Soong [35] developed similar buckling equations using energy methods for closed section cylindrical shells with helical, longitudinal, and axial stiffeners. The equations are valid only for global buckling predictions. The torsion and out-of-plane deformation of the stiffeners along with stiffener eccentricity were included in the formulation. The results were in good agreement with experimental results for the case of uniaxial compression and combined compression and torsion buckling loads. Both of these studies did not take into account the in-plane (circumferential direction) bending stiffness of the stiffeners.

As demonstrated by Chen and Tsai [20], neglecting in-plane bending stiffness of the stiffeners leads to singular membrane stiffness matrix of the grid layer for an angle-grid configuration. This is the consequence of using the force equilibrium equations to derive the smeared stiffness coefficients of the angle-grid where simply supported boundary conditions at each stiffener end is implicitly assumed. An angle-grid configuration with simply supported stiffener ends would form a rigid body mechanism under all in-plane loads. However, when stiffeners, such as a family of longitudinal or transverse (circumferential) stiffeners, are added to the existing angle-grid, the final configuration (AT- or AL-grid) is a geometrically stable truss with finite in-plane stiffness. This would still lack the capability to capture any coupling due to the geometry of stiffeners since they behave as bar (only axial deformation) elements. For large diameter structures, flat unit cell assumption and simply supported stiffener boundaries do not lead to significant errors in stiffness predictions since the stiffeners effectively act as bar elements.

Almost all the models for grid-stiffened structure analyses available in the published domain are developed to predict the stability characteristics under different loading scenarios. Formulations such as layerwise theory developed by Reddy and Starnes [36] and the improved smeared model by Jaunky et al [24, 37] provide accurate platforms for the general stability predictions of stiffened structures. There are numerous studies that employed ESM based on planar unit cell assumption to design lightweight grid-stiffened structures with buckling constraints. Based on the literature review conducted, torsion and bending stiffness coefficients of closed cross-section grid-stiffened structures were not considered as design constraints. The present research aims to perform such a study with the aforementioned stiffness parameters as design constraints. Since the diameter of the spar structure is relatively small in comparison to the structures analyzed in the literature, the applicability of the ESM in predicting the stiffness coefficients must be evaluated. Note that the the grid-stiffened cylinders subjected to tip torque (shear load around the cross-section circumference) could result in in-plane (circumferential) deformation of the stiffeners, which is not captured in the traditional ESM.

The conventional force equilibrium method to develop smeared stiffness coefficients would become extremely difficult when various deflection modes of individual stiffeners are to be simultaneously considered. These deflections include in-plane (circumferential), out-of-plane (radial), and torsion of the stiffeners between their supports. These deflection modes could result in significant coupling effect when the diameter of the grid or grid-stiffened structures are small compared to the individual stiffener dimensions. The implication of ignoring high curvature of stiffeners when predicting various stiffness coefficients of grid and grid-stiffened cylinders is quantified later in Chapter 6. A new analytical model is developed in this research to include the effect of curvature of the stiffeners (for helical and circumferential) directly utilizing the corresponding stiffness matrices of the stiffeners. This is accomplished by considering the stiffeners as beam elements with appropriate boundary conditions.

1.4 Research objectives

The overall objective of the present research is to develop and integrate a set of efficient design analysis tools to conduct a feasibility study of employing advanced grid-stiffened structures for the spar of the heavy-lift helicopter blades. Specific tasks are enumerated as follows:

1. Develop and validate computationally efficient analytical tools to predict the stiffness coefficients of grid and grid-stiffened cylindrical structures

2. Perform experimental studies on angle-grid cylindrical specimens to determine their stiffness characteristics under various loading conditions for validation studies

3. Develop FEA models for validation studies and also to aid in analytical model development

4. Predict the strength characteristics of grid-stiffened cylindrical structures using established failure criteria

5. Conduct stability evaluation of grid-stiffened closed-cross section cylindrical structures under torque and bending induced axial compression loads

6. Conduct preliminary design studies to minimize the weight of general-grid stiffened spar structures with stiffness, strength and stability constraints

1.5 Novel Contributions

The contributions from the present research are summarized as:

1. First investigation to examine the application of grid-stiffened structures for rotor blade spars with the objective to reduce weight by including stiffness (bending and torsion), stability (torsion and bending induced compression), and strength constraints

2. A new unified analytical model is developed to predict the equivalent stiffness coefficients of grid and grid-stiffened structures from the stiffness matrices of individual stiffener elements.

3. The analytical model can explicitly prescribe various boundary conditions for the stiffeners in a grid structure. The boundary conditions considered in the present study are clamped, simply supported, and elastic (using in-plane torsion spring.)

4. The analytical model developed is applicable to model cylindrical grid and grid-stiffened structures. The oblique (off-axis) stiffeners are modeled using helical beams to accurately represent their geometry in the analytical model. Similarly,

the circumferential stiffeners are modeled using the stiffness matrix of a arch beam.

5. The new analytical model is capable of modeling a variety of stiffening configurations such as angle-grid, ortho-grid, and general-grid.

6. An FEM modeling methodology is developed to efficiently model the stiffener overlap that results from the automated filament winding process. This is performed using a commercial, general purpose finite element code.

1.6 Dissertation Outline

This research focuses on the application of grid-stiffened structures for heavy-lift rotor blade spar designs. Various aspects of this research are classified and described in relevant chapters.

The finite element modeling of grid and grid-stiffened structures are presented in Chapter 2. The experimental procedure to determine the deflections of cylindrical grid specimens under various loading conditions, in order to evaluate their stiffness characteristics, is also discussed.

Chapter 3 is dedicated to the new analytical model formulation using the smeared stiffness approach in order to predict the axial, bending, and torsion stiffness coefficients of grid and grid-stiffened cylindrical structures. The model developed is capable of capturing the exact geometry of the stiffeners while explicitly incorporating appropriate stiffener boundary conditions at their cross-over points.

The methodologies employed to predict the stability characteristics of the grid-stiffened cylindrical structures under various loading scenarios are provided in Chapter 4. The analytical models employed are obtained from published studies. The strategies used to predict buckling of grid-stiffened cylindrical structures under torque and bending induced axial compression are discussed.

A design methodology is presented in Chapter 5, to evaluate the weight savings of grid-stiffened structures by comparing to a monocoque baseline structure. The different design variables and constraints considered in this preliminary design investigation are enumerated. The newly formulated analytical model is used in this design study. No formal optimization algorithm is employed.

All the results generated from various analysis performed are provided in Chapter 6. The design results based on the methodology established in Chapter 5 are also presented in Chapter 6. Discussions on the results presented are provided in appropriate sections.

Finally, the conclusions obtained based on the present investigation and the directions for future work are presented in Chapter 7.

Chapter 2

Experiments and numerical models

The experimental evaluation to determine the load–deflection behavior of cylindrical grid specimens are described. These results are used to determine the axial, bending, and torsion stiffness of the cylindrical grid speciemens for validatin studies. The results are provided in the relevant sections of Chapter 6. A commercially available, general purpose finite element code, ABAQUS® [38] is employed to generate and analyze grid, grid-stiffened and monocoque composite models. Two different techniques to model the stiffener intersections in the grid and grid-stiffened structures are presented.

2.1 Experimental evaluation

2.1.1 Grid fabrication

The cylindrical grid specimens are fabricated using wet filament winding technique at the Composite Manufacturing Technology Center of the Dept. of Engineering Science and Mechanics at The Pennsylvania State University*. The S-glass/epoxy grid structures are wet filament wound on a McClean-Anderson® filament winding machine. A typical set up for filament winding is shown in Fig. 2.1. The epoxy is prepared using Epon® resin 8132 and the Jeffamine® T-403 as the curative, mixed with a resin to curative ratio by weight of five to two. The mandrel dimensions, fiber winding angle along with data pertaining to the ply thickness, etc., are input into the computer which controls the winding machine. The machine is instructed such that the tow is laid out on to the mandrel exactly over the previous one resulting in a grid like structure with a predetermined winding angle with respect to the mandrel axis. Note that no special tooling was used to fabricate these specimens. As a result, there is a practical limit of the number of plies that can be wound to fabricate the grid specimen without considerable 'tow flattening.'

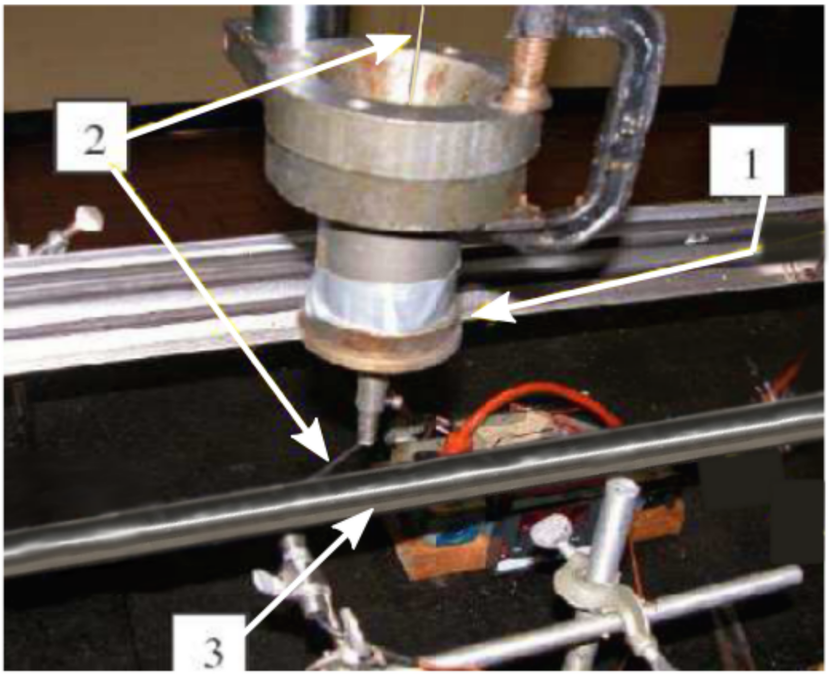

Figure 2.1. Filament winding set up: (1) filament feeder, (2) wet tow, and (3) mandrel

*Fabrication: Courtesy of Ms. Kirsten Bossenbroek (then a graduate student) and Prof. Charles E. Bakis

The angle-grid specimens fabricated for this study all have helical winding angle of 45°. The two varieties of specimens are shown in Fig. 2.2. The specimen, *S*8 has a total of 8 helical stiffeners–4 in each direction and the specimen, *S*4 has 2 stiffeners in each direction. Both specimens are of approximately the same weight. The geometric properties of the specimen are shown in Table 2.1. The stiffeners consist of unidirectional plies (fibers run parallel to the direction of the stiffeners.) As a result, the overlap has twice the number of plies. The thickness of the overlap is less than twice that of the ribs as a result of the compaction process for curing.

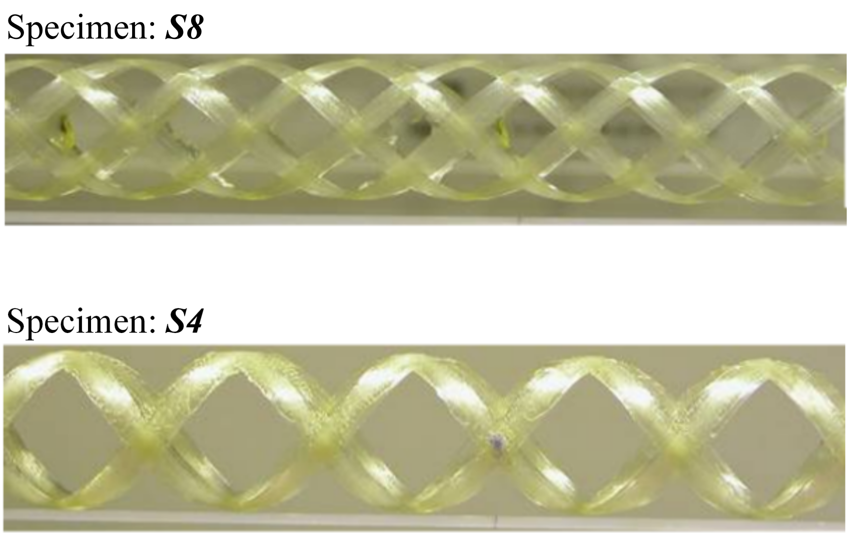

Figure 2.2. Angle-grid specimens fabricated by filament winding

The material properties of the ribs and the overlap are determined from the fiber and matrix volume fractions which are calculated from the fiber and matrix properties and geometric measurements directly obtained from the cured specimens. Halpin-Tsai equations [39] are used to determine material properties for the overlap sections.

$$E_{11} = E_f V_f + E_m V_m \tag{2.1}$$

Table 2.1. Geometric properties of grid specimens. (Dimensions in mm)

Specimens	$S8$	$S4$
Avg. length bet. supports	229	221
Inner diameter	19.05	19.05
Avg. ply thickness	0.229	0.228
Avg. ply thickness at overlap	0.193	0.193
Stiffener (tow) width	3.708	3.708
No. of plies in stiffener	2	4

$$\nu_{12} = \nu_f V_f + \nu_m V_m \tag{2.2}$$

$$E_{22} = E_m \frac{1 + \zeta_1 \eta_1 V_f}{1 - \eta_1 V_f} \tag{2.3}$$

where

$$\eta_1 = \frac{E_f - E_m}{E_f + \zeta_1 V_f} \tag{2.4}$$

and m and f refer to matrix and fiber respectively. A statistically valid value of fiber volume fraction, V_f is calculated by taking geometric measurements from multiple grid segments obtained from different specimens. The geometry parameter, $\zeta_1 = 1$ and the shear modulii are calculated as,

$$G_{12} = 0.8 E_{22} \tag{2.5}$$

$$G_{23} = \frac{E_{22}}{2(1 + V_m)} \tag{2.6}$$

Various parameters and calculated material properties are given in Table 2.2.

Table 2.2. Material properties of the stiffener and overlap region of the specimens. (Modulii in GPa)

Fiber and matrix		
Fiber modulus, E_f	86.90	
Matrix modulus, E_m	1.89	
ν_f	0.20	
ν_m	0.35	
ζ_1 (assumed)	1	
Parameter	**Stiffener**	**Overlap**
Fiber vol. fraction, V_f	0.31	0.57
Matrix vol. fraction, V_m	0.69	0.43
Properties	**Stiffener**	**Overlap**
E_{11}	28.24	50.34
E_{22}	3.85	7.43
G_{12}	1.29	2.40
G_{23}	1.37	2.65
ν_{12}	0.304	0.265

2.1.2 Experiment setup

An apparatus capable of applying pure torque at the free end of a cantilever beam is used to determine the twist response of the grid structure. Both ends are glued to metal fixtures to provide the necessary rigidity for the applications of boundary condition and load. The setup is shown in Fig. 2.3. The loads are applied incrementally using free weights and pulley arrangement. A moment arm is generated by the use of a near-frictionless rotating disc attached to the free end of the beam as demonstrated in Fig. 2.3b. The twist angle is directly measured from a protractor attached on the fixed part of the head assembly. The twist angle measurement has an accuracy of 0.5°. The rotating disc provides a lever arm of 56.89 mm (2.24 in) and the torque on the beam tip is simply the applied load multiplied by the lever arm. The tests are repeated at least three times and the data are averaged.

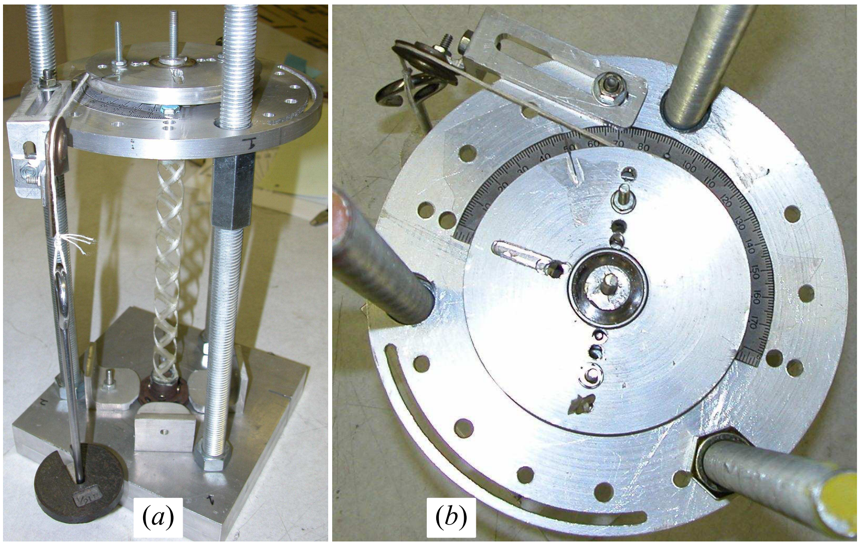

Figure 2.3. Torsion test of the grid cantilever beam

The apparatus shown in Fig. 2.3, with some modifications, is used for the bending test. The beam is cantilevered with the bottom end clamped. The load is applied using free weights and pulley arrangement. The deflections are directly read using a dial gauge. The apparatus arrangement for bending test is shown in Fig. 2.4. The load is applied in increments of 0.245 N (25 g). The dial gauge has a sensitivity of 0.0254 mm. The tests are repeated at least three times and data are averaged to minimize error in measurements.

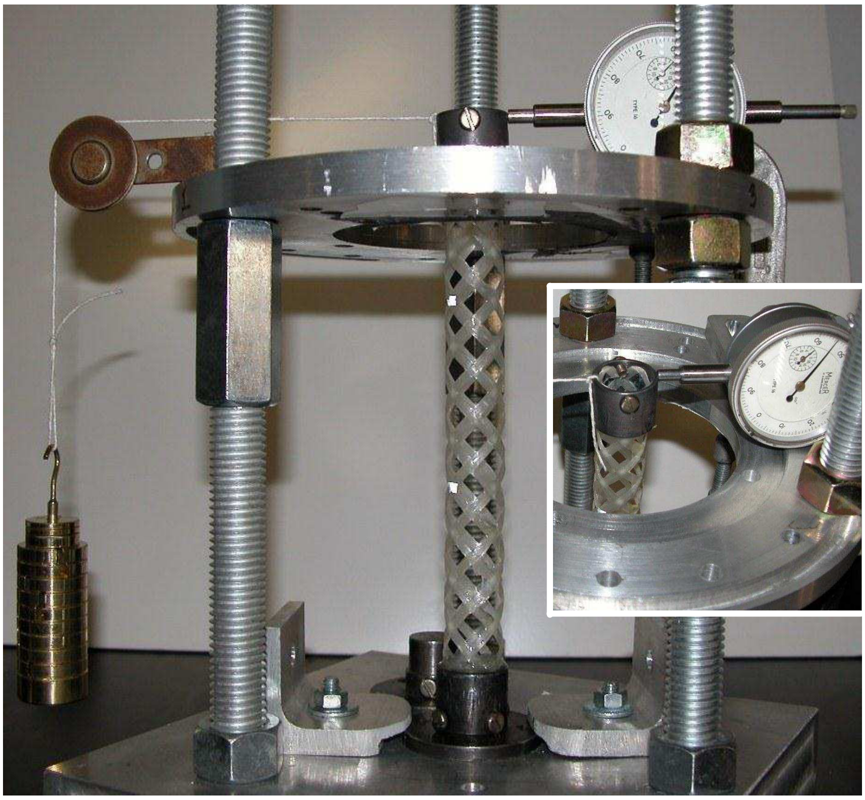

Figure 2.4. Bending test of the dense grid cantilever beam

A displacement controlled axial test is performed[†] on a servo-hydraulic testing machine. The test is controlled and monitored using a computer connected to the machine (Fig. 2.5). The load is calculated and recorded real-time through a 111.2 N (25 lb) load cell attached to the top end of the beam. The fixtures at both ends of the beam are provided with articulated bolts to negate any bending moment that may develop in the grid beam due to possible but minor misalignment. Load sampling rate is set to about 6 readings per second and the maximum displacement is restricted to 1.5 mm (0.06 in) so as to not to overload the load cell.

[†]Testing: Courtesy of Dr. Zhu (then a graduate student) and Prof. Charles E. Bakis for guidance

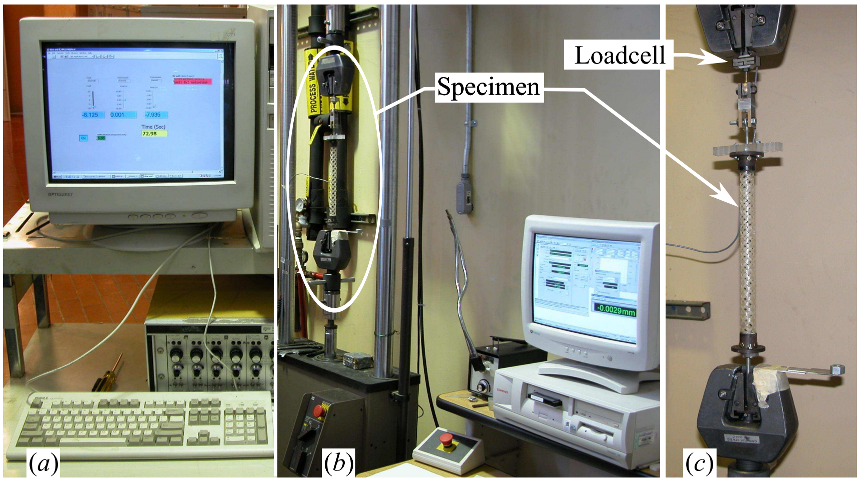

Figure 2.5. Axial test of the grid specimen

2.1.3 Cross-section stiffness

The experiment set ups described in the preceding section yield displacements in the direction of the applied loads. The bending, axial, and torsion stiffness values are determined from the displacement values using Euler beam theory [40]. The bending stiffness EI_{gE} of the grid specimen is determined using

$$EI_{gE} = \frac{P_a L_{gE}^3}{3 w_{gE}} \tag{2.7}$$

The axial and torsion stiffness values are determined using Eqs. (2.8) and (2.8) respectively.

$$EA_{gE} = \frac{F_a L_{gE}}{u_{gE}} \tag{2.8}$$

$$GJ_{gE} = \frac{T_a L_{gE}}{\phi_{gE}} \tag{2.9}$$

where the subscript, E refers to experiements. P_a, F_a, and T_a are the applied tip transverse bending load, axial load, and torque respectively. Tip transverse bending deflection, w_{gE}, tip axial deflection, u_{gE}, and tip twist, ϕ_{gE} are the experimentally determined values. L_{gE} is the length of the grid specimen.

2.2 Numerical models

2.2.1 Finite element modeling of grid structures

The FEA models developed in this study to analyze grid and grid-stiffened structures are broadly classified as:

1. Shell element models
   (a) Blade-like stiffener (BLS)
   (b) Strip-like stiffener (SLS)
2. Solid element grid models

The primary distinction between BLS and SLS models is in the way the geometric planes of the stiffeners are oriented. Figure 2.6 illustrates these two types. The planes for BLS are oriented perpendicular and that for the SLS are parallel to the xy plane as demonstrated. The other distinction is in the element section definition input; specifically, the way the composite ply layups are defined at the stiffener overlap regions and shell–stiffener attachment. The motivation behind developing the SLS model is represent the geometry of overlapping sections as accurate as possible compared to the grid specimens fabricated.

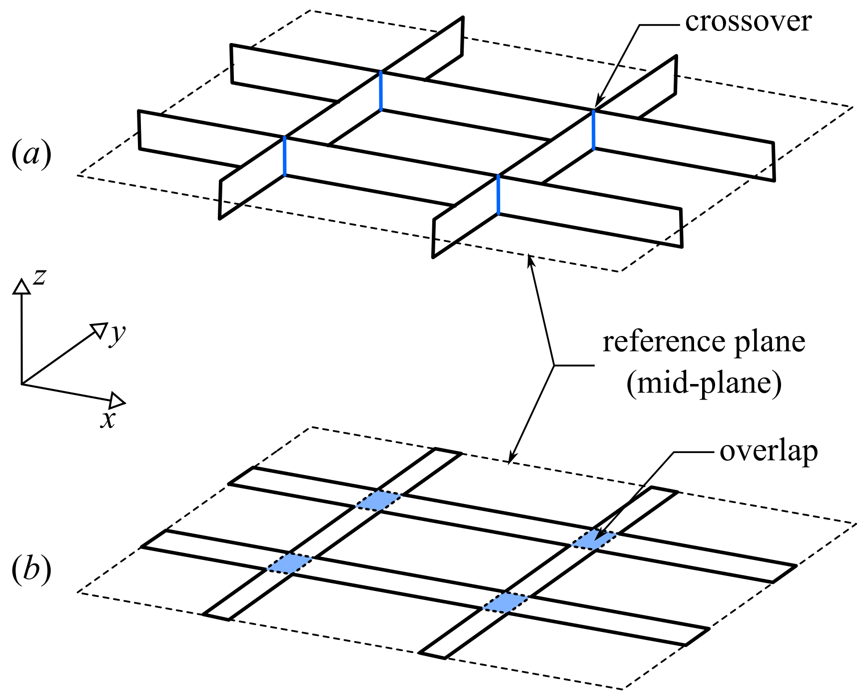

Figure 2.6. Stiffener modeling technique: (*a*) BLS and (*b*) SLS modeling. Applicable also to cylindrical profile

Reference points (RP) are created at the centroid of the cross-sections of the structure end and the respective edges are tied to these points using kinematic coupling constraints. This is demonstrated in Fig. 2.7. Constraints are prescribed in the form of BCs to avoid warping of the cross-section. The loads and boundary conditions are applied at these reference points.

The cylindrical models used for bending analysis have simple support boundary conditions and those for torsion analysis have fixed-free boundary conditions. A change in the stiffener width, b_s (dimension along the cylindrical plane) requires that the FEM stiffener geometry be regenerated. Appropriate dimensions, ply thickness and materials properties are input for the stiffeners and overlap regions. The axial, bending, and torsion loads are applied independently and the respective axial, transverse, and twist

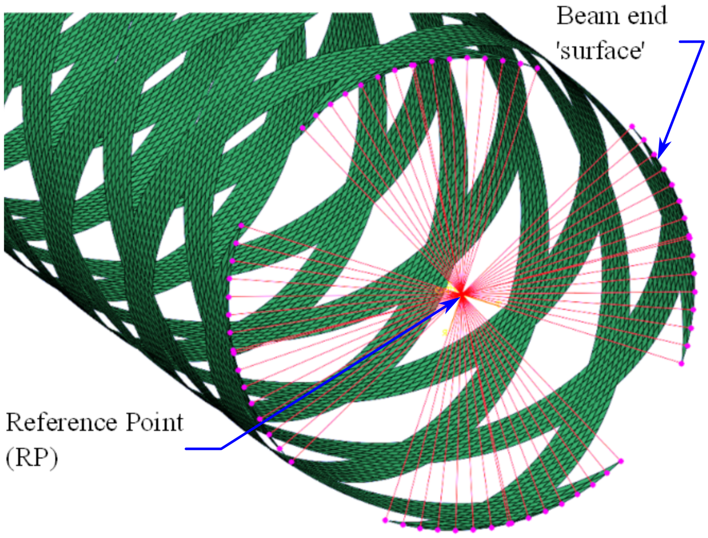

Figure 2.7. Reference point (RP) and constraint 'surface' at the grid beam end for the application of loads and BCs. RP is located at the centroid of the cross-section. Kinematic coupling constraints are used to connect the surface to the RPs

deformations are determined from the nodal displacement results. The nodal displacements are measured at multiple locations along the length of the beam for all load cases to obtain robust sets of data. The ply orientation for each stiffener is prescribed appropriately by defining local coordinate systems. The ply orientation angles are provided such that the stiffeners are made of uniaxial fibers. This is depicted in Fig. 2.8. Note that the helical stiffeners in only one direction are highlighted for clarity. All finite element analyses performed are linear elastic. The effects of cross-section and restraint warping are not included in the analysis.

The grid winding process is illustrated in Fig. 2.9. The filament feeder pass back and forth while the grooved mandrel is rotating on its axis generating the grid layer. The feeder should be programmed to lay the fibers exactly over the previous layer in the groove. The resulting stiffener overlap section, is modeled as illustrated in Fig. 2.10.

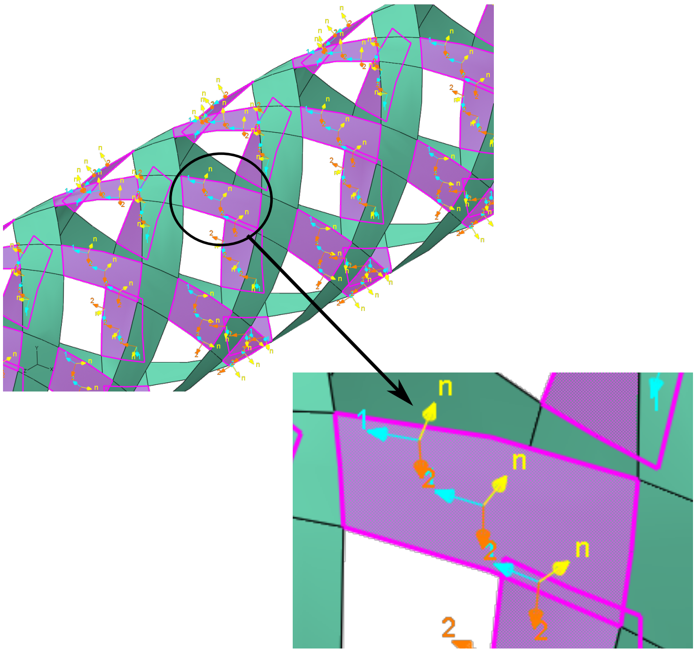

Figure 2.8. Ply orientation specified for the helical stiffeners in the cylindrical coordinate system. 1, 2, and n correspond to the fiber, transverse to fiber, and normal (stacking) directions respectively

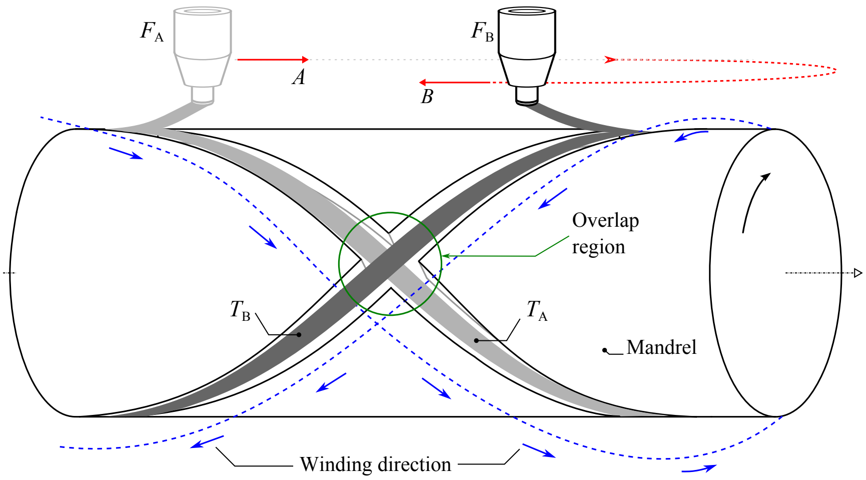

Figure 2.9. Schematic of angle-grid fabrication by filament winding on a grooved mandrel

The methodology to model overlapping composite plies is discussed in the documentation (§21.5 Modeling composite layups) [38] of the CAE® User's manual. According

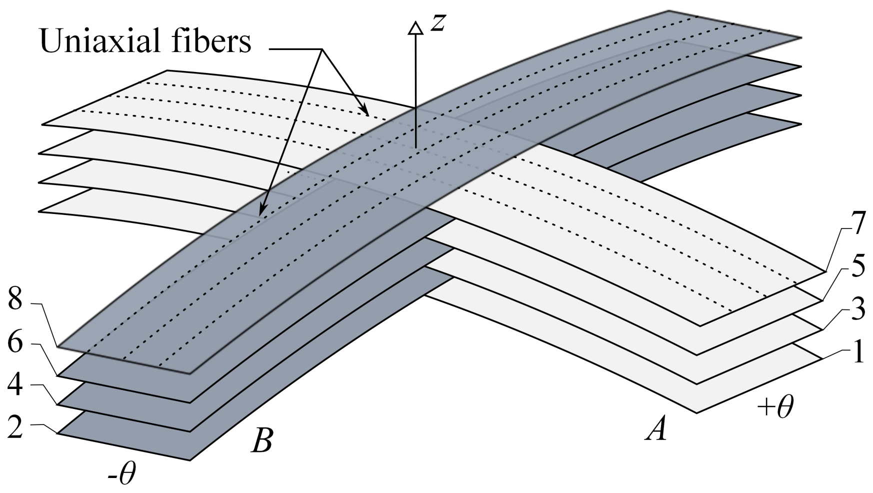

Figure 2.10. Schematic of ply by ply FEM modeling of stiffeners

to the numbering scheme shown, ply numbers in the overlap section in $+z$ direction is then $1, 2, 3, \ldots, 8$. With a careful geometry partitioning scheme, appropriate section definitions can be provided for the stiffeners and the overlapping regions independently.

The section definition includes ply name, ply thickness, material properties, ply orientation angle, number of integration points and node offset. The outer ($+z$ direction) surface of the stiffener overlapping regions should be flush with that of the stiffener profile in order to have the grid fit perfectly inside the cylindrical shell. This is accomplished by providing appropriate offset for the shell element nodes.

The geometric plane that represents the nodal plane of a conventional shell model is shown in Fig. 2.11. The nodal plane for the stiffeners is the middle surface as shown, which has, for e.g., the nodes (1) and (2). The nodal plane of the overlap section is at a distance e_o from the node ($2'$), which is, by default, situated at half-thickness of the overlap section. The purpose of this exercise is to make all the nodes lie on the reference plane representative of an equivalent grid layer. This node is provided with an offset of e_o so that the outer surface of the overlapping region is flush with the rest of the stiffeners.

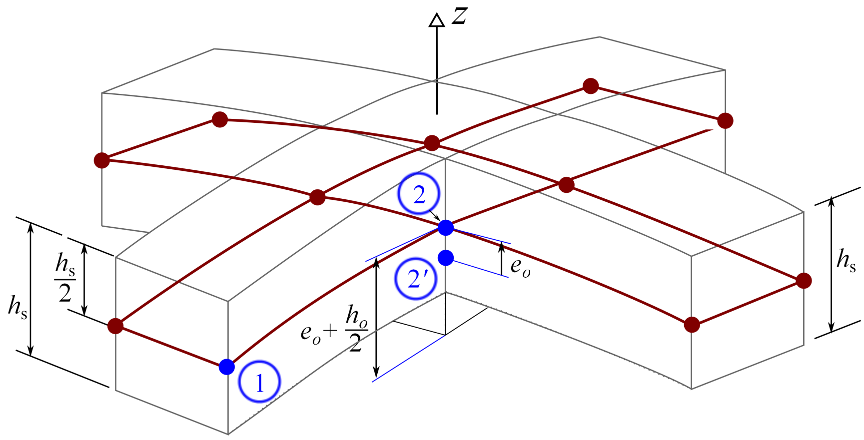

Figure 2.11. FEA modeling strategy for a stiffener overlap region using conventional shell elements. Only corner nodes are shown for clarity. Final form is obtained after applying the offset

Considerable attention is given to generate regular mesh where ever possible, though it is found that in some cases, such as in the case of grid-stiffened general-grid models, it is not always possible without tedious geometry partitioning schemes. The element distortion effect is minimized by providing sufficient density to the mesh. To maintain reliability, data are collected at various locations along the length of the beam.

A small number of FEM 3D solid models of angle-grid and ortho-grid tubes are also generated. Since the modeling aspect is cumbersome and costly for 3D models, they are only used to study the deflection characteristics of individual stiffeners when the grid cylinder is subjected to torsion loads. The angle-grid and ortho-grid cylindrical models in torsional deflection modes are depicted in Fig. 2.12 and Fig. 2.13 respectively.

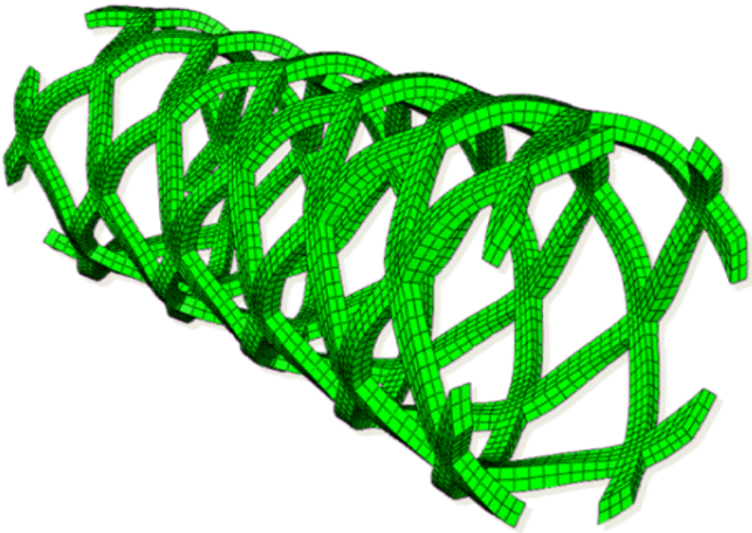

Figure 2.12. 3D FEA model of a cylindrical angle-grid structure showing deflection under tip torque. Out-of-plane (radial) deflection of the stiffeners can be observed

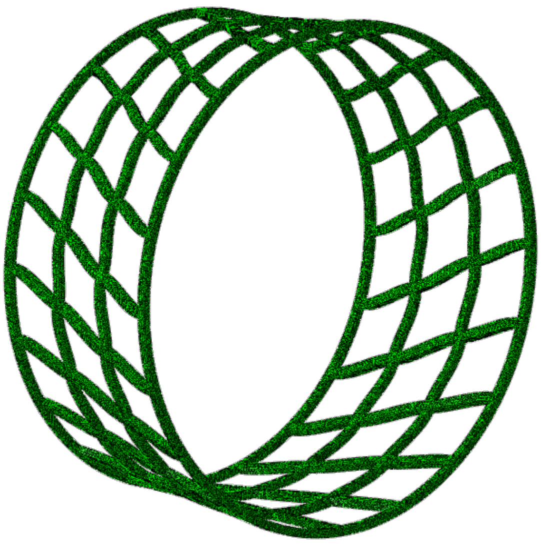

Figure 2.13. 3D finite element model of a cylindrical ortho-grid structure showing deflection under tip torque. In-plane (along cylindrical surface) deflection of the stiffeners can be observed

Generating grid and grid-stiffened models based on BLS technique is relatively simple compared to SLS technique. An angle-grid cylindrical model is shown in Fig. 2.14. Reference points for application of loads and boundary conditions are also shown. In the present research, most of the finite element simulations are performed using models

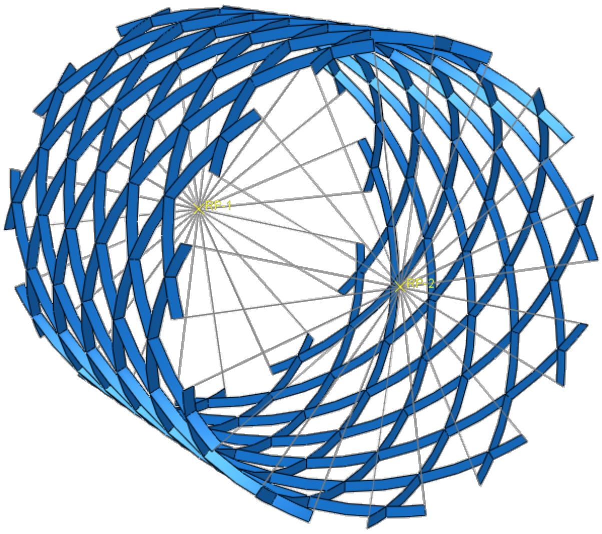

Figure 2.14. Unmeshed model of a cylindrical angle-grid generated using BLS technique with reference points (RPs)

developed using BLS method. A few exceptions are– FEM validation studies of grid specimens and torsional buckling study of grid-stiffened cylinders.

2.2.2 Grid-stiffened structures

The methodology developed for grid structures can be extended to model grid-stiffened structures. The technique for modeling shell–stiffener attachment is demonstrated in Fig. 2.15. The difference between BLS and SLS modeling aspects are discussed. For illustration purpose, the shell of the grid-stiffened structure has a stacking sequence $[\beta_1, \beta_2, \beta_3, \beta_4]$ as illustrated. The ply stacking directions are also indicated. In the case of BLS model, the common area highlighted in the schematic has both the section properties of the shell and the stiffener; this area is not modeled explicitly.

On the contrary, the SLS model provides accurate representation of the shell–stiffener attachment (as illustrated on the left) when appropriate nodal offset values are provided. Offsetting the nodes shifts the reference plane of the structure because the conventional

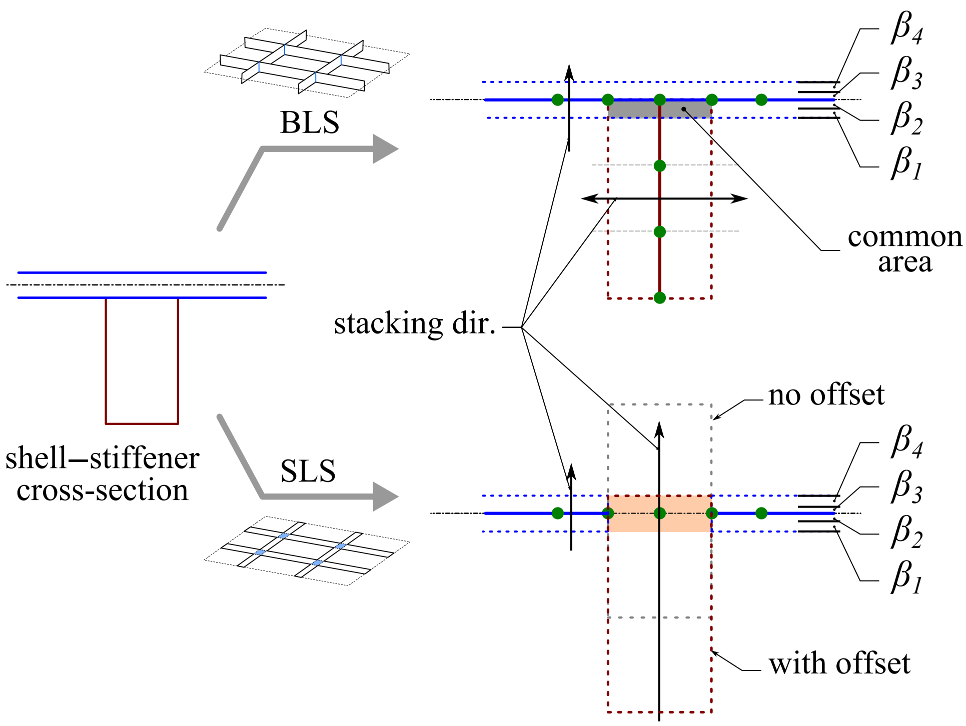

Figure 2.15. FEM modeling technique to represent grid–stiffener sections using conventional shell elements

shell element, (S4R) has only a single node through the thickness [38]. When the offset value is +0.5 the reference plane shifts to the top surface of the shell, an offset of −0.5 shifts the reference plane to the bottom, and a zero offset value distributes the plies equally on either side of the mid-plane [38](§24.6.5), which is indicated in Fig. 2.15 as 'no offset.' In the SLS method, the shaded region has the ply angles for the shell laminate which are provided in the section definition of the stiffener elements. Specifically, given the stacking direction, the last four ply angles in the stiffener laminate are β_1, β_2, β_3, and β_4. This means that the shell and stiffener geometries can be independently modeled with suitable section definitions. The eccentricity of the grid-layer from the reference plane (mid-plane of the shell) of the grid-stiffened structures is implicitly taken into account in the calculations. The general-grid stiffened cylindrical models (meshed and unmeshed) developed using BLS methodology are shown in Fig. 2.16.

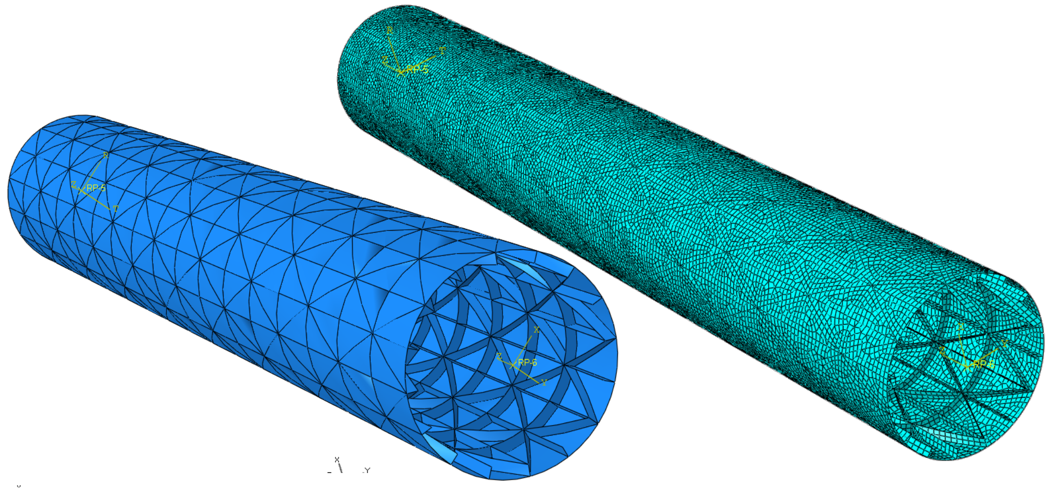

Figure 2.16. A complete shell model geometry of a general-grid stiffened cylinder and the corresponding meshed model for FEA simulations

A solid model with solid composite elements or continuum (3D) shell elements can capture complex geometries, for e.g., variable thickness and drastic curvature changes, with a high computational cost penalty. Unless the model is relatively simple, such as a structure with smooth geometry, it is cumbersome to develop the grid-stiffened models using composite solid sections. The procedure is especially cumbersome when the helical stiffeners are included. Therefore, 3D grid-stiffened models are not generated.

A mesh sensitivity study is performed on representative grid-stiffened models, such as the one shown in Fig. 2.16. A series of eigenvalue analysis are conducted on models with different mesh densities under axial compression to check for convergence. The solutions are also verified against a model with high mesh density. From the models with converged solutions, the coarsest mesh density is selected for further modeling procedures. Once the nodal displacements from FEA results are obtained, the equations provided in Sec. 2.1.3 can then used to predict the stiffness coefficients of grid and grid-stiffened cylinders.

Chapter 3

Analytical formulation

A novel analytical model is developed to determine the stiffness properties of grid and grid-stiffened structures. This analytical model is formulated from beam stiffness matrices facilitating accurate representation of geometry. This model also provides capabilities to prescribe boundary conditions for the stiffeners explicitly. The objective is to directly employ the stiffness matrices of the constituent stiffener components to derive the equivalent stiffness coefficients ($\boldsymbol{A}$, $\boldsymbol{B}$, $\boldsymbol{D}$ matrices) of grid- and grid-stiffened shells. From these coefficients, the axial, bending, and torsion stiffness of the cylindrical structures are calculated. First, a the methodology is demonstrated and validated against published results on flat unit cells and then extended to more complex stiffener geometries such as cylindrical grid and grid-stiffened structures.

3.1 A new approach

A grid layer with closely spaced stiffeners can be represented as an equivalent stiffness plate or shell layer by smearing the stiffness properties of the stiffeners [19]. The accuracy of such a model depends on how accurately the deflection modes of the stiffeners are represented in the smeared model. The traditional equivalent stiffness models employ direct force equilibrium relations to derive the stiffness contribution from the stiffeners. The force equilibrium method implicitly assumes that the stiffener joints provide simply supported boundary conditions and thus the moment carrying capabilities of all stiffener elements are ignored. This assumption eliminates the coupling between various deflection modes to obtain simple solutions. One of the consequences, apart from the possible inaccuracies, is that in certain cases the deflection solutions for the grid layer cannot be obtained. For example, an angle-grid configuration with the stiffeners joints that are assumed to be pinned, does not have any in-plane rigidity. Thus the in-plane stiffness matrix, $\boldsymbol{A}$ becomes singular [20]. Similarly, the shear stiffness of the ortho-grid configuration is null with pinned nodes. Also, the direct force balancing procedure becomes difficult to apply when the stiffener geometry is complex, such as in the case of a helical stiffener in a cylindrical angle-grid.

A new, unified methodology is developed to derive the equivalent stiffness coefficients of the grid layer *analytically* which can accurately capture the exact geometry (for example, curvature) of the stiffeners and explicitly include either clamped, pinned, or elastic boundary conditions at the nodes. The effects of transverse shear in the stiffeners are also included in the analysis. Initially, the grid structures are analyzed to determine the in-plane and out-of-plane bending stiffness matrices for various grid topologies. Subsequently, the stiffness coefficients of grid-stiffened structures are obtained. In the new approach, the equivalent stiffness coefficients of the grid layer are obtained from stiffness matrices of the stiffeners. Appropriate stiffness matrices are determined to match the geometry, orientation, and boundary conditions of the stiffeners for various stiffening configurations and structural geometry.

The equivalent stiffness matrices for various stiffening configurations that include combinations of longitudinal, transverse, and oblique stiffeners are formulated for both flat panel and cylindrical shell equivalents. As in a laminated plate or shell theory, two sets of parameters need to be derived; in-plane and out-of-plane stiffness coefficients. A set of assumptions are employed that are consistent with well established linear elastic plate, shell, and beam theories:

1. All structures are perfectly elastic and exhibit linear behavior.

2. Deflection are assumed to be small and thus the superposition principle is valid.

3. Stiffeners are modeled as prismatic structures made of uniaxially reinforced fiber composite material.

4. Stiffeners have identical cross-section geometries and made of the same material system. All stiffeners have rectangular cross-sections and thus, their product moment of area is zero.

5. All stiffeners lie on the same plane. The reference plane of the grid layer is defined as the plane formed by the centroid of the cross-sections of the stiffeners.

6. Angle (oblique) stiffeners appear in symmetric pairs of $\pm\theta$ orientation with respect to the structural longitudinal axis. $\boldsymbol{B}_{ij}^{g} = 0$ for the equivalent grid layer.

7. Stiffeners intersect at common, dimensionless 'nodes' where the boundary conditions are imposed and loads are applied. The radial displacements of these nodes are assumed to be zero (out-of-plane in the case of planar grids.)

8. The arrangement of stiffeners is periodic in a given grid configuration so that a unit cell can be established. It is also assumed that the stiffeners are continuous; there are no missing stiffeners or cut-outs in the structure.

One of the important steps in the present derivation is to determine the boundary conditions of the stiffeners considering their periodicity and the behavior of various grid elements within the unit cells under external loads. The analysis is greatly simplified when the representative grid beam members are identified and appropriate loading and boundary conditions are prescribed. It is only necessary to analyze two fundamental topologies viz., ortho-grid and angle-grid.

The stiffness contributions from each set of parallel stiffeners (family of stiffeners) are combined using the principle of superposition to obtain the stiffness coefficients of grid layers with various stiffener orientations [12, 13, 19, 20, 33]. The analysis reference plane of each family of stiffeners must coincide in order to combine their stiffness contributions. Also, it requires that the grid layer can be defined in terms of a representative segment, the unit cell, the periodic repetition of which defines the entire grid layer.

It is required to derive stiffness coefficients for both flat plate and cylindrical shell equivalents. The geometry of the stiffeners have to conform to the exact geometry of the plate or shell to be stiffened. Thus a stiffened *plate* has straight stiffeners (no out-of-plane curvature) while a *cylindrical* stiffened shell has straight, arch, and helical beams for longitudinal, transverse, and angle stiffeners respectively. It is also noted that a plate structure can have in- curvilinear stiffeners (in-plane curvature) [41] although such configurations are not considered in this study.

3.2 Flat grids: In-plane stiffness

The analytical derivation conducted in this study is based on the assumption, as stated earlier, that the stiffener distribution is periodic and the stiffness coefficients of the entire structure can be determined from its unit cell. A generalized grid unit cell is shown in

Fig. 3.1. The spacing between stiffeners, stiffener orientations, and the unit-cell dimensions are also shown. Note that the oblique stiffeners are in pairs of $\pm\theta$ orientation with respect to the x (longitudinal) axis.

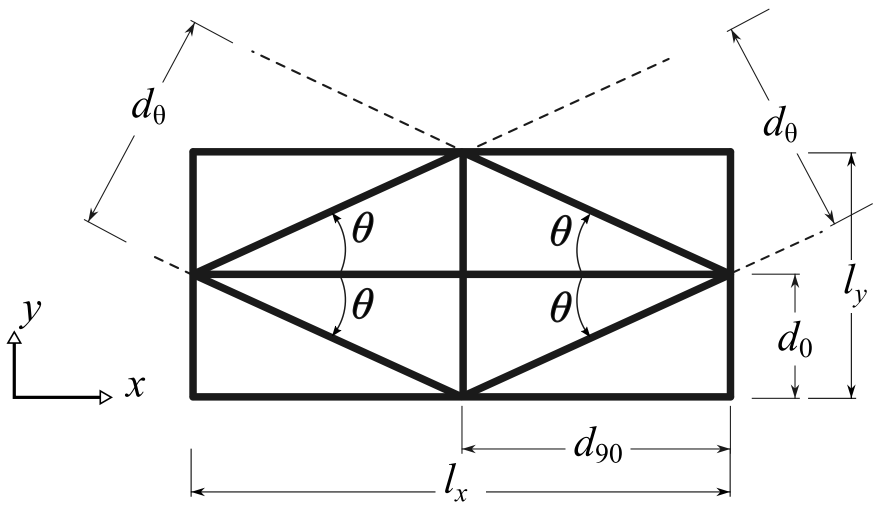

Figure 3.1. Unit cell of a general-grid

Based on the coordinate system shown in Fig. 3.1, the combination of only the vertical (transverse) and horizontal (longitudinal) stiffeners form the ortho-grid. A topology with only oblique stiffeners is called an angle-grid. The effect of various boundary conditions (BC) at the stiffener joints (nodes) is analyzed in this study and the unit cells are depicted in Figs. 3.2(a) simply supported (SS), (b) Clamped–clamped (CC), and (c) elastic–elastic (EE) BCs.

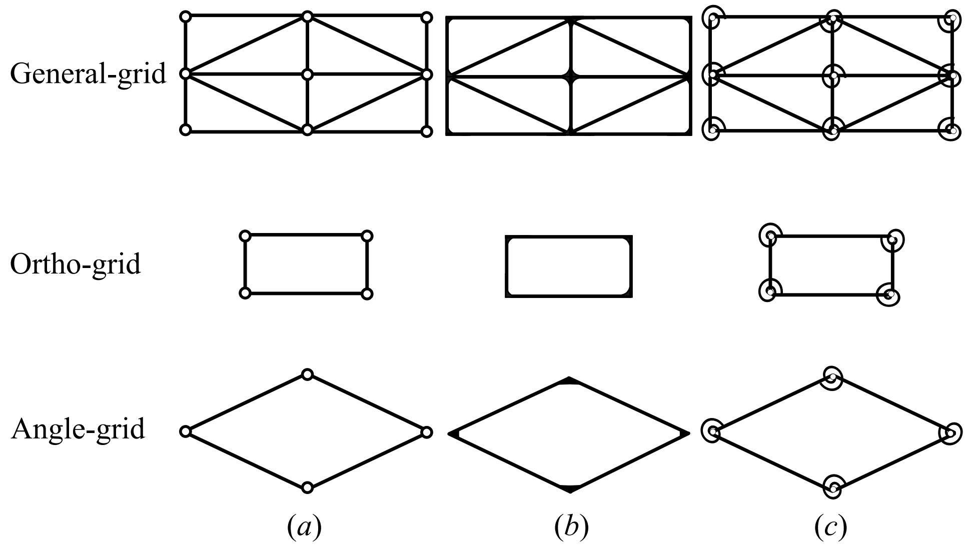

Figure 3.2. Boundary conditions at stiffener joints for various topologies. (*a*) Simply supported, (*b*) Clamped, and (*c*) elastic (in-plane torsion springs)

3.2.1 Ortho-grid

The constitutive relations for the equivalent stiffness panel of a general-grid can be represented as

$$\begin{Bmatrix} n_x \\ n_y \\ n_{xy} \end{Bmatrix}^g = \begin{bmatrix} A_{11} & A_{12} & 0 \\ A_{12} & A_{22} & 0 \\ 0 & 0 & A_{66} \end{bmatrix}^g \begin{Bmatrix} \varepsilon_x \\ \varepsilon_y \\ \gamma_{xy} \end{Bmatrix}^g \tag{3.1}$$

where xyz is the global coordinate system. The superscript, g refers to grid and n_x, n_y, n_{xy} are the in-plane stress resultants. A_{16}^g and A_{26}^g are zero since there is no extension-shear coupling in the grid panel due to the presence of symmetric stiffener pairs. The strain–displacement relations for the equivalent stiffness plate are given by

$$\begin{Bmatrix} \varepsilon_x \\ \varepsilon_y \\ \gamma_{xy} \end{Bmatrix}^g = \begin{Bmatrix} \dfrac{\partial \delta_x}{\partial x} \\ \dfrac{\partial \delta_y}{\partial y} \\ \dfrac{\partial \delta_x}{\partial y} + \dfrac{\partial \delta_y}{\partial x} \end{Bmatrix}^g \tag{3.2}$$

All the stiffeners in a flat grid are planar (xy plane) beams. Thus, only three DOFs (2 in-plane displacements and 1 in-plane rotation) per node need to be considered to calculate the in-plane stiffness coefficients, $\boldsymbol{A}^g_{ij}$. The local coordinate system, forces, moment, displacements, and rotation are shown in Fig. 3.3. Note that for the longitudinal and transverse beams, the local coordinate system coincides with the global coordinate system and the subscripts are changed to x, y, and z accordingly.

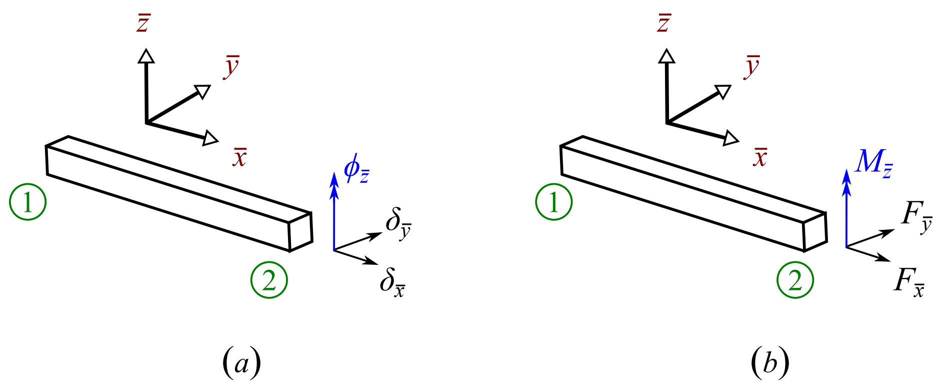

Figure 3.3. 2D planar beam element of length, l. (a) displacements and rotation, and (b) forces and moment. The local coordinate system is also shown

The force displacement relation for a two-node beam-column in matrix form is

$$\boldsymbol{F}_i = \boldsymbol{k}_{bc}\, \boldsymbol{\delta}_i \tag{3.3}$$

where

$$\boldsymbol{F_i} = [F_{x_1}, F_{y_1}, M_{z_1}, F_{x_2}, F_{y_2}, M_{z_2}]^T \tag{3.4}$$

$$\boldsymbol{\delta_i} = [\delta_{x_1}, \delta_{y_1}, \phi_{z_1}, \delta_{x_2}, \delta_{y_2}, \phi_{z_2}]^T \tag{3.5}$$

Equation (3.6) provide the (6×6) stiffness matrix $\boldsymbol{k}_{bc}$ of the beam-column of length, l [42].

$$\boldsymbol{k}_{bc} = \begin{bmatrix} \frac{EA}{l} & 0 & 0 & \frac{-EA}{l} & 0 & 0 \\ 0 & \frac{12EI_z}{(\overline{\alpha}_y+1)\,l^3} & \frac{6EI_z}{(\overline{\alpha}_y+1)\,l^2} & 0 & \frac{-12EI_z}{(\overline{\alpha}_y+1)\,l^3} & \frac{6EI_z}{(\overline{\alpha}_y+1)\,l^2} \\ 0 & \frac{6EI_z}{(\overline{\alpha}_y+1)\,l^2} & \frac{(\overline{\alpha}_y+4)\,EI_z}{(\overline{\alpha}_y+1)\,l} & 0 & \frac{-6EI_z}{(\overline{\alpha}_y+1)\,l^2} & \frac{(2-\overline{\alpha}_y)\,EI_z}{(\overline{\alpha}_y+1)\,l} \\ \frac{-EA}{l} & 0 & 0 & \frac{EA}{l} & 0 & 0 \\ 0 & \frac{-12EI_z}{(\overline{\alpha}_y+1)\,l^3} & \frac{-6EI_z}{(\overline{\alpha}_y+1)\,l^2} & 0 & \frac{12EI_z}{(\overline{\alpha}_y+1)\,l^3} & \frac{-6EI_z}{(\overline{\alpha}_y+1)\,l^2} \\ 0 & \frac{6EI_z}{(\overline{\alpha}_y+1)\,l^2} & \frac{(2-\overline{\alpha}_y)EI_z}{(\overline{\alpha}_y+1)\,l} & 0 & \frac{-6EI_z}{(\overline{\alpha}_y+1)\,l^2} & \frac{(\overline{\alpha}_y+4)EI_z}{(\overline{\alpha}_y+1)\,l} \end{bmatrix} \tag{3.6}$$

where

$$\overline{\alpha}_y = \frac{12EI_z}{\alpha_{sc}\,GA\,l^2} \tag{3.7}$$

$\overline{\alpha}_y$ is the non-dimensional shear correction parameter and α_{sc} is the shear correction factor (see Sec. A.2 in Appendix A). EI_z and GA are the in-plane bending and shear stiffness of the beam respectively. Setting $\overline{\alpha}_y = 0$ in Eq. (3.6) reduces it to the Euler-Bernoulli beam-column element stiffness matrix.

3.2.1.1 Simply supported nodes

The model employed is shown in Figs. 3.4. The dark and lighter shades are used to represent the beams in the schematics. Dark shaded beam elements undergo elastic deformation whereas the gray shaded beam elements undergo rigid body motion. The gray shaded elements are provided only as a reference to a connecting member. Also, the lengths of the beam shown in the diagrams for ortho-grid are the spacing between the stiffeners. For example, the length of a longitudinal (x direction) stiffener would be d_{90} since the length is determined by the spacing between 90° (y direction or transverse) stiffeners.

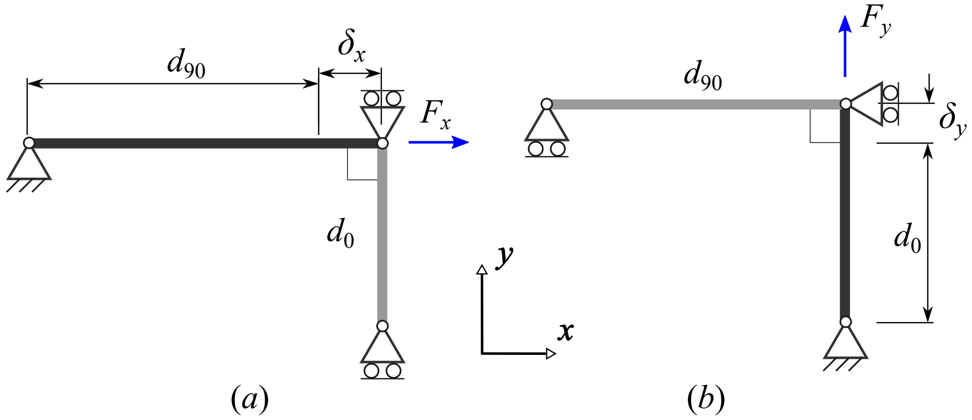

Figure 3.4. Loading and BCs for ortho-grid in-plane stiffness calculations. (a) A_{11}, and (b) A_{22}

Applying the BCs $\delta_{x_1} = \delta_{y_1} = \delta_{y_2} = 0$ and setting $F_{x_2} = F_x$, $\delta_{x_2} = \delta_x$, and the length of the longitudinal stiffeners $l = d_{90}$ in Eq. (3.6) gives

$$F_x = \frac{EA}{d_{90}}\,\delta_x \tag{3.8}$$

Considering Eq. (3.2), converting the beam displacement to plate strain and beam force to plate load using the following equations result in,

$$\delta_x = \varepsilon_x d_{90} \tag{3.9}$$

$$F_x = n_x d_0 \tag{3.10}$$

to get

$$n_x = A^g_{11} \varepsilon_x \tag{3.11}$$

with

$$A^{os}_{11} = \frac{EA}{d_0} \tag{3.12}$$

The superscripts 'o' and 's' stand for ortho-grid—the topology and SS—the BCs respectively. Following a similar procedure, A^{os}_{22} can also be obtained by analyzing the transverse stiffener which is oriented in the y direction. For this case, apply the BCs $\delta_{x_1} = \delta_{y_1} = \delta_{x_2} = 0$ in Eq. (3.6) and set $F_{y_2} = F_y$, $\delta_{y_2} = \delta_y$, and the length of the transverse stiffener $l = d_0$. The beam displacement and force are represented in terms of the corresponding plate parameters employing the expressions in Eq. (3.2).

$$\delta_y = \varepsilon_y d_0 \tag{3.13}$$

$$F_y = n_y d_{90} \tag{3.14}$$

The in-plane stiffness can be written as

$$A^{os}_{22} = \frac{EA}{d_{90}} \tag{3.15}$$

$A^{os}_{12} = 0$ for an ortho-grid since there is no x direction deflection due to F_y or y direction deflection due to F_x. The in-plane stiffness matrix $\boldsymbol{A}_{ij}$ of an ortho-grid layer with simply supported nodes can be represented in the conventional matrix form as

$$\begin{Bmatrix} n_x \\ n_y \\ n_{xy} \end{Bmatrix} = \begin{bmatrix} \dfrac{EA}{d_0} & 0 & \\ 0 & \dfrac{EA}{d_{90}} & 0 \\ 0 & 0 & 0 \end{bmatrix} \begin{Bmatrix} \varepsilon_x \\ \varepsilon_y \\ \gamma_{xy} \end{Bmatrix} \tag{3.16}$$

These results are in perfect agreement with several published works [13, 19–21, 33].

3.2.1.2 Clamped nodes

A_{11}^{oc} and A_{22}^{oc} for the clamped BC case are identical to that obtained for the simply supported case in Eq. (3.16). This is because the loads are purely axial for both longitudinal and transverse beams as demonstrated in Fig. 3.5.

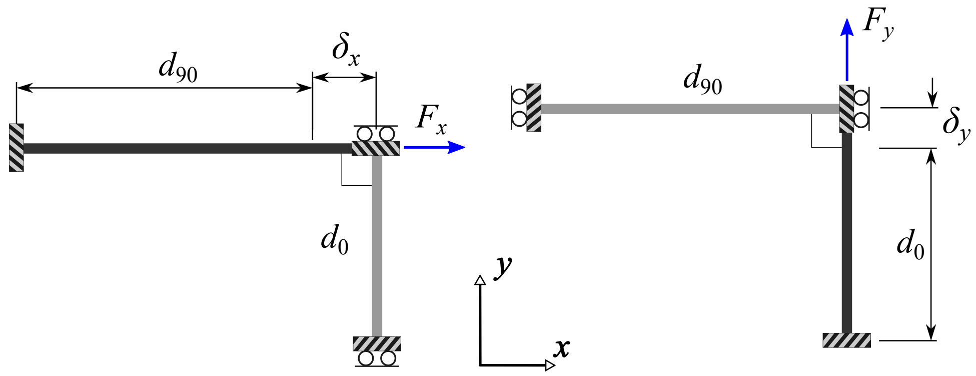

(a) (b)

Figure 3.5. Loading and clamped BCs for ortho-grid in-plane stiffness calculations. (a) A_{11}, and (b) A_{22}

However, $A_{66}^{oc} \neq 0$ when clamped BCs are imposed at the nodes [20]. The shear stiffness of the panel comes from the in-plane bending of the stiffeners. In order to determine the shear strains, δ_x and δ_y need to be calculated as per the equation for γ_{xy} in

Eq. (3.2). The boundary conditions and loading patterns are provided in Fig. 3.6.

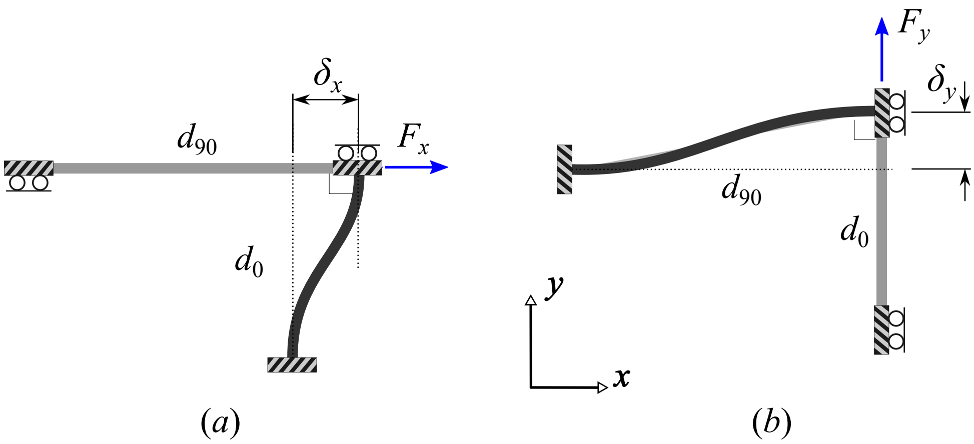

Figure 3.6. Loading and clamped BCs for ortho-grid shear stiffness calculations

The tip bending deflections can be calculated directly by inverting reduced $\boldsymbol{k}_{bc}$. Beam loads are then applied at the beam tips independently to get δ_x from the transverse beam and δ_y from the longitudinal beam under bending. The equivalent loads and rotations are represented as

$$F_y = n_{xy} d_0 \tag{3.17}$$

$$F_x = n_{xy} d_{90} \tag{3.18}$$

$$\gamma_y = \frac{\delta_y}{d_{90}} \tag{3.19}$$

$$\gamma_x = \frac{\delta_x}{d_0} \tag{3.20}$$

$$\gamma_{xy} = \gamma_x + \gamma_y \tag{3.21}$$

The compliance coefficients are defined as the inverse of the matrix in Eq. (3.1). The shear compliance of an ortho-grid panel with clamped nodes is determined to be

$$a_{66}^{oc} = \frac{d_0 d_{90}^2}{EI} + \frac{d_{90} d_0^2}{EI} + \frac{d_0}{\alpha_{sc} GA} + \frac{d_{90}}{\alpha_{sc} GA} \tag{3.22}$$

The other compliance coefficients are given by

$$a_{11}^{oc} = \frac{d_0}{EA} \tag{3.23}$$

$$a_{22}^{oc} = \frac{d_{90}}{EA} \tag{3.24}$$

They are identical to that obtained by Chen and Tsai [20], where the derivation of these expressions was not provided.

3.2.1.3 Elastic nodes

Ideally, a node provides neither a perfectly clamped nor a perfectly pinned boundary condition for the stiffeners. It is identified to be somewhere between the two [20]. A flexibility condition can be imposed at the nodes analytically by considering the in-plane shear compliance of the laminate structure at the overlapping section. The nodal laminate and in turn its stiffness properties depend on the manufacturing technique employed. For example, the stacking sequence depends on the grid fabrication process and the elastic constants of the lamina depend on the volume fraction.

In-plane torsion springs are added at the nodes and the procedure for the clamped case is repeated with the spring constants added to $\boldsymbol{k}_{bc}$. The stiffeners are isolated as explained earlier and the loading schemes and boundary conditions are provided in Figs. 3.8. Equation (3.25) gives the (6×6) torsion spring stiffness matrix, the derivation of which is based on Ref. [43]. Similar to the stiffeners with clamped BCs, elastic BCs do not change A_{11}, and A_{22} since the loads are parallel to the stiffener elastic axis as shown in Fig. 3.7.

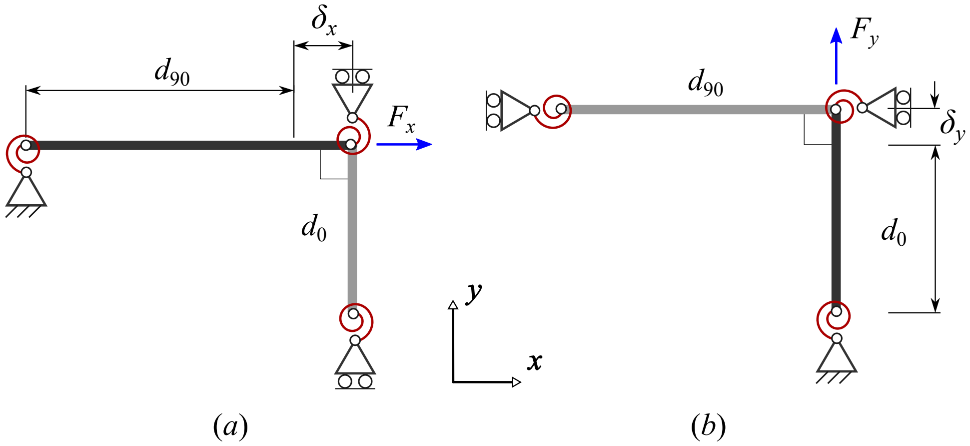

Figure 3.7. Loading and BCs for ortho-grid in-plane stiffness calculations. (*a*) A_{11}, and (*b*) A_{22}

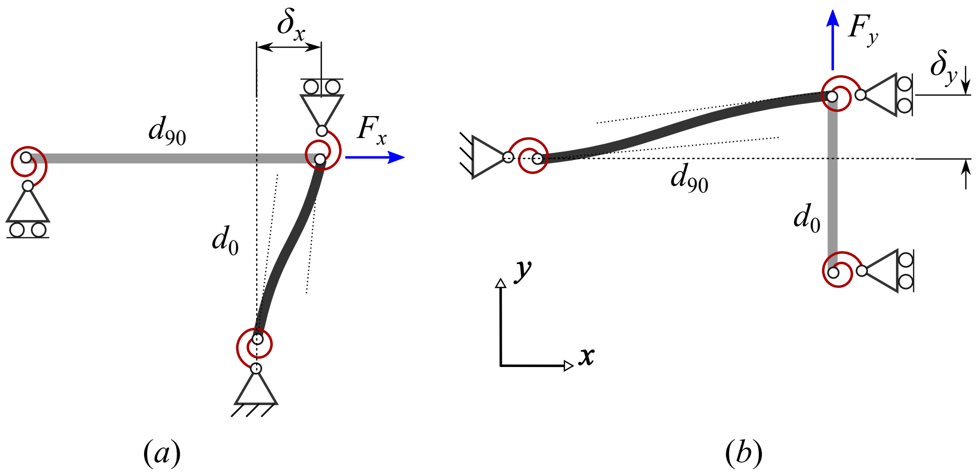

Figure 3.8. Loading and elastic BCs for ortho-grid shear stiffness calculations

$$\boldsymbol{k}_\theta = \begin{bmatrix} 0 & 0 & 0 & 0 & 0 & 0 \\ 0 & 0 & 0 & 0 & 0 & 0 \\ 0 & 0 & k_\theta & 0 & 0 & 0 \\ 0 & 0 & 0 & 0 & 0 & 0 \\ 0 & 0 & 0 & 0 & 0 & 0 \\ 0 & 0 & 0 & 0 & 0 & k_\theta \end{bmatrix} \tag{3.25}$$

where k_θ is the in-plane shear stiffness of the stiffener overlapping regions. The stiffness matrix of the assembly is then obtained by algebraically adding $\boldsymbol{k}_{bc}$ and $\boldsymbol{k}_\theta$. There are three DOFs for an isolated beam representing a stiffener such as the one shown in Fig. 3.8(a); rotations at the supports and the deflection δ_x. Note that the node flexibility is associated with the rotation at the nodes. Upon employing the procedure developed for ortho-grid panels in Sec. 3.2.1.2, the following shear compliance coefficient for an ortho-grid panel with elastic nodes is obtained.

$$a_{66}^{oe} = \frac{d_0^2\, d_{90}}{EI} + \frac{d_0\, d_{90}^2}{EI} + \underline{\frac{d_0\, d_{90}}{k_\theta}} + \frac{d_0}{\alpha_{sc}\, GA} + \frac{d_{90}}{\alpha_{sc}\, GA} \tag{3.26}$$

The first and the second terms correspond to longitudinal (0°) and transverse (90°) stiffeners respectively. The underlined term is due to the elastic BCs at the nodes, which is a newly derived parameter in this study. Since the grid layer is orthotropic, the shear stiffness coefficient is obtained by

$$A_{66}^{oe} = \frac{1}{a_{66}^{oe}} \tag{3.27}$$

Identical results can be obtained also by solving the differential equation of an Euler beam bending problem with torsion spring added to its boundaries. When the torsion spring stiffness $k_\theta \to \infty$ in Eq. (3.26), the expression reduces to the shear compliance

a_{66}^{oc} given in Eq. (3.22). Note that setting $k_\theta = 0$ to obtain simply supported nodes would result in zero shear stiffness, which is consistent with the observation made previously. A finite value of k_θ would reduce the overall shear stiffness of the panel compared to the clamped BC case. The coefficients a_{11}^{oe} and a_{22}^{oe} are identical to that of the clamped BC case since the stiffeners are parallel to the global axes and hence do not exhibit bending. Thus,

$$a_{11}^{oe} = \frac{d_0}{EA} \tag{3.28}$$

$$a_{22}^{oe} = \frac{d_{90}}{EA} \tag{3.29}$$

The in-plane compliance matrix of an ortho-grid panel is given in Eq. (3.30). The stiffness matrix is the inverse of $\boldsymbol{a}_{ij}^{oe}$.

$$\boldsymbol{a}_{ij}^{oe} = \begin{bmatrix} a_{11}^{oe} & 0 & 0 \\ 0 & a_{22}^{oe} & 0 \\ 0 & 0 & a_{66}^{oe} \end{bmatrix} \tag{3.30}$$

The effect of various stiffener BCs such as simply supported, clamped, and elastic on the in-plane stiffness coefficients can be obtained from Eq. (3.30) by the proper selection k_θ.

3.2.2 Angle-grid

The angle-grid stiffeners are oriented at an angle θ with respect to the x axis. The schematic used for derivation is shown in Fig. 3.9.

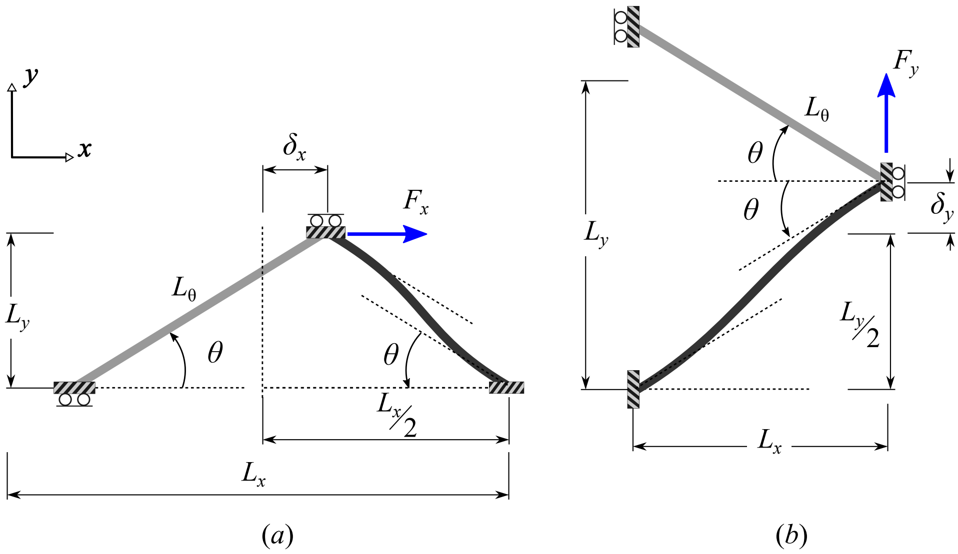

Figure 3.9. Loading and clamped BCs for angle-grid shear stiffness calculations

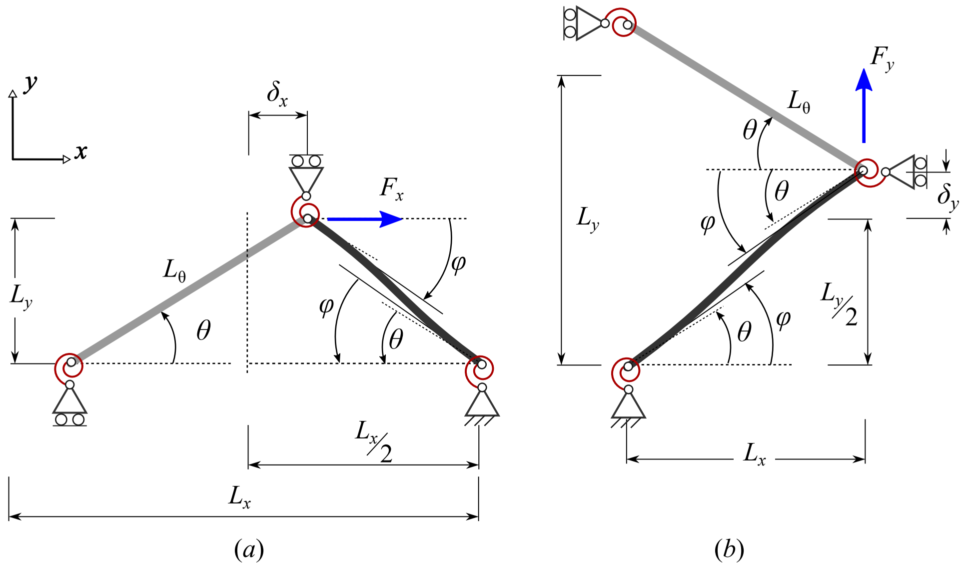

Figure 3.10. Loading and elastic BCs for angle-grid shear stiffness calculations. φ is due to the elastic rotation in the springs

The initial step is to transform the stiffness matrix of a stiffener arbitrarily oriented

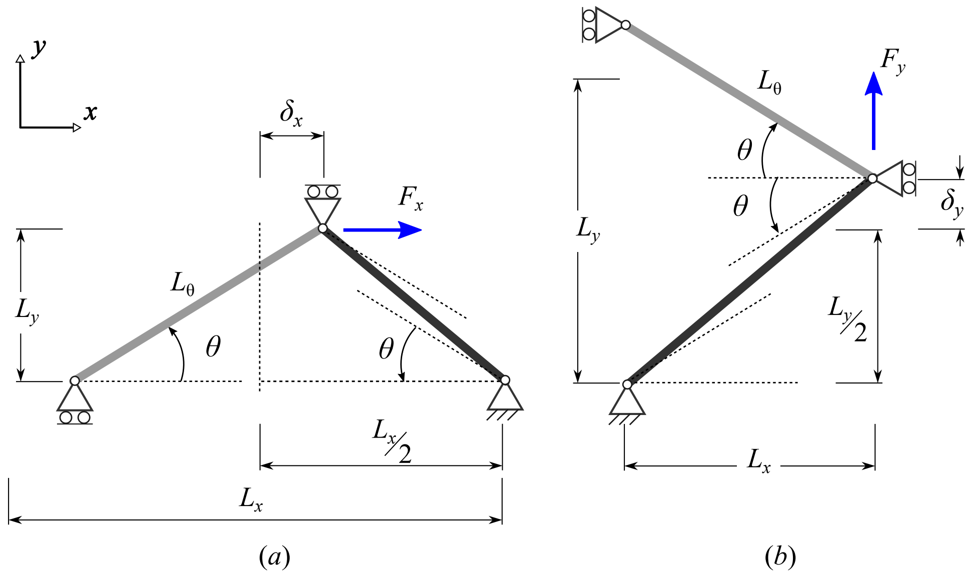

Figure 3.11. Loading and simply supported BCs for angle-grid shear stiffness calculations. Rigid-body rotation at the joints and so there is no flexure in the stiffeners

at an angle θ to the global coordinates as shown in Eq. (3.31).

$$\boldsymbol{K}_{bc} = \boldsymbol{T}_{bc}^{T}\,\boldsymbol{k}_{bc}\,\boldsymbol{T}_{bc} \tag{3.31}$$

$$\boldsymbol{T}_{bc} = \begin{bmatrix} c & s & 0 & 0 & 0 & 0 \\ -s & c & 0 & 0 & 0 & 0 \\ 0 & 0 & 1 & 0 & 0 & 0 \\ 0 & 0 & 0 & c & s & 0 \\ 0 & 0 & 0 & -s & c & 0 \\ 0 & 0 & 0 & 0 & 0 & 1 \end{bmatrix} \tag{3.32}$$

where $s = \sin\theta$ and $c = \cos\theta$.

As stated earlier, the in-plane stiffness matrix of the simply supported angle-grid configuration is singular. So the elastic node case is derived first and the other two cases are subsequently derived from the elastic BC solution. The compliance coefficients are calculated directly by inverting the reduced (after applying appropriate BCs) beam-column stiffness matrix given in Eq. (3.6). The torsion spring stiffness matrix is also transformed to the global coordinate system using Eq. (3.33).

$$\boldsymbol{K}_{\theta} = \boldsymbol{T}_{bc}^{T}\, \boldsymbol{k}_{\theta}\, \boldsymbol{T}_{bc} \tag{3.33}$$

Due to the symmetry of the angle stiffener orientation, stiffener lengths are identical, i.e. $L_{(+\theta)} \equiv L_{(-\theta)} = L_{\theta}$. The global stiffness matrix that includes the effect of transverse shear and elastic BCs is obtained by

$$\boldsymbol{K}_{ag} = \boldsymbol{K}_{bc} + \boldsymbol{K}_{\theta} \tag{3.34}$$

The presence of torsion springs at the support requires that the node rotations are retained. Applying the BCs $\delta_{x_1} = \delta_{y_1} = 0$ to get the (4×4) stiffness matrix $\boldsymbol{K}_{ag}$ for the angle-grid. Displacement vector is obtained by inverting $\boldsymbol{K}_{ag}$ and multiplying by the force vector as

$$[\phi_{z_1},\, \delta_x,\, \delta_y,\, \phi_{z_2}]^T = \boldsymbol{K}_{ag}^{-1}\, [0,\, F_x,\, F_y,\, 0]^T \tag{3.35}$$

The deflections δ_{x_1} and δ_{y_1} are set to δ_x and δ_y respectively. Using Eqs. (3.17) to (3.21) for forces and shear strains, and Eq. (3.2) for normal strains, the smeared stiffness matrix can be obtained for an angle-grid panel with elastic BCs. The lengths of the beams in the above equations are altered to reflect the angle-grid calculation model as,

$$d_0 = L_{\theta}\, s \tag{3.36}$$

$$d_{90} = L_\theta\, c \tag{3.37}$$

After performing the substitutions, the partial compliance matrix of an angle-grid is represented in the matrix form as

$$\begin{Bmatrix} \varepsilon_x \\ \varepsilon_y \end{Bmatrix} = \begin{bmatrix} a_{11} & a_{12} \\ a_{12} & a_{22} \end{bmatrix} \begin{Bmatrix} n_x \\ n_y \end{Bmatrix} \tag{3.38}$$

where

$$a_{11}^{ae} = \frac{L_\theta\, s}{c}\left[\frac{c^2}{EA} + s^2\left(\frac{L_\theta}{2K_\theta} + \frac{(\overline{\alpha}_y + 1)\, L_\theta^2}{12EI_z}\right)\right] \tag{3.39}$$

$$a_{22}^{ae} = \frac{L_\theta\, c}{s}\left[\frac{s^2}{EA} + c^2\left(\frac{L_\theta}{2K_\theta} + \frac{(\overline{\alpha}_y + 1)\, L_\theta^2}{12EI_z}\right)\right] \tag{3.40}$$

$$a_{12}^{ae} = L_\theta\, c\, s\left[\frac{1}{EA} - \left(\frac{L_\theta}{2K_\theta} + \frac{(\overline{\alpha}_y + 1)\, L_\theta^2}{12EI_z}\right)\right] \tag{3.41}$$

The forces and deflections required to determine a_{66}^{ae} are depicted in Fig. 3.10. The shear stiffness derivation is similar to that of the ortho-grid panel. Employing Eqs. (3.17) and (3.21) and using stiffener length L_θ, the shear compliance of the angle-grid configuration with elastic BCs is

$$a_{66}^{ae} = \frac{1}{2cs}\left[\frac{s^2}{s^2\dfrac{EA}{L_\theta} + c^2\dfrac{12EI_z}{L_\theta^3\left((\overline{\alpha}_y + 1) + \dfrac{6EI_z}{K_\theta L_\theta}\right)}}\right.$$

$$+\left.\frac{c^2}{c^2\,\dfrac{EA}{L_\theta}+s^2\,\dfrac{12\,EI_z}{L_\theta^3\left((\overline{\alpha}_y+1)+\dfrac{6\,EI_z}{K_\theta\,L_\theta}\right)}}\right] \tag{3.42}$$

The effect of transverse shear is also captured in the formulation. The spacing between the angle stiffeners d_θ (see Fig. 3.1) determines the grid density. L_θ and d_θ are related by,

$$L_\theta = \frac{d_\theta}{2\,c\,s} \tag{3.43}$$

Setting $K_\theta \to \infty$ and substituting for $\overline{\alpha}_y$ from Eq. (3.7) lead to the clamped condition as represented in the following equations.

$$a_{11}^{ac} = \frac{L_\theta\,s}{c}\left[\frac{c^2}{EA}+s^2\left(\frac{1}{\alpha_{sc}\,GA}+\frac{L_\theta^2}{12\,EI_z}\right)\right] \tag{3.44}$$

$$a_{22}^{ac} = \frac{L_\beta\,c}{s}\left[\frac{s^2}{EA}+c^2\left(\frac{1}{\alpha_{sc}\,GA}+\frac{L_\theta^2}{12\,EI_z}\right)\right] \tag{3.45}$$

$$a_{12}^{ac} = L_\theta\,c\,s\left[\frac{1}{EA}-\left(\frac{1}{\alpha_{sc}\,GA}+\frac{L_\theta^2}{12\,EI_z}\right)\right] \tag{3.46}$$

$$a_{66}^{ac} = \frac{1}{2\,c\,s}\left[\frac{s^2}{s^2\,\dfrac{EA}{L_\theta}+c^2\,\dfrac{12\,EI_z}{L_\theta^3\left(\overline{\alpha}_y+1\right)}}+\frac{c^2}{c^2\,\dfrac{EA}{L_\theta}+s^2\,\dfrac{12\,EI_z}{L_\theta^3\left(\overline{\alpha}_y+1\right)}}\right] \tag{3.47}$$

The expressions for a_{11}^{ac}, a_{12}^{ac}, and a_{22}^{ac} are identical to that reported in [20]. a_{66}^{ac} is a newly derived coefficient. The effect of transverse shear can be neglected by setting

$\overline{\alpha}_y = 0$. The general compliance and stiffness matrices of an angle-grid panel are

$$\boldsymbol{a}_{ij}^{a} = \begin{bmatrix} a_{11} & a_{12} & 0 \\ a_{12} & a_{22} & 0 \\ 0 & 0 & a_{66} \end{bmatrix}^{a} \tag{3.48}$$

$$\boldsymbol{A}_{ij}^{a} = \boldsymbol{a}_{ij}^{a\;-1} \tag{3.49}$$

3.2.3 General-grid

General-grid is a combination of ortho-grid and angle-grid. By invoking the principle of superposition, the in-plane stiffness matrix for a grid configuration with any stiffener BCs is determined by

$$\boldsymbol{A}^{(\text{general-grid})} = \boldsymbol{A}^{(\text{angle-grid})} + \boldsymbol{A}^{(\text{ortho-grid})} \tag{3.50}$$

3.3 Flat grids: Bending stiffness

Chen and Tsai [20] conducted analytical and experimental studies to validate the accuracy of their bending stiffness formulation which was based on the implicit assumption that the stiffeners have simply supported BCs. The same assumption, although explicitly, is applied in the present formulation. As in the earlier sections, ortho-grid and angle-grid topologies are analyzed for bending stiffness coefficients. The grid layers considered in the present research do not exhibit extension-bending coupling. As a result, the moment–curvature relations can be expressed as

$$[m_x, m_y, m_{xy}]^T = \boldsymbol{D}^g_{ij}\,[\kappa_x, \kappa_y, \kappa_{xy}]^T \tag{3.51}$$

with

$$\boldsymbol{D}^g_{ij} = \begin{bmatrix} D^g_{11} & D^g_{12} & 0 \\ D^g_{12} & D^g_{22} & 0 \\ 0 & 0 & D^g_{66} \end{bmatrix} \tag{3.52}$$

Effect of transverse shear is also included in the analysis. The transverse shear strains in the equivalent stiffness panel is determined by conducting the bending analysis of the grid members. For moderately thick and thick beams, there is an additional rotation of the cross-section [44–46]. A first-order shear deformation theory (FSDT) [47] is employed to derive the transverse shear stiffness matrix which relates transverse shear forces to transverse shear strains. The rotation of the beam cross-section under a bending moment is illustrated in Fig. 3.12. The additional rotation of the cross-section is the transverse shear strain γ_{xz} [48].

$$\gamma_{xz} = \phi_{ys} - \phi_y \tag{3.53}$$

where ϕ_{ys} is that total rotation of the cross-section when shear effects are included in the formulation. ϕ_y is the end rotation, which can be directly obtained when shear deformation is ignored. Equation (3.53) shows that when the end rotations from both with-shear and without-shear calculations are known, the difference between the two gives the transverse shear strain. The model to compare the cross-section rotations for both cases is illustrated in Fig. 3.13. An equilibrating shear force Q_x is developed in the cross-section (x face, z direction) to counteract the applied moment. From the Fig. 3.13,

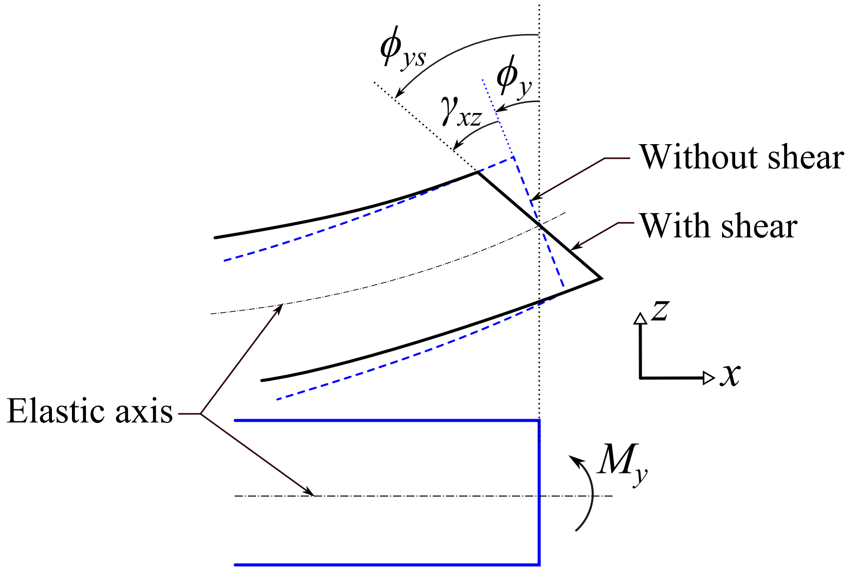

Figure 3.12. Beam cross-section rotation including transverse shear deformation due to bending moment

$$M_y = \frac{Q_x l}{2} \tag{3.54}$$

Similarly, Q_y (y face, z direction) is computed using

$$M_x = \frac{Q_y l}{2} \tag{3.55}$$

Based on the loading scheme given in Fig. 3.13, the rotations ϕ_{ys} and ϕ_y can be obtained from the 3D stiffness matrix given in Eq. (B.1) of the Appendix B. A 3D beam stiffness matrix is used since the one in Eq. (3.6) does not have the bending degrees of freedom in x and y directions. It is also with the intention that a general methodology can be developed to apply it for stiffeners with more complex geometry, which is discussed in Section 3.4.

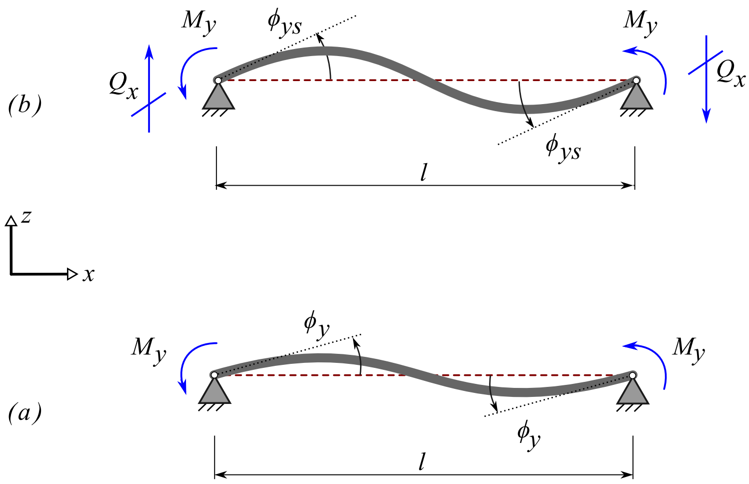

Figure 3.13. Beam end rotations due to antisymmetric bending under applied end moments; (*a*) no shear included and (*b*) transverse shear included. Q_x and Q_y are the reaction shear forces

Using Eq. (3.53), the strains can be expressed in terms of the applied moment in the form

$$\gamma_{xz} = \left(\overline{d}_{ys} - \overline{d}_y\right) M_y \tag{3.56}$$

where $\overline{d}_{ys}$ and $\overline{d}_y$ are the effective bending compliance of the beam with respect to the y axis with-shear and without shear respectively. Similarly, for bending with respect to x axis,

$$\gamma_{yz} = \left(\overline{d}_{xs} - \overline{d}_x\right) M_x \tag{3.57}$$

Substituting for moments in Eqs. (3.56) and (3.57) respectively from Eqs. (3.54) and (3.55) to obtain the transverse shear stiffness coefficients for beams oriented in x and y directions. They can be expressed in matrix form as

$$\begin{Bmatrix} Q_x \\ Q_y \end{Bmatrix} = \begin{bmatrix} \overline{H}_{11} & 0 \\ 0 & \overline{H}_{22} \end{bmatrix} \begin{Bmatrix} \gamma_{xz} \\ \gamma_{yz} \end{Bmatrix} \tag{3.58}$$

where $\overline{H}_{11}$ and $\overline{H}_{11}$ are the transverse shear stiffness coefficients for a beam.

3.3.1 Angle-grid

The bending deformations of an angle stiffener oriented at an angle θ with the x axis in transverse and axial directions are shown in Figs. 3.14 and 3.15. The dotted lined sketches represent the stiffener layer at which the equivalent stiffness coefficients are determined. The task is to determine the bending stiffness of an equivalent plate layer representing the angle stiffener. The boundary conditions are assumed to be simply supported and the moments are applied such that the structure exhibits symmetric bending. The curvatures and moments of the plate equivalent in terms of the beam parameters are

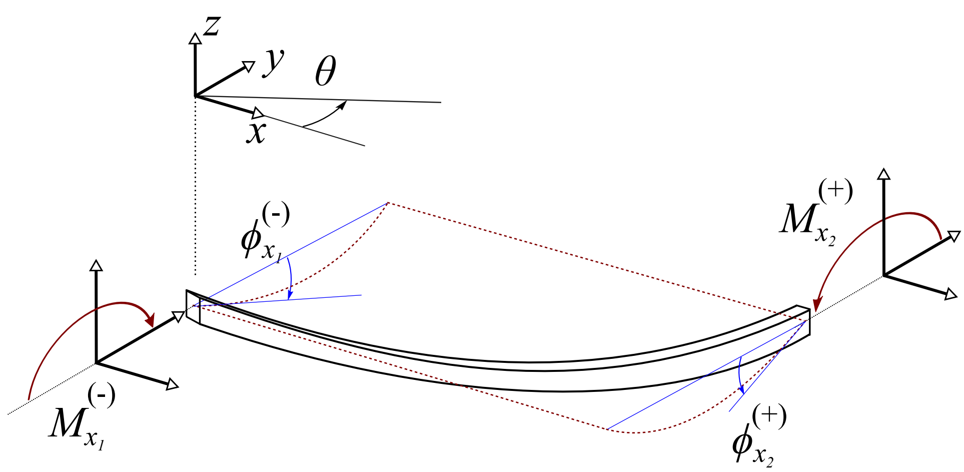

Figure 3.14. Bending of an angle-grid beam in the transverse direction

$$\kappa_x = \frac{2\,\phi_y}{L_x} \tag{3.59}$$

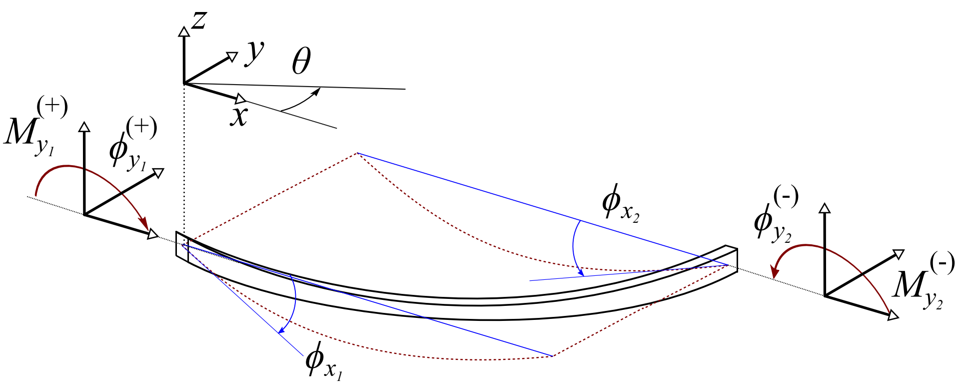

Figure 3.15. Bending of an angle-grid beam in the longitudinal direction

$$\kappa_y = \frac{2\,\phi_x}{L_y} \tag{3.60}$$

$$m_x = \frac{M_y}{L_y} \tag{3.61}$$

$$m_y = \frac{M_x}{L_x} \tag{3.62}$$

with $L_x = Lc$ and $L_y = Ls$. The plate bending and moment resultants are shown in Fig. 3.16. It is important to distinguish between the parameters used to define beam and plate bending. In beam bending, the subscript in the moment parameter represents the axis with which the moment is applied whereas in plate bending the subscript indicates the axis that bends upon the application of the moment. This can be observed by comparing Figs. 3.15 and 3.16. Isolating curvatures in x and y directions and representing

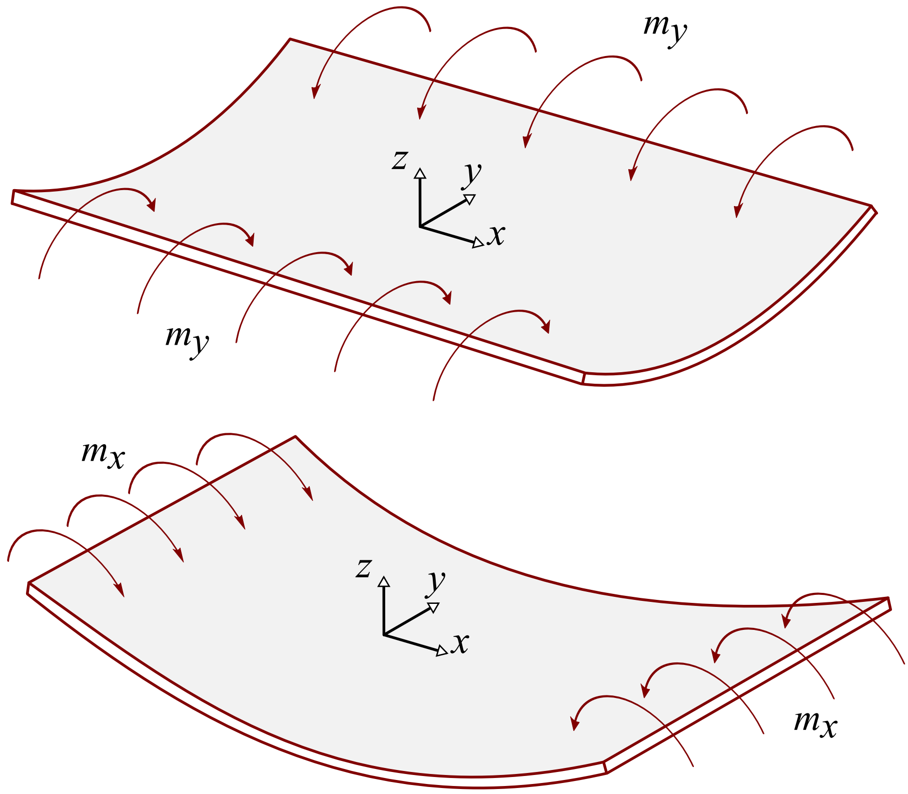

Figure 3.16. Plate bending and moments in x and y directions

them in terms of displacements using Eq. (3.51),

$$\begin{Bmatrix} M_x \\ M_y \end{Bmatrix} = 2 \begin{bmatrix} D_{22}\frac{s}{c} & D_{12} \\ D_{12} & D_{11}\frac{c}{s} \end{bmatrix} \begin{Bmatrix} \phi_x \\ \phi_y \end{Bmatrix} \tag{3.63}$$

The bending stiffness coefficients of an equivalent plate from a grid layer can be derived using the stiffness matrix of a beam in $3D$.

$$\boldsymbol{K}_{3D} = \boldsymbol{T}_{3D}^{T}\,\boldsymbol{k}_{3D}\,\boldsymbol{T}_{3D} \tag{3.64}$$

$$\boldsymbol{T}_{3D} = \begin{bmatrix} \boldsymbol{T} & 0 & 0 & 0 \\ 0 & \boldsymbol{T} & 0 & 0 \\ 0 & 0 & \boldsymbol{T} & 0 \\ 0 & 0 & 0 & \boldsymbol{T} \end{bmatrix} \tag{3.65}$$

$$\boldsymbol{T} = \begin{bmatrix} c & -s & 0 \\ s & c & 0 \\ 0 & 0 & 1 \end{bmatrix} \tag{3.66}$$

The (12×12) stiffness matrix of the beam in space $\boldsymbol{k}_{3D}$, in local coordinate system is given in Eq. (B.1) of Appendix B. The force–displacement relations for a beam in xyz coordinates are expressed in the general form as

$$\boldsymbol{F} = \boldsymbol{K}_{3D}\,\boldsymbol{\Delta} \tag{3.67}$$

where $\boldsymbol{K}_{3D}$ is the (12×12) stiffness matrix. The force and displacement vectors are

$$\boldsymbol{F} = [F_{x_1}, F_{y_1}, F_{z_1}, M_{x_1}, M_{y_1}, M_{z_1}, F_{x_2}, F_{y_2}, F_{z_2}, M_{x_2}, M_{y_2}, M_{z_2}]^T \tag{3.68}$$

$$\boldsymbol{\Delta} = [\delta_{x_1}, \delta_{y_1}, \delta_{z_1}, \phi_{x_1}, \phi_{y_1}, \phi_{z_1}, \delta_{x_2}, \delta_{y_2}, \delta_{z_2}, \phi_{x_2}, \phi_{y_2}, \phi_{z_2}]^T \tag{3.69}$$

Applying simply supported BCs at both ends and introducing proper sign conventions, the moment–twist relations become

$$\begin{Bmatrix} (-)M_{x_1} \\ (+)M_{y_1} \\ (+)M_{x_2} \\ (-)M_{y_2} \end{Bmatrix} = \underset{(4\times4)}{[\overline{\boldsymbol{D}}_{ij}]} \begin{Bmatrix} (-)\phi_{x_1} \\ (+)\phi_{y_1} \\ (+)\phi_{x_2} \\ (-)\phi_{y_2} \end{Bmatrix} \tag{3.70}$$

The signs for moments and rotations are from Fig. 3.17. Once the above matrix is obtained, expressions for end moments are set as $M_{x_1} = -M_x$, $M_{x_2} = M_x$, $M_{y_1} = M_y$, and $M_{y_2} = -M_y$. Combining the expressions for the respective moments leads to

$$\begin{Bmatrix} M_x \\ M_y \end{Bmatrix} = \begin{bmatrix} \overline{D}_{11} & \overline{D}_{12} \\ \overline{D}_{12} & \overline{D}_{22} \end{bmatrix} \begin{Bmatrix} \phi_x \\ \phi_y \end{Bmatrix} \tag{3.71}$$

The matrix in the above equation can be directly obtained from the stiffness coefficients in Eq. (3.67). Comparing Eq. (3.71) to Eq. (3.63) gives the expressions for the elements in the matrix given in Eq. (3.63) in terms of the beam stiffness coefficients. The coefficients thus obtained are for a stiffener oriented at an arbitray angle prescribed in Eq. (3.134). In order to obtain the contributions of both the $+\theta$ and $-\theta$ stiffeners are obtained by adding the corresponding stiffness coefficients. Again, as explained earlier, this is possible since it is assumed that the principle of superposition is valid. Thus the bending stiffness coefficients of representing equivalent stiffness plate representing the angle-grid configuration are

$$D_{11}^{ag} = 2\frac{EI}{d_\theta}c^4 + 2\frac{GJ}{d_\theta}c^2 s^2 \tag{3.72}$$

$$D_{22}^{ag} = 2\frac{EI}{d_\theta}s^4 + 2\frac{GJ}{d_\theta}c^2 s^2 \tag{3.73}$$

$$D_{12}^{ag} = 2\frac{EI}{d_\theta}c^2 s^2 - 2\frac{GJ}{d_\theta}c^2 s^2 \tag{3.74}$$

where d_θ is the spacing between the oblique stiffeners.

Derivation of D_{66}^{g} follows a similar procedure except that the beam rotations are expressed in terms of the equivalent plate twists as shown in Eq. (3.75). The beam twisting moments and rotations are presented on an equivalent stiffness plate element in Fig. 3.17. The sign conventions used for the moments and rotations are also indicated. The plate twist is given by [49]

$$\kappa_{xy} = 2\frac{\partial^2 w}{\partial x \partial y}\,\mathrm{d}x \quad \text{leads to}$$

$$\kappa_{xy} = \frac{2\,\phi_x}{L_x} \quad \text{or} \quad \frac{2\,\phi_y}{L_y} \tag{3.75}$$

The expression for m_{xy} is obtained following the assumption that the net twisting moment is the average of the twisting moments on the adjacent edges [20].

$$m_{xy} = \frac{1}{2}\left(\frac{M_x}{L_y} + \frac{M_y}{L_x}\right) \tag{3.76}$$

The plate twisting moment and plate twist are related by,

$$m_{xy} = D_{66}^{g}\,\kappa_{xy} \tag{3.77}$$

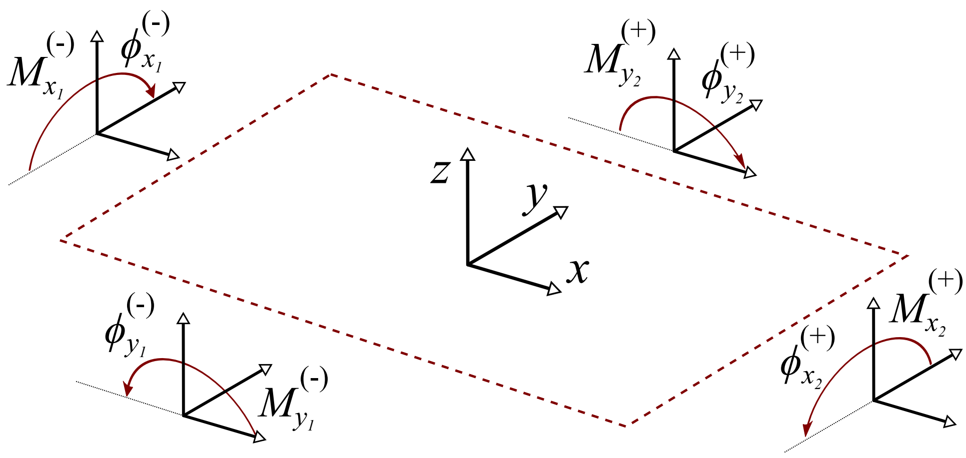

Figure 3.17. Beam twisting moments and beam end rotations illustrated in a plate representative of a grid layer

Upon following the procedure explained for deriving the bending stiffness coefficients employing Eqs.(3.77), (3.76), and (3.75) and adopting the sign conventions in Fig. 3.17,

$$D_{66}^{ag} = 2\frac{EI}{d_\theta}c^2 s^2 + \frac{GJ}{2\,d_\theta}\left(c^2 - s^2\right)^2 \tag{3.78}$$

It is interesting to note that when the stiffener angle is 45°, the second term in Eq. (3.78) involving the torsion stiffness GJ vanish. This means that there is no twisting of the stiffener which is the consequence of the assumption given in Eq. (3.76).

3.3.2 Ortho-grid

To derive the parameters in Eq. (3.52), the moments are applied such that the structure exhibits pure bending. The bending of transverse and longitudinal stiffeners are illustrated in Figs. 3.18 and 3.19 respectively. The sign conventions used for the beam moments and rotations are also shown. The methodology is identical to that of angle-

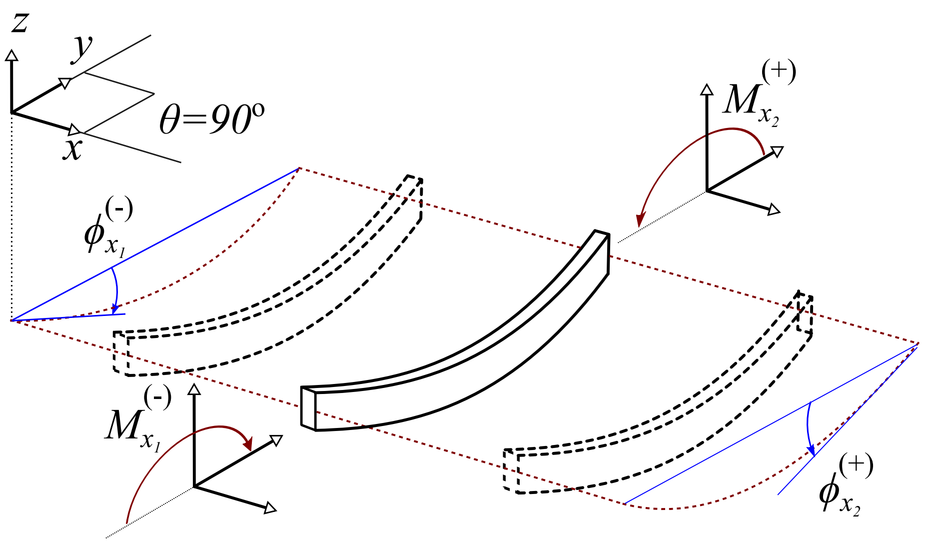

Figure 3.18. Moments applied to the transverse stiffener

grid. The stiffness matrices should be altered from that of an angle-grid by specifying appropriate stiffener orientation angles. Setting $\theta = 0$ and $\theta = 90$ gives the stiffness matrices for longitudinal and transverse stiffeners respectively. D_{11}^{og} and D_{22}^{og} are determined independently as there are no M_x moments for longitudinal stiffeners and M_y moments for transverse stiffeners for the loading conditions shown. This also leads to Eq. (3.81). Thus, the bending coefficients are given by

$$D_{11}^{g} = \frac{EI}{d_0} \tag{3.79}$$

$$D_{22}^{g} = \frac{EI}{d_{90}} \tag{3.80}$$

$$D_{12}^{g} = 0 \tag{3.81}$$

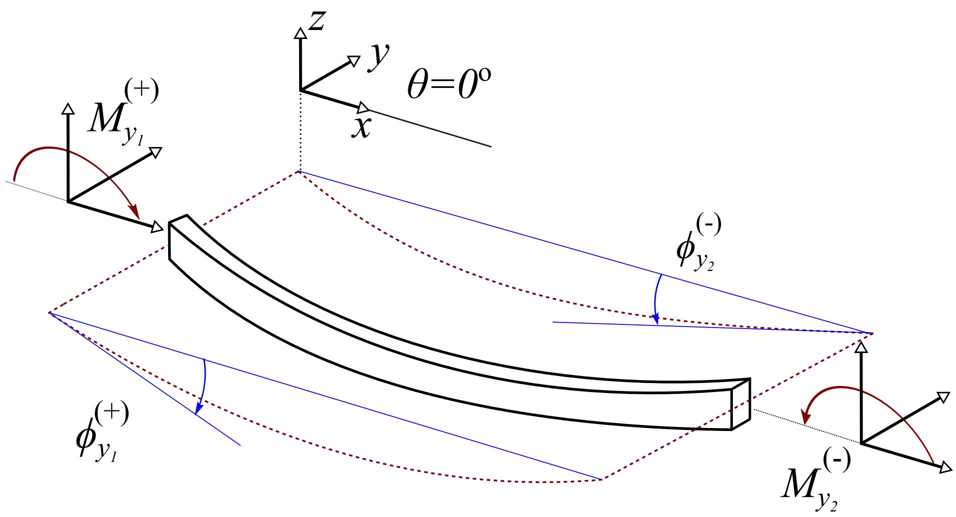

Figure 3.19. Moments applied to the longitudinal stiffener

d_0 and d_{90} are the spacing between longitudinal and transverse stiffeners respectively. Following the same procedure for angle-grid, D_{66}^{og} is evaluated to be

$$D_{66}^{og} = \left(\frac{GJ}{4\,d_0} + \frac{GJ}{4\,d_{90}} \right) \tag{3.82}$$

The expressions obtained for the D_{ij}^{g} for both angle- and ortho-grid are identical to that reported in the literature [20], where there was no derivation provided.

3.3.3 General-grid

The bending stiffness matrix of a general-grid can be obtained from ortho-grid and angle-grid by using the principle of superposition as

$$\boldsymbol{D}^{(\text{general}-\text{grid})} = \boldsymbol{D}^{(\text{angle}-\text{grid})} + \boldsymbol{D}^{(\text{ortho}-\text{grid})} \tag{3.83}$$

where the $\boldsymbol{D}$ is given in Eq. (3.52).

3.4 Cylindrical grids

The methodologies developed to derive the equivalent stiffness coefficients of the flat grids can be directly applied for the case of cylindrical grids. The ortho-grid and general-grid stiffening configurations are shown in the Figs. 3.20 and 3.21 respectively. The

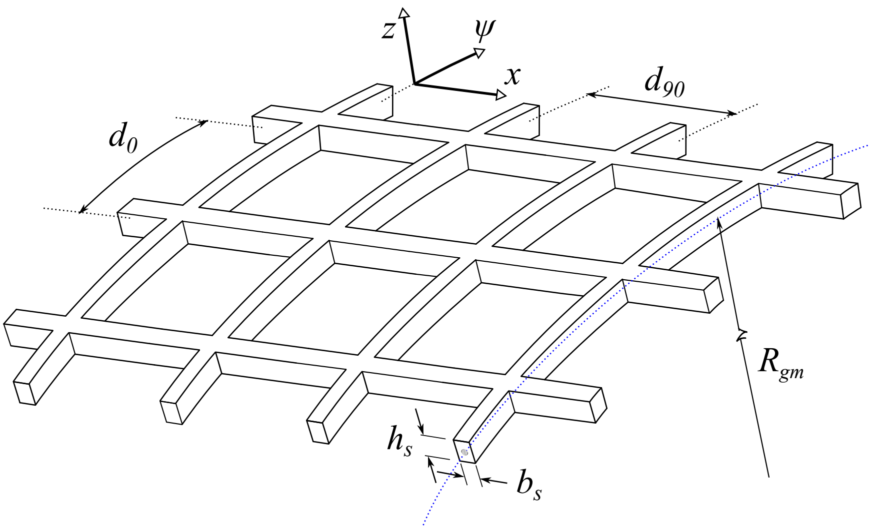

Figure 3.20. Cylindrical ortho-grid structure. Transverse stiffener is a circular arch

transverse stiffeners of the ortho-grid are circular arch beams and the angle-stiffeners of the general- and angle-grid are circular helical beams as illustrated. The task is to derive the stiffness matrices of the these stiffeners since the equivalent stiffness coefficients are developed directly from them. The stiffness matrix of the circular arch can be derived from the more general case of the helical beam, the stiffness matrix of the helical beam is derived first.

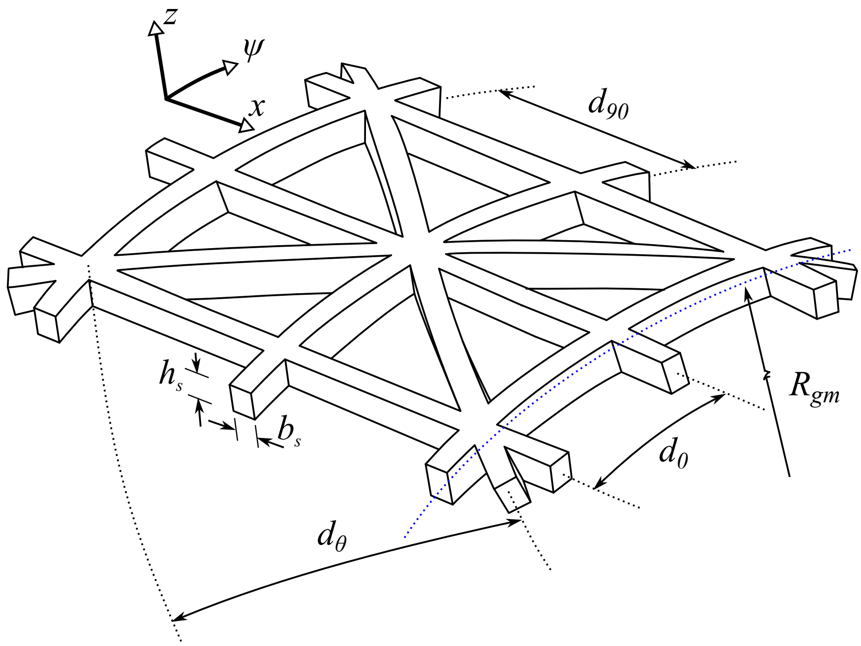

Figure 3.21. Cylindrical general-grid structure. Angle stiffener is a helical beam and transverse stiffener is a circular arch

3.4.1 Derivation of the stiffness matrix

An exact derivation of the stiffness coefficients of helical stiffeners is performed using the transfer matrix method (TMM) [42, 50, 51]. Detailed derivations and applications of the TMM are provided by Wunderlich and Pilkey [42]. The beam that is used to represent a helical stiffener is shown in Fig. 3.22. The pitch of the helix is given by $p = 2\pi h$ and the height $z = h\xi$. Various parameters for the helix are defined as,

$$h = c_h \sin\psi \tag{3.84}$$

$$R_{gm} = c_h \cos\psi \tag{3.85}$$

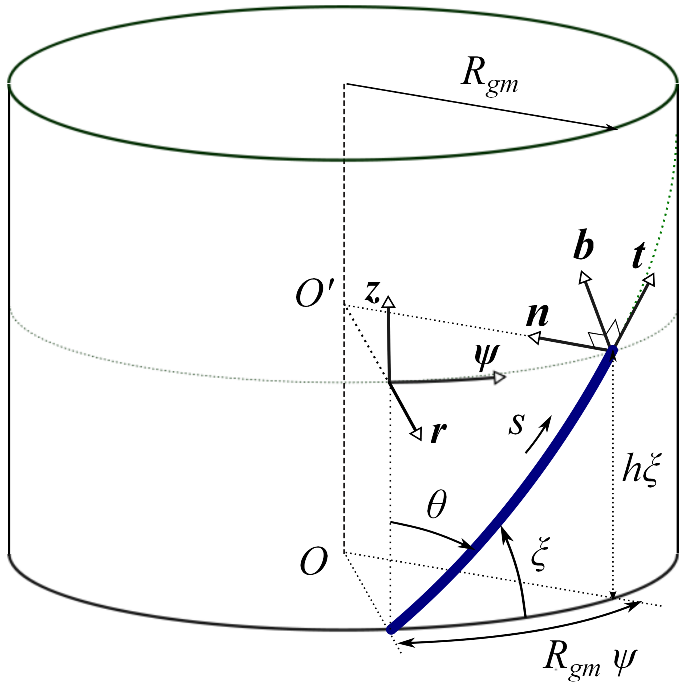

Figure 3.22. Helical beam orientation showing local $(\boldsymbol{t}, \boldsymbol{n}, \boldsymbol{b})$ and cylindrical $(\boldsymbol{r}, \boldsymbol{t}, \boldsymbol{z})$ coordinate systems. θ and ξ are the stiffener angle and pitch angle respectively

$$\chi = \frac{R_{gm}}{c_h^2} \tag{3.86}$$

$$\tau = \frac{h}{c_h^2} \tag{3.87}$$

h is the change in height of the helix after one full rotation. The helix geometry parameter c_h is given by

$$c_h = \sqrt{R_{gm}^2 + h^2} \tag{3.88}$$

χ and τ are the bending and torsional curvatures of the helix respectively. These quantities are constants for a given helix [52]. ψ is the circumferential coordinate of the cylinder and also referred to as the pitch angle of the helix. R_{gm} is the radius of the cylinder measured at the centroid of the helical stiffener cross-section. This is also the radius of the reference plane of the grid layer. The stiffener angle, θ is defined as the orientation of an angle stiffener with the longitudinal (x) axis of the cylinder.

$$\theta = \frac{\pi}{2} - \xi \tag{3.89}$$

Therefore the length of the helical stiffener between its boundaries in terms of the stiffener orientation is given by

$$L_\theta = \frac{R_{gm}\,\psi}{\sin\theta} \tag{3.90}$$

A local coordinate system is prescribed to generate the locus of the centroid of the helical stiffener using the Frenet trihedron tnb. The unit vectors $\hat{t}$, $\hat{n}$, and $\hat{b}$ represent the tangent, the normal which is directed radially inward, and the binormal which is perpendicular to the $t-n$ plane respectively. The local and global coordinate systems, forces, displacements, moments, and rotations in the stiffener cross-section are shown in Fig. 3.23. The shell structure is also shown for reference, although this section addresses only the grid structure.

3.4.1.1 Equilibrium equations

The equilibrium equations are as follows [50]:

Force equilibrium equations,

$$\frac{dV_t}{ds} - \chi V_n = 0 \tag{3.91a}$$

$$\chi V_t + \frac{dV_n}{ds} - \tau V_b = 0 \tag{3.91b}$$

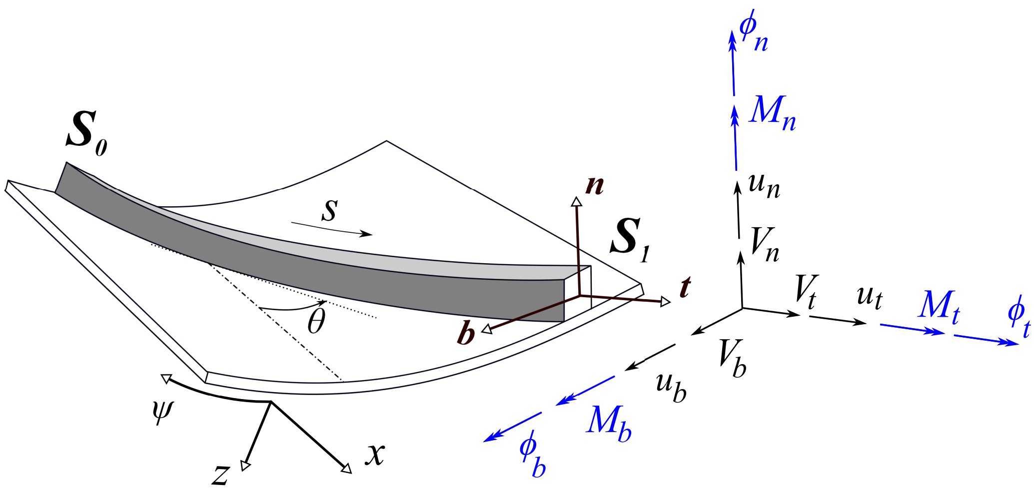

Figure 3.23. A helical stiffener displacements and internal forces

$$\tau V_n + \frac{dV_b}{ds} = 0 \tag{3.91c}$$

Moment equilibrium equations,

$$\frac{dM_t}{ds} - \chi M_n = 0 \tag{3.92a}$$

$$-V_b + \chi M_t + \frac{dM_n}{ds} - \tau M_b = 0 \tag{3.92b}$$

$$V_n + \tau M_n + \frac{dM_b}{ds} = 0 \tag{3.92c}$$

Compatibility of rotations,

$$-\frac{M_t}{GJ} + \frac{d\phi_t}{ds} - \chi\phi_n = 0 \tag{3.93a}$$

$$-\frac{M_n}{EI_n} + \chi\phi_t + \frac{d\phi_n}{ds} - \tau\phi_b = 0 \tag{3.93b}$$

$$-\frac{M_b}{EI_b} + \tau\phi_n + \frac{d\phi_b}{ds} = 0 \tag{3.93c}$$

Compatibility of displacements,

$$-\frac{V_t}{EA} + \frac{du_t}{ds} - \chi u_n = 0 \tag{3.94a}$$

$$-\frac{\alpha_n V_n}{GA} - \phi_b + \chi u_t + \frac{du_n}{ds} - \tau u_b = 0 \tag{3.94b}$$

$$-\frac{\alpha_b V_b}{GA} + \phi_n + \tau u_n + \frac{du_b}{ds} = 0 \tag{3.94c}$$

$\boldsymbol{Q}(s)$ relates the state vector $\boldsymbol{S}_0(s = s_1)$ to that of an arbitrary location $\boldsymbol{S}_I(s = s_2)$ is the *transfer* matrix [51]. For a homogeneous solution, i.e., in the absence of any external loads, the state vector at an arbitrary location is given by setting $s_1 = 0$ and $s_2 = s$ as demonstrated in Eq. (3.95).

$$\boldsymbol{S}(s) = \boldsymbol{Q}(s)\ \boldsymbol{S}(0) \tag{3.95}$$

Note that the transfer matrix $\boldsymbol{Q}(s)$ is a (12×12) matrix. The state vector at $s_2 = s$ can be represented as

$$\boldsymbol{S}(s) = [\boldsymbol{V}_s,\ \boldsymbol{M}_s,\ \boldsymbol{\Phi}_s,\ \boldsymbol{\Delta}_s]^T \tag{3.96}$$

where the force, moment, rotation, and displacement vectors are given in Eq. (3.97), (3.98), (3.99) and (3.100) respectively.

$$\boldsymbol{V}_s = [V_{t_s},\ V_{n_s},\ V_{b_s}]^T \tag{3.97}$$

$$\boldsymbol{M}_s = [M_{t_s},\ M_{n_s},\ M_{b_s}]^T \tag{3.98}$$

$$\boldsymbol{\Phi}_s = [\phi_{t_s},\ \phi_{n_s},\ \phi_{b_s}]^T \tag{3.99}$$

$$\boldsymbol{\Delta}_s = [\delta_{t_s},\ \delta_{n_s},\ \delta_{b_s}]^T \tag{3.100}$$

and the state vector at location $s_1 = 0$ is

$$\boldsymbol{S}(0) = [\boldsymbol{V}_0,\ \boldsymbol{M}_0,\ \boldsymbol{\Phi}_0,\ \boldsymbol{\Delta}_0]^T \tag{3.101}$$

where

$$\boldsymbol{V}_0 = [V_{t_0},\ V_{n_0},\ V_{b_0}]^T \tag{3.102}$$

$$\boldsymbol{M}_0 = [M_{t_0},\ M_{n_0},\ M_{b_0}]^T \tag{3.103}$$

$$\boldsymbol{\Phi}_0 = [\phi_{t_0},\ \phi_{n_0},\ \phi_{b_0}]^T \tag{3.104}$$

$$\boldsymbol{\Delta}_0 = [\delta_{t_0},\ \delta_{n_0},\ \delta_{b_0}]^T \tag{3.105}$$

3.4.1.2 Solution of the equilibrium equations

For a circular helix, the variable s can be expressed in ψ as [50].

$$s = c_h \, \psi \tag{3.106}$$

Thus,

$$ds = c_h \, d\psi \tag{3.107}$$

The solution methodology is explained using only a set of representative equations. For example, the force equilibrium equations can be solved as follows. Substituting Eqs. (3.91a) and (3.91c) in Eq.(3.91b) and writing the resulting expression in terms of the variable, ψ gives

$$V_n'' + V_n = 0 \tag{3.108}$$

The notation $()''$ is used to represent $d^2()/d\psi$. Equation (3.108) is a second order linear homogeneous ordinary differential equation which can be solved directly. Equation for V_t can be obtained as shown in Eq. (3.109), which is a first order linear ordinary differential equation that can also be solved directly.

$$V_t' = \chi \, c_h \, V_n \tag{3.109}$$

Once V_n and V_t are obtained, V_b can be determined from Eq. (3.91b) as,

$$V_b = \frac{1}{c_h \, \tau} V_n' + c_h \, \chi \, V_t \tag{3.110}$$

Similar procedure is employed to solve for moments, rotations, and displacements.

For moments, Eqs. (3.92a) to (3.92c) are rewritten as

$$M_n'' + M_n = V_b' c_h - \tau c_h^2 V_n \tag{3.111}$$

$$M_t' = \chi c_h M_n \tag{3.112}$$

$$M_b = \frac{1}{c_h \tau} \left(M_n' + c_h \chi M_t - c_h V_b \right) \tag{3.113}$$

and the rotations, in Eqs. (3.93a) to (3.93c) are

$$\phi_n'' + \phi_n = c_h^2 \left(\tau \frac{M_b}{EI_b} - \chi \frac{M_t}{GJ} \right) + c_h \frac{M_n'}{EI_n} \tag{3.114}$$

$$\phi_t' = c_h \left(\chi \phi_n + \frac{M_t}{GJ} \right) \tag{3.115}$$

$$\phi_b = \frac{1}{c_h \tau} \left(\phi_n' + c_h \chi \phi_t - c_h \frac{M_n}{EI_n} \right) \tag{3.116}$$

and finally the displacements in terms of the variable, ψ are

$$u_n'' + u_n = -c_h^2 \tau \phi_n + c_h^2 \left(\tau \frac{\alpha_b V_b}{GA} - \chi \frac{\chi V_t}{EA} \right) + c_h \left(\frac{\alpha_n V_n'}{GA} + \phi_b' \right) \tag{3.117}$$

$$u_t' = c_h \left(\chi u_n + \frac{V_t}{EA} \right) \tag{3.118}$$

$$u_b = \frac{1}{c_h \tau} \left[u_n' + c_h \left(\chi u_t - \phi_b - \frac{\alpha_n V_n}{GA} \right) \right] \tag{3.119}$$

These equations are solved sequentially in strict order; forces, moments, rotations, and finally the displacements. The general solution of the homogeneous differential equation given in Eq. (3.108) is of the form

$$V_n = k_1 \cos\psi + k_2 \sin\psi \tag{3.120}$$

where k_1 and k_2 are arbitrary constants. V_t is obtained by substituting V_n in Eq. (3.109) and performing direct integration to obtain

$$V_t = \chi\, c_h\, (k_1 \sin\psi - k_2 \cos\psi) + k_3 \tag{3.121}$$

where k_3 is an arbitrary integration constant. V_b is then determined from Eq. (3.110) as explained earlier. The general solution of nonhomogeneous second oder differential equation, such as the one in Eq. (3.111), is of the form

$$M_n = M_{n_h} + M_{n_p} \tag{3.122}$$

where M_{n_h} and M_{n_p} are the homogeneous and particular solutions respectively. The particular solution is not unique among the various equations that must be solved and so are not presented. The solution strategies are readily available in various calculus books, for example [52]. The rest of the equations can be solved analytically as explained earlier. It can be deduced that the solutions become progressively complex in terms of the analytical expressions. Consequently, a symbolic algebra tool such as Maxima [53] is employed.

3.4.1.3 Stiffness coefficients

The twelve arbitrary constants $k_1, k_2, k_3, \ldots, k_{12}$ are obtained by setting limits on the values of ψ. The initial step is to determine the transfer matrix relating the state vectors between any two arbitrary locations ψ_1 and ψ_2. To facilitate the analytical derivation, the state vector in Eq. (3.101) is evaluated at $\psi_1 = 0$ to obtain expressions for forces, moments, rotations, and displacements as shown in Eqs. (3.102) to (3.104). The twelve constants are solved in terms of these parameters. The constants are then substituted into $\boldsymbol{S}(\psi_2 = \psi)$. The resulting relations can then be expressed as shown earlier in Eq. (3.95) in terms of variable ψ in a concise form with $\boldsymbol{Q}(\psi)$ set to $\boldsymbol{Q}$ as

$$\begin{Bmatrix} \boldsymbol{F}_\psi \\ \boldsymbol{d}_\psi \end{Bmatrix} = \begin{bmatrix} \boldsymbol{Q}_{11} & \boldsymbol{Q}_{12} \\ \boldsymbol{Q}_{21} & \boldsymbol{Q}_{22} \end{bmatrix} \begin{Bmatrix} \boldsymbol{F}_0 \\ \boldsymbol{d}_0 \end{Bmatrix} \tag{3.123}$$

where

$$\boldsymbol{F}_\psi = [\boldsymbol{V}_\psi,\ \boldsymbol{M}_\psi]^T \tag{3.124}$$

$$\boldsymbol{F}_0 = [\boldsymbol{V}_0,\ \boldsymbol{M}_0]^T \tag{3.125}$$

$$\boldsymbol{d}_\psi = [\boldsymbol{\Delta}_\psi,\ \boldsymbol{\Phi}_\psi]^T \tag{3.126}$$

$$\boldsymbol{d}_0 = [\boldsymbol{\Delta}_0,\ \boldsymbol{\Phi}_0]^T \tag{3.127}$$

The sub-matrices $\boldsymbol{Q}$ in Eq. (3.123) are (6×6) matrices. Once $\boldsymbol{Q}(\psi)$ is determined, it is rearranged to obtain the stiffness matrix of the helical beam in local coordinates,

(t,n,b). The force–displacement relations are thus written as

$$[\boldsymbol{F}_0, \boldsymbol{F}_\psi]^T = \overline{\boldsymbol{k}}_h \, [\boldsymbol{d}_0, \boldsymbol{d}_\psi]^T \tag{3.128}$$

where

$$\overline{\boldsymbol{k}}_h = \begin{bmatrix} \overline{\boldsymbol{k}}_{h_{11}} & \overline{\boldsymbol{k}}_{h_{12}} \\ \overline{\boldsymbol{k}}_{h_{21}} & \overline{\boldsymbol{k}}_{h_{22}} \end{bmatrix} \tag{3.129}$$

with

$$\overline{\boldsymbol{k}}_{h_{11}} = -\boldsymbol{Q}_{21}{}^{-1}\,\boldsymbol{Q}_{22} \tag{3.130}$$

$$\overline{\boldsymbol{k}}_{h_{12}} = \boldsymbol{Q}_{21}{}^{-1} \tag{3.131}$$

$$\overline{\boldsymbol{k}}_{h_{21}} = -\boldsymbol{Q}_{11}\,\boldsymbol{Q}_{21}{}^{-1}\,\boldsymbol{Q}_{22} + \boldsymbol{Q}_{12} \tag{3.132}$$

$$\overline{\boldsymbol{k}}_{h_{22}} = \boldsymbol{Q}_{11}\,\boldsymbol{Q}_{21}{}^{-1} \tag{3.133}$$

The stiffness matrix $\overline{\boldsymbol{k}}_h$ in Eq. (3.128) is symmetric. The size of $\overline{\boldsymbol{k}}_h$ is (12×12), representing the 6 DOFs at each end of the helical beam as illustrated in Fig. 3.23. An alternate method to determine stiffness matrix from the TM is provided in Sec. B.3 of Appendix B.

$\overline{\boldsymbol{k}}_h$ is in the tnb local coordinate system and is transformed to the cylindrical $r\psi z$ coordinates to obtain the global (12×12) stiffness matrix $\overline{\boldsymbol{K}}_h$, which is shown in Eq. (3.134). The stiffness matrix is transformed to the cylindrical coordinates system to facilitate the application of boundary conditions and loads.

$$\overline{\boldsymbol{K}}_h = \begin{bmatrix} \boldsymbol{G}_{t0}^T\,\boldsymbol{B}_{t0}^T\,\overline{\boldsymbol{k}}_{h_{11}}\,\boldsymbol{G}_{t0}\,\boldsymbol{B}_{t0} & \boldsymbol{G}_{t0}^T\,\boldsymbol{B}_{t0}^T\,\overline{\boldsymbol{k}}_{h_{12}}\,\boldsymbol{G}_{t}\,\boldsymbol{B}_{t} \\ \boldsymbol{G}_{t}^T\,\boldsymbol{B}_{t}^T\,\overline{\boldsymbol{k}}_{h_{21}}\,\boldsymbol{G}_{t0}\,\boldsymbol{B}_{t0} & \boldsymbol{G}_{t}^T\,\boldsymbol{B}_{t}^T\,\overline{\boldsymbol{k}}_{h_{22}}\,\boldsymbol{G}_{t}\,\boldsymbol{B}_{t} \end{bmatrix} \tag{3.134}$$

where $\boldsymbol{B}_{t0} = \boldsymbol{B}_t(0)$, $\boldsymbol{G}_{t0} = \boldsymbol{G}_t(0)$ and

$$\boldsymbol{B}_t = \boldsymbol{B}_t(\psi) = \begin{bmatrix} \cos\psi & -\sin\psi & 0 \\ \cos\psi & \sin\psi & 0 \\ 0 & 0 & 1 \end{bmatrix} \tag{3.135}$$

$$\boldsymbol{G}_t = \boldsymbol{G}_t(\psi) = \begin{bmatrix} -\sin\psi\cos\xi & \cos\psi\cos\xi & \sin\xi \\ -\cos\psi & -\sin\psi & 0 \\ \sin\psi\sin\xi & -\cos\psi\sin\xi & \cos\xi \end{bmatrix} \tag{3.136}$$

The force–displacement relation of the helical beam in the cylindrical coordinate system is given as

$$\boldsymbol{F}_c = \overline{\boldsymbol{K}}_h\, \boldsymbol{\Delta}_c \tag{3.137}$$

where $\boldsymbol{F}_c$ and $\boldsymbol{\Delta}_c$ are the force and displacement vectors in cylindrical coordinates system. They are defined as,

$$\boldsymbol{F}_c = [F_{r_1}, F_{\psi_1}, F_{z_1}, M_{r_1}, M_{\psi_1}, M_{z_1}, F_{r_2}, F_{\psi_2}, F_{z_2}, M_{r_2}, M_{\psi_2}, M_{z_2}]^T \tag{3.138}$$

$$\boldsymbol{\Delta}_c = [\delta_{r_1}, \delta_{\psi_1}, \delta_{z_1}, \phi_{r_1}, \phi_{\psi_1}, \phi_{z_1}, \delta_{r_2}, \delta_{\psi_2}, \delta_{z_2}, \phi_{r_2}, \phi_{\psi_2}, \phi_{z_2}]^T \tag{3.139}$$

3.5 Cylindrical grids: In-plane stiffness

The strains at the mid-plane of a typical cylindrical shell element after first-order approximations are [54],

$$\varepsilon_x^\circ = \frac{\partial \delta_x}{\partial x} \tag{3.140}$$

$$\varepsilon_{\psi}^{\circ} = \frac{\partial \delta_{\psi}}{\partial \psi} + \frac{1}{R_{gm}} \delta_r \tag{3.141}$$

$$\varepsilon_{x\psi}^{\circ} = \frac{1}{R_{gm}} \frac{\partial \delta_x}{\partial \psi} + \frac{\partial \delta_{\psi}}{\partial x} \tag{3.142}$$

The term δ_r / R_{gm} in the circumferential strain in Eq. (3.141) denotes the uniform radial expansion of the shell calculated from the change in the circumference after deformation and not from the circumferential displacement u_{ψ}. However, in order to not to violate the assumption that the stiffener nodes are constrained to the plane of the undeformed cylinder, the radial displacement δ_r is set to zero at the supports. The coupling between various deflection modes due to the beam geometry is already taken into account in the stiffness matrix formulation of the helical and circumferential stiffeners.

The derivation of the in-plane shear stiffness calculation of the cylindrical ortho-grid configuration with clamped BCs is presented. The loading and BCs for the calculation of the shear stiffness is shown in Fig. 3.24. Figure 3.24a shows the contribution of the longitudinal stiffeners, which is identical to the flat ortho-grid problem defined in Fig. 3.6a. The deflections in the transverse stiffeners for cylindrical and flat ortho-grid are shown in Fig. 3.24b and Fig. 3.6b respectively. They are different only in terms of the stiffness matrices employed to determine the deflection in the direction of x axis. The cylindrical ortho-grid uses the stiffness matrix of an arch beam instead of a planar beam.

The shear compliance of the cylindrical ortho-grid with clamped BCs is calculated to be

$$_c a_{66}^{oc} = \frac{d_{90}^2 d_0}{12EI} + \bar{c}_{66} \frac{d_{90}}{\bar{d}_0} \tag{3.143}$$

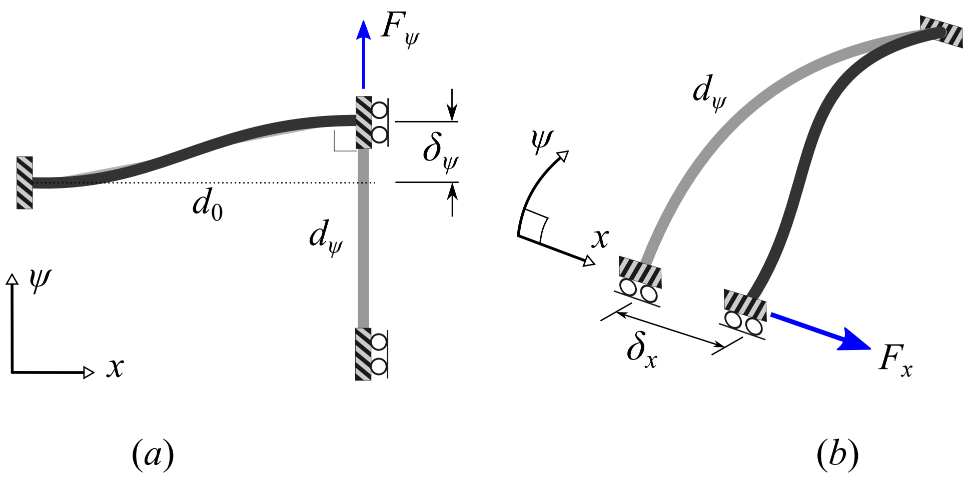

Figure 3.24. Shear stiffness calculation scheme for cylindrical ortho-grid

where

$$\overline{d}_0 = 2\,R_{gm}\,\sin\left(\frac{\psi}{2}\right) \tag{3.144}$$

and

$$\overline{c}_{66} = \frac{\left[\psi\,(s-\psi)\,GJ - ((s+\psi)+4\,(c-1))\;EI_n\right]\,R_{gm}^3}{GJ\,\left[(s-\psi)\,GJ-(s+\psi)\,EI_n\right]} + \frac{\alpha_{sc}\,\psi\,R_{gm}}{GA} \tag{3.145}$$

where $c = \cos\psi$ and $s = \sin\psi$.

The equivalent stiffness coefficients with other boundary conditions and topologies are determined following the methodologies developed for the flat grids. The expressions are very complex in terms of their analytical expressions and are not provided here.

3.6 Cylindrical grids: Bending stiffness

The curvature changes in a cylindrical shell are [54]

$$\kappa_x = \frac{\partial^2 w}{\partial x^2} \tag{3.146}$$

$$\kappa_\psi = \frac{\partial^2 w}{\partial \psi^2} + \frac{1}{R^2} w \tag{3.147}$$

$$\kappa_{x\psi} = 2\frac{\partial^2 w}{\partial x \partial \psi} - \frac{1}{R}\frac{\partial v}{\partial x} + \frac{1}{R}\frac{\partial u}{\partial \psi} \tag{3.148}$$

The analytical derivation becomes tedious, especially in the case of helical stiffeners, if a direct force equilibrium relations are used to derive the stiffness properties of the equivalent shell structure. As discussed in the previous section, the explicit inclusion of BCs facilitates the derivation of equivalent bending stiffness coefficients via arch and helical beam stiffness matrices. The bending and twisting moments are shown for the cylindrical ortho-grid structure in Fig. 3.25.

For bending stiffness calculations only simply supported BCs are considered. Since the stiffener nodes are assumed to be constrained in the plane of the undeformed cylinder, the curvatures are determined directly from the slope as in the case of flat grids. Various stiffener members are isolated and moment–slope analyses are performed as explained in the case of flat grids.

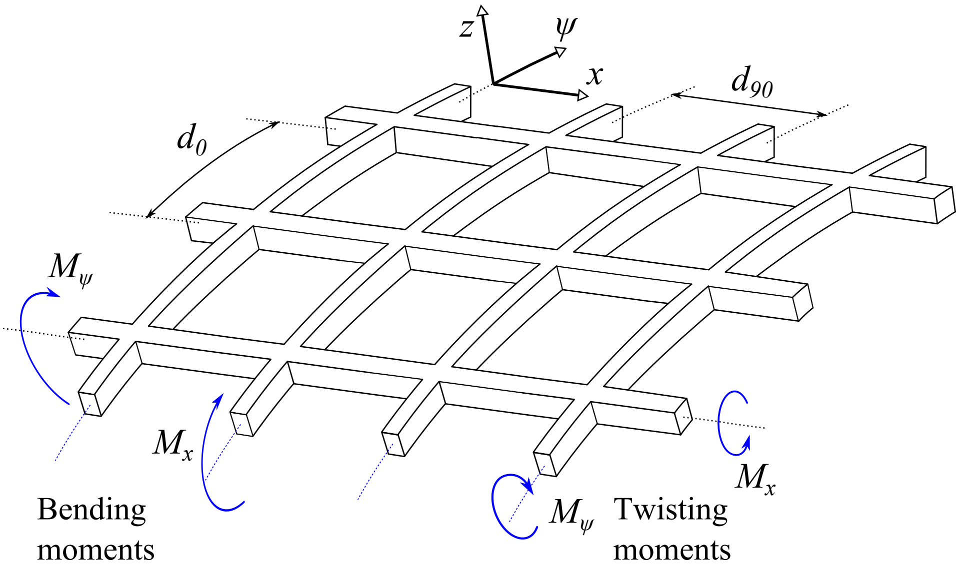

Figure 3.25. Beam bending and twisting moments on the stiffeners for bending and twisting stiffness calculations

3.7 Grid-stiffened structures

A grid-stiffened structure is analyzed as a multilayer system with the mid-plane of the shell taken as the reference plane. This is illustrated in Fig. 3.26. The grid-layer offset is e_s from the reference plane and is negative when the grid is 'inside' ($-z$ direction) of the shell. The effect of eccentricity of the stiffening in the buckling loads of stiffened cylinders has been shown to be extremely significant [34, 54–57]. Both the magnitude and the sign of e_s can significantly affect the buckling behavior of the grid-stiffened structures. A schematic of the grid-stiffened cylinder is shown in Fig. 3.27. According to the coordinate system adopted, the eccentricity $e_s < 0$ when the stiffeners are inside of the cylinder and vice versa.

The mean radius of the grid-stiffened structure is R_m measured at the reference plane of the structure where the loads and BCs are applied. For the present study, the outer

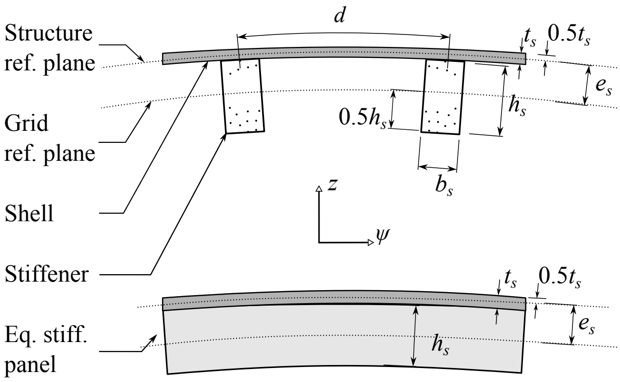

Figure 3.26. Stiffened shell and equivalent continuum shell

radius is fixed and the other parameters shown in Fig. 3.27 are determined accordingly. The effect of eccentricity can be captured in the equivalent stiffness model using compatibility equations. Thus, for a plate element in *xy* plane [58],

$$\varepsilon_x^g = \varepsilon_x^s - e_s\,\kappa_x^g \tag{3.149}$$

$$\varepsilon_y^g = \varepsilon_y^s - e_s\,\kappa_y^g \tag{3.150}$$

$$\varepsilon_{xy}^g = \varepsilon_{xy}^s - 2\,e_s\,\kappa_{xy}^g \tag{3.151}$$

$$\kappa_x^g = \kappa_x^s \tag{3.152}$$

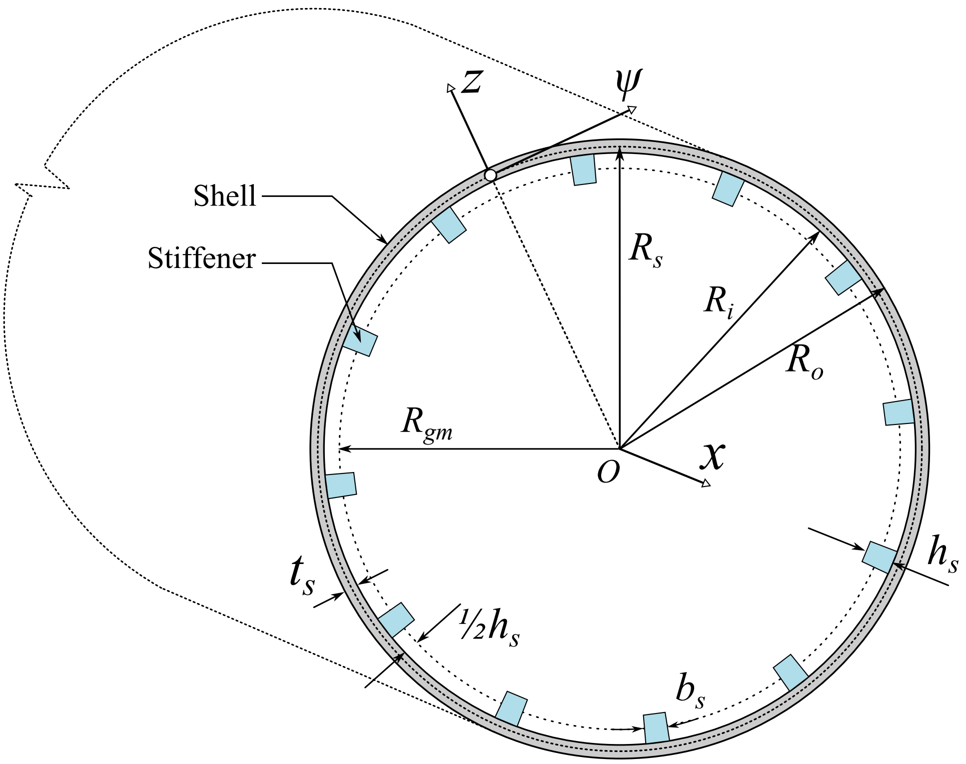

Figure 3.27. Cross-section of a grid-stiffened circular cylindrical structure

$$\kappa_y^g = \kappa_y^s \tag{3.153}$$

$$\kappa_{xy}^g = \kappa_{xy}^s \tag{3.154}$$

where $()^g$ and $()^s$ denote grid and shell (reference) plane respectively. Similar expressions can be written for a cylindrical shell where the y coordinate is replaced with ψ. Note that the above equations are similar to that of a laminated plate or shell where the strains are determined at the reference surface. The force and moment resultants at the reference surface can be determined using

$$\boldsymbol{n}^{gs} = \boldsymbol{n}_s + \boldsymbol{n}_g \tag{3.155}$$

$$\boldsymbol{m}^{gs} = (\boldsymbol{m}_g - e_s \boldsymbol{n}_g) + \boldsymbol{m}_s \tag{3.156}$$

where $\boldsymbol{n}$ and $\boldsymbol{m}$ are the 3×1 force and moment resultant vectors from Eqs. (3.1) and (3.51) respectively.

The cross-sectional stiffness properties of helical beam segments are evaluated based on the works by Yildirim [59, 60]. The cross-section stiffness coefficients EA, GA_n, GA_b, EI_n, EI_b, and GJ of a composite beam (stiffener) made of unidirectional plies are

$$EA = \overline{Q}_{11} A_{cs} \tag{3.157}$$

$$GA_n = \overline{Q}_{66} A_{cs} \tag{3.158}$$

$$GA_b = GA_n \tag{3.159}$$

$$EI_n = \overline{Q}_{11} I_n \tag{3.160}$$

$$EI_b = \overline{Q}_{11} I_b \tag{3.161}$$

$$GJ = \overline{Q}_{66} J \tag{3.162}$$

where A_{cs} is the area of the beam cross-section. I_n and I_b are the area moment of inertia of the cross-section with respect to the normal n and bi-normal b axes respectively (see Fig. 3.22). Here the $(1,2,3)$ axes coincide with the Frenet coordinates (t,n,b). $\overline{Q}_{ij}$ terms are the lamina stiffness coefficients with fiber direction oriented at an arbitrary angle. In the present case the angle is zero. The polar moment of inertia, J of the cross-section is given in Eq. (A.1) Appendix A.

The stiffness matrix of the grid-stiffened cylindrical structure when the shell lay-up is symmetric can be written in the conventional matrix form as

$$\begin{Bmatrix} n_x \\ n_\psi \\ n_{x\psi} \\ m_x \\ m_\psi \\ m_{x\psi} \end{Bmatrix}^{gs} = \begin{bmatrix} A_{11} & A_{12} & 0 & B_{11} & B_{12} & 0 \\ A_{12} & A_{22} & 0 & B_{12} & B_{22} & 0 \\ 0 & 0 & A_{66} & 0 & 0 & B_{66} \\ B_{11} & B_{12} & 0 & D_{11} & D_{12} & D_{16} \\ B_{12} & B_{22} & 0 & D_{12} & D_{22} & D_{26} \\ 0 & 0 & B_{66} & D_{16} & D_{26} & D_{66} \end{bmatrix}^{gs} \begin{Bmatrix} \varepsilon_x \\ \varepsilon_\psi \\ \gamma_{x\psi} \\ \kappa_x \\ \kappa_\psi \\ \kappa_{x\psi} \end{Bmatrix}^{gs} \tag{3.163}$$

The non-zero B_{ij} elements are due to the eccentricity of the stiffeners with respect to the shell mid-plane. The compliance coefficients of the closed cross-section cylindrical grid-stiffened structure can be determined by inverting the square matrix in Eq. (3.163) to obtain a_{ij}^{gs}, b_{ij}^{gs}, and d_{ij}^{gs}. They are the axial, extension-bending, and bending compliance coefficients respectively.

The wall of the grid-stiffened structures, after smearing the stiffness coefficients, is similar to the non-symmetric layup, although there is no explicit layup definition for the equivalent stiffness grid layer. To determine the axial, bending, and torsion stiffness, the grid-stiffened cylinders are treated as closed cross-section beams. These stiffness coefficients are approximately determined using the formulations given by Kollár and Springer [49]. The expressions for axial stiffness EA_{gs}, bending stiffness EI_{gs}, and torsion stiffness GJ_{gs} are given as,

$$EA_{gs} = \frac{2\pi R_s}{\hat{a}_{11}^{gs}} \tag{3.164}$$

$$EI_{gs} = \pi \left(R_s^3 \frac{1}{a_{11}^{gs}} + R_m \frac{1}{d_{11}^{gs}} \right) \tag{3.165}$$

$$GJ_{gs} = \frac{2\pi R_s^3}{\hat{a}_{66}^{gs}} \tag{3.166}$$

where R_s is the radius of the cylindrical shell measured at the shell mid-plane and the parameter $\hat{a}_{66}^{gs}$,

$$\hat{a}_{66}^{gs} = a_{66}^{gs} - \frac{{b_{66}^{gs}}^2}{d_{66}^{gs}} \tag{3.167}$$

In summary, the stiffness coefficients of grid and grid-stiffened closed cross-section tubes are derived directly from the stiffness coefficients of the constituent structure representing the stiffeners using smeared stiffness approach. This is conducted by identifying and incorporating periodicity of boundary conditions of the stiffeners. The methodology can be readily extended to incorporate more complex stiffener boundary conditions. Validation and parametric studies are presented in Chapter. 6.

Chapter 4

Stability and strength

The methodology to determine the torsional buckling loads of monocoque and grid-stiffened circular cylindrical tubes is described. The critical torsional buckling loads are determined with the assumption that the tubes are *long* such that the effect of boundary conditions on the buckling loads can be neglected. The stability analyses performed in this study are based on linear eigenvalue formulations. The buckling under bending loads are characterized by conducting axial compression buckling of the grid-stiffened panels in the compression regions. The procedure to predict the strains in the grid-stiffened models under bending, axial, and torsion loads are described. Failure analysis is conducted using maximum strain criterion for the grid layer and Tsai-Wu quadratic failure criterion for the laminated shells.

4.1 Stability evaluation

The linear eigenvalue analyses are performed in the initial design phase to predict the critical loads to establish the design space for various load cases since they provide sufficiently accurate representation of the instability loads [12]. The thin walled structures could exhibit geometric nonlinear (large deflection) behavior prior to the onset of buckling [54]. However, the present investigation is confined to the purview of preliminary analysis and consequently factors such as geometric imperfections, thermals effects, pre-buckling deformations, boundary effects, and transverse shear effects are not considered. The buckling instabilities under torsion and bending loads are determined where each of these cases are analyzed separately.

The linear buckling instabilities of thin walled structures under various loading and boundary conditions have been studied extensively by many researchers [44, 54, 56, 61]. Due to their wide applications in light weight structural designs, stability characteristics of composite structures are also extensively investigated. Some of the studies addressed stability of composite stiffened structures using computationally efficient formulations [33, 55, 57, 62–66].

A grid-stiffened cylindrical shell can exhibit different buckling modes such as global buckling, skin buckling, and stiffener crippling. The skin and stiffener buckling are local buckling modes which cannot be predicted by the smeared stiffness approach employed in the present study since the contributions of the stiffeners are homogenized to an equivalent continuum [13, 27, 33]. However, the global instability of stiffened shells can be predicted with reasonable accuracy using smeared model for a variety of loading scenarios including axial compression [22, 34, 35, 55, 64, 65], torsion [35, 57, 67], and pure bending [35, 68].

In the present study, existing analytical models are utilized to predict the buckling characteristics of grid-stiffened structures. The stability equations employed to derive the stability equations in the present investigation is identical to that of generally anisotropic monocoque shells. Recall that the stiffness matrix of the grid-stiffened shells in the present investigation has non-zero coupling between extension and bending due to the eccentricity of the stiffeners with respect to the shell mid-plane. The stiffness coefficients developed earlier (Eq. (3.163)) in Chapter 3 are directly employed to predict the general buckling loads of the cylindrical grid-stiffened cylinder. In the classical shell theory, the internal forces and moments of a cylindrical shell are represented in terms of forces and moments per unit distance along the edges of a shell element as shown in Fig. 4.1.

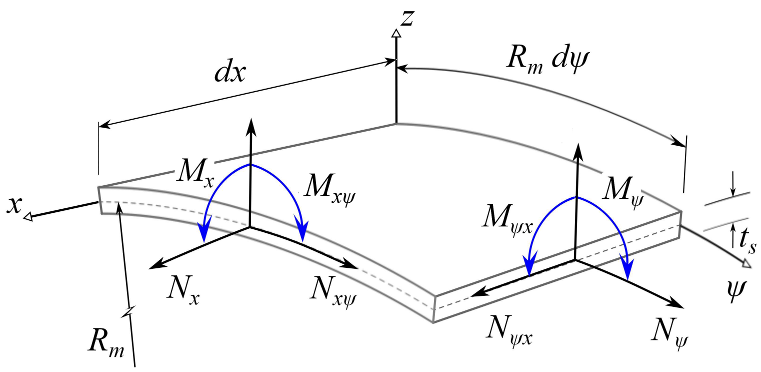

Figure 4.1. Internal forces and moments in a typical infinitesimal cylindrical shell element

4.1.1 Torsional instability

Considering that the heavy lift blade spar has a large length to diameter ratio, long tube assumption is adopted. The stability of thin walled long tubes under torsional loading has been studied by many researchers [56, 61, 69]. The long tube assumption indicates that the mode shapes are unaffected by the boundary conditions. An appropriate set of displacement functions are selected that capture the buckled modes [56]. The equilibrium equations in terms of stress resultants in the absence of applied or body loads can be expressed as shown in Eqs. (4.1) to (4.3) [69].

$$n_{x,x} + n_{\psi x,\psi} - \frac{1}{2R_m} m_{x\psi,\psi} - 2N_{x\psi 0}\, u_{,x\psi} = 0 \tag{4.1}$$

$$n_{x\psi,x} + n_{\psi,\psi} + \frac{3}{2R_m} m_{x\psi,x} + \frac{1}{R_m} m_{\psi,\psi} - 2N_{x\psi 0}\left(v_{,x\psi} + \frac{1}{R_m} w_{,x}\right) = 0 \tag{4.2}$$

$$m_{x,xx} + 2m_{x\psi,x\psi} + m_{\psi,\psi\psi} - \frac{1}{R_m} n_{\psi} + 2N_{x\psi 0}\left(\frac{1}{R_m} v_{,x} - w_{,x\psi}\right) = 0 \tag{4.3}$$

where n_i and m_i are in-plane and out-of-plane stress resultants. $N_{x\psi 0}$ is the shear load, u, v, w are the axial, circumferential, and out-of-plane displacements. '$()_{,}$' indicates partial differentiation with respect to the subscript following the comma.

Flügge [56] provided the displacement modes to model the torsional buckling of long tubes, with length L and mean radius (measured at the shell mid-plane), R_m, and are given in Eqs. (4.4) to (4.6).

$$u = U_{mn} \sin\left(\frac{\lambda x}{R_m} + n\psi\right) \tag{4.4}$$

$$v = V_{mn} \sin\left(\frac{\lambda x}{R_m} + n\psi\right) \tag{4.5}$$

$$w = W_{mn} \cos\left(\frac{\lambda x}{R_m} + n\psi\right) \tag{4.6}$$

where U_{mn}, V_{mn}, and W_{mn} are the arbitrary amplitudes and $\lambda = m\pi R_m/L$. n is the number of waves in the circumferential direction and m is the number of half-waves in the axial direction. Note that the assumed displacements in Eq. (4.4) do not satisfy clamped or pinned boundary conditions. However, for long tubes where the support conditions do not significantly impact the torsion buckling modes, such as the tubular structure representative of the heavy lift blade spar, these modes can be adopted [58, 61]. The procedure developed by Bert and Kim [69] is employed with the assumed modes as given earlier.

The strain–displacement relations are from the thin shell theory due to Sanders [70]. They are demonstrated [69] to be reliable for modeling composite tubes with arbitrary wall laminate lay-ups. The mid-surface strains of the shell (indicated by $(\,)^{\circ}$) are provided in Eqs. (4.7) to (4.9)

$$\varepsilon_x^{\circ} = u_{,x} \tag{4.7}$$

$$\varepsilon_{\psi}^{\circ} = v_{,\psi} + \frac{w}{R_m} \tag{4.8}$$

$$\varepsilon_{x\psi}^{\circ} = u_{,\psi} + v_{,x} \tag{4.9}$$

and the curvatures

$$\kappa_x = -w_{,xx} \tag{4.10}$$

$$\kappa_{\psi} = -w_{,\psi\psi} + \frac{1}{R_m} v_{,\psi} \tag{4.11}$$

$$\kappa_{x\psi} = -2\,w_{,x\psi} + \frac{3}{2R_m} v_{,x} - \frac{1}{2R_m} u_{,\psi} \tag{4.12}$$

The stress resultants are calculated from the general laminate constitutive relations given in Eq. (4.13). For the case of grid-stiffened tubes, the coefficients A_{ij}, B_{ij}, and D_{ij} in Eq. (4.13) are replaced by A_{ij}^{gs}, B_{ij}^{gs}, and D_{ij}^{gs} respectively, which are provided in Eq. (3.163) in Chapter 3.

$$\begin{Bmatrix} n_x \\ n_\psi \\ n_{x\psi} \\ m_x \\ m_\psi \\ m_{x\psi} \end{Bmatrix} = \begin{bmatrix} A_{11} & A_{12} & 0 & B_{11} & B_{12} & 0 \\ A_{12} & A_{22} & 0 & B_{12} & B_{22} & 0 \\ 0 & 0 & A_{66} & 0 & 0 & B_{66} \\ B_{11} & B_{12} & 0 & D_{11} & D_{12} & D_{16} \\ B_{12} & B_{22} & 0 & D_{12} & D_{22} & D_{26} \\ 0 & 0 & B_{66} & D_{16} & D_{26} & D_{66} \end{bmatrix} \begin{Bmatrix} \varepsilon_x^\circ \\ \varepsilon_\psi^\circ \\ \varepsilon_{x\psi}^\circ \\ \kappa_x \\ \kappa_\psi \\ \kappa_{x\psi} \end{Bmatrix} \tag{4.13}$$

The strains are represented in displacements and substituted into the equilibrium equations given in Eqs. (4.1) to (4.3). The assumed displacements are input into the resulting equilibrium equations to obtain three algebraic equations in three unknown non-zero amplitudes, U_{mn}, V_{mn}, and W_{mn}. This is the characteristic equation and is shown in Eq. (4.14).

$$\begin{bmatrix} c_{11} & c_{12} & c_{13} \\ c_{21} & c_{22} & c_{23} \\ c_{31} & c_{32} & c_{33} \end{bmatrix} \begin{Bmatrix} U_{mn} \\ V_{mn} \\ W_{mn} \end{Bmatrix} = \begin{Bmatrix} 0 \\ 0 \\ 0 \end{Bmatrix} \tag{4.14}$$

where c_{ij} are the coefficients of the amplitudes in terms of wavelength parameters, m and n, and shear load per unit circumferential length, $N_{x\psi 0}$. The non-trivial solutions are obtained by equating the determinant of the coefficient matrix in Eq. (4.14) to zero. The buckling shear per unit length is then determined by searching for the lowest value of $N_{x\psi 0}$ by iterating the wavelength parameters, m and n. The critical buckling torque,

T_{cr} on the cross-section is then determined as shown in Eq. (4.15).

$$T_{cr} = 2\,(N_{x\psi 0})_{cr}\,\pi R_m^2 \tag{4.15}$$

4.1.2 Bending instability

The rotor blades of a helicopter experience significant bending (both flap and lag) deflection modes. These bending modes generate high compressive loads along the length of the blade spar. Such high compressive loads could cause the thin shell region between the stiffeners to buckle locally. Depending on the shell laminate, stiffener geometry and topology, individual stiffeners could also buckle independently or in mixed interaction modes. Another mode is when the stiffener boundaries essentially provide elastic boundary conditions to the included shell where the stiffeners merely participate in the shell buckling via elastic deformation rather than exhibiting instability mode themselves. Analytically predicting these buckling modes is extremely difficult especially when the shell topology has curved profile, non-rectangular plan form, with elastic boundaries.

Various analytical solutions exist [35, 68] for cases when the global bending buckling loads of stiffened cylindrical shells need to be determined under pure bending moments. Since the length to diameter ratio of the blade spar is large, global bending buckling solution (under pure bending) does not provide adequate representation of the instability. What is being sought is a methodology to capture the local instability in the compression regions of the tube under bending using computationally efficient tools. As a result, axial compression buckling analysis is performed on cylindrical shell panels in the compression region of the tube. The terminology ‘cylindrical shell panel’ (sometimes ‘curved panels’) is used in the literature [71, 72] to indicate the shell structure that does not form a closed profile.

To illustrate an earlier note regarding the complexity in capturing the effect of stiffeners in predicting the buckling loads, consider the following axial compression buckling problem. Two different plates with identical properties are stiffened with blade stiffeners but with different stiffener densities. Figure. 4.2 shows the buckling modes from FEA linear eigenvalue solutions. The plate in Fig. 4.2b has half the number of stiffeners in both direction than plate-(a). The plate-a exhibits global plate buckling mode similar to that of the critical mode of an unstiffened plate under axial compression. In this case, the stiffeners merely conforms to the buckled shape without any in-plane deformation. The plate-b behaves differently where the stiffeners rotate elastically to maintain their profile normal to the plate after buckling. The behavior of plate-(a) can be predicted reasonably accurately using the smeared stiffness approach since the critical buckling mode is identical to that of an unstiffened plate. In the case of plate-(b), accurate analytical prediction using conventional (similar to the one one developed in this study) smeared theory is not possible, since the discreteness of the stiffeners are not available in the final form of the formulation. This is one of the limitations in the smeared approach when the stiffeners are not 'closely spaced.' Identifying these modes requires support

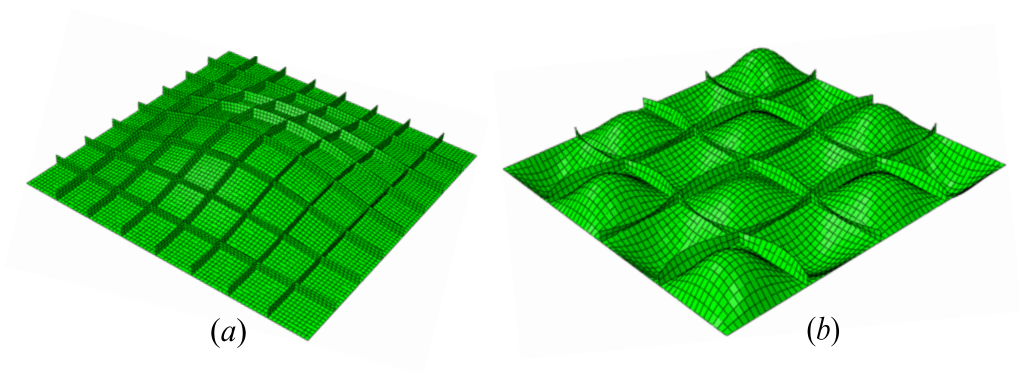

(a) (b)

Figure 4.2. Critical buckling mode of stiffened plates under uniaxial compression and simply supported BCs. (a) global mode similar to an unstiffened plate (b) local skin buckling with the stiffeners deflect elastically

from detailed finite element models.

From the computationally efficient analytical model perspective, a methodology is needed to compare the stability of grid-stiffened and monocoque structures under transverse bending. A methodology is adopted to study the axial compression problem of the cylindrical shell panel. The geometry of the shell panel is selected such that the compression region of the cylinder under bending can be analyzed for buckling. The model is illustrated in Fig. 4.3. Figure 4.3a shows a clamped-free cylindrical tube under transverse bending load and Fig. 4.3b shows the isolated compression region of the tube. For the present analysis, it is assumed that the bending induced compression region has an axial length of $L_{xu} = \pi R$ from the support. In calculating the circumferential length, the included angle of the isolated shell is kept at π radians resulting in a circumferential length of πR. The radius, R shown has the value R_m for the monocoque structure and R_s for the grid-stiffened structure.

The analytical formulation to predict the buckling loads is adopted from published works and are presented below. Note that the critical buckling mode of the semi-cylindrical shell is a global mode for the model shown whereas it is a local mode when the entire grid-stiffened cylindrical structure is considered. No particular relevance is given to the source of the compressive load except that it is a resultant of the bending induced stresses developed in the spar structure. To simplify the analysis, the boundary conditions are assumed to be simply supported on all four edges for the present investigation.

The formulations to obtain the stability equations for grid-stiffened shells is identical to that of generally anisotropic monocoque shell stability. Recall that the stiffness matrix of the grid-stiffened shells in the present investigation has non-zero coupling between extension and bending due to the eccentricity of the stiffeners with respect the mid-

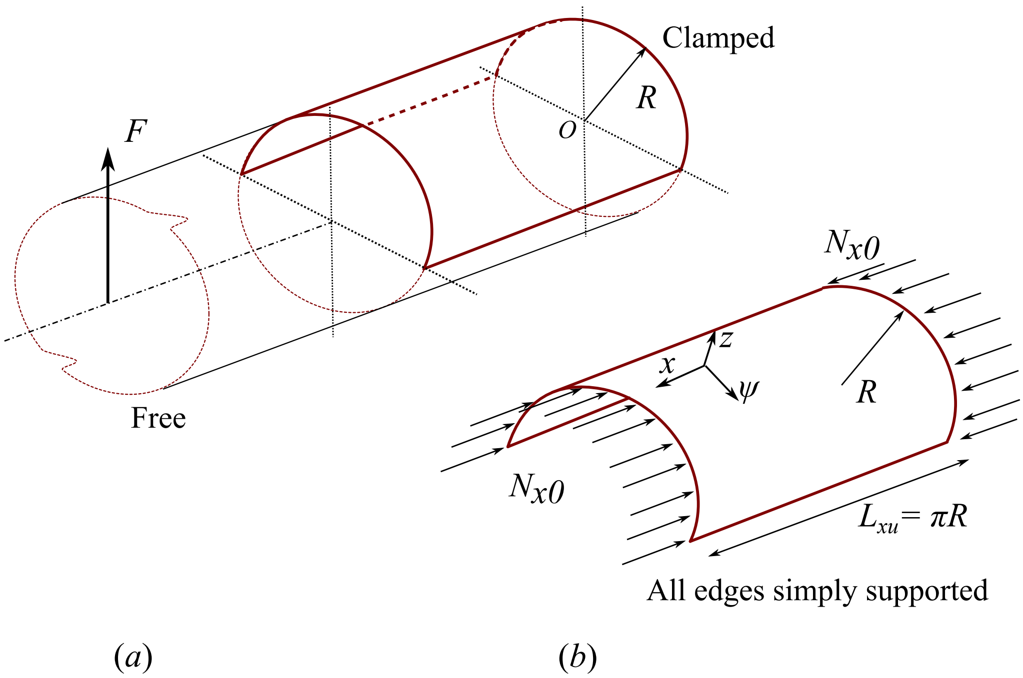

Figure 4.3. (a) Clamped-free thin walled cylinder under transverse bending showing compression region. (b) Cylindrical shell panel isolated for bending induced uniaxial compression buckling study

plane (reference surface) of the attached shell. Leissa [71] developed detailed stability equations for cylindrical shells using energy methods to include the effect of general anisotropy of the composite shells arising from various coupling coefficients. Also see the studies by [34, 47, 54, 55, 73, 74] for the theory and detailed studies on shell stability.

Without repeating the derivation of the equilibrium equations that are well established and validated, the assumed displacement modes and differential operators for cylindrical shell stability are given by [71, 73]. The mid-surface displacements (reference plane of the shell) at buckling are selected as,

$$u^{\circ}(x,y) = \sum_{m=1}^{\infty}\sum_{n=1}^{\infty} \quad A_{mn}\cos(m\pi x/l)\,\sin(n\pi y/b)$$

$$v^\circ(x,y) = \sum_{m=1}^{\infty}\sum_{n=1}^{\infty} \quad B_{mn}\sin(m\pi x/l)\,\cos(n\pi y/b)$$

$$\tag{4.16}$$

$$w^\circ(x,y) = \sum_{m=1}^{\infty}\sum_{n=1}^{\infty} \quad C_{mn}\sin(m\pi x/l)\,\sin(n\pi y/b)$$

where l and b are the axial and circumferential dimensions of the cylindrical shell respectively and m, $n = 1,2,3,\ldots$. The y coordinate in the equations can be represented in ψ as subsequently stated. The governing buckling equations can be written as

$$\begin{bmatrix} L_{11} & L_{12} & L_{13} \\ L_{21} & L_{22} & L_{23} \\ L_{31} & L_{32} & L_{33} \end{bmatrix} \begin{Bmatrix} u^\circ \\ v^\circ \\ w^\circ \end{Bmatrix} = \begin{Bmatrix} 0 \\ 0 \\ 0 \end{Bmatrix} \tag{4.17}$$

where the differential operators, L_{ij} [71] are

$$L_{11} = A_{11}\,\partial_{,xx} + 2A_{16}\,\partial_{,xy} + A_{66}\,\partial_{,yy}$$

$$L_{12} = L_{21} = \left(A_{16} + \frac{B_{16}}{R}\right)\partial_{,xx} + \left(A_{12} + A_{66} + \frac{B_{12}+B_{66}}{R}\right)\partial_{,xy} + \left(A_{26} + \frac{B_{26}}{R}\right)\partial_{,yy}$$

$$\begin{aligned} L_{13} = L_{31} = &-B_{11}\,\partial_{,xxx} - B_{26}\,\partial_{,yyy} - 3B_{16}\,\partial_{,xxy} - \left(B_{12} + 2B_{66}\right)\partial_{,xyy} \\ &+ \frac{A_{12}}{R}\,\partial_{,x} + \frac{A_{26}}{R}\,\partial_{,y} \end{aligned} \tag{4.18}$$

$$L_{22} = \left(A_{66} + \frac{2B_{66}}{R}\right)\partial_{,xx} + \left(2A_{26} + \frac{4B_{26}}{R}\right)\partial_{,xy} + \left(A_{22} + \frac{2B_{22}}{R}\right)\partial_{,yy}$$

$$L_{23} = L_{32} = \left(-B_{16} - \frac{D_{16}}{R}\right)\partial_{,xxx} + \left(-B_{22} - \frac{D_{22}}{R}\right)\partial_{,yyy} + \left(-3B_{26} - \frac{3D_{26}}{R}\right)\partial_{,xyy}$$

$$+\left(-B_{12}-2B_{66}-\left[\frac{D_{12}+2D_{66}}{R}\right]\right)\partial_{,xxy}$$
$$+\left(\frac{A_{26}}{R}+\frac{B_{26}}{R^2}\right)\partial_{,x}+\left(\frac{A_{22}}{R}+\frac{B_{22}}{R^2}\right)\partial_{,y}$$

$$L_{33}=D_{11}\,\partial_{,xxxx}+4D_{16}\,\partial_{,xxxy}+2\Big(D_{12}+2D_{66}\Big)\,\partial_{,xxyy}+4D_{26}\,\partial_{,xyyy}+D_{22}\,\partial_{,yyyy}$$
$$-2\Big(\frac{B_{12}}{R}\,\partial_{,xx}+2\frac{A_{26}}{R}\,\partial_{,xy}+\frac{B_{22}}{R}\,\partial_{,yy}\Big)+\frac{A_{22}}{R^2}+N_{x0}\,\partial,xx$$

where $\partial_{,(\,)}$ represents the differential of the assumed displacement function with respect to the parameter(s) in the parenthesis following the comma. N_{x0} is the compressive load to be determined. The above equations can be written in terms of (x,ψ) by substituting $\partial_{,y}=(1/R)\,\partial_{,\psi}$. A_{ij},B_{ij},D_{ij} are the stiffness coefficients of the monocoque or grid-stiffened shell laminate. Note that the radius R is measured at the reference plane of the shell and is equal to the mean radius R_m for monocoque and R_s for grid-stiffened shell.

The characteristic equations are then determined using Galerkin's method [75] by taking the first variation (by method of Euler–Lagrange equations). Thus,

$$\int_0^{L_{xu}}\int_0^{b}\Big[L_{11}(u^\circ)+L_{12}(v^\circ)+L_{13}(w^\circ)\Big]\cos(m\pi x/l)\ \sin(n\pi y/b)\,d\psi\,dx=0$$

$$\int_0^{L_{xu}}\int_0^{b}\Big[L_{12}(u^\circ)+L_{22}(v^\circ)+L_{23}(w^\circ)\Big]\sin(m\pi x/l)\ \cos(n\pi y/b)\,d\psi\,dx=0$$

$$\int_0^{L_{xu}}\int_0^{b}\Big[L_{13}(u^\circ)+L_{23}(v^\circ)+L_{33}(w^\circ)\Big]\sin(m\pi x/l)\ \sin(n\pi y/b)\,d\psi\,dx=0 \tag{4.19}$$

where L_{xu} is the axial (parallel to the cylinder axis) length of the unitcell determined from the grid stiffening configuration. $b=R\psi$ gives the circumferential length of the shell and $\psi=\pi$ radians for the semi-circular shell problem. Upon performing the integration, the resulting algebraic eigenvalue problem can be written in matrix form as shown in Eq. (4.20).

$$\begin{bmatrix} e_{11} & e_{12} & e_{13} \\ e_{21} & e_{22} & e_{23} \\ e_{31} & e_{32} & e_{33} \end{bmatrix} \begin{Bmatrix} A_{mn} \\ B_{mn} \\ C_{mn} \end{Bmatrix} = \begin{Bmatrix} 0 \\ 0 \\ 0 \end{Bmatrix} \tag{4.20}$$

where e_{ij} are the elements of the coefficient matrix of the amplitudes. Iterating through different values of m and n in the expression after setting the determinant of the square matrix, $\boldsymbol{e}$ in Eq. (4.20) to zero and determining the lowest possible value of N_{x0} (see differential operator, L_{33} in Eq. (4.18)), the critical axial compressive load on the shell edge is calculated by,

$$P_{cr} = \min(N_{x0})\, \psi R \tag{4.21}$$

For the design study, monocoque shells are also analyzed in an identical manner. A MATLAB® code is developed to predict the buckling loads which is validated by generating results for various shell models and compare them against published results. The compression buckling problem for closed cylindrical laminated shells are calculated for various laminates from Wong et al. [76] and compared for checking the accuracy of the code developed in the present study.

Additionally, pertaining to the problem at hand, semi-circular cylindrical models are analyzed to specify the circumferential dimensions corresponding to an included angle of π as stated. The results are compared against those provided in the literature [37, 77]. Once the results are reproduced successfully there by validating the code, it can be directly employed to analyze the grid-stiffened structures for stability. All that is needed is to validate the accuracy of the stiffness coefficients $(\boldsymbol{A}, \boldsymbol{B}, \boldsymbol{D})$ formulation developed in the present study for the grid-stiffened cylindrical structures. Validation studies are performed and the results are provided in Chapter 6.

4.2 Strength evaluation

The quadratic polynomial failure theories such as Tsai-Wu and Tsai-Hill are commonly used to predict the onset of failure by a ply by ply analysis of a laminate. The limit theories such as the maximum stress and maximum strain criteria on the other hand adopt a much direct method where the stresses or strains in each ply in the laminate is compared against the corresponding material stress or strain allowables.

As noted earlier, the discreteness of the stiffeners is discarded when the effective stiffness coefficients of a grid or grid-stiffened structure are derived using smeared stiffness approach. The stress distribution in a grid-stiffened structure is complex due to abrupt changes in geometry and stiffness that a detailed analytical prediction of strength of various components using quadratic failure theories is not possible [12]. It should be noted that there are no 'plies' in the grid layer once the individual stiffness contributions from the stiffeners are smeared. Thus, maximum strain criterion is used in the present study following the methodology employed by Phillips and Gürdal [12].

No attempt is made in the analytical model developed in the present study to include the stiffener–shell interactions. As a result, grid and shell layers are treated as separate entities to apply the strength constraints. To further simplify the approach, only the membrane strains in the grid layer are considered, similar to previous published works on the topic [12, 78]. This assumption is reasonable since stiffeners are primarily designed to sustain axial strains [12, 20, 79].

The maximum strain criterion is described as shown in shown in Eqs. (4.22) and (4.23), says that the calculated strains in the stiffeners must be less than the corresponding material strain allowables to avoid failure. For the grid layer in a grid or grid-stiffened structure,

$$\varepsilon_L^t < {}_a\varepsilon_L^t \tag{4.22}$$

$$\varepsilon_L^c < {}_a\varepsilon_L^c \tag{4.23}$$

The strain in the grid layer is calculated from global strains developed under the externally applied loads. Then the grid layer strains are transformed to the corresponding principal axial directions of the stiffeners. For example, if the topology is angle-grid, then the global strain tensor is rotated at θ to obtain the axial strains in the θ direction stiffeners and $-\theta$ direction for stiffeners in the $-\theta$ stiffeners. The same procedure is repeated if there exist stiffener in other directions depending on the stiffening configuration. The transformation from the global $x\psi$ to the lamina principal coordinates, LT is performed by

$$[\varepsilon_L,\, \varepsilon_T,\, \gamma_{LT}]^T = \boldsymbol{T}_s\, [\varepsilon_x,\, \varepsilon_\psi,\, \gamma_{x\psi}]^T \tag{4.24}$$

where the strain transformation matrix $\boldsymbol{T}_s$ is given in Eq. (4.25) [80].

$$\boldsymbol{T}_s = \begin{bmatrix} 1 & 0 & 0 \\ 0 & 1 & 0 \\ 0 & 0 & 2 \end{bmatrix} \begin{bmatrix} c^2 & s^2 & cs \\ s^2 & c^2 & -cs \\ -2cs & 2cs & c^2 - s^2 \end{bmatrix} \begin{bmatrix} 1 & 0 & 0 \\ 0 & 1 & 0 \\ 0 & 0 & \frac{1}{2} \end{bmatrix} \tag{4.25}$$

with $c = \cos\theta$ and $s = \sin\theta$.

The shell of a grid-stiffened structure is analyzed for first play failure using Tsai-Wu failure criterion [80, 81]. For the plane stress condition, the lamina failure can be expressed as,

$$f_1\,\sigma_L + f_2\,\sigma_T + f_{11}\,\sigma_L^2 + f_{22}\,\sigma_T^2 + f_{66}\,\sigma_{LT}^2 + 2\,f_{12}\,\sigma_L\,\sigma_T \leq 1 \tag{4.26}$$

with the coefficients given as,

$$f_1 = \frac{1}{\sigma_L^t} - \frac{1}{\sigma_L^c}, \quad f_2 = \frac{1}{\sigma_T^t} - \frac{1}{\sigma_T^c} \tag{4.27}$$

$$f_{11} = \frac{1}{\sigma_L^t\,\sigma_L^c}, \quad f_{22} = \frac{1}{\sigma_T^t\,\sigma_T^c} \tag{4.28}$$

$$f_{66} = \frac{1}{{\tau_{LT}^a}^2}, \quad f_{12} \approx -\frac{1}{2}\sqrt{f_{11}\,f_{22}} \tag{4.29}$$

where σ_L^t, σ_L^c and σ_T^t, σ_T^c are the lamina tensile, compressive stresses in the fiber and transverse to the fiber directions respectively. τ_{LT}^a is the allowable shear stress in the lamina, which is direction independent.

The strain vector for the grid-stiffened structure is determined from the smeared constitutive equations under independently applied load cases using Eq. (3.163) given in Chapter 3. Once the strains are transformed into the lamina coordinate system using Eq. (4.24), the stresses in principal coordinates of a lamina can be calculated using Eq. (4.30). For a given set of material and associated strength properties, Tsai-Wu failure checks are performed as explained.

$$\begin{Bmatrix} \sigma_L \\ \sigma_T \\ \sigma_{LT} \end{Bmatrix} = \begin{bmatrix} \overline{Q}_{11} & \overline{Q}_{12} & \overline{Q}_{16} \\ \overline{Q}_{12} & \overline{Q}_{22} & \overline{Q}_{26} \\ \overline{Q}_{16} & \overline{Q}_{26} & \overline{Q}_{66} \end{bmatrix} \begin{Bmatrix} \varepsilon_L \\ \varepsilon_T \\ \varepsilon_{LT} \end{Bmatrix} \tag{4.30}$$

The failure analyses are performed for both compressive and tensile loads and the minimum value among these loads is the failure load of the laminate. When employing maximum strain criterion, allowable strains are identified depending on whether the calculated lamina strain in the fiber direction is compressive or tensile. For the grid-stiffened structure, the maximum load determined from the Tsai-Wu criterion for the shell of the grid-stiffened structure and the maximum load obtained via the maximum strain rule for the grid layer are compared. The lowest of the two loads is the failure load of the grid-stiffened structure. The results from the analyses stated are provided in Chapter 6.

Chapter 5

Design methodology

A design study is conducted to evaluate the potential weight savings of grid-stiffened cylindrical structures compared to conventional monocoque structures. The circular cross-sections are considered simple surrogates for a heavy-lift rotor blade spar. Various constraints such as stiffness, strength, and stability under different loading conditions are imposed to identify the design candidates. No formal optimization tool such as an evolutionary algorithm is implemented to conduct the design study. In this chapter the methodology is presented. The results are provided in Chapter 6.

5.1 Parameters and constraints

The cross-section of the monocoque and grid-stiffened cylinders are shown in Fig. 5.1a and 5.1b respectively. The baseline monocoque laminate is selected as $[45, 0, 90, -45]_{4s}$— a balanced symmetric configuration. The outer diameter of the baseline, $D_o = 165$ mm (6.5 in). The monocoque cylinder is analyzed as thin walled structure with $t_m/D_o = 0.025 \ll 0.1$ [82].

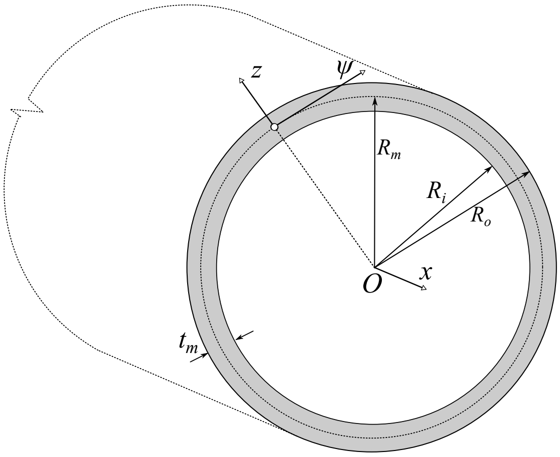

(a) Baseline monocoque

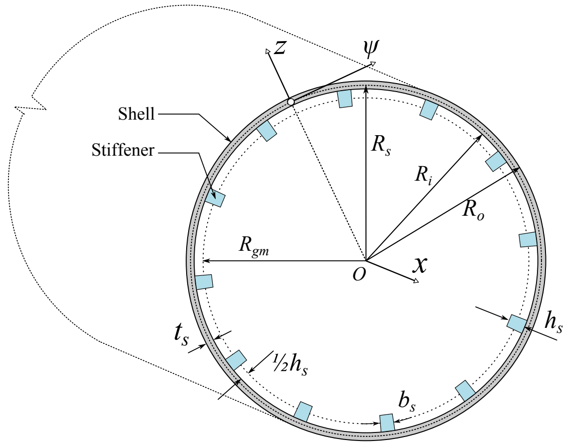

(b) Grid-stiffened

Figure 5.1. Schematic of the cross-sections of monocoque and grid-stiffened cylindrical structures

AGS structures have a large number of design variables compared to monocoque structures, making the optimal design process significantly challenging. For a given material system and ply thickness, Table 5.1 demonstrates the difference between monocoque and AGS structures in terms of the number of design variables. At the same time, having a large number of variables presents an excellent opportunity for design. In this investigation, a manual design study is conducted using a limited set of parameters highlighted with boxes in Table 5.1.

A general-grid stiffening configuration (see Fig. 3.21) is selected since this configuration provides higher stiffness values compared to the other (ortho-grid and angle-grid) configurations discussed earlier. The general-grid stiffness coefficients are calculated as a linear combination of ortho-grid and angle-grid stiffness coefficients. Note that this linear combination is valid only for the grid portion of the AGS structure since the reference planes of both the ortho- and angle-grid coincide with the resulting general-grid, which in turn differs from the reference plane of the skin.

The grid-stiffened and monocoque shell structures are made of the material system

Table 5.1. Overview of various design variables available for monocoque and grid-stiffened structures. Boxed parameters are the only design variables considered in the present study

	Component		
Design	Shell	Grid	
Monocoque	Shell thick.: t_s	-	
	Ply angles: β_s	-	
Grid-stiffened	Shell thick.: $\boxed{t_{gs}}$	(1) Stiffener cross-section	Width, $\boxed{b_s}$
	Ply angles: $\boxed{\beta_{gs}}$	See Fig. 5.1	Height, $\boxed{h_s}$
		(2) Topology	Ortho-grid
		(See Fig. 1.11)	Angle-grid
			$\boxed{\text{General-grid}}$
			AL-grid
			AT-grid
			Isogrid
		(3) Stiffener spacing	$\boxed{d_\theta}$
		(See Fig. 3.1)	$\boxed{d_0}$
			$\boxed{d_{90}}$
		(4) Stiffener angle	$\boxed{\theta}$

and hence the material density is set to unity for convenience. Since the weights are to be compared, the unit cell geometry, where the dimension of the reference geometry are the axial and circumferential dimensions of the unit cell. These quantities are calculated first and then these dimensions along with the radius of curvature and wall thickness are used to calculate the weight of monocoque shell.

The number of one-direction helical stiffeners in the cross-section, N_{a1} and the helical stiffener spacing, d_θ are mutually dependent parameters for a given tube radius.

They are related as shown in Eq. (5.1).

$$d_\theta = \frac{2\pi R_{gm}}{N_{a1}} \cos\theta \tag{5.1}$$

where R_{gm} is the radius measured at the reference plane of the grid layer (see Fig. 5.1b). The weight of the general-grid layer, W_g is calculated considering that all the stiffeners have identical cross-section geometry. W_g is given in Eq. (5.2) and this quantity is obtained by calculating the total length of all the stiffeners (helical, longitudinal, and circumferential) in a unitcell and multiplying it by the stiffener cross-section area, A_s. The contribution from the stiffener cross-over regions are not deducted when calculating weight, which is conservative.

$$W_g = 2A_s N_{a1} L_a \left[\frac{\cos\theta + \sin\theta + 1}{\cos\theta}\right] \tag{5.2}$$

where L_a is the length of the unitcell in the axial direction of the cylindrical tube. The weight contribution from the shell of the grid-stiffened structure is given in Eq. (5.3).

$$W_s = 2L_a t_s \pi R_s \tag{5.3}$$

where R_s is measured at the mid-plane of the shell of the grid-stiffened structure as shown in Fig. 5.1b. The weight of the grid-stiffened shell, W_{gs} is given in Eq. (5.4).

$$W_{gs} = W_g + W_s \tag{5.4}$$

For the monocoque cylinder with shell thickness, t_m and radius, R_m, the weight (with unit density) is given in Eq. (5.5).

$$W_m = 2L_a t_m \pi R_m \tag{5.5}$$

The range of variability of each design parameter for the grid-stiffened structure is prescribed for the design investigation. As explained earlier in Chapter 3, the longitudinal stiffener spacing, d_0 and the circumferential stiffener spacing, d_{90} are dependent on the helical stiffener spacing, d_θ. d_θ can be established by specifying the number of helical stiffeners in one direction around the circumference, N_{a1} and the stiffener angle θ as shown in Eq. (5.1). The stiffener angle, θ is varied discretely in 5° increments. The cross-section dimensions b_s and h_s are varied in 0.1 mm increments where as the quantity N_{a1} is incremented by unity. The limits on the varied parameters are prescribed as,

$$6 \leq N_{a1} \leq 16 \tag{5.6}$$

$$30^\circ \leq \theta \leq 60^\circ \tag{5.7}$$

$$t_{gs} \leq b_s \leq 10 t_{gs} \tag{5.8}$$

$$b_s \leq h_s \leq 6 b_s \tag{5.9}$$

The quantities given in Eqs. (5.6) to (5.9) completely define the general-grid geometry for a fixed outer diameter of the cylinder and the shell laminate. Consequently, these

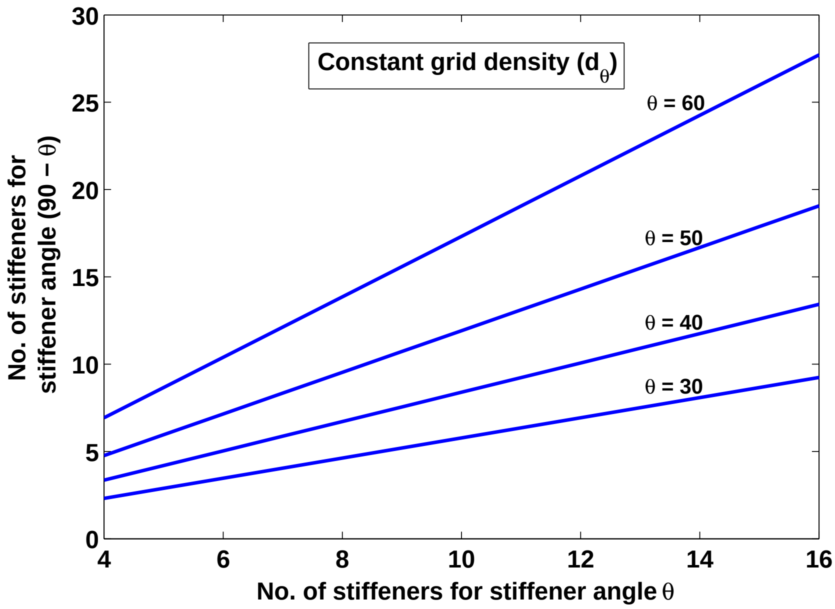

Figure 5.2. Number of stiffeners (around the cylindrical surface) needed to maintain constant grid density for θ and $(90-\theta)$ stiffener angles

parameters are the input from which the stiffness, stability, and strength are calculated.

The limiting values of N_{a1} given in Eq. (5.6) should be ascertained before the values are implemented. The relationship between these parameters is noteworthy. Figure 5.1 shows the number of stiffeners, N_{a1} needed around the circumference of an angle-grid cylinder with stiffener angle, $(90-\theta)$ to maintain the same grid density as of an angle-grid with a stiffener angle, θ. As an example, without considering the practicality, to obtain the grid density of a 60° angle-grid with 12 stiffeners, a 30° angle-grid should have nearly 20 stiffeners in one direction around the circumference. Generating detailed finite element models can thus become extremely tedious if it is required to manipulate the aforementioned parameters.

The objective of the design study is to minimize the weight of the grid-stiffened structure compared to the baseline monocoque. To conduct the design study, constraints have to be set for stiffness, strength, and stability in order to maintain structural integrity of the designs. The constraint parameters are defined as the ratio of the parameter of grid-stiffened to that of the monocoque baseline structure. There are four classes of constraints imposed in the present design study. Three of them are the comparison between grid-stiffened design and the baseline— stiffness (bending and torsion), strength (bending induced axial and torsion induced shear), and stability (bending induced axial compression and global buckling under torque). The fourth constraint is imposed on the grid-stiffened structure itself where the ratio of the laminate failure loads to that of the corresponding critical buckling loads. That is, the critical buckling load under axial compression is compared to that of the axial strength of the laminate. Similarly, for torsion, the critical torsional buckling load is compared to that of the failure torque of the grid-stiffened structure. The dimensions, boundary conditions, and the methodologies to calculate the buckling loads are provided in Chapter 2.

The objective function is defined as the minimization of the weight parameter, $\overline{W}$, the ratio of the weights of grid-stiffened to monocoque as shown in Eq. (5.10).

$$\text{minimize} \quad (\overline{W}) \quad | \quad \overline{W} < 1 \tag{5.10}$$

subject to the different design constraints given in Eq. (5.11) and (5.12). The subscripts $()_{cr}$ and $()_{max}$ denote the critical buckling and strength failure loads respectively.

$$\left\{\overline{EI}, \quad \overline{GJ}, \quad \overline{P}_{cr}, \quad \overline{T}_{cr}, \quad \overline{P}_{max}, \quad \overline{T}_{max}\right\} \quad \geq 1 \tag{5.11}$$

The constraints imposed on the grid-stiffened designs are shown in Eq. (5.12). These constraints stipulate that the strength failure precedes the stability failure for the grid-stiffened designs.

$$\left\{\frac{(P_{cr})_{gs}}{(P_{max})_{gs}}, \quad \frac{(T_{cr})_{gs}}{(T_{max})_{gs}}\right\} \quad \geq 1 \tag{5.12}$$

where the subscripts, $()_{gs}$ and $()_m$ represent grid-stiffened and monocoque structures respectively. The parameters that appear in Eqs. (5.10) and (5.11) are defined in Eqs. (5.13) to (5.19).

$$\overline{W} = \frac{W_{gs}}{W_m} \tag{5.13}$$

$$\overline{EI} = \frac{EI_{gs}}{EI_m} \tag{5.14}$$

$$\overline{GJ} = \frac{GJ_{gs}}{GJ_m} \tag{5.15}$$

$$\overline{P}_{cr} = \frac{(P_{cr})_{gs}}{(P_{cr})_m} \tag{5.16}$$

$$\overline{T}_{cr} = \frac{(T_{cr})_{gs}}{(T_{cr})_m} \tag{5.17}$$

$$\overline{P}_{max} = \frac{(P_{max})_{gs}}{(P_{max})_m} \tag{5.18}$$

$$\overline{T}_{max} = \frac{(T_{max})_{gs}}{(T_{max})_m} \tag{5.19}$$

EI_m and GJ_m are the bending and torsion stiffness respectively. P_{max} and T_{max} denote axial compression and torsion failure loads respectively.

The stiffness coefficients of the baseline tubular structure are determined using cross-section stiffness analysis developed by Rehfield et al. [83]. The expressions for bending and torsional stiffness coefficients of the monocoque baseline are given in Eqs. (5.21) to

(5.22).

$$EA_m = 2\pi R_m K_{11} \tag{5.20}$$

$$EI_m = \pi R_m^3 K_{11} \tag{5.21}$$

$$GJ_m = 2\pi R_m^3 K_{22} \tag{5.22}$$

where the coefficients K_{ij} are obtained from the monocoque laminate membrane stiffness, $\boldsymbol{A}$ as

$$K_{11} = A_{11} - \frac{A_{12}^2}{A_{22}} \tag{5.23}$$

$$K_{22} = A_{66} - \frac{A_{26}^2}{A_{22}} \tag{5.24}$$

The bending and torsion stiffness coefficients for the grid-stiffened designs are determined using the newly formulated model. The expressions to calculate these coefficients are presented earlier in Eq. (3.164) in Chapter 3.

5.2 Loads

Two separate analyses are conducted to determine the maximum (critical buckling and strength failure) loads: (*i*) linear static analysis for laminate failure loads and (*ii*) linear eigenvalue analysis for critical buckling loads. The methodologies used to determine these parameters are described in the following sections.

5.2.1 Design loads

The critical buckling and failure loads of the monocoque baseline that appear in the denominators of Eqs. (5.16) to (5.19) are the design loads. As discussed earlier, laminate failure analyses are conducted to calculate the strength of the baseline. Note that no combined loading cases are considered in this investigation. Only the maximum values of the stress resultants, $N_{x\psi}$ and N_x need to be determined. The hoop stress resultant, N_ψ is assumed to be zero since there is no internal of external pressure loads and the radius of curvature of both structures are assumed to be unchanged between the deformed and the undeformed states. The stiffness matrix, $\boldsymbol{ABD}_m$ of the monocoque laminate is used for calculating the strains due to the above mentioned applied loads.

The maximum axial load, P_{max} is determined from the axial stress resultant, N_x at which the first ply failure occurs as per the Tsai-Wu failure criterion. Both the tension and compression failure loads are calculated and the minimum value of these loads is taken as the failure stress resultant, $(N_x)_{max}$. The net axial load on the cross-section of the monocoque structure, P_{max} is calculated as shown in Eq. (5.25).

$$(P_{max})_m = 2\,(N_x)_{max}\,\pi R_m \tag{5.25}$$

An identical procedure is employed to determine the maximum shear load with applied load, $N_{x\psi}$. The maximum value of torque is then determined using Eq. (5.26) [49].

$$(T_{max})_m = 2\,(N_{x\psi})_{max}\,\pi R_m^2 \tag{5.26}$$

As in the case of strength calculations, critical axial compression buckling load, $(P_{cr})_m$ and critical torque, $(T_{cr})_m$ can be calculated. The procedure to calculate the critical buckling loads are explained in Sec. 4.1.1 for the case of torsion and Sec. 4.1.2 for the case of axial compression in Chapter 4. The critical loads of the baseline are found using Eq. (5.27) for axial compression and Eq. (5.28) for the buckling torque.

$$(P_{cr})_m = (N_{x0})_{cr}\,\pi R_m \tag{5.27}$$

$$(T_{cr})_m = 2\,(N_{x\psi 0})_{cr}\,\pi R_m^2 \tag{5.28}$$

5.2.2 Grid-stiffened structure loads

Instead of applying the design loads calculated in the previous sections to the grid-stiffened designs and checking for failure, the failure loads of the grid-stiffened design candidates are directly determined. This is done since the ratios of failure loads can be obtained to apply the constraint conditions given in Eq. (5.11) for verification. The overall methodology is identical to the one adopted for the baseline. However, the procedure is more involved in the case of strength calculations of the grid-stiffened structures since two different failure criteria are used as explained in Sec. 4.2 of Chapter 4.

The critical buckling loads are calculated exactly as defined for the baseline with the exception of the stiffness matrix, $\boldsymbol{ABD}_{gs}$ and the radius of curvature used. The radius can be different for grid-stiffened structures, which is identified as R_s (see Fig. 5.1b). Note that $R_m = R_s$ if $t_m = t_s$ since the outer diameter is identical for both the baseline and the grid-stiffened structure. The axial critical buckling load can be found using Eq. (5.29).

$$(P_{cr})_{gs} = (N_{x0})_{cr}^{gs}\,\pi R_s \tag{5.29}$$

where as the critical torque is,

$$(T_{cr})_{gs} = 2\,(N_{x\psi 0})_{cr}^{gs}\,\pi R_s^2 \tag{5.30}$$

The failure loads of the shell attached to the grid and the grid layer are calculated separately as explained in Sec. 4.2. Similar to the critical buckling loads calculations, the stiffness matrix, $\boldsymbol{ABD}_{gs}$ is used to determine the strains and stresses in the shell laminate by considering independently applied loads N_x and $N_{x\psi}$. The values for these applied loads are iterated until the first ply failure occurs,evaluated as per the Tsai-Wu failure theory. They are represented as $(N_x)_s$ and $(N_{x\psi})_s$ where $(\,)_s$ indicates the skin or shell of the grid-stiffened structure.

For the grid layer, maximum strain failure criterion is used as described in Sec. 4.2. The maximum axial and shear loads that satisfy the inequalities given in Eq. (4.22) and Eq. (4.23) are calculated by iteration. They can be represented, respectively as $(N_x)_g$ and $(N_{x\psi})_g$ where $(\,)_g$ here indicates the grid layer of the grid-stiffened structure. Having obtained the maximum values of these loads, the failure loads of the grid stiffened designs can be found using Eq. (5.31) for the net axial load and Eq. (5.32) for the torque.

$$(P_{max})_{gs} = \min\left\{(N_x)_s, (N_x)_g\right\}\,\pi R_s \tag{5.31}$$

$$(T_{max})_{gs} = 2\,\min\left\{(N_{x\psi})_s, (N_{x\psi})_g\right\}\,\pi R_s^2 \tag{5.32}$$

Once the failure (critical buckling and material strength) loads for the grid-stiffened structure are obtained, the load constraints defined earlier in Eq. (5.11) can be calculated. The procedure for design study conducted in the present investigation is described in the next section.

5.3 Design process

The initial step is to identify the quantities that define the general-grid topology completely. As mentioned earlier, these quantities and their value domain are given in Eqs. (5.6) to (5.9). For a given shell laminate of the grid-stiffened structure, a vector, V_i of the design variables is defined as shown in Eq. (5.33).

$$V_i = [N_{a1}, \theta, b_s, h_s]_i, \quad i = 1, 2, 3, \ldots \tag{5.33}$$

where the subscript i indicates different combinations obtained by varying the range of each design variable. The effect of various shell laminates is discussed in Sec. 6.3 of Chapter 6.

A MATLAB® design code is developed to perform all the comparisons and calculations. A large number of combinations are generated and the weight constraint given in Eq. (5.10) is applied as a filter to reduce the number of combinations. The code implementation and the design procedure are depicted in Fig. 5.3. The weight ratio, $\overline{W}$ is prescribed as a range between 0.75 to 0.99 in the main program. The resulting reduced vector, V_r is submitted to various subroutines to calculate various quantities. The tasks undertaken by various subroutines are also indicated in Fig. 5.3. The output from the subroutines are returned to the main program to calculate various design constraints.

Several iterations among different design variables are performed to establish whether all the design constrains are satisfied or not. It is also required to manipulate the $\overline{W}$ range to obtain a manageable number of grid-stiffened design candidates. Design candidates are those that satisfy all the design constraints within the range of design variable input. These are done manually after evaluating the output each time the parameter set in V_r are processed. The results from the design study are presented in Sec. 6.3 of Chapter 6.

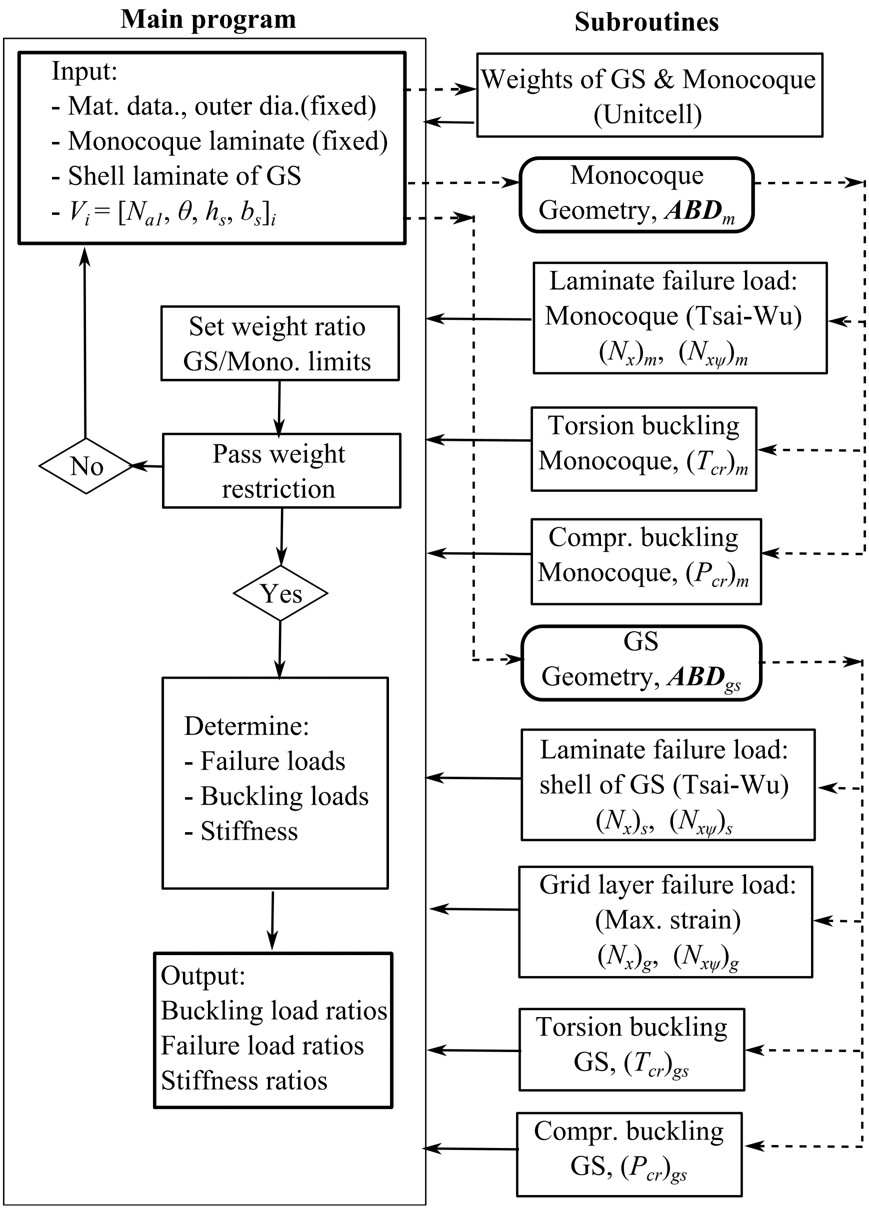

Figure 5.3. Code implementation of the design study. Dotted arrows represent calls to subroutines. GS refers to grid-stiffened structure

Chapter 6

Results and discussions

Validations studies on stiffness predictions from the model developed in the present study are conducted on selected cylindrical grid-stiffened models using FEM and experimental evaluation. Limitations in the state-of-the-art analytical models in predicting the stiffness properties of grid structures are also quantified. Parametric studies on stiffness evaluations are performed on grid and grid-stiffened structures using the newly derived analytical models. Torsional buckling predictions are conducted on cylindrical grid-stiffened tubes by employing the analytical methods available in the literature. The bending buckling evaluation is performed by considering a representative cylindrical section under uniaxial compression. A preliminary design study is presented to demonstrate the weight savings potential of grid-stiffened structures compared to a monocoque baseline. Failure predictions are conducted using the methodology outlined in Chapter 4.

6.1 Stiffness evaluation

6.1.1 Planar grids

Planar grid (no attached skin) structures are analyzed first. The analytical formulations developed for axial and bending stiffness for the grid structures in the present research, as stated earlier in Chapter 3, are identical to that demonstrated by Chen and Tsai [20], which they validated against FEM and experiments. Thus the methodology by which the equivalent stiffness coefficients are derived along with the formulations themselves are validated for the axial and bending stiffness. Consequently, the results for bending and axial stiffness are not reproduced here. However, the analytical model developed in the present study for predicting *shear* stiffness for the flat angle-grid structures is novel for the case of stiffeners with clamped BCs. Therefore, only the results for shear stiffness are presented.

As explained earlier in Chapter 3, the angle-grid configuration requires a non-pinned support at the nodes to determine the in-plane shear stiffness. The present analytical formulations are validated against shell FEA results. The validity of the angle-grid FEA models generated in the present study are evaluated by successfully reproducing the axial and bending deflection results provided in Ref. [20]. In-plane shear stiffness of the grid is of particular interest in this study. This is due to the fact that the torsional stiffness, which is derived from the shear stiffness, is of significant importance for a rotor blade spar. An FEA model of a planar grid showing deformed and undeformed states shown in Fig. 6.1. Also shown in Fig. 6.2 is a slightly oriented view of the same planar angle-grid structure to demonstrate the deflection of the blade stiffeners.

The stiffeners exhibit in-plane bending deformation under in-plane loads on the grid structure. Several of these models are analyzed and the results averaged to obtain reli-

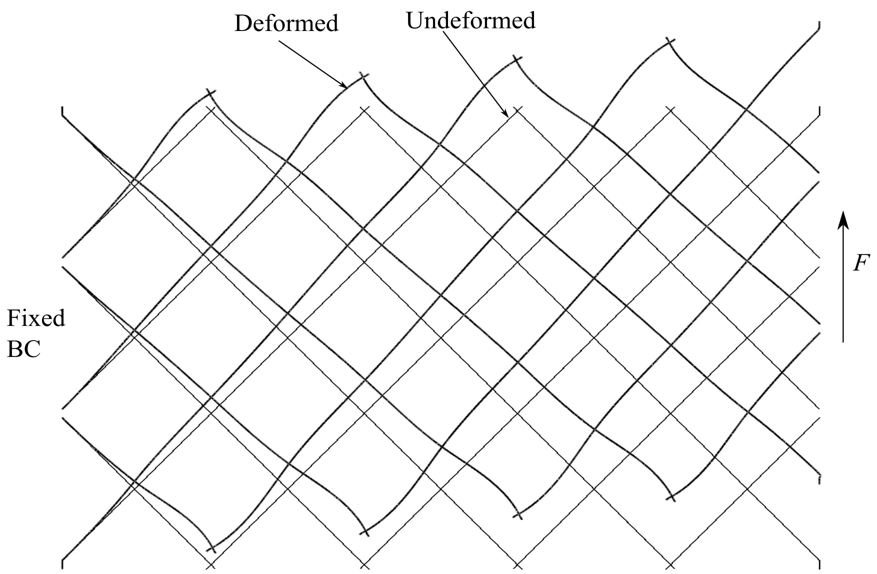

Figure 6.1. FEA (Abaqus) model of a planar angle-grid showing deformed and undeformed shapes. In-plane bending of the stiffeners is evident

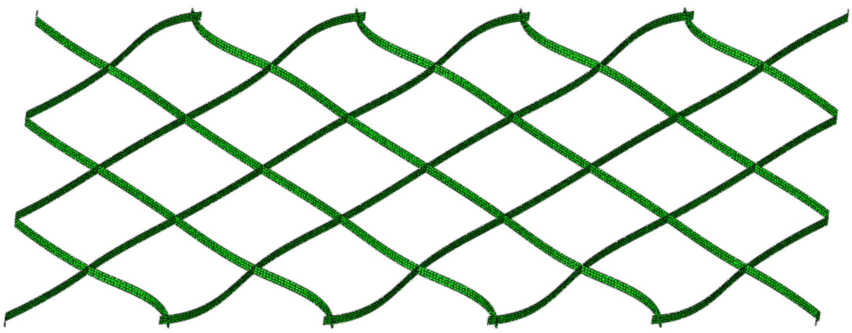

Figure 6.2. Planar angle-grid shear deformation showing the blade stiffeners

able results. The shear stiffness is determined from the angle made by a hypothetical line passing through the stiffener nodes (joints) with respect to the undeformed state. Boundary effects, where relatively large in-plane deflections in the stiffeners occur, can be noticed in the model. It is not possible to completely avoid this phenomenon. However, a simpler and more convenient methodology is to provide a sufficient number of unit-cells away from the boundaries. Upon performing a few trials, it is found that at least 2 units cells in the interior regions provide reliable results. Reliability is assessed by comparing the slope of a series of hypothetical lines connecting the stiffener joints (cross-over locations) with respect to the structural axes.

The angle-grid geometry from Ref. [20] is analyzed for pure shear. The material system used is T300/5208 which has the properties, in GPa, $E_L = 181.0$, $E_T = 10.30$, $G_{LT} = 7.17$, and the major Poisson's ratio $\nu_{LT} = 0.28$. The stiffener cross-section parameters are $b_s = 4$ mm and $h_s = 8$ mm and the stiffener spacing $d_\theta = 100$ mm. Shear stiffness per unit width, A_{66}, from the new closed-form analysis and FEA simulations for various stiffener orientation angles are compared and presented in Fig. 6.3. Note that the stiffener BCs are considered to be clamped for this problem. The effect of stiffener cross-section width (b_s) is also analyzed since this is the parameter that defines the in-plane bending rigidity of the stiffener. b_s, parallel to the grid plane, is varied from 1 mm to 4 mm in 0.5 mm increments while keeping the stiffener depth h_s constant at 8 mm. The variation of shear stiffness for a range of stiffener angles are also demonstrated in the figure.

The analytical results from the newly formulated models are in excellent agreement (of the order of 4% difference) with the FEA simulations for all the stiffening angles and different stiffener widths analyzed. Thus the shear stiffness model developed for angle-grid structures in the present study is validated. It can be noted that the shear stiffness increases as the stiffener width is increased, indicating the influence of in-plane bending rigidity of the stiffeners on the in-plane shear of an angle-grid structure.

The curves are symmetric with respect to the 45° stiffener angle for which the shear stiffness peaks. The variation of in-plane shear stiffness of an angle-grid with $\pm\theta$ stiffeners follows the trend similar to a symmetric orthotropic laminate; the coupling matrix $\boldsymbol{B} = 0$ and the coefficients $A_{12} = A_{16} = 0$ for the present model as shown earlier in Chapter 3. The variation of stiffener length to spacing ratio, with which the shear stiff-

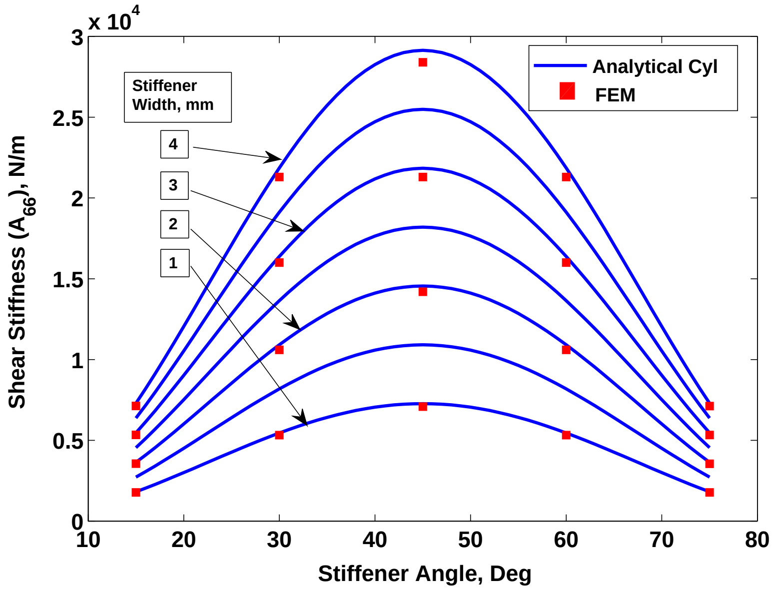

Figure 6.3. Variation of shear stiffness with stiffener orientation. Curves showing the effect of different stiffener widths (1–4 mm). Stiffener depth, $h_s = 8$ mm

ness of the planar grid is calculated, is shown for different stiffener orientation angles for a given grid density (stiffener spacing, d_θ) in Fig. 6.4. Note that the variation is symmetric with respect to 45° angle where L_θ is at its minimum making the stiffener less compliant. This leads to the shear stiffness peaking at 45° angle. The factor that determines the symmetry is the combination of deflections calculated to determine the shear stiffness. As a demonstration, consider two different stiffener orientation angles 30° and 60°, where according to Fig. 6.3 give identical values for shear stiffness. Referring to Fig. 3.9 in Chapter 3, the deflection determined in the x direction for the 30° stiffener is identical to the deflection calculated for the 60° in the y direction and vice versa. This leads to the symmetry observed for the shear stiffness in Fig. 6.3.

As noted earlier, Chen and Tsai [20] validated the models developed to predict the in-plane and bending stiffness properties of planar ortho-grid structures and axial and bending stiffness properties of planar angle-grid structures. Considering that the expressions for these parameters obtained in the present study are identical to that reported in

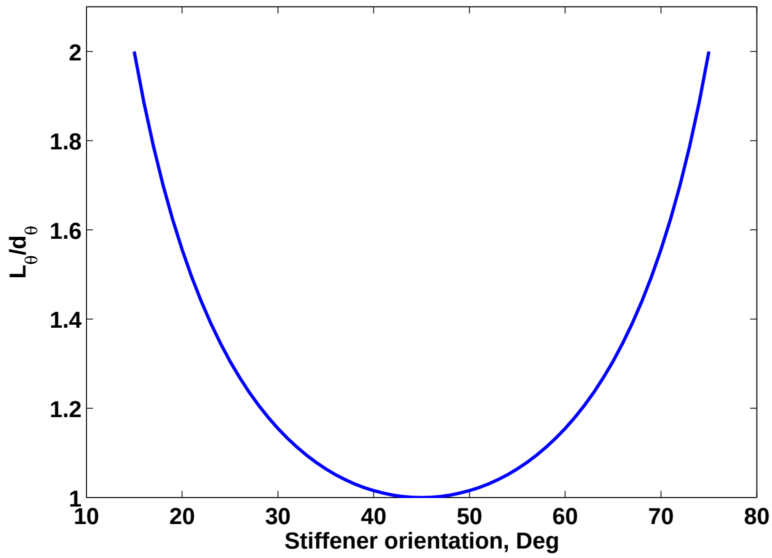

Figure 6.4. Variation of stiffener (beam) length, L_θ in a planar grid with stiffener orientation for fixed stiffener spacing, d_θ

[20] and that the general-grid structures can be modeled by the superposition of angle-grid and ortho-grid, general-grid derivations are also validated. Consequently, results for general-grid are not presented here.

The effect of stiffener joint (node region) compliance was investigated by Sandhu et al. [84]. The in-plane joint flexibility was determined by experiments and concluded that such compliance can significantly affect the overall grid behavior. It was also demonstrated that the in-plane flexibility ('scissoring') of the joint has to be determined from experiments. Using the analysis developed in this study for stiffeners with elastic boundary conditions, some preliminary results are generated with a set of arbitrary values for in-plane torsion spring stiffness. These are provided in Appendix B. It is found that, for the set of grid parameters employed, the effect of torsional compliance at the joints has no significant impact in the shear stiffness behavior of the angle-grid. Further investigation into this aspect must be conducted before a conclusion can be made. Thus, the present study on elastic BCs is declared inconclusive.

6.1.2 Cylindrical grids

6.1.2.1 Validation studies

The grid specimens are tested for deflection under various loading conditions to determine their cross-section stiffness properties. Deflection simulations are also performed using FEM and analytical formulations. The material properties used for this study are given in Table 2.2 of Chapter 2. The overlap section material properties are used in their respective stiffener overlap locations in SLS FEA models. The same material system is used for all parametric studies on stiffness and stability conducted in this research. Since the analytical formulation developed assumes that the stiffener intersect at dimensionless node points, properties of the overlap section are not needed. Similarly, the BLS FEA models do not require separate modeling of the stiffener joints as well.

The tip deflections under tip transverse bending loads are presented in Fig. 6.5. Two analytical solutions are employed, both of which are based on smeared stiffness approach as explained in Chapter 3; the planar grid formulation indicated as 'Analytical Flat' and the newly developed closed-form analysis indicated as 'Analytical Cyl.' The results from FEM and analytical predictions are also presented. The results shows excellent correlation (of the order of 5%) between experiment, FEM, and the analytical model based on cylindrical grid formulation. The planar grid model predicts 26% higher stiffness compared to the FEM and experiment data. This indicates that the compliance due to coupling between various deflection modes of the stiffeners viz., out-of-plane deflection and torsion of the stiffeners must be included in the formulation in order to accurately predict the deflections of grid structures with non-planar topology.

Axial deflection tests are performed on the cylindrical grid specimens and the results are compared to FEM simulations and analytical predictions using the planar and

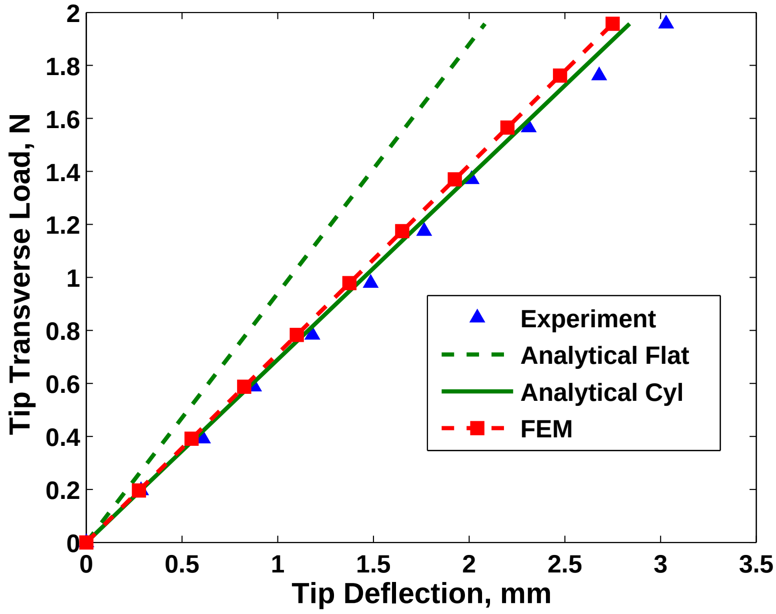

Figure 6.5. Comparison of bending tests, analytical and FEM simulations of the S8 (angle-grid) specimen

cylindrical grid models. The cross-section stiffness is determined using Euler beam theory and the axial stiffness coefficients for the S8 grid tube from various analyses are compared in Fig. 6.6. Excellent correlation between test results and results predicted by FEM and the new analytical model can be observed. This is a validation for the new formulation which includes the coupling between different deflection modes due to the complex geometry of the stiffeners. The planar grid formulation over predicts the axial stiffness by nearly 17%.

The torsion stiffness determined from various simulations and tests are shown in Fig. 6.7. Without accounting for the in-plane bending of the stiffeners in the formulation, the analysis over predicts the torsion stiffness by more than 80% (not shown). When the in-plane bending is introduced [20] in the formulation, also derived in Eq.(3.42) in Chapter 3, the error drops to nearly 39%. When the helical geometry is appropriately represented, using the newly derived formulation in the present research, the analytical

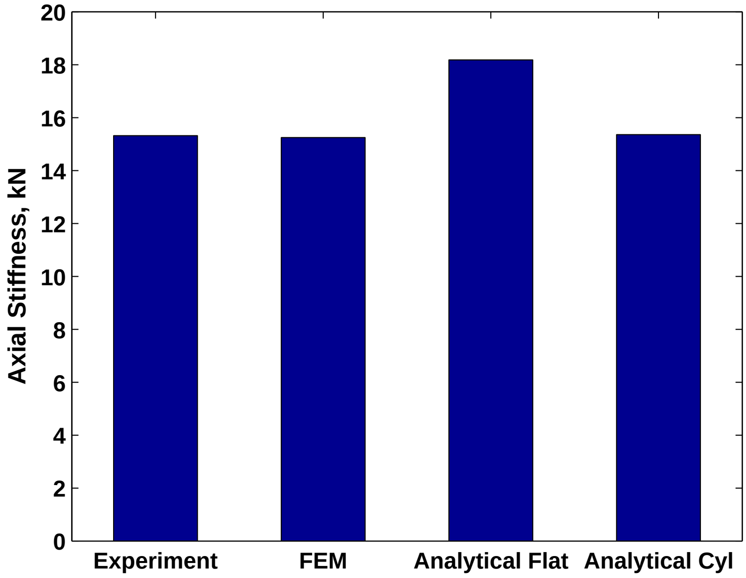

Figure 6.6. Axial stiffness of the S8 (angle-grid) specimen from tension tests, analytical and FEM simulations

prediction matches with the FEM and experiment with in 5%. It can be concluded that, for the range of parameters considered, the coupling between various deflection modes in the helical stiffeners due to the complex geometry is significant and cannot be neglected when predicting the torsion stiffness of tubular grid structures with helical stiffeners.

A section of the FEA SLS model demonstrating out-of-plane deflection is shown in Fig. 6.8. The complex deformation modes in the stiffeners can be easily observed. A flat panel based analytical model cannot capture these complex deflection modes. The stiffener response, when subjected to a tip torque on the angle-grid tube, characterizes coupled twist, out-of-plane (radial), in-plane (along the cylindrical surface) deflections of the stiffeners between the stiffener overlap regions. For the structures analyzed, the out-of-plane bending mode is more significant than the in-plane bending mode due to the cross-section aspect ratio, $ar_s = h_s/b_s = 0.126$, being very low.

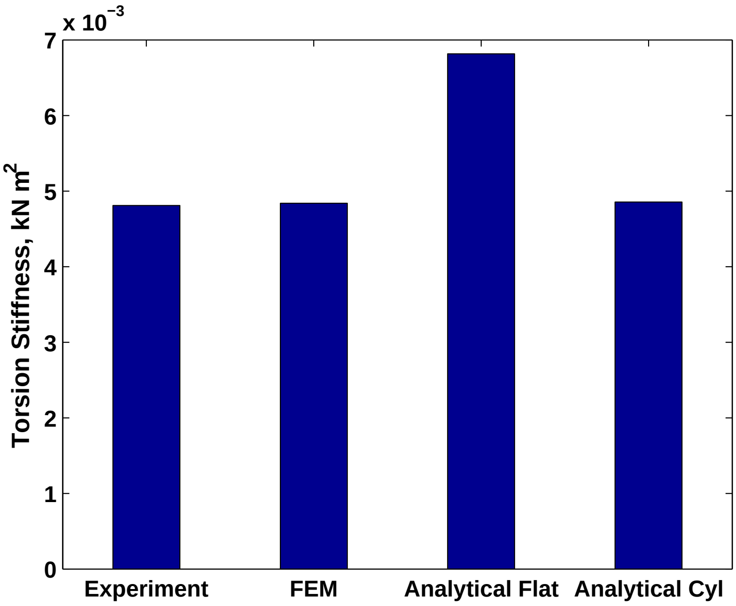

Figure 6.7. Torsion stiffness of the S8 (angle-grid) specimen from torsion tests, analytical and FEM simulations

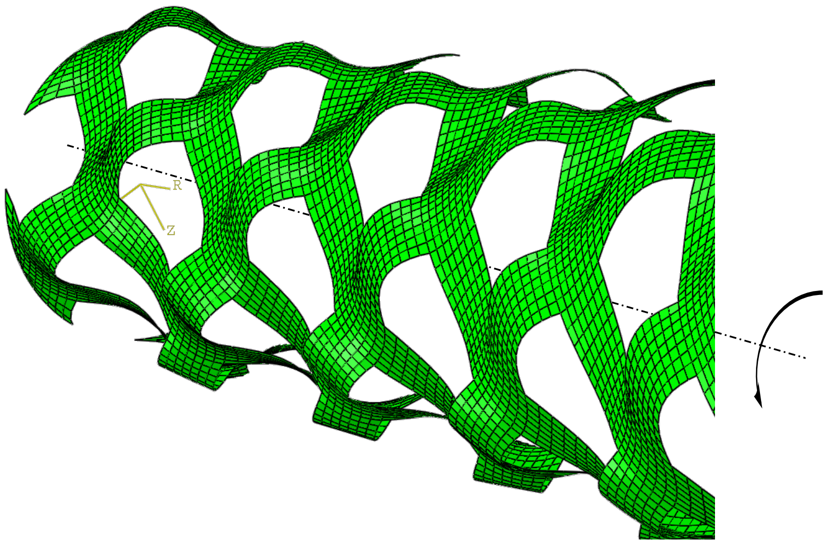

Figure 6.8. Complex deflection modes in the stiffeners of an angle-grid tube (S8 specimen validation model) under torque captured using SLS FEA model. Only one lateral section (axial cut) is shown for clarity

The coupling from the stiffener geometry changes with stiffener angle. In order to further validate the present model, the stiffness coefficients of the specimen grid structures are predicted for various stiffener angles. The torsion, axial, and bending stiffness, respectively, are demonstrated in Figs. 6.9, 6.10, and 6.11. The FEA (using SLS models) predictions and experiments results (identical to the ones shown earlier) are also shown.

The specimen, S4 is found to be not a good candidate for validation. The smeared stiffness approach could not be applied to this geometry since the grid is very sparse—two helical stiffeners in one direction around the circumference. Large discrepancy between analysis predictions and experimental results are observed. Consequently, the studies on this specimen are not provided.

The new analytical model is capable of accurately predicting all the stiffness coefficients with excellent accuracy. The maximum error between FEA predictions and analytical results is observed to be of the order of 7% for torsion stiffness. Also, for bending and axial stiffness, excellent correlation is observed with maximum deviation of the order of 6% between analytical and FEM predictions. It is noted that the deflected mode shown in the Fig. 6.8, the stiffeners almost behaves like plate elements with the overlap regions clearly showing complex deflected shape. The new analysis is not set up to predict this behavior since the stiffeners are assumed to be beams where the calculations are performed at their cross-section centroid. However, since all the deflection modes in the stiffener segments, such as the out-of-plane, in-plane, torsion, axial (along the stiffener axis) are included in the formulation, the complex nature of the stiffener axis is captured. The geometric centers of the overlap regions (where the stiffener joints are defined in the new analysis) are observed to be not exhibiting significant displacements in the radial direction. The regions within the overlap section, are observed to be providing almost-clamped support for the stiffener ends, which is the assumption used for the stiffener ends in the analysis employed.

The validation studies conducted so far has been on cylindrical grids with 19 mm

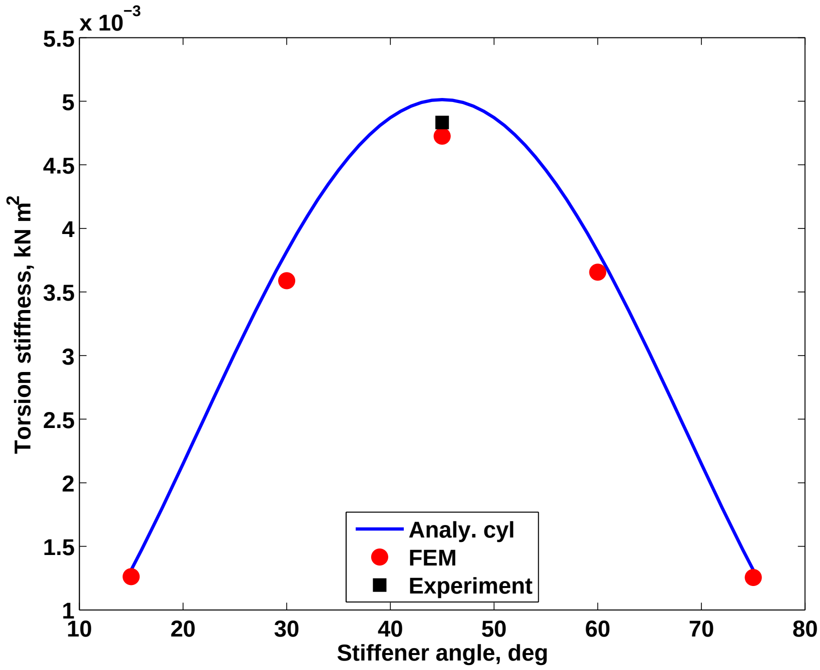

Figure 6.9. Variation of torsion stiffness of cylindrical angle-grid structures with stiffener orientation angles, θ. Geometric parameters of the structure are identical to the S8 specimen

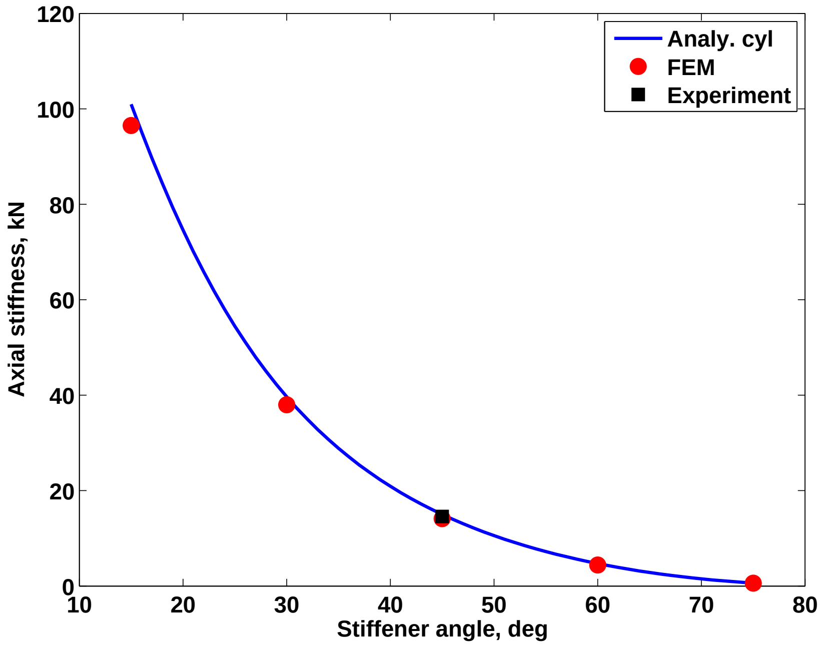

Figure 6.10. Variation of axial stiffness of cylindrical angle-grid structures with stiffener orientation angles. Geometric parameters of the structure are identical to the S8 specimen

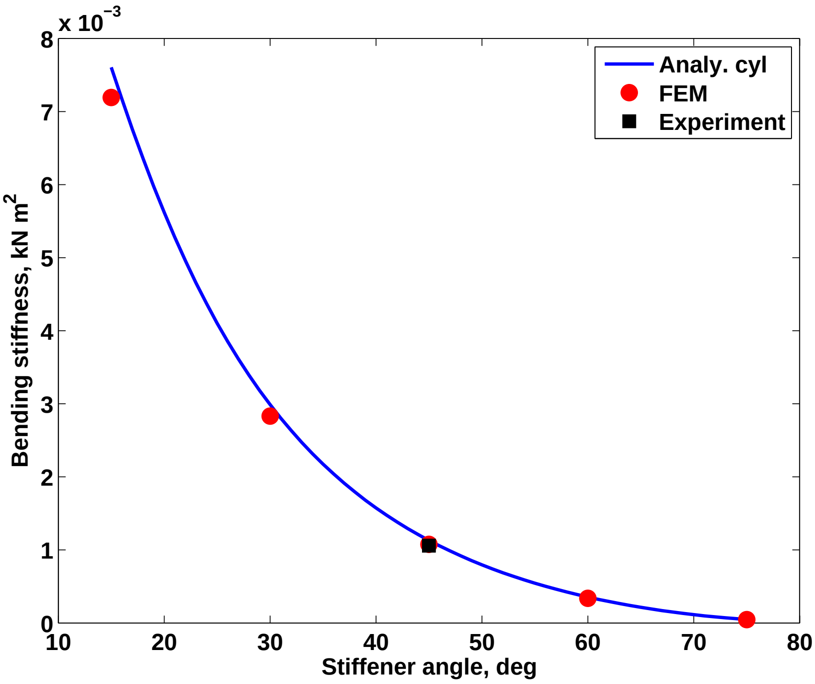

Figure 6.11. Variation of bending stiffness of cylindrical angle-grid structures with stiffener orientation angles, θ. Geometric parameters of the structure are identical to the S8 specimen

diameter, identical to that of the grid specimens. A change in diameter could affect the deflection behavior of individual stiffeners. To verify this, the outer diameter of the cylinder is increased to 165 mm (6.5 in.) This value is selected since this is approximately equal to chord thickness of the heavy-lift blade spar (see data [2] given in Table C.1 of Appendix C.)

The relative performances between the new analytical model and FEM (BLS method) are presented in Fig. 6.12 for the torsion stiffness and Fig. 6.13 for the axial stiffness. Three different stiffener angles, 30, 45, 60 degrees are considered. The effect of a range of stiffener aspect ratio on these stiffness coefficients are also evaluated. It can be seen that the new analytical model can predict the torsion and stiffness behavior of the angle-grid structure with excellent accuracy for all cases presented. The maximum deviation observed is within 7% for both the torsion stiffness and axial stiffness.

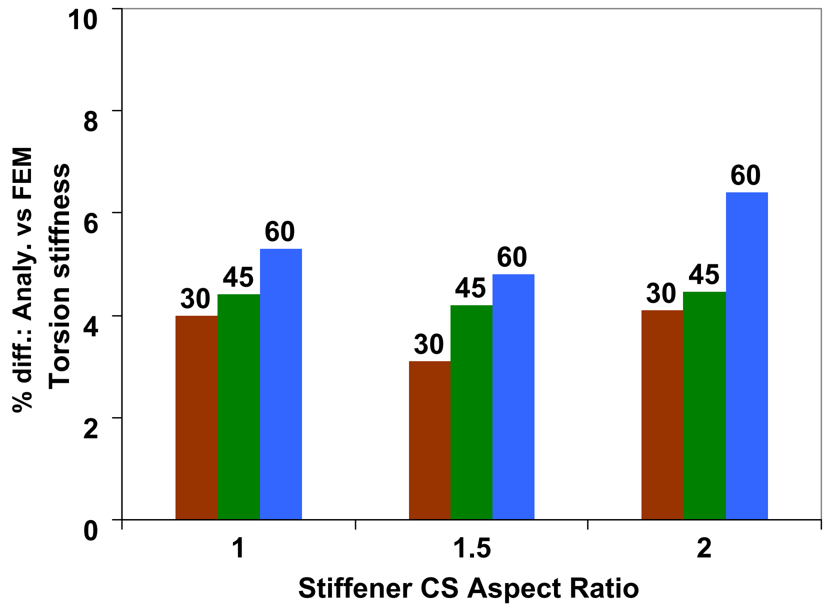

Figure 6.12. Comparison study of angle-grid torsion stiffness between new analysis and FEM. Various stiffener angles 30, 45, and 60° and stiffener CS aspect ratios, $\frac{h_s}{b_s}$. Stiffener spacing, $d_\theta \approx 38$ mm. Stiffener width, $b_s = 4$ mm

The complex deflection modes of the stiffeners captured by the new analytical model can be illustrated using the deflected shapes obtained from the finite element simulations. Figure 6.14 demonstrates the out-of-plane bending of the stiffeners under torsion load on the cylindrical angle-grid with 30° stiffener angle. The in-plane bending is not as pronounced as the out-of-plane deformation under torque loading. For the 45° angle-grid, shown in Fig 6.15, the out-of-plane deformation of the stiffeners is more pronounced than the former model.

The response under an axial load on a 45° angle-grid is depicted in Fig 6.16. The dominant response of the stiffeners are in-plane as expected. The major contribution to the cylindrical grid axial stiffness comes from the in-plane rigidity of the stiffeners.

It can be concluded that the newly formulated analytical model can predict the torsion, bending, and axial stiffness of grid structures with helical stiffeners with excellent

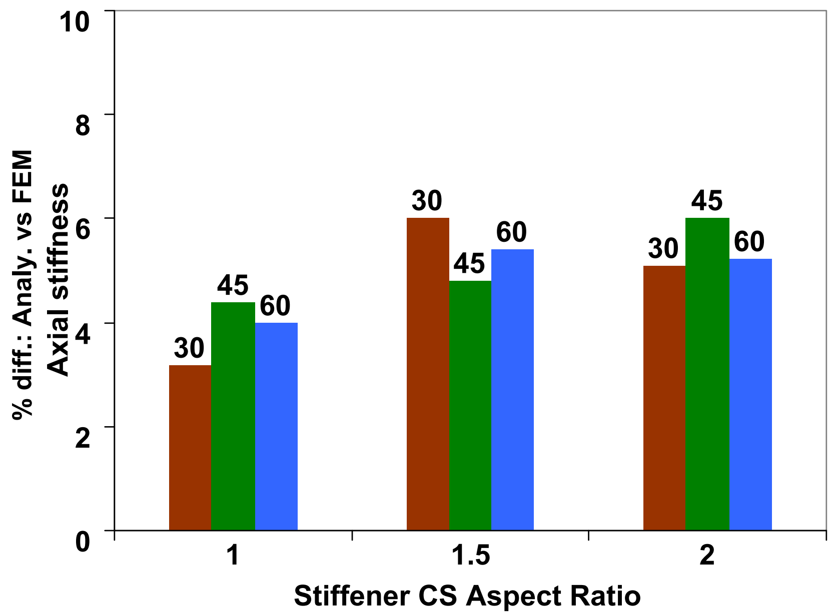

Figure 6.13. Comparison study of angle-grid axial stiffness between new analysis and FEM. Various stiffener angles, θ =30,45,60° and stiffener CS aspect ratios, $\dfrac{h_s}{b_s}$. Stiffener spacing, $d_\theta \approx 76$ mm. Stiffener width, $b_s = 4$ mm

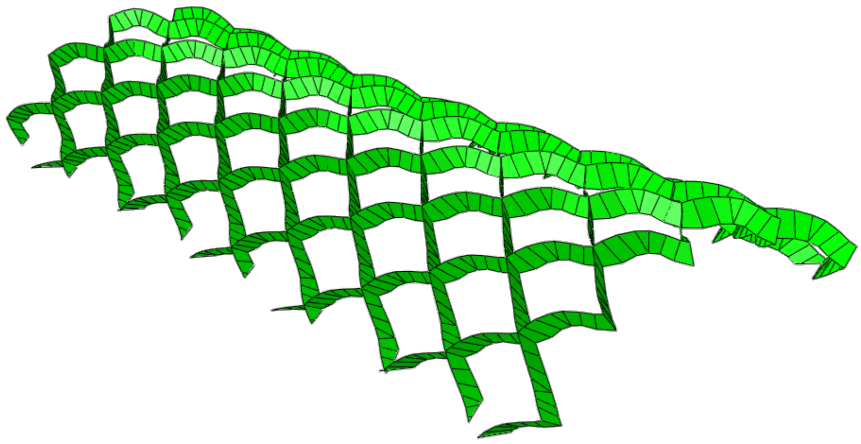

Figure 6.14. Section of the FEA model of a 30° angle-grid under torsion. Out-of-plane and in-plane deflections of the stiffeners can be noticed

accuracy. Having validated the new analytical model by comparing the stiffness predictions to FEM simulations and experiments, numerous parametric studies are conducted on grid and grid-stiffened structure with different stiffening configuration. The purpose

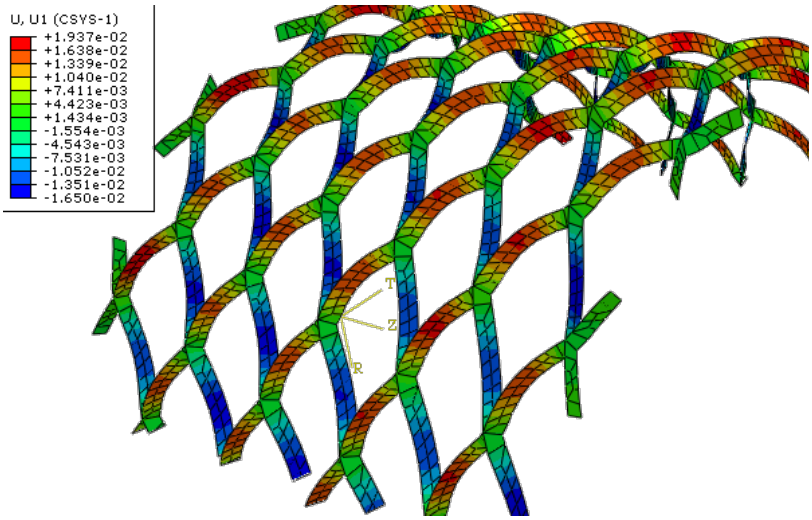

Figure 6.15. Section of the FEA model of a 45° angle-grid with a finer mesh showing out-of-plane stiffener response. Stiffeners under compression and tension deflect radially outward and inward respectively. U1 in the legend denotes radial displacement (cyl. coord. system)

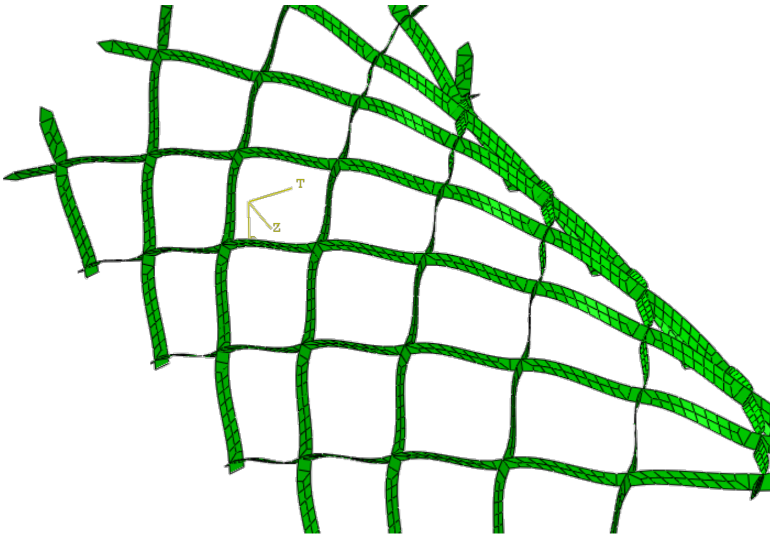

Figure 6.16. Section of FEA model of a 45° angle-grid under axial load. Stiffeners deflect primarily in-plane

is to study the influence of various design variables (see Table 5.1 in Chapter 5) such as the grid density, d_θ (directly related to N_{a1}), cross-section dimensions, h_s and b_s, and stiffener angle, θ on the axial, bending, and torsion stiffness behavior of the cylindrical grid structures.

6.1.3 Parametric studies

6.1.3.1 Angle-grid

The effect of various design parameters such as the stiffener cross-section dimensions, stiffener spacing, and diameter of the cylindrical angle-grid structures is investigated. The material system used is identical to that of the grid specimen as stated before. The cylinder outer diameter, $D_o = 165$ mm for all structures investigated. The effect of grid density, which is dictated by the stiffener spacing, d_θ, is evaluated. The stiffener cross-section values are kept constant as, width, $b_s = 4$ mm, and depth, $h_s = 2b_s = 8$ mm.

Figure 6.17 shows the variation of torsion stiffness with different stiffener angles. The torsion stiffness increases with increasing grid density (decreasing d_θ) for all stiffener angles as expected. Their values peak at 45° stiffener angle. The bending stiffness, shown in Fig. 6.18 and axial stiffness shown in Fig. 6.19 exhibit the same trend between the two. They both decrease with increase in stiffener orientation angles, which is expected. Note that the axial and bending stiffness coefficients present proportional variation for all the parameters as demonstrated.

The effect of stiffener cross-section aspect ratio is analyzed for various stiffener angles next. Initially, the stiffener width, $b_s = 4$ mm, is kept constant. The stiffener cross-section depth, h_s, is varied between 4 mm to 12 mm such that the aspect ratio, $ar_s = \dfrac{h_s}{b_s}$ ranges from 1 to 3. Stiffener spacing, $d_\theta = 76.2$ mm, and is fixed. Figure 6.20 shows the torsion stiffness variation for a range of stiffener angles and aspect ratios. As the aspect ratios increase, torsion stiffness of the structure also increases for all stiffener angles. Similar observation can be drawn on both the axial (Fig. 6.21) and bending (Fig. 6.22) stiffness variations. The lower values of stiffener angles generate high values of axial and bending stiffness compared to higher stiffener angles.

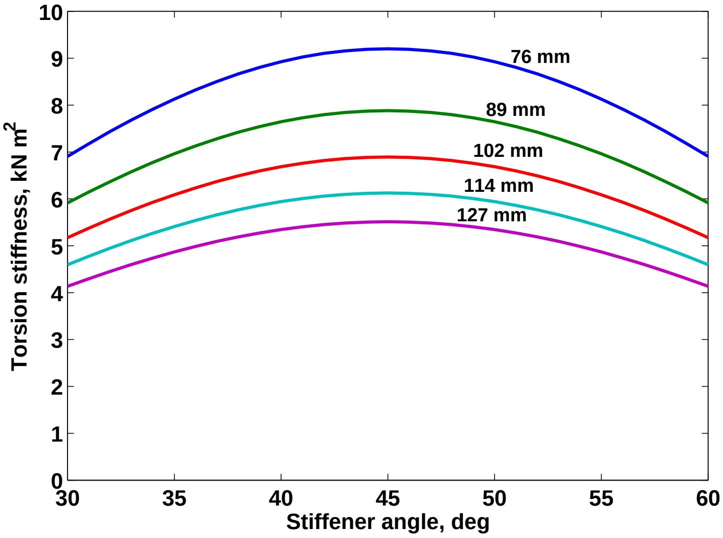

Figure 6.17. Variation of torsion stiffness of cylindrical angle-grid with stiffener orientation angles, θ for various stiffener spacing, d_θ

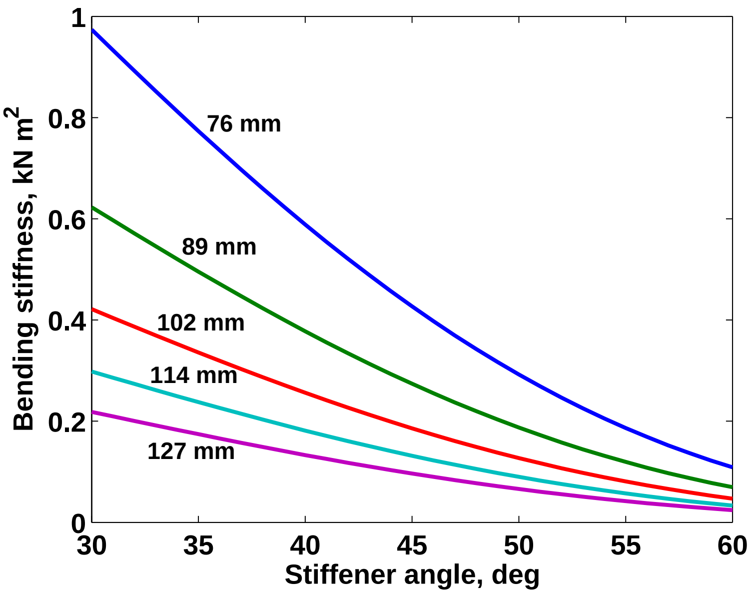

Figure 6.18. Variation of bending stiffness of cylindrical angle-grid structures with stiffener orientation angles, θ for various stiffener spacing, d_θ

The stiffener depth, h_s is now set constant and the effect of stiffener cross-section aspect ratio is investigated. The torsion stiffness variation shown in Figure 6.23 also

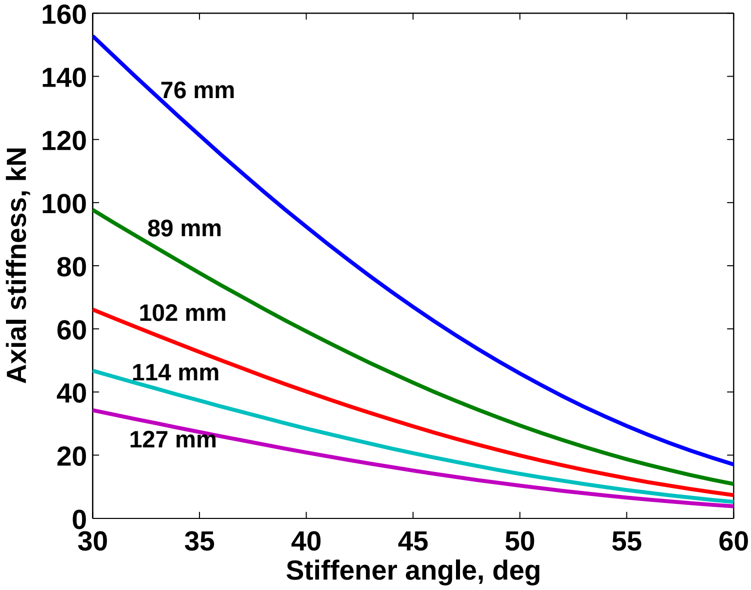

Figure 6.19. Variation of axial stiffness of cylindrical angle-grid structures with stiffener orientation angles, θ for various stiffener spacing, d_θ

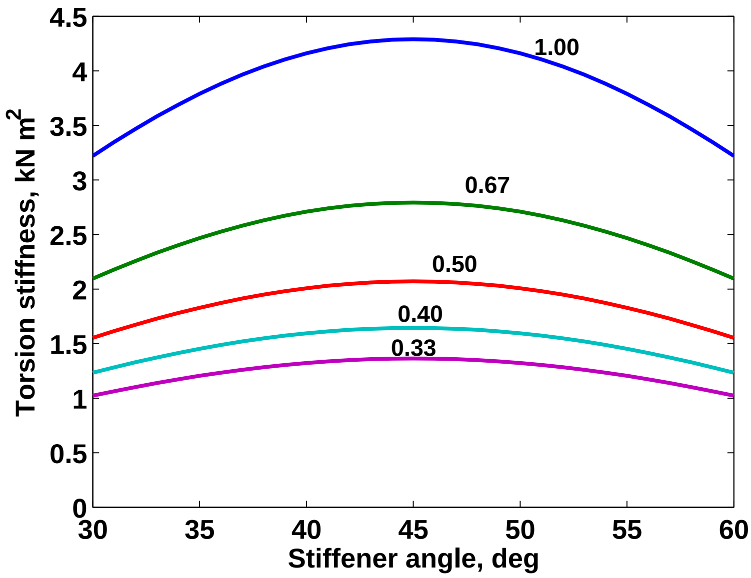

Figure 6.20. Variation of torsion stiffness of cylindrical angle-grid structures with stiffener orientation angles, θ for various stiffener cross-section aspect ratios, $\frac{h_s}{b_s}$. Stiffener spacing, $d_\theta =$ 76.2 mm, stiffener width, $b_s = 4$ mm

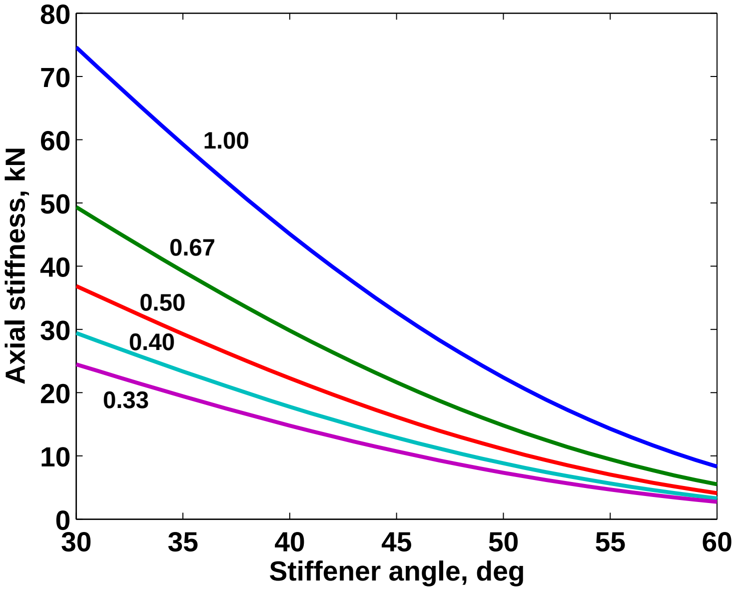

Figure 6.21. Variation of axial stiffness of cylindrical angle-grid structures with stiffener orientation angles, θ for various stiffener cross-section aspect ratios, $\frac{h_s}{b_s}$. Stiffener spacing, $d_\theta = 76.2$ mm, stiffener width, $b_s = 4$ mm

in agreement with the previous observation of having high values at higher aspect ratios. However, compared to Fig. 6.20, higher values of stiffener width (circumferential direction) significantly increase the torsion stiffness. This is due to the fact that the stiffeners now have high bending stiffness in-plane. So, for a given cross-section area of the stiffener, $ar_s > 1$ would provide higher torsion stiffness compared to $ar_s < 1$. Similar observations can be made in the case of bending stiffness by comparing Figs. 6.22 and 6.24. Recall that the bending stiffness is calculated from the global axial strain for the grid tubes (see Eq. (5.21) in Chapter 5.) Identical reasoning can be applied in the case of axial stiffness (see Eq. (5.20) in Chapter 5.) Consequently, axial stiffness variation is not presented.

The difference between planar and cylindrical grid formulation is investigated for 45° angle-grid cylinders. The results are provided in Fig. 6.25. Curves are generated for

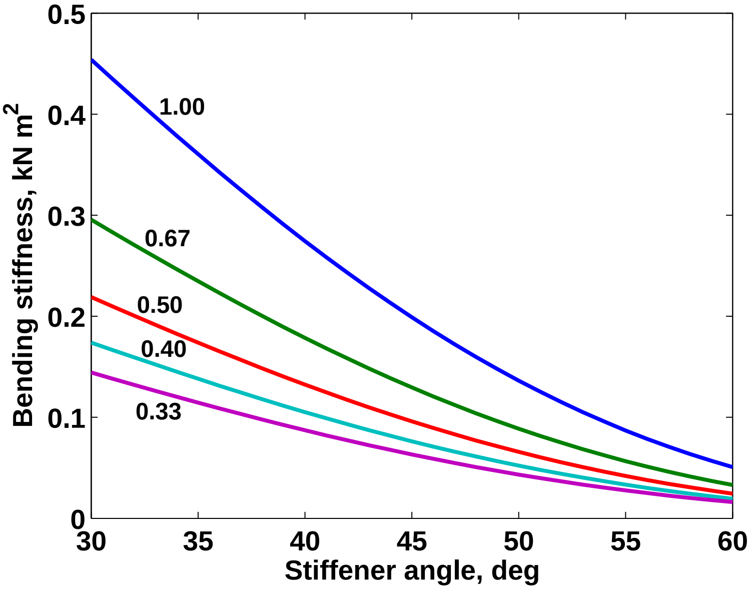

Figure 6.22. Variation of bending stiffness of cylindrical angle-grid structures with stiffener orientation angles, θ for various stiffener cross-section aspect ratios, $\dfrac{h_s}{b_s}$. Stiffener spacing, $d_\theta =$ 76.2 mm, stiffener width, $b_s = 4$ mm

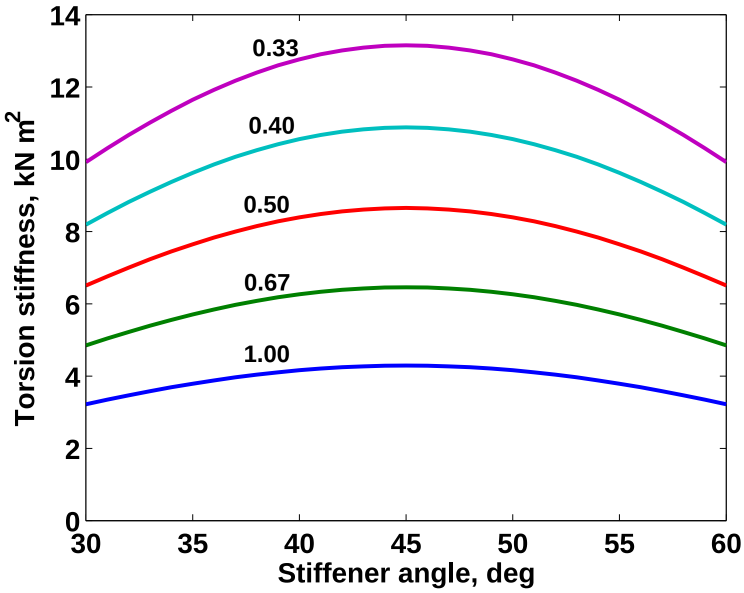

Figure 6.23. Variation of torsion stiffness of cylindrical angle-grid structures with stiffener orientation angles, θ for various stiffener cross-section aspect ratio, $\dfrac{h_s}{b_s}$. Stiffener depth, $h_s = 4$ mm

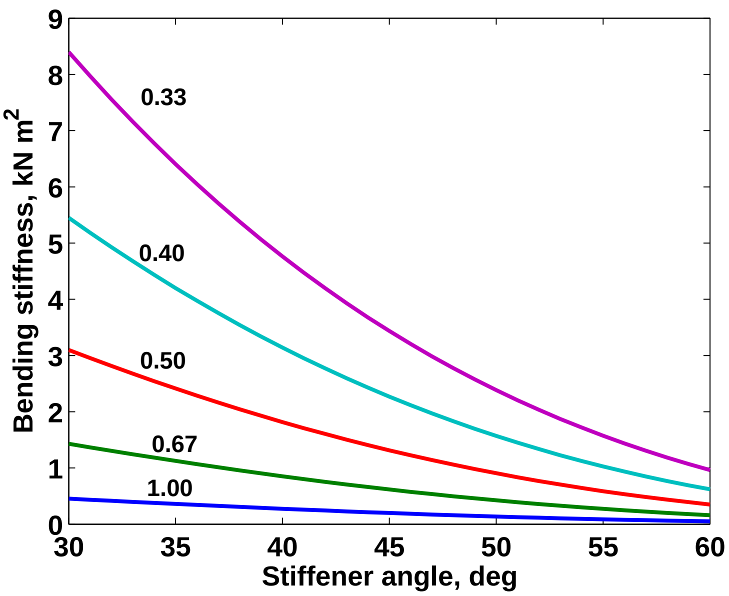

Figure 6.24. Variation of bending stiffness of cylindrical angle-grid structures with stiffener orientation angles, θ for various stiffener cross-section aspect ratio, $\frac{h_s}{b_s}$. Stiffener depth, $h_s = 4$ mm

different stiffener spacing values, d_θ. It is clear that the length of the angle-grid stiffener between support (from d_θ) and the curvature play significant roles in torsion stiffness. The error observed is of the order of 60% when the cylinder diameter and the spacing, d_θ are at their maximum. The error goes down to less than 10% for all cases when the cylinder diameter is increased by 40%. At the maximum grid density and 165 mm diameter, the differences between the two analysis is nearly 22%.

6.1.3.2 Ortho-grid

The cylindrical ortho-grid configuration has the circumferential stiffeners modeled as arch segments with clamped BCs. The curvature of the transverse (circumferential for ortho-grid) stiffeners is newly introduced in the present formulation. The significance of including this parameter is investigated. This is performed by comparing the anal-

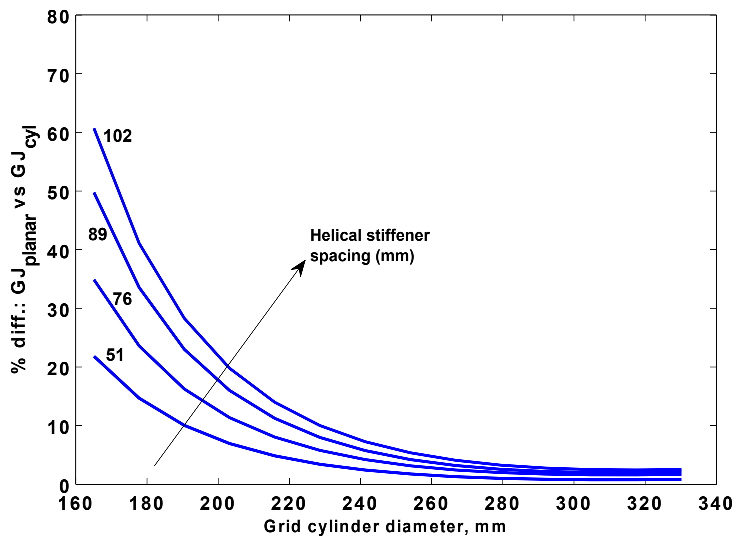

Figure 6.25. Relative error between angle-grid torsion stiffness predictions from planar and cylindrical grid formulation with respect to different cylinder diameter, D_o. $b_s = 4$ mm and $h_s = 8$ mm

yses where the torsion stiffness derivations are based on cylindrical and planar grids. For the case when the stiffener cross-section aspect ratio, $ar_s = \dfrac{h_s}{b_s} = 2$, the maximum difference between cylindrical and planar formulation is observed to be 15% when the grid is the coarsest, as shown in Fig. 6.26. This indicates that the in-plane bending of the circumferential stiffeners dominates with minimum coupling effect from torsional mode.

The aspect ratio is now decreased to obtain $ar_s = \dfrac{h_s}{b_s} = 0.5$, to study the effect of coupling between in-plane bending and torsion of the circumferential stiffeners. Note that the longitudinal stiffeners exhibit in-plane bending only. It can be observed from Fig. 6.27 that the difference between cylindrical and planar formulation in predicting the torsion stiffness of the cylindrical grid can reach as high as 45% when the grid is at its minimum dense configuration.

The significance of curvature of the circumferential (transverse) stiffener is investi-

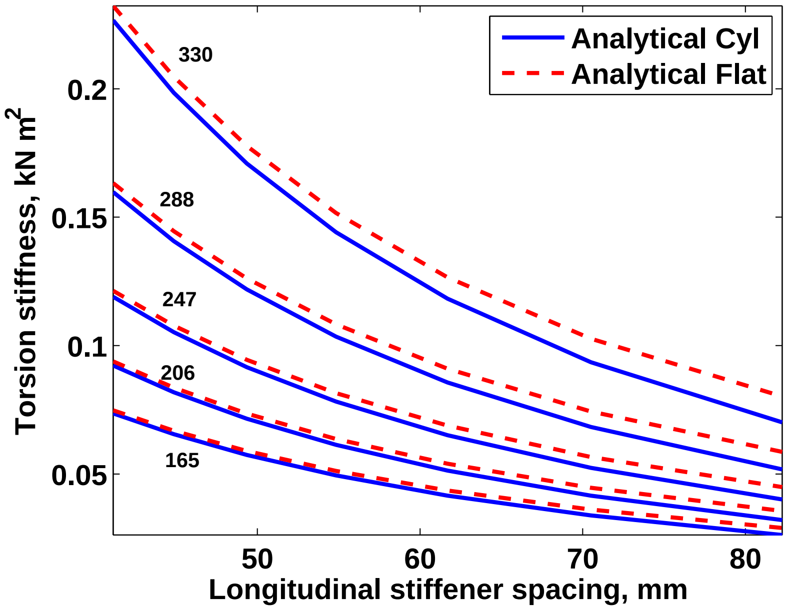

Figure 6.26. Variation of torsion stiffness of cylindrical ortho-grid structures with different stiffener spacing, d_θ. Effect of diameter, D_o (in mm) of circumferential stiffeners on torsion stiffness is also compared. Stiffener CS width, $b_s = 4$ mm and stiffener CS height, $h_s = 8$ mm

gated by analyzing ortho-grid tubes with different outer diameters ranging from 165 mm to 330 mm and the aspect ratio, $ar_s = 2$. The variation of torsion stiffness is shown in Fig. 6.28 for different longitudinal stiffener spacing, $d_0 = 50.8$ to 127 mm . It is evident that the larger the diameter (lower curvature), the lower the error between the two analyses for a given d_0. When the diameter is 165 mm, the error increases from 4% to 43% as d_0 is increased (increased circumferential length of the transverse stiffeners) in the range specified. It can be concluded that a careful investigation on the effect of curvature, stiffener spacing, and stiffener CS aspect ratio is necessary before planar grid formulation can be used for torsion stiffness prediction of small diameter ortho-grid structures.

The general-grid stiffness coefficients are obtained by algebraically adding the corresponding stiffness parameters of angle-grid and ortho-grid topologies as narrated in Chapter 3. Consequently separate results for general-grid configuration are are not pre-

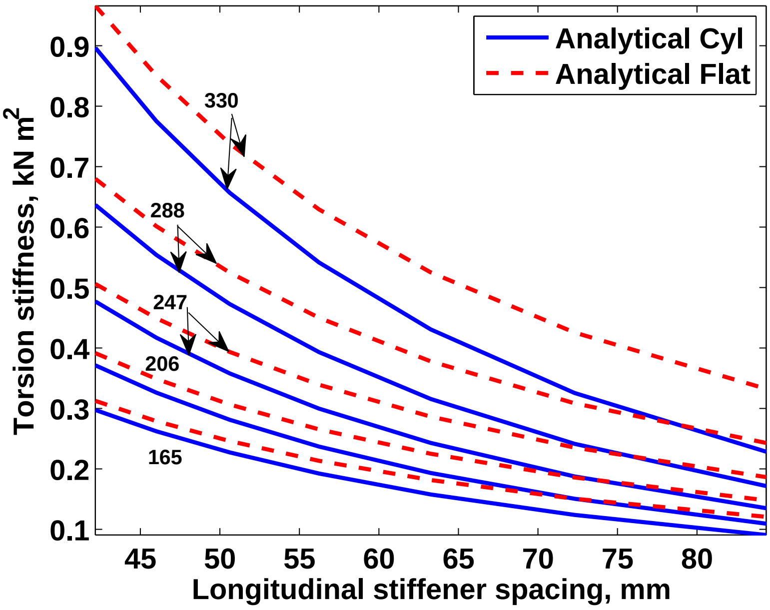

Figure 6.27. Variation of torsion stiffness of cylindrical ortho-grid structures with different stiffener spacing, d_θ. Effect of diameter, D_o of circumferential stiffeners on torsion stiffness is also compared. Stiffener CS width, $b_s = 8$ mm and stiffener CS height, $h_s = 4$ mm

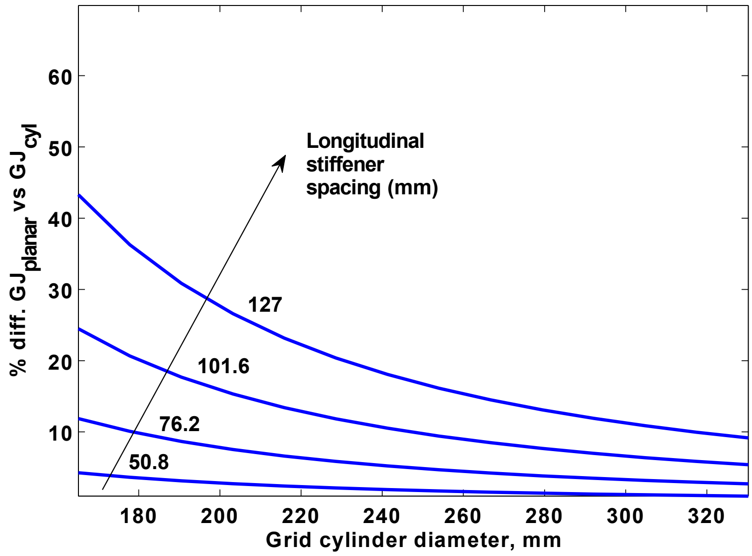

Figure 6.28. Relative error in the prediction of cylindrical ortho-grid structures using planar and cylindrical formulation for different grid cylinder diameters, D_o. Stiffener CS width, $b_s = 4$ mm, stiffener CS height, $h_s = 8$ mm

sented. From the parametric studies conducted, it is observed that, the largest of errors occur for the torsion stiffness predictions when planar grid formulation is employed.

6.1.4 Grid-stiffened cylinders

Two shell laminates for grid-stiffened cylinders are arbitrarily selected as $[\pm 45]_s$ and $[\pm 45]_{2s}$ with 's' indicating symmetry. The stiffeners have geometry parameters similar to the grid structures studied in earlier sections. The materials properties are also identical to those used in the grid parametric study. Having established the influence of stiffener geometry in the grid structure stiffness, the effect of skins on the compliance of the stiffeners is examined in this section. Only general-grid designs under torsion are considered for this study.

The planar grid model is compared against the model developed in the present study, which captures the exact geometry of the curved stiffeners. Of particular interest is the magnitude of error between the two models in predicting the torsional stiffness with different shell thicknesses. Torsion stiffness is examined since this coefficient has been identified earlier to be the most impacted when the stiffener curvature is ignored.

The outer diameter of the shell is 165 mm (6.5 in). The schematic of the grid-stiffened shell and the stiffener cross-section are shown earlier in Fig. 3.27 in Chapter 3. A validation study is performed using FEM BLS shell model that provides clamped BCs at the stiffener cross-over locations as described in Chapter 2. By setting the topology of angle-grid, the topology of ortho-grid is also fixed because of the assumption that the stiffeners pass through common nodes (see Fig 3.1 of Chapter 3.) Thus, a general-grid topology can be completely defined by prescribing the stiffener angle and helical stiffener spacing. The spacing between helical stiffeners, $d_\theta = 76.2$ mm (3 in) is kept constant. The stiffener angle is set to 45° with respect to the cylinder longitudinal axis. A comparison study between the two analyses in predicting torsion stiffness is demonstrated in Fig. 6.29. Also shown for reference is the relative difference between analytical and FEM predictions of the monocoque cylinder (first data bar.)

The data indicated as 'GS: FEM/Ana' shows the ratio of data from FEM to that of from the newly developed analytical model demonstrates excellent correlation (with in 5%). The third data in the chart shows nearly 20% over-prediction by planar grid formulation. This difference can be attributed to ignoring (in fact not including) the curvature of the stiffeners. It is interesting to note that the error is reduced from 35% in the case of grid structure as shown earlier (see Fig. 6.25), to nearly 20% in the present case. This indicates that the presence of the shell structure, although reduced, does not eliminate the influence of coupled deformations of the stiffeners in torsional stiffness prediction.

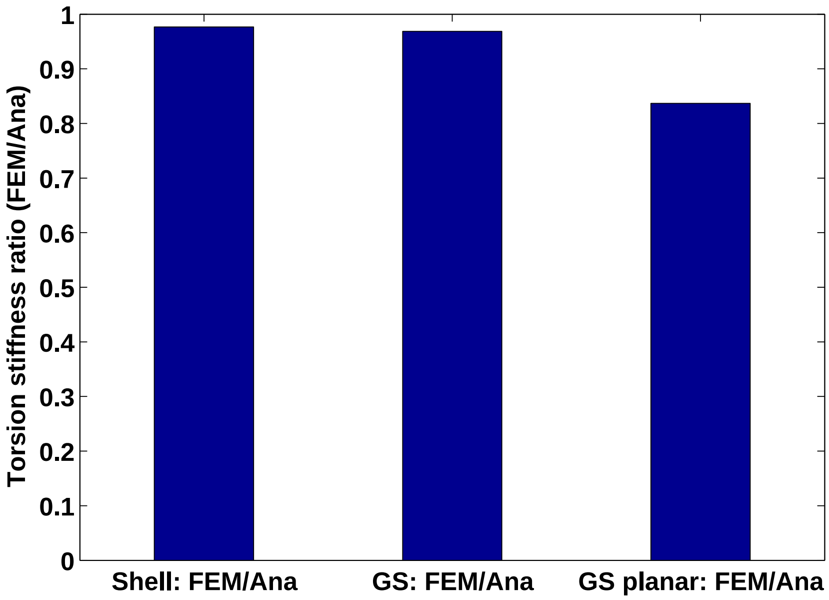

Figure 6.29. Torsion stiffness ratio of cylindrical general-grid stiffened shell using planar and cylindrical shell analysis. Stiffener CS width, $b_s = 4$ mm and stiffener CS height, $h_s = 8$ mm, diameter, $D_o = 165$ mm. Shell is $[\pm 45]_s$

The relative errors between the two analyses in predicting the torsional stiffness of general-grid stiffened cylindrical shell are presented in Fig. 6.30. The shell laminate for this model is $[\pm 45]_{2s}$. Note that the maximum error dropped to nearly 36% compared to the grid structure presented earlier in Fig. 6.25. The presence of the shell has significant impact in governing the stiffener compliance associated with the complex curvature. When the diameter of the cylinder is large, the error between the analyses drops to negligible amount for all grid densities evaluated. However, the designer has to be careful with the tool employed when the parameters vary in the range shown. Comparing the results in Fig. 6.30 to the third data bar in Fig. 6.29, it is clear that the thickness of the shell significantly alter the relative error between the planar and curved shell analytical models. A decrease of error from nearly 20% to 13% when the shell thickness is doubled. Also, a drop in error from 36% (see Fig. 6.25) for diameter, 165 mm and spacing, $d_\theta = 76$ mm. For the minimum stiffener spacing, the error drops below 10% for all diameters.

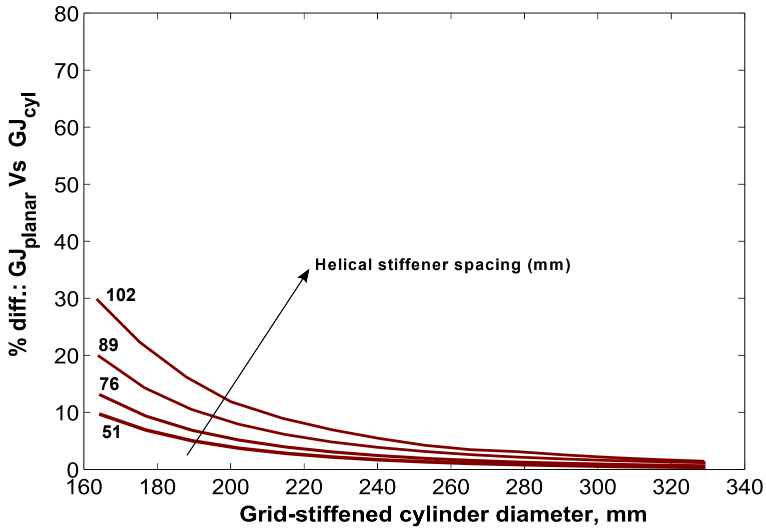

Figure 6.30. Relative error between general-grid stiffened cylindrical shell torsion stiffness predictions from planar grid and newly developed analysis for different grid spacing, d_θ. Stiffener CS width, $b_s = 4$ mm and stiffener CS height, $h_s = 8$ mm

In summary, the effect of complex geometry of stiffeners must be included in the formulation when the cylinder diameter is small as demonstrated. In the case of axial (consequently bending) stiffness, the error is with in the range of 7–12% for grid structures. The error is expected to only reduce when the shell is attached to the grid. The results presented are only typical of the nature of the parameters considered. The behavior demonstrated could be different for different shell laminates with various stiffness couplings present.

6.2 Stability evaluation

6.2.1 Torsion

A code is developed based on existing analytical models [61, 69, 85, 86] to predict the critical buckling torques of long laminated composite cylinders. This code is validated against published results [87] to verify its accuracy. The results generated in the current investigation are presented in Table 6.1. In the study cited, the results were validated with finite element models which are also provided here for reference.

The buckling formulation employed in this study permits direct substitution of stiffness coefficients, A_{ij}, B_{ij}, and D_{ij}. Several grid-stiffened cylinders are analyzed for buckling under tip torque by means of linear eigenvalue buckling analysis using FEM. The material used are same as the one used for the parametric studies on stiffness presented earlier. Various examples of torsional buckling of grid-stiffened tubes of finite length are shown in Fig. 6.31. These models are generated using SLS modeling technique (see Sec. 2.2.1 of Chapter 2) and as a result the stiffeners are not visible. The SLS modeling is selected since it is relatively easier to change the stiffener depth compared to the BLS models.

Table 6.1. Critical torsion buckling loads of various *long* thin walled composite monocoque cylinders. Minimum buckling load occurs for circumferential wave parameter, $n = 2$ [61] and axial wave number from the present study, m as shown

Tube laminate	Analy. [87] N m	FEM [87] N m	Analy. present N m	m
$[15, -15]_4$	193	210	193	4
$[-15, 15]_4$	197	214	197	4
$[30, -30]_4$	254	263	255	6
$[-30, 30]_4$	259	268	260	6
$[45, -45]_4$	383	385	383	9
$[-45, 45]_4$	382	385	383	9
$[0_2, 45, -45, 45, -45, 0_2]$	218	230	221	5
$[0_2, -45, 45, -45, 45, 0_2]$	208	219	210	5
$[0_2, 45, 0, -45, 0, 45, -45]$	342	358	343	5
$[0_2, -45, 0, 45, 0, -45, 45]$	315	329	318	5
$[0_2, 45, 0, 0, -45, 45, -45]$	340	355	340	5
$[0_2, -45, 0, 0, 45, -45, 45]$	300	313	302	5
$[-45, -15, 15, 45, 15, -15, -45, 45]$	375	389	377	6
$[45, 15, -15, -45, -15, 15, 45, -45]$	449	439	449	6
$[15, -15, -45, -15, 15, 45, 15, -15]$	206	219	208	5
$[-15, 15, 45, 15, -15, -45, -15, 15]$	226	241	227	4

An angle-grid stiffened model is selected to present various buckling modes. All models shown have the same diameter and length. There are four helical stiffeners around the circumference. The only variables in these models are the skin thickness and stiffener depth. The stiffener angle, $\theta = 45^\circ$, outer diameter, $D_o = 165$ mm, length is approximately $8D_o$. Simply supported BCs are applied at both ends using reference points with opposing torques applied to determine the buckling modes.

The images in Fig. 6.31 are selected out of numerous critical modes to explain the complexities involved in modeling as well as the sensitiveness of various parameters.

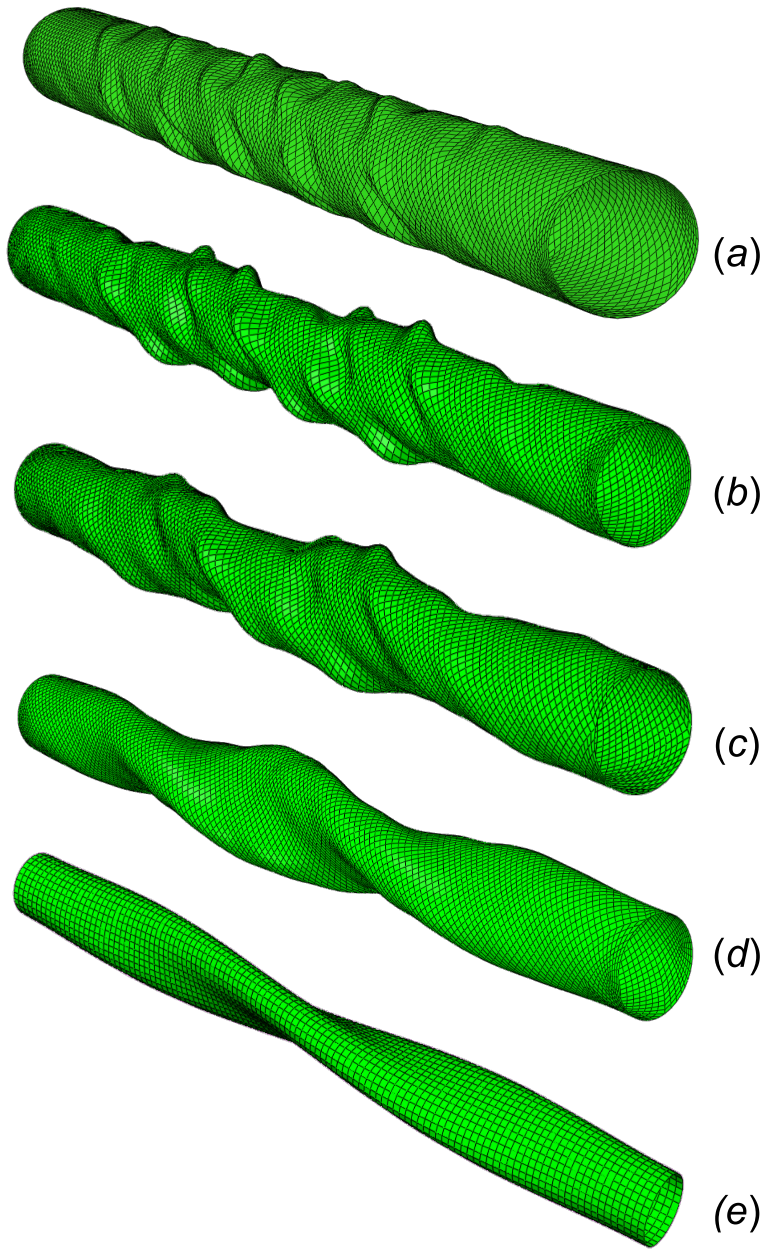

Figure 6.31. Critical buckling modes of angle-grid stiffened cylinders using FEA simulations. (a) local skin buckling, (b) local stiffener crippling, (c) local skin and stiffener mode interaction, (d) global buckling mode, (e) global torsion buckling mode of a monocoque tube

The stiffener width is set as constant, $b_s = 4$ mm. Figure 6.31a with $h_s = 4$ mm, has the lowest skin ($[\pm 45]_s$) thickness where the local buckling occurs predominantly in the skin regions. An increase in the stiffener depth to 8 mm forces the structure to buckle in a mixed mode (local skin and stiffener buckling) as shown in Fig. 6.31b. Figure 6.31c is showing local stiffener crippling combined with a global mode. In this case, the skin is supplemented with additional $[\pm 45]$ plies compared to that in (a). Figure 6.31d shows the global mode obtained with an increased stiffener depth of 12 mm with $[\pm 45]_{2s}$ shell laminate.

The only criterion used to describe this mode as a global mode is by comparing it to the critical mode of a composite monocoque tube, which such mode is demonstrated in Fig. 6.31e. Based on the parameters employed such the stiffener angle, stiffener spacing, aspect ratio of the stiffener cross-section, ply thickness, and the diameter of the cylinder, it was found that at least six plies of symmetric or alternating ± 45 are required in the shell laminate to obtain the global buckling mode.

Developing an analytical model to predict the aforementioned local mode interactions and local–global modes is extremely difficult. This is especially true if there exist critical modes where multiple unit cells participate in the buckling mode. A solution methodology where the structure is assumed to be infinitely long is therefore implemented, based on existing formulations, as stated in Chapter 4. A set of results are presented for the general-grid stiffened tubes to demonstrate the impact of various design parameters. The choice of shell laminate is arbitrary while the total number of plies are kept to at least six.

Figure 6.32 shows the variation of critical torques with respect to the stiffener angles for different helical stiffener spacing, d_θ. The stiffener aspect ratio is set to 1 (4×4 mm) and the shell laminate is $[\pm 45]_{2s}$. The buckling loads peak at 48° for all the cases presented and the critical buckling load increases with increasing grid densities.

The effect of stiffener aspect ratio, $ar_s = \dfrac{h_s}{b_s}$ is studied by varying that quantity and predicting buckling torque for different stiffener angles. The stiffener spacing is kept

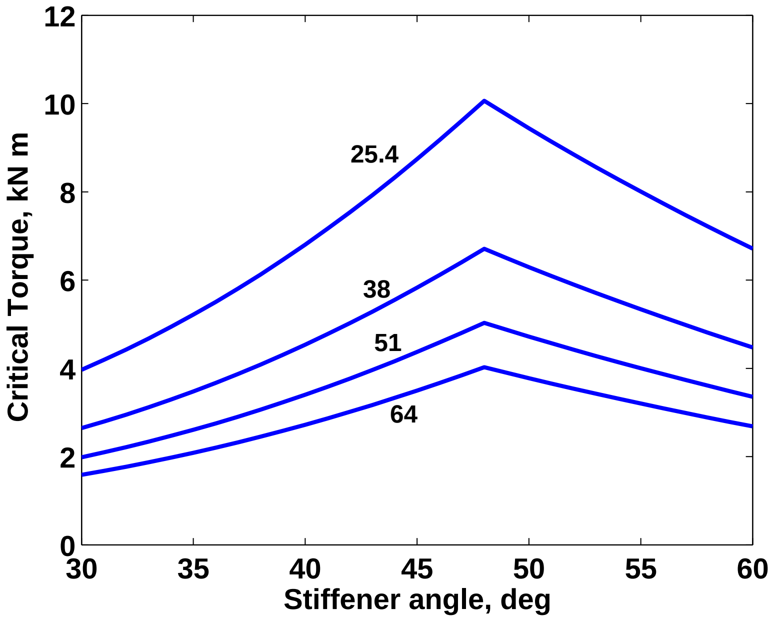

Figure 6.32. Buckling behavior of general-grid stiffened tubes under torque for different stiffener spacing, d_θ mm. Stiffener CS is 4×4 mm. Shell $[\pm 45]_{2s}$

constant at $d_\theta = 25.4$ mm. The results are shown in Fig. 6.33. The buckling loads for the aspect ratio of 1 is provided for reference. As the width of the stiffener is increased, the buckling loads also increase peaking at the same stiffener angle, $\theta = 48°$. However, high aspect ratios provide high buckling loads with maximum values exhibited at lower stiffener angles. A maximum of 60% increase in buckling load is obtained for the same stiffener cross-section area (same weight), when the cross-section dimensions are switched, 8×4 to 4×8 mm. This attribute would help in the design process where high buckling loads are sought. Considering this specific example, this high aspect ratio would adversely affect the torsion stiffness of the grid-stiffened structure as discussed earlier. Also, high aspect ratio result in increased stiffener eccentricity effects from the coupling coefficients in $\boldsymbol{B}$ matrix.

The impact of increased skin thickness on the buckling is studied by varying the shell laminate as depicted in Fig. 6.34. It is seen that the increased skin thickness not

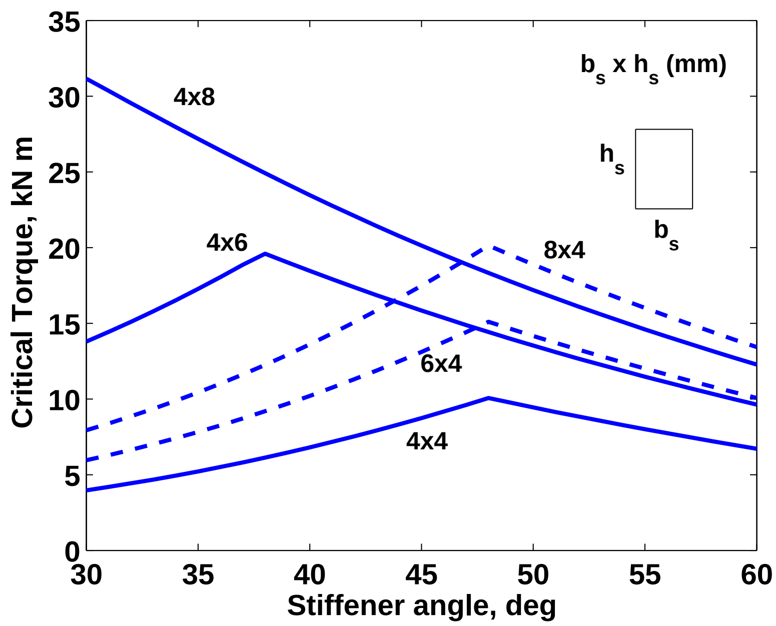

Figure 6.33. Buckling behavior of general-grid stiffened tubes under torque for different stiffener aspect ratios, $\dfrac{h_s}{b_s}$. Shell $[\pm 45]_{2s}$, $d_\theta = 25.4$ mm

only increased the buckling load but also shifted the peaks to lower stiffener angles. A 33% increase in the buckling when the skin thickness is doubled from 0.91 to 1.82 mm ($t_{ply} = 0.229$ mm) while a 17% increase in buckling load when the thickness is increased from 1.82 to 2.73 mm.

Since the global buckling modes are characterized predominantly by the radial displacement of the stiffeners, high aspect ratios augment the critical buckling loads. The critical torque is very sensitive to the stiffener depth. This can also be verified by the buckling loads peaking at lower stiffener angles because a lower stiffener angle provides maximum out of plane stiffness due to reduced coupling effect from their low curvature. Note that the contribution of circumferential stiffeners are included in the analysis. Another important aspect is how the stiffener placement would 'break' the buckle waves. A stiffener with 'sufficient' stiffness at a crest or trough of the buckling waves would

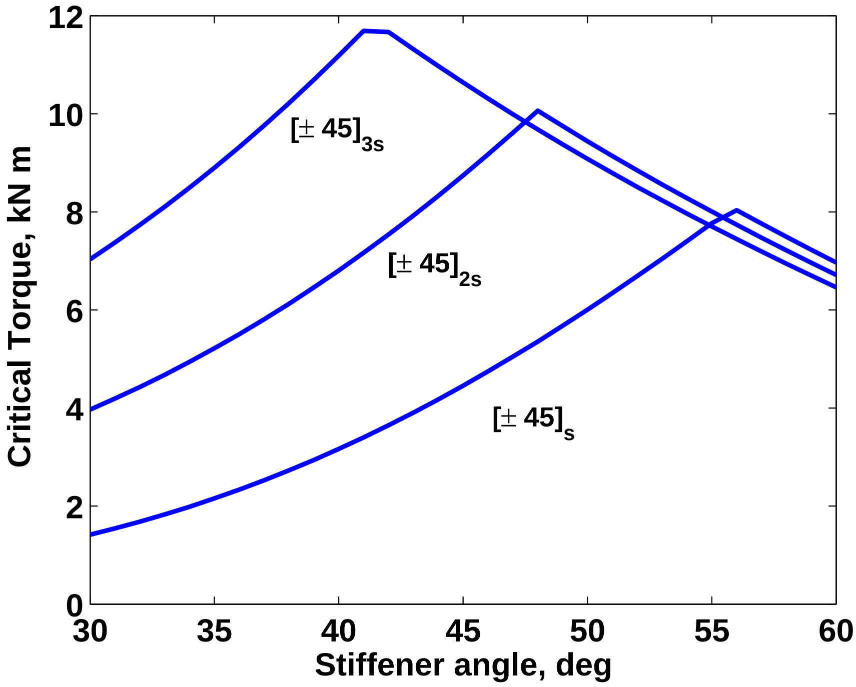

Figure 6.34. Buckling behavior of general-grid stiffened tubes under torque for different skin layup and thickness. Stiffener CS is 4×4 mm. $d_\theta = 25.4$ mm

essentially establish a boundary thereby increasing the buckling loads. Improvement in the buckling load by increasing the stiffener width is not as significant as increasing the stiffener depth.

6.2.2 Bending

As explained in Chapter 4, Sec. 4.1.2, stability of grid-stiffened tubes under bending loads are evaluated by compression buckling of a representative section in the compression region of the cylinder under transverse bending.

The subroutines developed in this study, based on well established analytical models, are validated against the results published by Wong and Weaver [76]. The comparison study is depicted in Table. 6.2. It can be observed from the data presented that the code developed in the present study gives accurate results.

Table 6.2. Critical compression buckling loads of various composite monocoque closed cross-section cylindrical shells [76]. Material ($T800-924$ prepreg) properties (GPa): $E_{11}=161$, $E_{22}=11.5$, $G_{12}=7.17$, $\nu_{12}=0.349$. Cylinder length, $L=150$ mm, mean radius, $R=80$ mm, Ply thickness, $t_{ply}=0.125$ mm

Shell laminate	Analy. [76] kN	FEM [76] kN	Analy. present kN
$[90,-45,0,45]_s$	156	156	158
$[90,-45,0,45]_{as}$	172	169	172
$[90,-45,-45,0]_s$	138	130	138
$[90,90,90,0]$	29	30	29
$[90,-45,45,45,0,-45,-45,45]$	158	156	160
$[90,-45,0,45,-45,90,45,0]$	196	194	196
$[90,-45,0,45,90,0,-45,45]$	190	186	189
$[90,-45,0,45,-45,0,-45,90]$	170	176	170
$[90,-45,0,45,0,0,90,-45]$	154	160	153

Another code validation that is directly applicable to the semi-circular cross-section shell model is provided in Table. 6.2.2. The results generated using the code are in excellent agreement with the published data by Januky et al. [37]. Additional verifications are performed (not reported) by analyzing the models and comparing to the data (shown in Fig. 6.37) given in Ref. [77] and observing excellent correlation.

To predict the behavior of grid-stiffened structures, the monocoque stiffness coefficients are replaced by that of the grid-stiffened structures derived using the newly developed analytical model. The critical axial compression buckling loads of isogrid stiffened cylinders provided by Reddy et al. [13] are compared against those predicted by the new model. The results are presented in Table. 6.4. The critical buckling loads are in excellent agreement for the structures shown. The mode shapes, represented by

Table 6.3. Critical compression buckling loads of various composite monocoque semi-circular cylindrical shell panels [37]. Material properties (Msi): $E_{11} = 13.75$, $E_{22} = 1.03$, $G_{12} = 0.42$, $\nu_{12} = 0.25$. Cylinder length, $L = 22$ in, mean radius, $R = 40$ in, Shell laminate: $[\pm 45, 0, 90, \pm 45]_s$

Shell wall thickness, t in	Analy. [37] lb/in	FEM [37] lb/in	Analy. present lb/in
0.072	391	375	368
0.144	1459	1481	1438
0.216	3288	3328	3235

axial wave, m and circumferential wave number, n , are different. Note that the smeared model employed in Ref. [13] is based on a flat unit cell. It is believed that the presence of compliance of stiffeners from coupled deflection modes captured in the new model is the source of the difference in the mode shapes identified via the wave numbers, m and n.

There is little variation in the buckling loads between the present and the cited results. This implies that the effect of curvature is not significant when the diameter of the cylinder is large (990 mm) with closely spaced stiffeners. This observation is consistent with the results from the parametric studies on the stiffness characteristics presented earlier.

Table 6.4. Validation study of critical compression global buckling loads of composite *isogrid* stiffened closed cylindrical shells [13]. AS4/3502 graphite/epoxy material system. Cylinder length, $L = 1168$ mm, diameter, $D = 990$ mm, Shell thickness 1.22 mm

Shell laminate	Ring stiff. #	Stiff. CS $h_s \times b_s$, mm	Mode (m, n) [13]; Present	$N_{xy_{cr}}$ [13] kN/m	$N_{xy_{cr}}$ Present kN/m	Error %
$[0, 90]_s$	50	4.44×1.53	(7, 10); (8, 12)	176	170	3
$[\pm 45]_s$	55	3.81×2.03	(15, 1); (18, 1)	181	172	6.6

Similar to the FEM torsional buckling exercise, bending buckling predictions under transverse bending of clamped-free tubes are conducted using FEM. Some example cases are presented in Fig. 6.35. It can be seen that grid-stiffened tubes exhibit local buckling modes under transverse bending. Not only the skin layup, but all the grid design variables contribute to this behavior. This makes it difficult to establish their interdependency on the buckling behavior. Figure 6.35a shows only axial waves which is entirely different from the other modes shown.

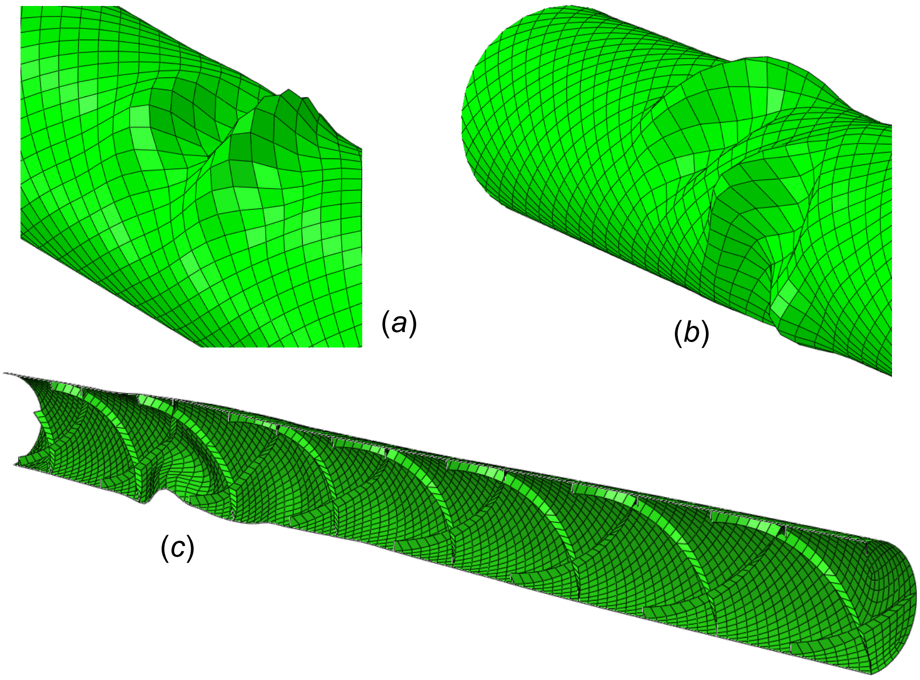

Figure 6.35. Bending buckling behavior of grid stiffened tubes with 45° stiffeners under transverse bending. (a) local buckling with only axial waves, (b) local buckling interaction of shell and stiffeners, and (c) lateral cross-section of BLS angle-grid model showing local buckling

An interesting observation is that several grid-stiffened unit cells could participate in local buckling which is evident from Figs. 6.35b and 6.35c. This aspect poses significant challenges in terms of isolating the shell between a set of stiffeners and prescribing simply supported or clamped boundary conditions . Even an assumption of elastic boundary conditions imposed by the stiffeners on the shell within a unit cell would not completely alleviate the challenge since multiple unit cells or shell bays could be involved as shown.

Thus, the whole semi-circular section in the compression region of the tube under transverse bending is isolated with simply supported boundaries to study the local buckling behavior under bending as explained in Chapter 4. For the grid-stiffened structure, the semi circular cylindrical section is represented by the smeared coefficients. The entire segment is evaluated as a single shell with simply supported boundary conditions.

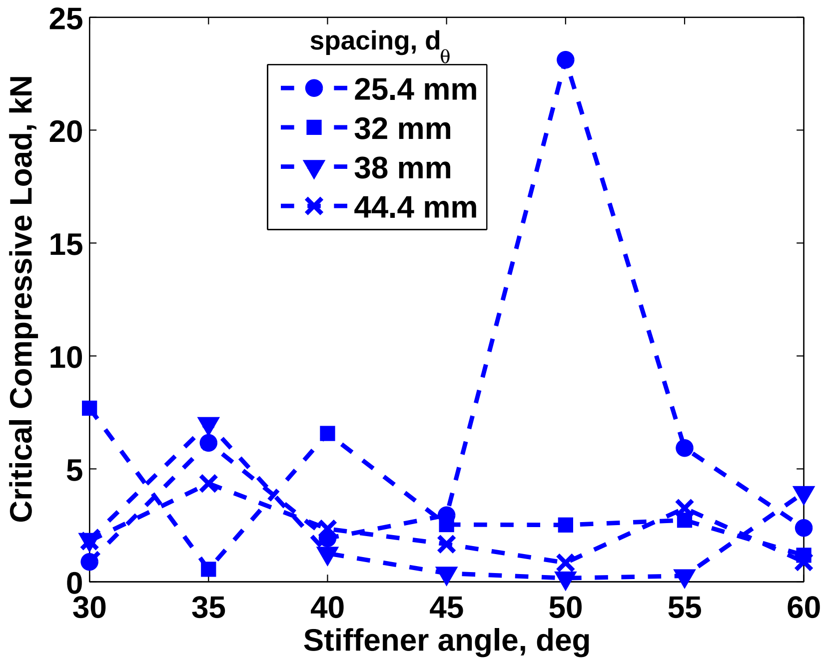

Figure 6.36. Critical buckling loads of general-grid stiffened semi-circular shells under compressive loads for different helical stiffener spacing, d_θ (mm). Shell $[\pm 45]_{2s}$, stiffener CS: 4×4 mm.

The axial length of the semi-circular length of the grid-stiffened shell is taken as $l_{xu} = \pi R_{ms}$. The buckling predictions performed for the grid-stiffened semi-circular shell segment for various stiffener angles and helical stiffener spacing are shown in Fig 6.36. The buckling load trend is not unusual even for a monocoque shell structure. Jaunky and Knight [77] evaluated the accuracy of various shell theories using numerical models and the plot from their publication is shown in Fig. 6.37. The observation from the present study that the buckling loads are high for lower stiffener angles is in agreement with that given in Fig. 6.37. Also, the similarity in the non-uniform variation with respect to the winding angle in both grid-stiffened and monocoque cases is noteworthy. The buckling loads do not generally follow a uniform trend which makes it difficult to apply intuition prior to the analysis. This is especially critical for the case of grid-stiffened cylindrical structures as the deviation has greater variability compared to the monocoque composite shells.

These drastic variation can be attributed to mode switching. It is likely that, a slight variation in input parameters could trigger a completely different mode. A detailed finite element model would be able to predict these modes, provided the critical modes are global in nature. However, quantitative assessments are not made since no such study is conducted. The best practical design could not be deduced from the results presented. Those designs that are less sensitive to slight variations in parameters could be extracted by a thorough search on various parameter range and discreteness.

It must be reiterated that the skin-stiffener interaction is not captured in the present model. Thus, if the geometric parameters are such that this interaction may become significant, an even higher degree of non-uniformity can be expected. The results presented demonstrate that, generalizing the stability behavior of grid-stiffened structures based on a given set of parameters is difficult. This makes the design study significantly more challenging when buckling constraints are imposed.

Additional justification of the foregoing discussion can be seen in Fig. 6.38, where the buckling loads are presented for various stiffener cross-section aspect ratios for a range of stiffener angles. It is generally possible to obtain high buckling loads by increasing the stiffener depth in radial direction. However, an increase in stiffener depth increases the coupling between extension and bending stiffness due to high eccentric-

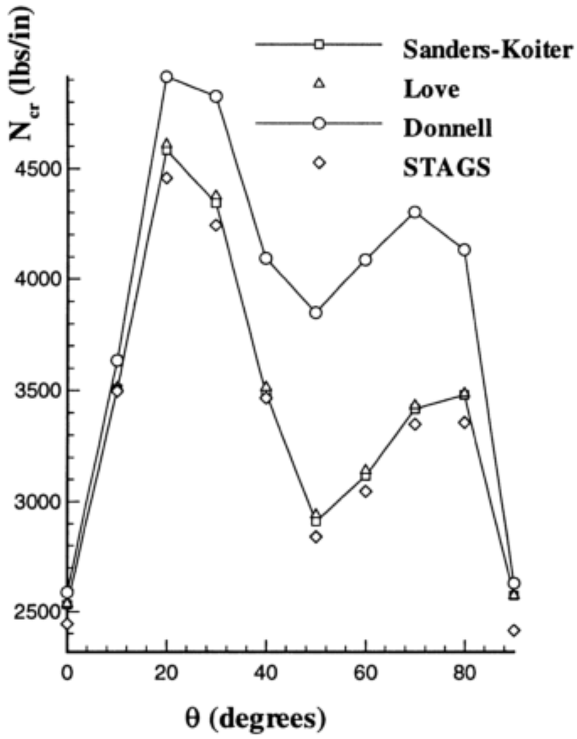

Figure 6.37. Critical axial compression buckling load predictions using various theories and numerical evaluation of semi-circular monocoque shells for different ply angles, θ. Shell laminate $[\pm\theta, \pm\theta, \theta]_s$ [77]

ity of stiffeners from the reference (shell mid-plane) surface. This coupling can affect the buckling loads adversely [64]. For the cases presented, it is seen that significant increase in buckling loads is obtained when the aspect ratio is between 1.5 and 2 when the stiffener angles are between 40 and 45°.

Figure 6.39 also shows significant variations in the buckling loads for different stiffener angles. The critical buckling loads when the stiffener cross-section, 6×4 and 8×4 are generally lower than 4×6 and 4×8 (see Fig. 6.38).

Based on the parametric studies conducted, it is observed that the stiffness and stability behavior of grid-stiffened structures are sensitive in a very broad range of design variables. A code is developed to connect various subroutines that determine stability,

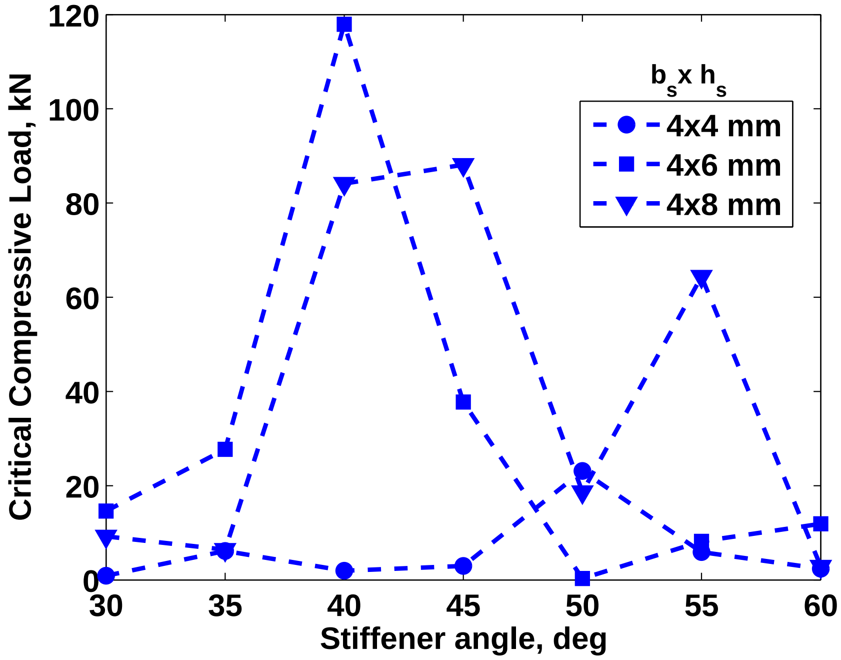

Figure 6.38. Critical buckling loads of general-grid stiffened semi-circular shells under compressive loads for different stiffener CS aspect ratios, ($ar_s = h_s/b_s \geq 1$). Shell $[\pm 45]_{2s}$, $d_\theta = 25.4$ mm, h_s measured in radial direction

strength, stiffness, and weight of both the baseline and grid-stiffened tubular designs. The design results and discussions are provided in subsequent sections.

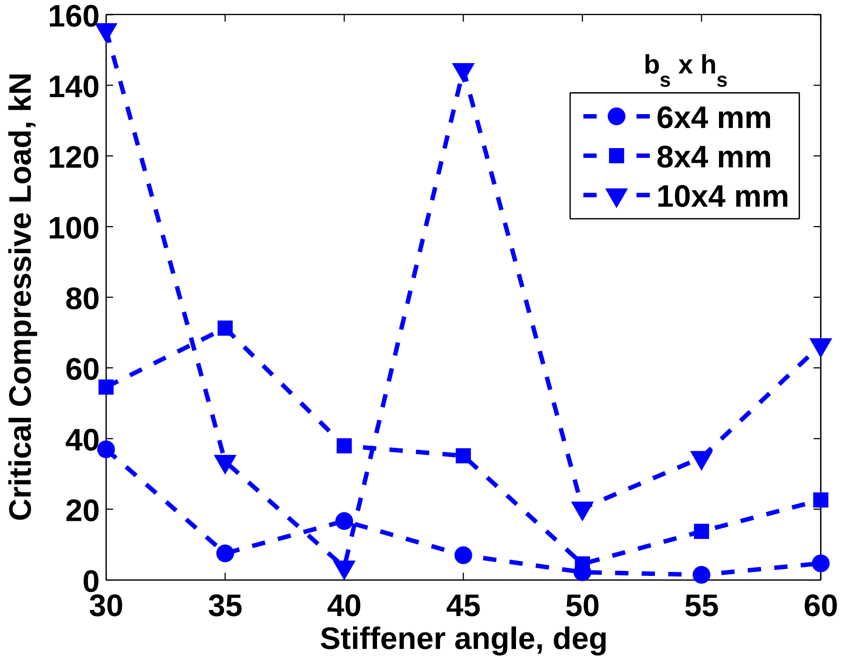

Figure 6.39. Critical buckling loads of general-grid stiffened semi-circular shells under compressive loads for different stiffener CS aspect ratios, ($ar_s = h_s/b_s < 1$). Shell $[\pm 45]_{2s}$, $d_\theta = 25.4$ mm, h_s measured in radial direction

6.3 Design study

The procedure described in Chapter 5 is implemented in the present design study. The material system used is IM7/8552 and the material properties are as given in Table 6.5.

The baseline monocoque model presented in Fig. 5.1 in Chapter 5, is analyzed to predict the failure loads in strength and stability. Various parameters of the monocoque baseline for calculating the design constraints are predicted and are provided in Table 6.6. Note that the weight of the baseline is not provided. This quantity changes since the geometry (axial and circumferential length) used to calculate the baseline weight is dependent on the grid-stiffened unit cell geometry. The unit cell geometry changes with respect to the design variables such as the stiffener spacing, d_θ and the stiffener angle, θ, which are variables in the design investigation.

Table 6.5. Material properties of IM7/8552 used for the design study [2]. Modulii units in GPa (column A) and msi (column B). Strength allowable units in GPa (column A) and ksi (column B). Ply thickness, $t_{ply} = 0.127$ mm (0.005 in)

Properties		A	B
Long. modulus	E_L	164.10	23.80
Trans. modulus	E_T	11.72	1.70
Shear. modulus	G_{LT}	5.20	0.75
Major Poisson's ratio	ν_{LT}	0.32	0.32
Strength allowables			
Long. tensile	σ_L^t	2.72	395
Long. compressive	σ_L^c	1.69	245
Trans. tensile	σ_T^t	0.11	16.10
Trans. compressive	σ_T^c	0.15	21.80
Shear	τ_{LT}^a	0.12	17.40

The parameters shown for the baseline in Table 6.6 are determined for the grid-stiffened structures as explained in Chapter 5. The range for each design variable is given earlier in Eqs. (5.6) to (5.9). An exploratory study is conducted to evaluate the impact of various parameters on various design constraints established. The shell laminate of the grid-stiffened structure is initially selected as $[\pm 45]_{2s}$ with the subscript s indicating symmetry. Initially the weight constraint, $\overline{W}$ is arbitrarily set to a maximum value of 0.750 in order to explore the designs. Since there are a large number of grid-

Table 6.6. Monocoque stiffness, strength, and stability predictions. $D_o = 165$ mm, ply thickness, $t_{ply} = 0.127$ mm, shell mid-plane radius, $R_m = 80.5$ mm

	Stiffness		Strength		Stability	
Laminate	EI_m $kN \cdot m^2$	GJ_m $kN \cdot m^2$	$(P_{max})_m$ kN	$(T_{max})_m$ $kN \cdot m$	$(P_{cr})_m$ kN	$(T_{cr})_m$ $kN \cdot m$
$[45, 0, 90, -45]_{4s}$	418	317	1120	53	3978	96

stiffened designs possible that are much lighter than the baseline, a lower limit for the weight ratio is also set as 0.730. Eleven designs that satisfy the weight constraint limits are generated with the design variable vector defined in Eq. (5.33) in Chapter 5, which are shown in Table 6.7.

Table 6.7. Different cylindrical general-grid stiffened designs generated with only weight constraint, $0.73 < \overline{W} < 0.75$. N_{a1} is the number of helical stiffeners in one direction. i indicates the design number for V_i (see Eq. (5.33).) Skin layup, $[\pm 45]_{2s}$. Data sorted with θ°

Design i	No. stiff. N_{a1}	Stiff. angle θ°	Stiff. width b_s, mm	Stiff. depth h_s, mm	Weight ratio $\overline{W}$
1	7	30	4	6.3	0.732
2	7	30	4	6.4	0.739
3	7	30	4	6.5	0.747
4	7	30	4.1	6.2	0.735
5	7	30	4.1	6.3	0.743
6	7	30	4.2	6	0.730
7	7	30	4.2	6.1	0.739
8	7	30	4.2	6.2	0.747
9	7	30	4.3	6	0.742
10	7	35	4	6	0.739
11	7	35	4	6.1	0.748

The constraints, stiffness, strength, and stability ratios, along with the ratios of buckling loads to strength values of the grid-stiffened designs are presented. The numbers labeled on the data points in the following plots represent cylindrical general-grid stiffened designs indicated as i, given in Table 6.7. Figure 6.40 shows the bending, $\overline{EI}$ and torsion, $\overline{GJ}$ ratios for the designs generated with the weight constraints as discussed. The ratios, being less than 1, show that the stiffness constraints are not satisfied invalidating the grid-stiffened designs. However, the behavior of bending and torsion stiffness is noteworthy. Considering that the stiffness values of the baseline is fixed, the bending and torsion stiffness of grid-stiffened behave in an inverse relation where the designs that provide high bending stiffness give low torsion stiffness. It is interesting to note that the combination, V_{11} (11^{th} design) that provides the highest $\overline{GJ}$ is 19% lower than the baseline. The same design exhibits a drop in bending stiffness ratio, $\overline{EI}$ of nearly 19% compared to the baseline.

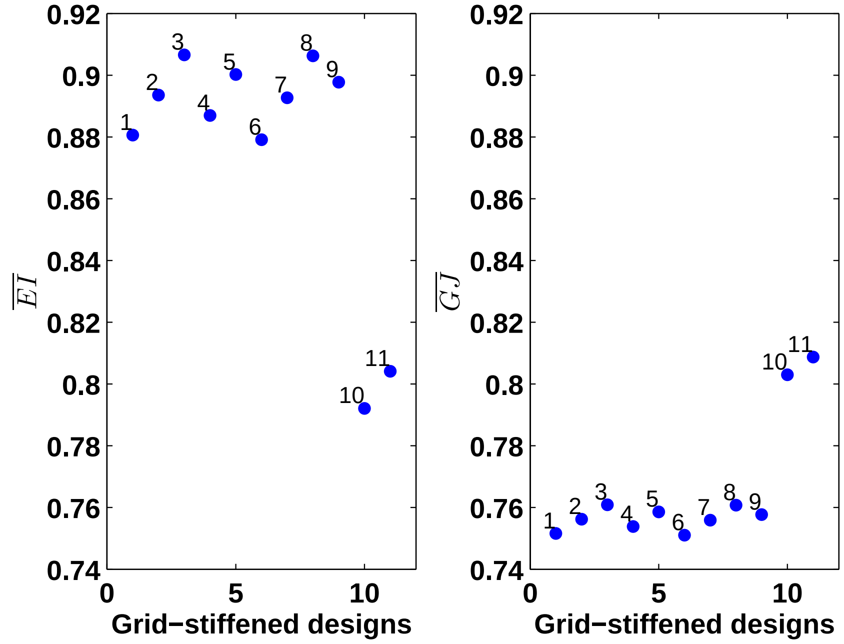

Figure 6.40. Stiffness ratios for different grid-stiffened designs when $0.73 < \overline{W} < 0.75$. Bending stiffness ratio, $\overline{EI}$. Torsion stiffness ratio, $\overline{GJ}$

Figure 6.41 presents the critical buckling load ratios. In general, all of the axial compression buckling ratios satisfy the design constraints. The design, V_6 shows a drop of only 2.5%. The critical torque constraints, all ratios being less than one, are violated. In the case of torsion buckling, nine of the variable sets exhibit nearly the same ratios. These values correspond to the stiffener angle of 30°. When the stiffener angle becomes 35° ($V_1 0$ and $V_1 1$), the drop in buckling loads are significant. This is the opposite of what is seen for $\overline{GJ}$ in Fig. 6.40. This inverse relation makes it challenging to design for both buckling and stiffness constraints in the case of torsion.

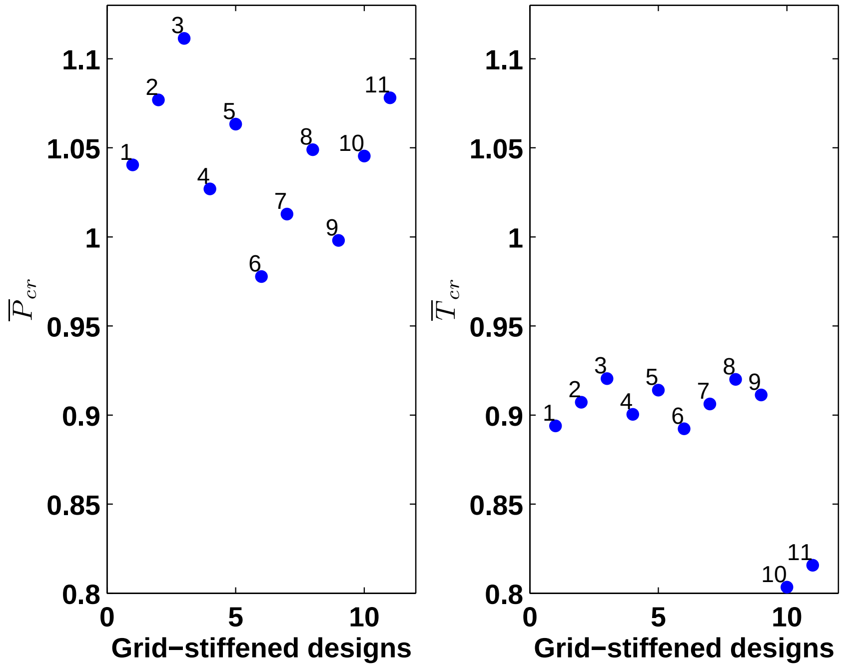

Figure 6.41. Critical buckling load ratios for different grid-stiffened designs when $0.73 < \overline{W} < 0.75$. Axial buckling ratio, $\overline{P}_{cr}$. Torsional buckling ratio, $\overline{T}_{cr}$

The strength ratios are presented in Fig. 6.42. $\overline{P}_{max}$ values, which relate the axial strength of grid-stiffened to baseline are all satisfied in the set of designs shown. The torsion buckling ratios, $\overline{T}_{max}$ on the other hand drop significantly. Similar behavior is shown earlier for the case of torsion stiffness ratio in Fig. 6.40 demonstrating a direct relation between torsion stiffness and laminate strength under torque.

The ratios of buckling loads to the strength values for the grid-stiffened structures are greater than 2 as depicted in Fig. 6.43. This behavior is observed in almost all the designs considered in this design study. Notice that, as in the case of torsion stiffness ratios, the torsion parameters in Fig. 6.43 show high sensitivity to a change (from 30° to 35°) in the helical stiffener angle.

From the different iterations performed without altering the shell laminate, it was found that, obtaining a weight saving of 25% is difficult within the range and discreteness specified for the design variables in V_i. The key controlling aspect in these designs are the stiffness constraints, specifically, $\overline{GJ}$. As a result, the study is repeated by increasing the shell thickness by setting the skin laminate to $[\pm 45]_{3s}$. To compensate for this added weight, the lower bound of the stiffener width, b_s is set to 3 mm. After performing some trials, it is determined that any feasible design solutions are only possible with relaxing the weight constraint, $\overline{W}$. Thus the upper bound of $\overline{W}$ is raised to 0.915. The number of designs obtained is 4 by prescribing a lower bound of $\overline{W} = 0.909$. Out of these four designs, the two sets of design variables that provide the highest weight savings are tabulated in Table 6.8.

The designs depicted have large values (> 2) for $\dfrac{(P_{cr})_{gs}}{(P_{max})_{gs}}$ and $\dfrac{(T_{cr})_{gs}}{(T_{max})_{gs}}$, the con-

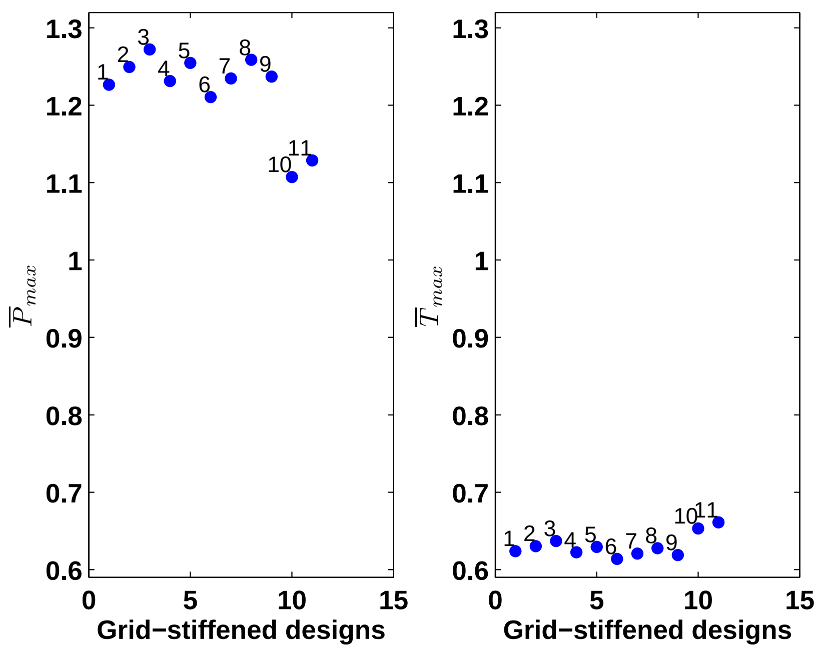

Figure 6.42. Strength failure ratios for different grid-stiffened designs with $0.73 < \overline{W} < 0.75$. Axial strength ratio, $\overline{P}_{max}$. Torsional strength ratio, $\overline{T}_{max}$

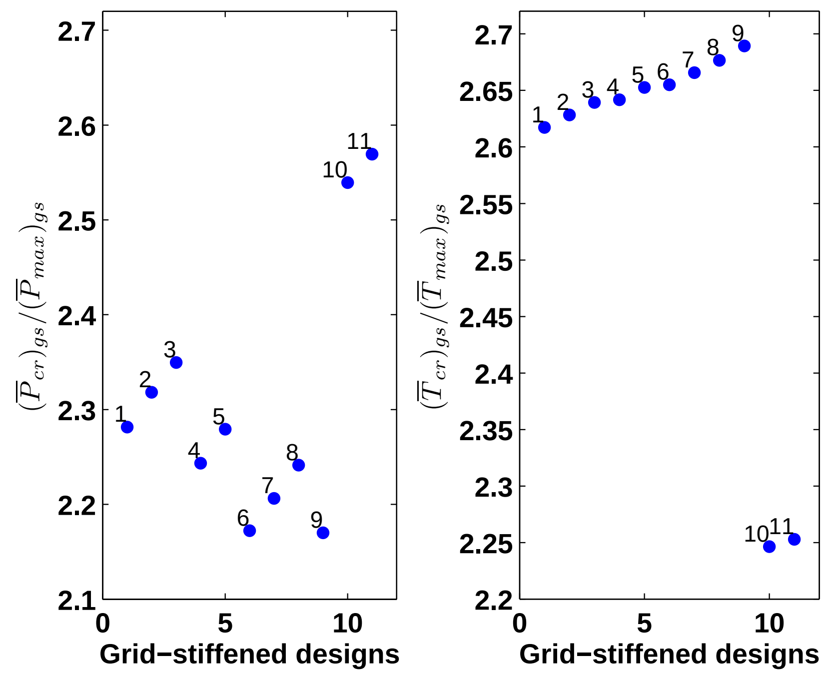

Figure 6.43. Critical buckling to failure load ratios for different cylindrical general-grid stiffened designs with $0.73 < \overline{W} < 0.75$

Table 6.8. Grid-stiffened design results. $D_o = 165$ mm, ply thickness, $t_{ply} = 0.127$ mm, shell mid-plane radius, $R_s = 81.8$ mm, b_s and h_s are in mm. Skin layup, $[\pm 45]_{3s}$

	Variables				Stiffness		Strength		Stability		Wt. Saving
Shell	N_{a1}	θ	b_s	h_s	$\overline{EI}$	$\overline{GJ}$	$\overline{P}_{max}$	$\overline{T}_{max}$	$\overline{P}_{cr}$	$\overline{T}_{cr}$	%
$[\pm 45]_{3s}$	7	30	3.0	9.1	1.01	1.00	1.35	1.29	1.75	1.02	9.1
$[\pm 45]_{3s}$	6	30	3.2	9.9	1.01	1.00	1.38	1.32	1.93	1.03	9.0

straints defined in Eq. (5.12).

Several attempts are made to obtain increased weight savings by replacing 45° plies with 0° or 90° ply angles while keeping number of plies identical to that of the laminates in Table 6.8. 0° plies generate high bending stiffness and buckling loads (both in torsion and axial compression). However, the torsion stiffness and failure torque ratios are adversely affected while failing to meet these constraints. 90° plies do not improve the weight performance either. In fact, in general, these designs perform even more poorly compared to the shell laminate with 0° plies. The ply angles other than 45°, 90°, and 0° are not considered for the shell laminate of the grid-stiffened designs. Additional trials conducted on the grid-stiffened designs indicate that the maximum weight saving within the specified ranges of the design variables, *without* relaxing any of the design constraints established is nearly 9%. All possible options in terms of the ranges and discreteness of the design variables are not evaluated.

The results presented show that there is potential for further investigation by conducting a thorough sweep of the design space using formal optimization routines. For example, an evolutionary algorithm would be capable of extracting higher weight savings than those reported in this study. The primary variable that could provide additional weight savings within the framework of the analytical models employed would be the stiffener angle, θ. A finer increment on the cross-section dimensions of the stiffeners could provide additional weight savings although such dimensions would be of no practical significance.

The analytical models employed for the present design study do not have the capability to predict any local buckling modes. Note that the minimum number of stiffeners in one direction around the circumference is set to 6 in the present design study. It is intentionally kept to this value so as to avoid generating designs that has a high likelihood of buckling locally.

Robust analytical tools which can accurately predict various local buckling modes (including different mode interactions) would facilitate a high fidelity search of the design space for increased weight savings from using grid-stiffened structures. At the very least, computationally efficient tools which can conduct a thorough evaluation of the design variables to set their limits such that certain instability modes can be avoided are required. The designs discussed here are of approximate nature considering the assumptions employed, especially for instability and strength predictions. It must be mentioned that the maximum weight saving achieved is within the range of accuracy of the analytical models employed.

It is known that the co-curing of the grid layer and the skin would provide sufficient strength for several aerospace applications [88]. However, in practical designs, several knockdown factors are imposed to consider the effect of structural imperfections arising from manufacturing limitations and errors. No such factors are used in the present design study while calculating the design constraints discussed.

Chapter 7

Conclusions and future work

An innovative structural concept to replace the conventional monocoque spar of the heavy-lift rotor blades with grid-stiffened composite shells was proposed. The present research is the first study to consider grid-stiffened shells for rotor blade spars with the objective to reduce blade weight with stiffness, strength, and stability constraints. Limitations in various state-of-the-art analytical models were identified in predicting the stiffness coefficients of close cross-section grid-stiffened structures with high length to diameter ratios. These analytical models are not capable of analytically capturing the exact geometry of the stiffeners in the grid-stiffened cylindrical structures.

A new analytical model was developed which can accurately capture the exact geometry of the helical stiffeners incorporating capability to capture the coupling between their deflection modes due to their complex geometry. The new model is capable of explicitly prescribing boundary condition for the stiffeners, which is novel. Validation studies of certain analytical predictions were performed using FEM and experiments. Several parametric studies were conducted to quantify the structural behavior of grid and grid-stiffened structures. A design study was conducted to determine the weight saving potential of general-grid stiffened structures compared to a baseline monocoque structure with stiffness, stability, and strength constraints.

Based on the studies conducted, the following conclusions can be drawn:

7.1 New analytical model

A methodology was successfully developed to derive the stiffness coefficients of grid structures from the stiffness matrices of the stiffeners modeled as beams. The validity of the procedure was established by comparing the planar grid model derivations with previously published and validated formulations. The analysis developed in the present study employed the equivalent stiffness (smeared approach) method to determine the stiffness characteristics of grid and grid-stiffened structures. The model is capable of analyzing a variety of stiffening configuration such as angle-grid, ortho-grid, isogrid, and general-grid. The procedure entails the direct use of stiffness matrices of the constituent structural members of the grid structure, which can be straight, curved, or helical beams. This methodology also facilitates the explicit definition of any boundary conditions at the stiffener ends, which is novel.

7.1.1 Stiffness evaluation

An FEM methodology was developed using a commercial, general purpose tool to model the overlapping sections of the stiffeners with reasonable accuracy. The results from this FEA and experiments match within 6%.

The stiffness coefficients of planar grid were derived using the new methodology developed and the analytical model is validated against various published results for different grid topologies. The in-plane shear stiffness of angle-grid structure was predicted using the present model and the results were demonstrated to be in excellent agreement (within 5%) with FEM results, thereby validating the model.

Cylindrical grid specimens were fabricated by wet filament winding technique and tested for deflections under axial, bending, and torsion loading to determine their stiffness behavior. The new model predicted all of these stiffness coefficients within 6% of experimental and FEM results. The existing state-of-the-art showed significant errors (39%) in predicting torsion stiffness. This is because the planar grid formulation does not capture the coupling between various deflection modes of the stiffeners due to their curved geometry. Several parametric studies were also conducted on cylindrical grids using the new formulation and demonstrated excellent correlation between FEM results. The maximum error, considering various stiffener angles, aspect ratios of the stiffener cross-section, was less than 10%. The new analysis demonstrated excellent accuracy in capturing various complex deflection modes of the stiffeners, especially, the helical and the circumferential ones.

It was shown that, the torsion and axial stiffness of the cylindrical grids were directly influenced by the stiffener width (circumferential direction.) Also demonstrated were the effects of cylinder diameter and stiffener spacing on torsion stiffness behavior of the grid structures. As the diameter of the cylinder was increased, for a constant stiffener spacing, the effect of curvature of the stiffeners on the cylindrical grids was diminished. The planar grid formulation exhibited an error of 60%, when the diameter is small compared to the stiffener spacing. From the models analyzed, with the maximum grid density and a 165 mm diameter, the differences between the planar and the new model was nearly 20%. As the thickness of the skin increased, the error reduced to 13% between the planar and cylindrical models.

The axial, bending, and torsion stiffness evaluation of cylindrical grid-stiffened structures were also performed. The effect of in-plane bending rigidity of the stiffeners on the in-plane shear stiffness could be significant and not to be neglected. However, when the structure had large diameter compared to the stiffener dimensions, planar based formulation gave minimal error of the order of 5-10%.

It was established using different validation studies that the newly developed model is robust and accurate for predicting the stiffness coefficients of cylindrical grid and grid-stiffened structures.

7.1.2 Stability evaluation

Well-established stability formulations were employed to predict the buckling loads of grid-stiffened models by integrating the newly developed analysis. The torsional buckling problem was conducted assuming that the structure is infinitely long where the effect of boundary conditions on the critical buckling loads can be neglected.

A set of complex buckling modes exhibited by finite length grid-stiffened tubes obtained using finite element models were presented. The global buckling mode was identified by visually comparing those of grid-stiffened cylinders to the critical buckling mode of a monocoque tube. The critical torsional buckling modes of grid-stiffened structures are observed to be sensitive to all the variables that define the structures, especially that of the grid layer.

It was shown that, for the models considered, the torsional buckling loads of the general-grid stiffened cylinders peak at 48° stiffener angle when the aspect ratio of the stiffener cross-section is 1. The critical buckling loads increased with increasing grid density. All other parameters being the same, for a given cross-section area of the stiffeners, a change in the stiffener cross-section aspect ratio can alter the buckling load significantly. This means that, different torsional instability responses (of the order of 60% for a particular set of parameters) can be obtained for a given structural weight.

Also, a parametric study on the effect of aspect ratio on the torsional buckling loads showed that the stiffener angles at which the critical buckling load peaks could be varied. From the general-grid stiffened models analyzed with a prescribed limit on the stiffener angles, the critical torsional buckling load was found to be maximum for a stiffener angle of 30°.

The effect of skin thickness on the torsional buckling load was also evaluated. This was conducted by varying the shell thickness and was demonstrated that an increase in skin thickness not only could increase the buckling load but also could shift the stiffener angle at which the critical buckling loads peak. An increase of up to 33% was obtained when the thickness of the skin is increased keeping all other parameters constant except the stiffener angle.

Existing stability formulation were employed and the new smeared analysis was integrated to this formulation to predict the critical compressive buckling loads of general-grid stiffened structures. A semi circular cylindrical section, representative of the compression region of a cylinder under transverse bending was selected as the model for this study. This strategy was adopted since state-of-the-art analytical models are not capable of accurately predicting the complex local buckling and mode interactions of a stiffened cylinder.

The general-grid stiffened cylindrical structures analyzed exhibited dramatic variations in their critical compression buckling loads with respect to a range of stiffener angles. Similar behavior was also observed in a parametric study using stiffener aspect ratio as the variable. It was observed that a generalized conclusion of the compression buckling behavior is not possible due to the high sensitivity of various parameters on the buckling loads. It is believed that the abrupt variations in these buckling loads are due to mode switching, even on slight variations in the parameters used.

7.2 Design study

A preliminary design study is performed on grid-stiffened shell cylindrical structures to determine their weight savings potential compared to a monocoque baseline. No formal optimization algorithm was employed. The objective was to identify general-grid stiffened designs (with an outer diameter of 165 mm) that satisfy certain constraints at the same time lighter than the monocoque designs.

The constraints are established as the ratios of various parameters of grid-stiffened to that of the baseline. These parameters are the strength (axial and shear), stiffness (bending and torsion) , and stability (bending induced axial compression and torsion).

The key design variables were identified as the number of one-direction stiffeners in the cross-section N_{a1}, stiffener angle, θ, and the cross-section dimensions h_s and b_s. Several combinations of these parameters are generated so that the weight of the grid-stiffened structure is less than that of the baseline. Those parameters that satisfied this constraint, were used to determine all the constraints.

Initially, several grid-stiffened structures that are 25% lighter than the baseline were evaluate to study the effect of the design variables on stiffness, strength, and stability constraints. It was found that none of the design would satisfy all the design constraints simultaneously.

Eventually the weight constraint was gradually relaxed to determine several sets of design variables that can satisfy all the design constraints. It was found that the maximum weight savings, compared to the baseline selected, is 9.1%.

Note that no formal search algorithms are used. A broader sweep of the design space with the analytical tools employed was not possible. The critical constraints that were difficult to satisfy are the torsion stiffness of the grid-stiffened structure.

7.3 Future directions

During the present study, many challenges were identified, based on which a set of recommended future works are enumerated.

- A significant advantage in the methodology presented to derive the equivalent stiffness coefficients of grid and grid-stiffened structures is that the degrees of freedom of the stiffener joints can be manipulated efficiently. Analytical formulations were presented for various stiffener boundary conditions such as simply supported, clamped, and elastic. However, this study did not evaluate the relative merits of employing any of these boundary conditions in predicting the structural responses of grid and grid-stiffened structures. Also, the present research did not examine the validity domain of a particular stiffener boundary condition where the geometric and/or material parameters can be variables. It is recommended to address these voids by conducting appropriate parametric and validation studies. For example, elastic verses clamped boundary conditions when the stiffener height or width or both are changed. Notice that, depending on the degrees of freedom provided for the stiffener nodes (joints), appropriate plate or shell theory must be selected.
- Stiffened structures are primarily used in large structures to save weight. The advantages of these type structures are in buckling critical applications. It is required to evaluate the benefits of grid-stiffened structures by considering structures that

are larger than the ones presented. Specifically, quantify the size of the structure at which these designs become significantly efficient in reducing weight while satisfying several design constraints.

- Fabrication of grid-stiffened structures is a non-trivial task. Considering the advancements in fabrication techniques currently available, it is recommended to use the necessary tooling to fabricate different grid and grid-stiffened specimens for experimental studies.

- A rigorous experimental evaluation is required to obtain accurate insight into the deflection behavior of stiffeners in grid and grid-stiffened cylindrical structures. Also, explore their strength characteristics under bending, torsion, and axial loading conditions typically experience by a helicopter rotor blade. An empirical solution methodology to predict the strains at various locations of grid-stiffened structures would be beneficial for design studies. Also, studies on skin–stiffener debonding and intralaminar failure within the unidirectional grid must be conducted.

- Predicting the stability behavior of grid-stiffened structures is challenging. This is due to the complex critical buckling modes exhibited by these structures. The critical mode could be local (skin buckling), local–global interaction (skin or stiffener buckling along with the whole structure exhibiting global mode), local–local interaction (skin and stiffener buckle in combination.) Presently, computationally efficient analytical tools that can accurately predict these phenomena are not available. It is recommended to develop computationally efficient analytical models that can predict the buckling mode interactions under different loading scenarios. Possible mode switching behavior must be investigated for grid-stiffened structures buckling under compressive loads. Torsional buckling load estimation of grid-stiffened tubes of finite length should be added to the design matrix.

- It is recommended to employ formal optimization tools to thoroughly search the design space in order to identify potential weight savings of grid-stiffened structures for heavy-lift rotor blade spars.

- The practical significance in fabricating blade-like stiffeners were not considered while deriving the analyses. It was assumed that the stiffeners are rigidly connected to the shell structure. The stiffeners, considered to be made from uniaxial fiber reinforced composites, there is a practical limit of the stiffener height (radial direction) dimensions that can be achieved after which the stiffeners would not provide sufficient strength. This dimension can be ascertained by the careful study of the strain levels in the stiffeners. The failure checks must be performed relaxing the assumption used in the present study that the stiffeners only resist axial strains.

- It would be interesting to quantify the relative performances of the skin and the grid layer of grid-stiffened structures. Specifically, stiffness and strength. Compare the torsion and bending stiffness contribution as well as the maximum failure load obtained. This would assist further design study where these components may be independently optimized for the best performance.

- The effect of elastic boundary conditions at the stiffener joints should be studied in more detail. Experimental studies would provide insight into the behavior of the stiffener joints.

- It is recommended to evaluate the feasibility of providing the entire blade cross-section , not only the spar, with grid-stiffened design. The model developed in the present investigation can be extended to an elliptical cross-section, resulting in a useful tool for stiffness, and global stability predictions. It is expected to be a non-trivial task since the solutions for elliptical cross-section may not be closed-form. Numerical methods could be employed to determine equivalent stiffness characteristics, while not significantly sacrificing the analysis' computational efficiency.

- The local stability characteristics of grid-stiffened structures were not conducted for tensile loading. Although not studied, it is likely that a thin shell between the stiffeners could buckle due to lateral compressive loads. For example, an angle-grid stiffened panel under tension may buckle the skin between the stiffeners locally, when the stiffeners form elongated rhombic profiles.

- Combined load cases were not considered in the present study. It is recommended to evaluate the stability characteristics of grid-stiffened structures under combined bending, axial tension, and torsion loads

- Domain other than helicopter rotor blades, such a large wind turbine, blade should be explored. It is anticipated that, much higher weight savings could be obtained for such large structures. Note that very specialized analytical models that can predict the local buckling loads accurately are necessary to investigate this domain.

Appendix A

A.1 Polar Moment of Inertia

Reference [40] provides the expressions to determine the polar moment of inertia of a rectangular cross-section as:

$$J = \beta\, a\, b \tag{A.1}$$

where a and b are the width and depth of the cross-section. The parameter β is given by the expression in Eq. (A.2).

$$\beta\left(\frac{a}{b}\right) = \frac{256}{\pi^6} \sum_{m=1}^{\infty} \sum_{n=1}^{\infty} \frac{1}{m^2 n^2 \left[m^2 (b/a)^2 + n^2\right]} \tag{A.2}$$

where m and n are odd integers.

A.2 Shear correction factor

In determining the variation of transverse shear stress through a composite beam cross–section, the discrepancy between the actual state and the constant stress state predicted by the first–order shear deformation theory is often corrected in computing the transverse shear force resultants, (Q_x, Q_y) by multiplying with a parameter, α_{sc} called the shear correction coefficient [89]. Thus,

$$\begin{Bmatrix} Q_x \\ Q_y \end{Bmatrix} = \alpha_{sc} \int_{-\frac{h}{2}}^{\frac{h}{2}} \begin{Bmatrix} \sigma_{xz} \\ \sigma_{yz} \end{Bmatrix} dz \tag{A.3}$$

The shear correction coefficient, α_{sc} is determined such that the strain energy due to the transverse shear stresses in the above equation equals the strain energy due to the transverse stresses predicted by the three–dimensional elasticity theory. For a homogeneous beam with rectangular cross–section with width, b and height, h, the actual shear distribution through the thickness of the beam is determined using,

$$\sigma_{xz}^{c} = \frac{3Q}{2bh}\left[1 - \left(\frac{2z}{h}\right)^2\right], -\frac{h}{2} \leq z \leq \frac{h}{2} \tag{A.4}$$

where Q is the transverse shear force. The transverse shear stress in the first–order theory is constant, $\sigma_{xz}^{f} = Q/bh$. The strain energies due to the transverse shear stresses in the two theories are:

$$U_s^c = \frac{1}{2G_{13}} \int_A (\sigma_{xz}^c)^2 \, dA = \frac{3Q^2}{5G_{13}bh} \tag{A.5}$$

$$U_s^f = \frac{1}{2G_{13}} \int_A (\sigma_{xz}^f)^2 \, dA = \frac{Q^2}{2G_{13}bh} \tag{A.6}$$

Shear correction factor is the ratio of U_s^f to U_s^c which gives $\alpha_{sc} = 5/6$. The value of α_{sc} for a general laminate depends on lamina properties and lamination scheme. This value is applicable to the uniaxial fiber reinforced composite beams, such as the case used in this investigation [20].

A.3 Cartesian to Frenet frame

The Frenet frame is represented in vector form as $\vec{r}(\hat{t}, \hat{n}, \hat{b})$. Position vector of a point in a helix in the Cartesian coordinate system:

$$\vec{r} = R\cos\psi\,\hat{e}_i + R\sin\psi\,\hat{e}_j + h\psi\,\hat{e}_k \tag{A.7}$$

$$\hat{t} = \frac{d\vec{r}}{ds} \tag{A.8}$$

$$\hat{n} = \frac{\hat{t}}{||\hat{t}||} \tag{A.9}$$

$$\hat{b} = \hat{t} \times \hat{n} \tag{A.10}$$

where $ds = c\,d\psi$ for a helix where $c = \sqrt{R^2 + h^2}$ and $2\pi h$ is the pitch. R is the cylindrical radius. The transformation matrix is to convert from $\{t, n, b\}$ to the Cartesian coordinate system is given by [50],

$$T_{ijk} = \begin{bmatrix} -(R/c)\sin\psi & (R/c)\cos\psi & (h/c) \\ -\cos\psi & -\sin\psi & 0 \\ (h/c)\sin\psi & -(h/c)cos\psi & (R/c) \end{bmatrix} \tag{A.11}$$

Appendix B

B.1 Beam in 3D space

The stiffness matrix of a beam in space in the local coordinate system is given by

$$
k_{3D} = \begin{bmatrix}
\frac{EA}{l} & & & & & & & & & & & \\
0 & \frac{12EI_z}{l^3(1+\overline{\alpha}_y)} & & & & & & & & & & \\
0 & 0 & \frac{12EI_y}{l^3(1+\overline{\alpha}_z)} & & & & & & & & & \\
0 & 0 & 0 & \frac{GJ}{l} & & & & & & & & \\
0 & 0 & \frac{-6EI_y}{l^2(1+\overline{\alpha}_z)} & 0 & \frac{(4+\overline{\alpha}_z)EI_y}{l(1+\overline{\alpha}_z)} & & & & \text{sym.} & & & \\
0 & \frac{6EI_z}{l^2} & 0 & 0 & 0 & \frac{(4+\overline{\alpha}_y)EI_z}{l} & & & & & & \\
\frac{-EA}{l} & 0 & 0 & 0 & 0 & 0 & \frac{EA}{l} & & & & & \\
0 & \frac{-12EI_z}{l^3(1+\overline{\alpha}_y)} & 0 & 0 & 0 & \frac{-6EI_z}{l^2(1+\overline{\alpha}_y)} & 0 & \frac{12EI_z}{l^3(1+\overline{\alpha}_y)} & & & & \\
0 & 0 & \frac{-12EI_y}{l^3(1+\overline{\alpha}_z)} & 0 & \frac{6EI_y}{l^2(1+\overline{\alpha}_z)} & 0 & 0 & 0 & \frac{12EI_y}{l^3(1+\overline{\alpha}_z)} & & & \\
0 & 0 & 0 & \frac{-GJ}{l} & 0 & 0 & 0 & 0 & 0 & \frac{GJ}{l} & & \\
0 & 0 & \frac{-6EI_y}{l^2(1+\overline{\alpha}_z)} & 0 & \frac{(2-\overline{\alpha}_z)EI_y}{l(1+\overline{\alpha}_z)} & 0 & 0 & 0 & \frac{6EI_y}{l^2(1+\overline{\alpha}_z)} & 0 & \frac{(4+\overline{\alpha}_z)EI_y}{l(1+\overline{\alpha}_z)} & \\
0 & \frac{6EI_z}{l^2(1+\overline{\alpha}_y)} & 0 & 0 & 0 & \frac{(2-\overline{\alpha}_y)EI_z}{l(1+\overline{\alpha}_y)} & 0 & \frac{-6EI_z}{l^2(1+\overline{\alpha}_y)} & 0 & 0 & 0 & \frac{(4+\overline{\alpha}_y)EI_z}{l(1+\overline{\alpha}_y)}
\end{bmatrix} \tag{B.1}
$$

B.2 Grids with elastic supports for stiffeners

Ideally, a node provides neither a perfectly clamped nor a perfectly pinned boundary condition for the stiffeners. It is identified to be somewhere between the two [20]. A flexibility condition can be imposed at the nodes analytically by considering the compliance of the laminate structure at the overlapping section. The nodal laminate and in turn its stiffness properties depend on the manufacturing technique employed. For example, the stacking sequence depends on the grid winding process and the elastic constants of the lamina. A schematic of a grid fabrication using an automated filament winding technique is depicted in Fig. 2.9.

To simplify the analysis, it is assumed that the node has a square profile. As a direct consequence of having large number of plies (depending on the stiffener depth) in the nodal laminate, the coefficients, B_{ij} are relatively small. The flexibility provided by the nodes can be directly incorporated into the boundaries of the stiffeners as elastic supports. The in-plane shear stiffness of the laminate at the nodes can be captured by introducing torsion springs at the supports. The stiffeners are isolated as explained earlier in Sec. 3.2.1.3 and the loading and boundary conditions are provided in Figs. B.1. The shear stiffness coefficients are determined from the deflections and geometry. Eq. (3.25) gives the spring stiffness matrix. The stiffness matrix of the assembly is derived following the methodology used in Ref. [43].

There are three degrees of freedom for an isolated beam depicting a stiffener such as the one in Fig. B.1(b); rotations $\omega_{x=0,L_0}$ at the support and transverse deflection δ_y. Note that the joint flexibility is associated with the rotations ω_0 and ω_{L_0} at the nodes. The expressions for the displacements of the beam in Fig. B.1(b) in which the spring constants at the beam ends are not identical are provided in Eqs. (B.2) to (B.4). Consider

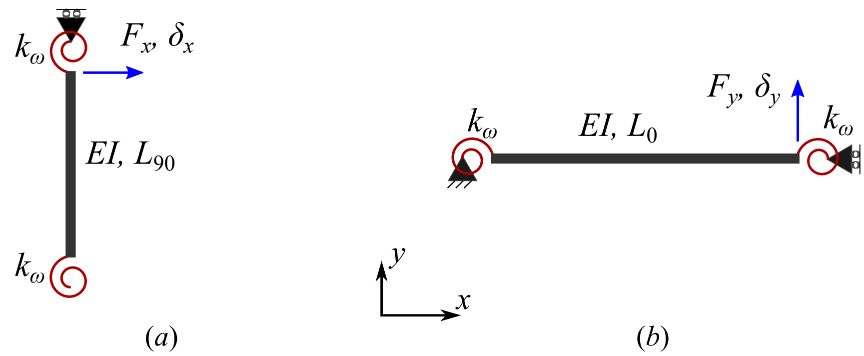

Figure B.1. Longitudinal and transverse stiffener loading and BCs

the spring constants at $x = 0$ and $x = L_0$ be k_{ω_0} and k_{ω_l} respectively. Then,

$$\omega_0 = \frac{F_y L_0^2}{\overline{L_0}} \left[\frac{1}{2k_{\omega_0}} + \left(\frac{EI}{L_0}\right) \frac{1}{k_{\omega_0} k_{\omega_l}} \right] \tag{B.2}$$

$$\delta_L = \frac{F_y L_0^3}{\overline{L_0}} \left[\frac{L_0}{12EI} + \frac{1}{3L_0}\left(\frac{1}{k_{\omega_0}} + \frac{1}{k_{\omega_l}}\right) + \left(\frac{EI}{L_0}\right) \frac{1}{k_{\omega_0} k_{\omega_l}} \right] \tag{B.3}$$

$$\omega_l = \frac{F_y L_0^2}{\overline{L_0}} \left[\frac{1}{2k_{\omega_l}} + \left(\frac{EI}{L_0}\right) \frac{1}{k_{\omega_0} k_{\omega_l}} \right] \tag{B.4}$$

$$\overline{L_0} = L_0 + EI\left(\frac{1}{k_{\omega_0}} + \frac{1}{k_{\omega_l}}\right) \tag{B.5}$$

When the end springs are identical with rigidity $k_{\omega_0} = k_{\omega_l} \equiv k_\omega$, then the displacement vector is given by Eq. (B.6). As the spring stiffness $k_\omega \to \infty$, the nodal rotations vanish and the displacement vector for the beam in Fig. B.1(b) given in Eq. (B.6) reduces to that of beams with clamped boundary conditions as shown in Eq. (B.7).

$$\begin{Bmatrix} \omega_0 \\ \\ \delta_L \\ \\ \omega_{L_0} \end{Bmatrix} = \begin{bmatrix} \dfrac{F_y L_0}{2k_\omega} \\ \dfrac{F_y {L_0}^3}{12EI} + \dfrac{F_y {L_0}^2}{2k_\omega} \\ \dfrac{F_y L_0}{2k_\omega} \end{bmatrix} \tag{B.6}$$

$$\begin{Bmatrix} \omega_0 \\ \\ \delta_L \\ \\ \omega_{L_0} \end{Bmatrix}_{k_\omega \to \infty} = \begin{bmatrix} 0 \\ \\ \dfrac{F_y {L_0}^3}{12EI} \\ \\ 0 \end{bmatrix} \tag{B.7}$$

Identical results can be obtained by solving the differential equation of an Euler beam with appropriate boundary conditions. For the structure shown in Fig. B.1(b), the boundary conditions are provided in Eq. (B.8) and the beam bending differential equation is given in Eq. (B.9). The slope and deflection solutions are provided in Eq. (B.10) and Eq. (B.11) respectively.

$$EI\,w''(x) = \begin{cases} +k_{\omega_0}\, w'(x), & \text{at } x = 0 \\ \\ -k_{\omega_l}\, w'(x), & \text{at } x = L_0 \end{cases} \tag{B.8}$$

$$EI\,w'''(x) = -F_y \tag{B.9}$$

$$EI\,w'(x) = -F_y\left(\frac{x^2}{2}\right) + C_1 x \tag{B.10}$$

$$EI\,w(x) = -F_y\left(\frac{x^3}{6}\right) + C_1\left(\frac{x^2}{2}\right) + C_2 x \tag{B.11}$$

and the constants C_1 and C_2 from the integration are provided in Eqs. (B.12).

$$C_1 = F_y L_0 \left[\frac{\dfrac{1}{k_{\omega_l}} + \dfrac{L_0}{2EI}}{\dfrac{L_0}{EI} + \left(\dfrac{1}{k_{\omega_0}} + \dfrac{1}{k_{\omega_l}} \right)} \right]$$
$$C_2 = C_1 \left(\frac{EI}{k_{\omega_0}} \right) \tag{B.12}$$

As for the case of the vertical beam in Fig. B.1(a), the displacements can be obtained by replacing the length L_0 with L_{90}, the external load F_y with F_x, and the coordinate x with y. The effect of elastic BCs is evaluated and compared with FEM models with overlap node designs as explained in Section. 2.2.1. Complexity arises in the elastic BC case since the value for the torsion spring constant is not readily obtained. A study on the effect of elastic stiffener BCs in a planar angle-grid configuration is presented. The stiffener orientation for the problem presented is 45° and the variation of shear stiffness of the angle-grid structure is plotted against different spring constants. The geometry and material properties are identical to that of the S8 specimen (see Table 2.1.) The shear stiffness of the overlap section is also noted along with the shear stiffness of the angle-grid with clamped BC case in Fig. B.2.

It is evident from Fig B.2 that the torsion spring constants determined from the overlap region in-plane stiffness do not have any significant effect on the shear stiffness of the grids analyzed. Only a maximum of 2% difference is observed between the in-plane shear stiffness determined using clamped and elastic stiffener BCs. This implies that the stiffeners are essentially clamped at their joints for the models analyzed.

Parametric studies are not performed to investigate the effect of different stiffener aspect ratios and attached skin. It is likely that the results could show a different trend. It is anticipated that there could be other sources of compliance at the stiffener joints apart

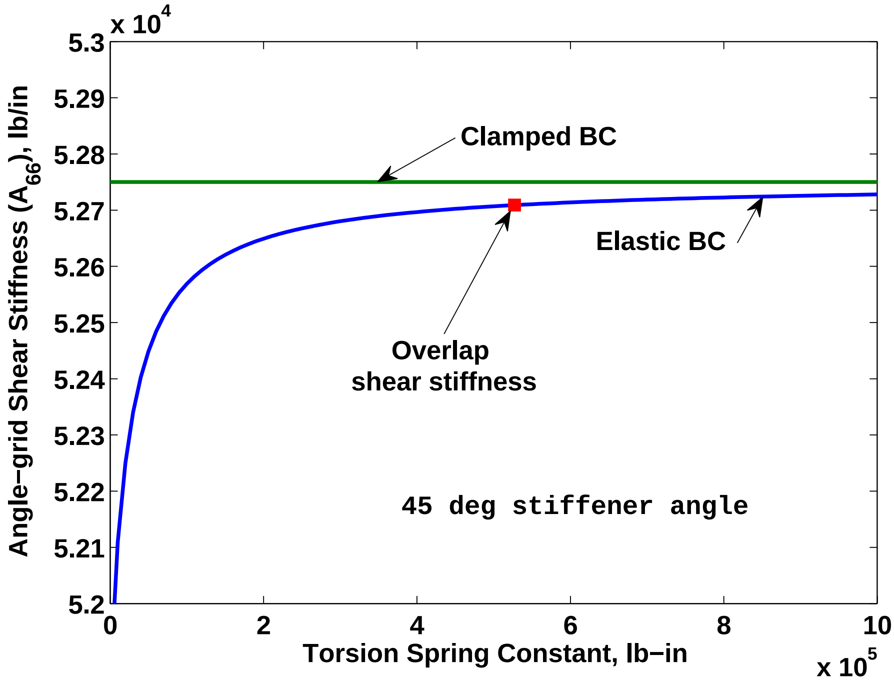

Figure B.2. Variation of shear stiffness of 45° angle-grid with different spring constant values for the elastic supports. Shear stiffness for the clamped BC case is also shown

from just the in-plane torsion of the overlap regions. Note that the results presented are not of a general nature and so are not conclusive. Further investigation is necessary to determine the effect of elastic boundary conditions at the stiffener joints in the overall behavior of grid and grid-stiffened structures.

B.3 Transfer to stiffness matrix

The stiffness matrix is obtained by reordering the TM after expanding Eq. (3.123) using Eqs. (3.125) to (3.127).

$$\boldsymbol{Q}(\psi)_{[12\times 12]} = \begin{bmatrix} \boldsymbol{Q}_{11} & \boldsymbol{Q}_{12} & 0 & 0 \\ \boldsymbol{Q}_{21} & \boldsymbol{Q}_{22} & 0 & 0 \\ \boldsymbol{Q}_{31} & \boldsymbol{Q}_{32} & \boldsymbol{Q}_{33} & 0 \\ \boldsymbol{Q}_{41} & \boldsymbol{Q}_{42} & \boldsymbol{Q}_{43} & \boldsymbol{Q}_{44} \end{bmatrix} \tag{B.13}$$

Rearranging the sub-matrices to separate forces and displacements by,

$$\begin{bmatrix} \boldsymbol{Q}_{11} & \boldsymbol{Q}_{12} & \boldsymbol{I} & 0 \\ \boldsymbol{Q}_{21} & \boldsymbol{Q}_{22} & 0 & \boldsymbol{I} \\ \boldsymbol{Q}_{31} & \boldsymbol{Q}_{32} & 0 & 0 \\ \boldsymbol{Q}_{41} & \boldsymbol{Q}_{42} & 0 & 0 \end{bmatrix} \begin{bmatrix} -\boldsymbol{V}_0 \\ -\boldsymbol{M}_0 \\ \boldsymbol{V}_\psi \\ \boldsymbol{M}_\psi \end{bmatrix} = \begin{bmatrix} 0 & 0 & 0 & 0 \\ 0 & 0 & 0 & 0 \\ 0 & \boldsymbol{Q}_{33} & 0 & -\boldsymbol{I} \\ \boldsymbol{Q}_{44} & \boldsymbol{Q}_{43} & -\boldsymbol{I} & 0 \end{bmatrix} \begin{bmatrix} \boldsymbol{\Delta}_0 \\ \boldsymbol{\Phi}_0 \\ \boldsymbol{\Delta}_\psi \\ \boldsymbol{\Phi}_\psi \end{bmatrix} \tag{B.14}$$

The stiffness matrix is then given by,

$$\boldsymbol{K}(\psi)_{[12\times 12]} = \begin{bmatrix} \boldsymbol{Q}_{11} & \boldsymbol{Q}_{12} & \boldsymbol{I} & 0 \\ \boldsymbol{Q}_{21} & \boldsymbol{Q}_{22} & 0 & \boldsymbol{I} \\ \boldsymbol{Q}_{31} & \boldsymbol{Q}_{32} & 0 & 0 \\ \boldsymbol{Q}_{41} & \boldsymbol{Q}_{42} & 0 & 0 \end{bmatrix}^{-1} \begin{bmatrix} 0 & 0 & 0 & 0 \\ 0 & 0 & 0 & 0 \\ 0 & \boldsymbol{Q}_{33} & 0 & -\boldsymbol{I} \\ \boldsymbol{Q}_{44} & \boldsymbol{Q}_{43} & -\boldsymbol{I} & 0 \end{bmatrix} \tag{B.15}$$

where $\boldsymbol{I}$ and $\boldsymbol{0}$ are the 3×3 identity and null matrices respectively.

Appendix C

C.1 Heavy lift blade properties

Table C.1. Blade cross-section stiffness [2]

Loc.	r/R_b	0.25	0.5	0.75	1
Chord	c	3.43	3.25	3.07	2.89
Thick. ratio	t/c	0.2	0.18	0.12	0.08
Flap bend	EI_b^f	1.87×10^7	8.07×10^6	1.98×10^6	3.96×10^5
Lag bend	EI_b^l	1.51×10^8	9.75×10^7	6.62×10^7	3.40×10^7
Torsion	GJ_b	2.34×10^7	1.65×10^7	5.52×10^6	1.98×10^6
Axial	EA_b	3.24×10^8	1.79×10^8	1.18×10^8	6.93×10^7

Table C.2. D-spar laminate stacking sequence at various blade locations. Spar width at 40% chord [2]

Rad. loc. r/R_b	D-spar laminate	No. plies	Spar width, w	Thick. ratio, t/c	Spar depth, d
0.25	$[\pm 45_{33}, 0_{60}, \pm 45_2]$	130	16.46	0.20	8.23
0.50	$[\pm 45_{33}, 0_{30}, \pm 45_2]$	100	15.60	0.18	7.02
0.75	$[\pm 45_{28}, 0_{20}, \pm 45_2]$	80	14.74	0.12	4.42
1.00	$[\pm 45_{28}, 0_{10}, \pm 45_2]$	70	13.87	0.08	2.77

Table C.3. Monocoque blade cross-section design loads [2]

Section	Flap BM, ft-lb	Lag BM, ft-lb	Torsion, ft-lb	Axial force, lb
0.25 R_b	85,000	70,000	-7500	92,000
0.50 R_b	38,000	40,000	-5000	71,000
0.75 R_b	22,000	11,500	2000	44,000
1.0 R_b	6400	3700	1000	30,000

References

[1] W. Johnson, G. K. Yamauchi, and M. E. Watts. NASA heavy lift rotorcraft systems investigation. *NASA TP*, 213467, 2005.

[2] J. Zhang and E. C. Smith. Design methodology and cost analysis of composite blades for a low weight rotor. *AHS Vertical Lift Aircraft Design Conference*, San Francisco, California., Jan 2005.

[3] M. C. Y. Niu. *Airframe Structural Design*. Conmilit Press Ltd., 1988.

[4] Image of the British Vickers Wellington bomber. (accessed: 4/15/2012). `http://www.flightglobal.com`.

[5] Image of the Airbus A380 fuselage rib–stringer construction. (accessed: 12/20/2011). `http://www.diplomatie.gouv.fr`.

[6] R. R. Meyer, O. P. Harwood, M. B. Harmon, and J. I. Orlando. Isogrid design handbook. *MDC G4295, McDonnell Douglas Astronautics, Huntington Beach, CA*, 1972.

[7] S. Harding. *US Army Aircraft Since 1947: An Illustrated Reference*. Schiffer Publishing Ltd., Atglen, PA, 1997.

[8] A. Pelletier. *Bell Aircraft Since 1935*. Naval Institute Press., Annapolis, MD, 1992.

[9] S. M. Huybrechts and T. E. Meink. Advanced grid stiffened structures for the next generation of launch vehicles. *IEEE Aerospace Conference*, Aspen, CO., 1997.

[10] V. V. Vasiliev, V. A. Barynin, and A. F. Rasin. Anisogrid lattice structures—survey of development and application. *Composite structures*, 54(2-3):361–370, 2001.

[11] V. V. Vasiliev and A. F. Razin. Anisogrid composite lattice structures for spacecraft and aircraft applications. *Composite structures*, 76(1-2):182–189, 2006.

[12] J. L. Phillips and Z. Gürdal. Structural analysis and optimum design geodesically stiffened composite panels. Technical report, NASA; CCMS-90-50 (VPI-E-90-08), 1990.

[13] A. D. Reddy, R. R. Valisetty, and L. W. Rehfield. Continuous filament wound grid stiffened composite structures for aircraft fuselages. *Journal of Aircraft*, 26(2):249–255, 1985.

[14] C. Gan, R. F. Gibson, and G. M. Newaz. Analytical/experimental investigation of energy absorption in grid-stiffened composite structures under transverse loading. *Experimental Mechanics*, 44(2):185–194, 2004.

[15] P. Jadhav and P. R. Mantena. Parametric optimization of grid-stiffened composite panels for maximizing their performance under transverse loading. *Composite Structures*, 77(3):353–363, 2007.

[16] G. Marsh. Composites lift off in primary aerostructures. *Reinforced Plastics*, 48(4):22–27, 2004.

[17] S. Pociluyko, C. F. Griffin, I. Figge, and L. Blad. Composite material geodesic structures–A structural concept for increased helicopter blade survivability. *Presented at the 30th Annual National V/STOL Forum of the American Helicopter Society*, Washington, D.C., 1974.

[18] C. F. Griffin. Increased rotor blade survivability. Technical report, Lockheed-California Co. Burbank, CA; USAAMRDL-TR-75-6., 1975.

[19] J. Sumec and M. Wohland. *Regular Lattice Plates and Shells*. Elsevier, 1990.

[20] H. J. Chen and S. W. Tsai. Analysis and optimum design of composite grid structures. *Composite Materials*, 30(4):503, 1996.

[21] D. R. Ambur and L. W. Rehfield. Effect of stiffness characteristics on the response of composite grid-stiffened structures. *Journal of Aircraft*, 30(4):541–546, 1993.

[22] B. Grail and Z. Gürdal. Structural analysis and design of geodesically stiffened composite panels with variable stiffener distribution. Technical report, NASA; NASA-CR-190608, 1992.

[23] D. R. Ambur, N. Jaunky, and N. F. Knight. Optimal design of grid-stiffened composite panels using global and local buckling analysis. Technical report, NASA–96N24094; ID: 19960020545; AIAA Paper 96-1581., 1996.

[24] N. Jaunky, N. F. Knight, and D. R. Ambur. Formulation of an improved smeared stiffener theory for buckling analysis of grid-stiffened composite panels. *Composites Part B, Engineering*, 27(5):519–526, 1996.

[25] S. Kidane. Buckling analysis of grid stiffened composite structures. Master's thesis, Louisiana State University., 2002.

[26] W. J. Stroud, W. H. Greene, and M. S. Anderson. *Buckling Loads of Stiffened Panels Subjected to Combined Compression and Shear: Results Obtained with PASCO, EAL, and STAGS Computer Programs*, volume 2215. NASA, TP, 1984.

[27] Z. Gürdal and G. Gendron. Optimal design of geodesically stiffened composite cylindrical shells. *Composites Engineering*, 3(12):1131–1147, 1993.

[28] C. Collier, P. Yarrington, and B. Van West. Composite, grid-stiffened panel design for post buckling using hypersizer®. *AIAA*, 1222:2002, 2002.

[29] D. Bushnell. PANDA2–Program for minimum weight design of stiffened, composite, locally buckled panels. *Computers & structures*, 25(4):469–605, 1987.

[30] D. J. Dawe. Finite strip buckling analysis of curved plate assemblies under biaxial loading. *International Journal of Solids and Structures*, 13(11):1141–1155, 1977.

[31] B. O. Almroth and F. A. Brogan. The stags computer code. Technical report, NASA CR-2950, NASA Langley Research Center, 1978.

[32] S. Venkataraman. *Modeling, analysis and optimization of cylindrical stiffened panels for reusable launch vehicle structures*. PhD thesis, University of Florida, 1999.

[33] S. Kidane, G. Li, J. Helms, S. S. Pang, and E. Woldesenbet. Buckling load analysis of grid stiffened composite cylinders. *Composites Part B*, 34(1):1–9, 2003.

[34] D. L. Block, M. F. Card, and M. M. Mikulas Jr. Buckling of eccentrically stiffened orthotropic cylinders. *NASA TN D-2960*, 1965.

[35] T. C. Soong. Buckling of cylindrical shells with eccentric spiral-type stiffeners. *AIAA Journal*, 7:65–72, 1969.

[36] J. N. Reddy and J. H. Starnes Jr. General buckling of stiffened circular cylindrical shells according to a layerwise theory. *Computers & structures*, 49(4):605–616, 1993.

[37] N. Jaunky, N. F. Knight, and D. R. Ambur. Buckling analysis of anisotropic variable-curvature panels and shells. *Composite structures*, 43(4):321–329, 1998.

[38] Dassault Systèmes Simulia Corp. *ABAQUS Documentation, Version 6.8*. USA, 2008.

[39] J. C. Halpin and J. L. Kardos. The halpin-tsai equations: a review. *Polymer Engineering and Science*, 16(5):344–352, 1976.

[40] B. K. Donaldson. *Analysis Of Aircraft Structures–An Introduction*. New York: McGraw-Hill, 1993.

[41] J. Li, R. K. Kapania, and H Kapoor. Optimal design of unitized panels with curvilinear stiffeners. *Proceedings of the AIAA ATIO Conference*, September 26–29, 2005.

[42] W. Wunderlich and W. D. Pilkey. *Mechanics of Structures: Variational and Computational Methods*. CRC Press., 2003.

[43] J. F. Doyle. *Static and Dynamic Analysis of Structures: with an Emphasis on Mechanics and Computer Matrix Methods*. Kluwer Academic Publishers, 1991.

[44] S. P. Timoshenko and J. N. Goodier. *Theory of Elasticity*. 3rd ed., McGraw-Hill, New York, 1970.

[45] C. W. Bert. Simplified analysis of static shear factors for beams of nonhomogeneous cross section. *Journal of Composite Materials*, 7:525–529, 1973.

[46] L. T. Tenek and J. H. Argyris. *Finite Element Analysis for Composite Structures*, volume 59. Kluwer Academic Pub, 1998.

[47] J. M. Whitney and Ashton J. E. *Structural Analysis of Laminated Anisotropic Plates*. CRC, 1987.

[48] Z. P. Bazant and L. Cedolin. *Stability of Structures*. Oxford University Press, New York, 1991.

[49] L. P. Kollár and G. S. Springer. *Mechanics of Composite Structures*. Cambridge University Press, 2003.

[50] V. Haktanir and E. Kiral. Statical analysis of elastically and continuously supported helicoidal structures by the transfer and stiffness matrix methods. *Computers & Structures*, 49(4):663–677, 1993.

[51] F. N Gimena, P. Gonzaga, and L. Gimena. Stiffness and transfer matrices of a non-naturally curved 3d-beam element. *Engineering Structures*, 30(6):1770–1781, 2008.

[52] E. Kreyszig. *Advanced Engineering Mathematics, 9th Edition*. John Wiley, 2005.

[53] W. Schelter and Maxima Users & Developers Group. Maxima: A computer algebra system. `http://maxima.sourceforge.net`.

[54] D. O. Brush and B. O. Almroth. *Buckling of Bars, Plates, and Shells*. McGraw-Hill New York, 1975.

[55] R. M. Jones. Buckling of circular cylindrical shells with multiple orthotropic layers and eccentric stiffeners. *AIAA Journal*, 6:2301–2305, 1968.

[56] W. Flügge. *Stresses in Shells*. Springer-Verlag, Berlin and New York, 1973.

[57] M. Baruch, J. Singer, and T. Weller. Effect of eccentricity of stiffeners on the general instability of cylindrical shells under torsion. *Performer: Technion - Israel Inst of Tech Haifa Dept of Aeronautical Engineering.1 Dec 1965.2p.Report: AFOSR66-1365*, 1965.

[58] L. R. Calcote. *The Analysis of Laminated Composite Structures*. Van Nostrand Reinhold, New York, 1969.

[59] V. Yildirim. Governing equations of initially twisted elastic space rods made of laminated composite materials. *International Journal of Engineering Science*, 37(8):1007–1035, 1999.

[60] V. Yildirim. Free vibration of uniaxial composite cylindrical helical springs with circular section. *Journal of sound and vibration*, 239(2):321–333, 2001.

[61] S. Cheng and B. P. C. Ho. Stability of heterogeneous aeolotropic cylindrical shells under combined loading. *AIAA Journal*, 1(4):892–8, 1963.

[62] J. Singer, M. Baruch, and O. Harari. On the stability of eccentrically stiffened cylindrical shells under axial compression. *International Journal of Solids and Structures*, 3(4):445–470, 1967.

[63] R. F. Crawford and D. B. Schwartz. General instability and optimum design of grid-stiffened spherical domes. *AIAA Journal*, pages 3–511, 1965.

[64] R. Milligan, G. Gerard, C. Lakshmikanthan, and H. Becker. General instability of orthotropically stiffened cylinders under axial compression. *AIAA Journal*, 4:1906–1913, 1966.

[65] S. Kidane, G. Li, J. Helms, S. S. Pang, and E. Woldesenbet. Buckling load analysis of grid stiffened composite cylinders. *Composites Part B: Engineering*, 34(1):1–9, 2003.

[66] M. P. Nemeth. A treatise on equivalent-plate stiffnesses for stiffened laminated-composite plates and plate-like lattices. Technical report, NASA/TP-2011-216882, 2011.

[67] R. R. Meyer. Buckling of 45° eccentric stiffened waffle cylinders. *Journal of the Royal Aeronautical Society*, 71:516, July 1967.

[68] D. L. Block. Buckling of eccentrically stiffened orthotropic cylinders under pure bending. Technical report, NASA TN D-3351, DTIC Document, 1966.

[69] C. W. Bert and C. D. Kim. Analysis of buckling of hollow laminated composite drive shafts. *Composites Science and Technology*, 53(3):343–351, 1995.

[70] Sanders J. L. *An Improved First-approximation Theory for Thin Shells*. NASA Report, 1959.

[71] A. W. Leissa. Buckling of laminated composite plates and shell panels. Technical report, Ohio State Univ. Research Foundation, Columbus (USA), 1985.

[72] D. R. Ambur and N. Jaunky. Optimal design of grid-stiffened panels and shells with variable curvature. *Composite Structures*, 52(2):173–180, 2001.

[73] M. S. Qatu. *Vibration of laminated shells and plates*. Academic Press, 2004.

[74] P. M. Weaver, J. R. Driesen, and P. Roberts. Anisotropic effects in the compression buckling of laminated composite cylindrical shells. *Composites Science and Technology*, 62:91–105, 2002.

[75] K. A. Lou and G. Yaniv. Buckling of circular cylindrical composite shells under axial compression and bending loads. *Journal of Composite Materials*, 25(2):162–187, 1991.

[76] K. F. Wong and P. M. Weaver. Approximate solution for the compression buckling of fully anisotropic cylindrical shells. *AIAA journal*, 43(12):2639–2645, 2005.

[77] N. Jaunky and N. F. Knight Jr. An assessment of shell theories for buckling of circular cylindrical laminated composite panels loaded in axial compression. *International journal of solids and structures*, 36(25):3799–3820, 1999.

[78] N. Jaunky, N. F. Knight Jr, and D. R. Ambur. Optimal design of general stiffened composite circular cylinders for global buckling with strength constraints. *Composite Structures*, 41(3-4):243–252, 1998.

[79] D. A. Reddy, R. R. Valisetty, and W. L. Rehfield. Continuous filament wound composite concepts for aircraft fuselage structures. *Proceedings of the 25th AIAA/ASME/ASCE/AHS/ASC Structures, Structural Dynamics, and Materials Conference*, Palm Springs, CA., May 1984.

[80] M. W. Hyer and S. R. White. *Stress Analysis of Fiber-Reinforced Composite Materials*. McGraw-Hill New York, 1998.

[81] S. W. Tsai and E. M. Wu. A general theory of strength for anisotropic materials. *Journal of Composite Materials*, 5(1):58, 1971.

[82] C. Kim and S. R White. Analysis of thick hollow composite beams under general loadings. *Composite Structures*, 34(3):263–277, 1996.

[83] L. W. Rehfield, A. R. Atilgan, N. Scholar, and D. H. Hodges. Nonclassical behavior of thin-walled composite beams with closed cross sections. *Journal of the American Helicopter Society*, 35:42, 1990.

[84] J. S. Sandhu, K. A. Stevens, and G. A. O. Davies. Torsional buckling and post-buckling of composite geodetic cylinders with special reference to joint flexibility. *Composite Structures*, 15:301–322, 1990.

[85] A. Takano. Improvement of flügge's equations for buckling of moderately thick anisotropic cylindrical shells. *AIAA Journal*, 46(4):903–911, 2008.

[86] A. Takano. Buckling of thin and moderately thick anisotropic cylinders under combined torsion and axial compression. *Thin-Walled Structures*, 49(2):304–316, 2011.

[87] O. Montagnier and C. Hochard. Optimisation of a high speed rotating composite drive shaft using a genetic algorithm-hybrid high modulus-high resistance carbon solutions. *Arxiv preprint arXiv:1110.1628*, 2011.

[88] M. Buragohain and R. Velmurugan. Study of filament wound grid-stiffened composite cylindrical structures. *Composite Structures*, 93(2):1031–1038, 2011.

[89] J. N. Reddy. *Mechanics of laminated composite plates: Theory and Analysis*. CRC Press, Inc., 1997.

Vita

Sreenivas Narayanan Nampy

Sreenivas Narayanan was born on May 20, 1976 in the state of Kerala, India. After earning a Bachelor's degree in Civil Engineering in 1997 from College of Engineering, Trivandrum, University of Kerala., he worked in several projects related to civil engineering structures. In 2003, he joined the department of Aerospace Engineering at Penn State to pursue his Master's degree, where he conducted research under the guidance of Prof. Edward C. Smith. He worked on flexible matrix composite tiltrotor blade analysis and design, exploring various elastic coupling effects for passive deflection controls.

After completing his MS in Aerospace Engineering, he started his doctoral research in the late December of 2006 under Prof. Edward C. Smith. His research focused on advanced grid-stiffened composite design concepts for applications in heavy-lift helicopter rotor blades. He has been an active member of American Institute of Aeronautics and Astronautics and American Helicopter Society. He is currently employed with UTC Aerospace Systems in San Diego, California.

Selected publications

S N. Nampy and E C. Smith., "An Innovative Structural Design Concept for Heavy–Lift Rotor Blades," *Presented at the Technical Specialist's Meeting on Rotorcraft Structures and Survivability*, Williamsburg, VA, Oct 27–29, 2009.

Nampy, S. N. and Smith, E. C., "Structural Behavior of Grid–Stiffened Tubes under Axial, Bending, and Torsion Loads," *Proceedings of the 49th AIAA/ASME/ASCE/AHS/ASC Structures, Structural Dynamics, and Materials Conference*, April 7–10, 2008, Schaumburg, IL.

Nampy, S. N. and Smith, E. C., "Thermomechanical Behavior and Experimental Testing of Flexible Matrix Composite Box–Beams with Extension–Twist Coupling," *Proceedings of the 47th AIAA/ASME/ASCE/AHS/ASC Structures, Structural Dynamics, and Materials Conference*, May 1–4, 2006, Newport, RI.

Nampy, S. N. and Smith, E. C., "Design Evaluation of Model and Full Scale Flexible Matrix Composite Tiltrotor Blades with Extension–Twist Coupling," *Proceedings of the American Helicopter Society 62nd Annual Forum*, Phoenix, AZ, May 9–11, 2006.

Nampy, S. N. and Smith, E. C., "Extension–Twist Coupled Tiltrotor Blades Using Flexible Matrix Composites," *Proceedings of the 46th AIAA/ASME/ASCE/AHS/ASC Structures, Structural Dynamics and Materials Conference*, April 18–21, 2005, Austin, TX.